

REPORT DOCUMENTATION PAGE

Form Approved
OMB No. 0704-0188

Public reporting burden for this collection of information is estimated to average 1 hour per response, including the time for reviewing instructions, searching existing data sources, gathering and maintaining the data needed, and completing and reviewing the collection of information. Send comments regarding this burden estimate or any other aspect of this collection of information, including suggestions for reducing this burden, to Washington Headquarters Services, Directorate for Information Operations and Reports, 1215 Jefferson Davis Highway, Suite 1204, Arlington, VA 22202-4302, and to the Office of Management and Budget, Paperwork Reduction Project (0704-0188), Washington, DC 20503.

| | | | |
|--|--|---|----------------------------------|
| 1. AGENCY USE ONLY (Leave Blank) | 2. REPORT DATE 8 July 2004 | 3. REPORT TYPE AND DATES COVERED final, 15 May 2000 to 31 March 2004 | |
| 4. TITLE AND SUBTITLE Boundary Layer Turbulence Measurements -- at Submarine Scale Reynolds Numbers -- to Support RANS Model Validation and Development | | 5. FUNDING NUMBERS G N00014-00-1-0753 | |
| 6. AUTHORS Joseph C. Klewicki | | | |
| 7. PERFORMING ORGANIZATION NAME(S) AND ADDRESS(ES) University of Utah Department of Mechanical Engineering 50 South Central Campus Drive, Room 2110 Salt Lake City, Utah 84112 | | 8. PERFORMING ORGANIZATION REPORT NUMBER PFD-01-2004 | |
| 9. SPONSORING / MONITORING AGENCY NAME(S) AND ADDRESS(ES) Office of Naval Research 800 North Quincy Street Ballston Centre Tower One Arlington, VA 22217-5660 | | 10. SPONSORING / MONITORING AGENCY REPORT NUMBER | |
| 11. SUPPLEMENTARY NOTES | | | |
| 12a. DISTRIBUTION / AVAILABILITY STATEMENT Unlimited | | 12b. DISTRIBUTION CODE | |
| 13. ABSTRACT (Maximum 200 words) Existing laboratory facilities cannot simultaneously create boundary layers at submarine scale Reynolds numbers and measure the small-scale turbulent motions. Because of this, the detailed mechanisms for momentum transport in these flows remains poorly understood. To overcome these challenges, the present project made novel use of the atmospheric surface layer that flows over the salt plays of Utah's west desert to obtain well resolved turbulence measurements in boundary layers at submarine scale Reynolds numbers. A particular emphasis was the exploration of scale separation effects on the momentum transport. The project obtained well resolved measurements of velocity and vorticity fluctuations for a range of positions normal to the surface, as well as over a limited range of equivalent sand-grain roughnesses. The Reynolds number scaling behaviors of a number of statistics have been established. An important overarching result is that the motions contributing to both the Reynolds stress and its wall normal gradient shift from large to intermediate scales at high Reynolds numbers. An unanticipated outcome related to this finding was the development of a new theoretical framework for turbulent wall-flows based directly on the relative magnitudes of the stress gradients that appear in the mean momentum balance equation. | | | |
| 14. SUBJECT TERMS high Reynolds number turbulent boundary layers, turbulent momentum transport, well-resolved wall turbulence measurements, scale separation, multiscale analysis | | 15. NUMBER OF PAGES 172 | 16. PRICE CODE |
| 17. SECURITY CLASSIFICATION OF REPORT UNCLASSIFIED | 18. SECURITY CLASSIFICATION OF THIS PAGE UNCLASSIFIED | 19. SECURITY CLASSIFICATION OF ABSTRACT UNCLASSIFIED | 20. LIMITATION OF ABSTRACT UL |

NSN 7540-01-280-5500

Standard Form 298 (Rev. 2-89)
Prescribed by ANSI Std. Z39-1
298-102

Approved for Public Release
Distribution Unlimited

PROJECT FINAL REPORT

Boundary Layer Turbulence Measurements – at Submarine-Scale Reynolds Numbers – to Support RANS Model Validation and Development

by

J. C. Klewicki
Physical Fluid Dynamics Laboratory
Department of Mechanical Engineering
University of Utah
Salt Lake City, UT 84112

(July 8, 2004)

University of Utah Contacts:

Technical: Joseph C. Klewicki
Department of Mechanical Engineering, Room 2110 MEB, Salt Lake City, UT 84112
Tel: (801) 581-7934, Fax: (801) 585-9826
klewicki@eng.utah.edu

Business: Elliott Kulakowski, Director Research Administration
Office of Sponsored Projects, 1471 Federal Way, Salt Lake City, UT 84112
Tel: (801) 581-3003, Fax: (801) 581-3007
ospawards@osp.utah.edu

20040713 047

Technical Section

The following technical section contains an overview of the project objectives, a status of progress at its funding endpoint, a synopsis of the on-going and new findings during the last year of the project, as well as an appendix containing four of the more major journal manuscripts that resulted from the present grant.

Technical Objectives

Relative to low Reynolds number flows, boundary layer turbulence at submarine-scale Reynolds numbers ($R_\theta = U\theta/\nu = O(10^7)$, where U is the free stream velocity, θ is the momentum deficit thickness and ν is the kinematic viscosity) is poorly understood. This is because there currently exists no combination of laboratory experimental facilities and techniques that can simultaneously *i*) create an $R_\theta = O(10^7)$ boundary layer flow, and *ii*) measure the small scale turbulent motions. Owing to the difficulties in developing reliable measurement techniques to meet these challenges, this situation is likely to exist for a considerable time in the future. Furthermore, understanding the mechanisms that underlie the transport of the stresses requires the measurement of velocity gradients and/or vorticity. This presents an even greater demand on the developer of measurement techniques.

Through the novel use of the atmospheric surface layer flow over the salt playa of western Utah, the present grant is, for the first time, providing well resolved measurements of velocity and vorticity fluctuations in an $R_\theta = O(10^7)$ boundary layer flow.

As stated in the original grant proposal, the focus of the measurement program is to:

1. Establish the behavior of the wall layer turbulent stresses at high R_θ and under rough wall conditions relevant to submarines,
2. Quantify the flow mechanisms (including length and time scales) underlying the wall-normal gradients of the Reynolds stress and turbulent kinetic energy, and
3. Quantify the terms in the axial stress budget that describes the transport of $\langle u^2 \rangle$.

A description of the technical approach taken to obtain these objectives is given in the next section. This is followed by a presentation of the results found over the past year relevant to these goals

Technical Approach

Attaining the desired objectives requires that three major challenges be overcome. These three challenges, and the technical approach used to address them, are now discussed.

1. **Reynolds Number:** The first challenge is associated with attaining a Reynolds number and surface roughness condition that is relevant to Navy submarines. These conditions may be described as an $R_\theta = O(10^7)$ boundary layer over a surface having an equivalent sand grain roughness in the approximate range $200 < k^+ = k u_\tau / \nu < 600$, i.e., in the traditional "fully rough" regime. (Note that owing to the random, small-scale nature of the salt playa surface, it is believed to effectively mimic a true sand grain roughness.) Sodar measurements at the SLTEST facility in Utah's west desert under near neutral thermal stratification indicate that a typical

Reynolds number for the surface layer is $R_\theta = 5 \times 10^6$, Metzger et al. (2001). Furthermore, as the summer proceeds the surface dries and cracks yielding increasing roughness. Direct quantification of the downward shift in the mean profile indicates that k^+ values between 5 and 500 can be obtained, depending on the time during the summer in which the measurements are acquired, Priyadarshana and Klewicki (2001), Klewicki and Metzger (2002), Metzger et al. (2002a).

2. **Sensor Resolution:** The second challenge (and this is the most difficult to achieve) requires that the measurement sensors attain nondimensional temporal and spatial resolutions sufficient to accurately capture the properties of the turbulence. Given the objectives stated above, these requirements must be met for velocity sensors, as well as, velocity gradient/vorticity sensors. This latter requirement is significant, since the resolution requirements for vorticity measurements are generally more difficult to attain than for velocity. Developing results over the past 15 years indicate that for accurate velocity measurements a nondimensional sensor scale of less than about 10 viscous units is needed to fully reveal near-wall Reynolds number dependencies, (Klewicki and Falco 1990, DeGraff and Eaton 2000, Metzger and Klewicki 2001). Similarly, for vorticity measurements a number of studies suggest a sensor size between about 3 and 7 Kolmogoroff scales is sufficient (Wyngaard 1969, Klewicki and Falco 1990, Folz 1997). Except under high wind conditions (say, greater than about 8 m/s), measurements at the SLTEST facility utilizing typical millimeter scale sensors satisfy both of these criteria. Thus, the measurements of the present grant are of higher resolution than the vast majority of typical laboratory studies, but at about three orders of magnitude higher Reynolds number. As for temporal resolution, because of the low speeds at the SLTEST site (relative to typical wind tunnel studies), Kolmogoroff frequencies rarely exceed more than a couple kilohertz, and thus standard anemometry and data acquisition instrumentation are more than sufficient. Finally, regarding the measurement of velocity gradients and vorticity it is important to note that the PIs have extensive experience (e.g., Wallace and Foss 1995, Klewicki and Falco 1990).
3. **Mean Flow and Integral Parameter Characterization:** The third challenge is associated with the sufficiently accurate determination of the boundary layer integral parameters in the given flow. That is, even though the SLTEST site flow field exhibits unusual horizontal homogeneity and consistent wind patterns, it is unreasonable to expect that dauntingly subtle issues such as the current open questions concerning the power law versus log law form of the mean velocity profile can be resolved. As evidenced by the data herein, however, it is clear that many important properties of the structure of the turbulence can be revealed – especially relating to the important length and time scales of the flow. Given this, integral parameter characterizations, to provide context and for normalization purposes, are required. In this regard, the present work is employing a large number of auxiliary instruments. These include a minisodar (which has been used to verify the existence of a logarithmic profile out to δ^+ about 1×10^6 , Metzger et al. 2001), sonic anemometer arrays (which provide mean velocity measurements up to about 5m, as well as, provide a means of estimating u_τ), a quartz thermometer array (that provides data relevant to determining thermal stability), and a 2.3m drag plate that gives an independent estimate of the skin friction.

Progress

Experimental efforts of 2002/2003 have focused on:

1. Continuing characterization of the mean and integral properties of the flow,

2. Continuing characterization of the wall layer turbulent stresses,
3. Determining the relevant turbulent length and time scale distributions, and their agreement/deviations from theoretical (locally isotropic) predictions, and
4. Determining the properties of the vorticity fluctuations and the velocity vorticity correlations associated with the gradients of the Reynolds stress and turbulent kinetic energy.

In addition, significant progress relating to the theoretical/physical description of boundary layer turbulence with increasing Reynolds number has been made. These results, largely revealed by the mean momentum balance data of Zagorola and Smits (1997) and DeGraaff and Eaton (2000), are shown to have a highly nontrivial impact on the interpretation, characterization and classification of rough-wall boundary layers with increasing Reynolds number.

Results relating to these efforts are now summarized and/or presented. In particular, results relating to items 1-4 above that are emerging from the totality of efforts of the grant to date are primarily summarized. These results, further confirmed by this year's results, are largely documented in the summary reports from years 1 and 2. These results, however, provide a useful context for better understanding the potential implications of the new theoretical findings. Other results, relating to the spectral characteristics of high Reynolds number boundary layer turbulence and spectral energy transfer across wavenumbers.

Continuing Results

Mean Flow Properties and Turbulent Stresses:

Analysis of 2002 field experiments, as well as continuing analysis of data derived from previous years Metzger and Klewicki (2001), Metzger (2002) and Klewicki and Metzger (2002), indicate that (to within experimental scatter) the inner normalized mean velocity profile at the SLTEST site shows a logarithmic variation with height. For the (nearly) smooth wall case, the data of Fig. 1 (from Metzger et al. 2002b) clearly show this to be the case. Furthermore, as shown in the 2002 yearly report, mean flow data at the site show the expected downward shift with increasing roughness. Relative to the issue of interpreting SLTEST data as being sampled from a canonical turbulent boundary layer, both the data of Fig. 1 and the downward shift are deemed particularly significant. This is because both of the logarithmic dependence and a consistent downward shift have been simultaneously observed in hot-wire and sodar measurements over the normalized range of wall-normal distances $2 < y^+ < 1,000,000$. Relevant to potentially significant buoyancy effects, these observations provide strong evidence that under near-neutral conditions the atmospheric surface layer at the SLTEST site remains mechanically coupled to the surface shear stress. Regarding the identification of "near-neutral" conditions, considerable effort has been devoted to developing more precise criteria than typically utilized. For example, Fig. 2 shows that the during near-neutral conditions the friction velocity estimated from the Reynolds stress is in good agreement with that found from the 2.3 m SLTEST facility drag plate. Also, during these times the stability parameter, z/L (where L is the Monin-Obukhov length), consistently exhibits a linear temporal dependence. Lastly, it is worth noting that significant modifications were made to the drag plate over the past year. These improvements were implemented to reduce the frequency response and increase the reliability of the device. These involved switching from water to glycerol, reconfiguring the load cells such that they are in tension and thus hold the floating element in place, and reducing both the mass of the floating element and the liquid gap width. A forth-coming paper describing these modifications and their outcomes is under preparation.

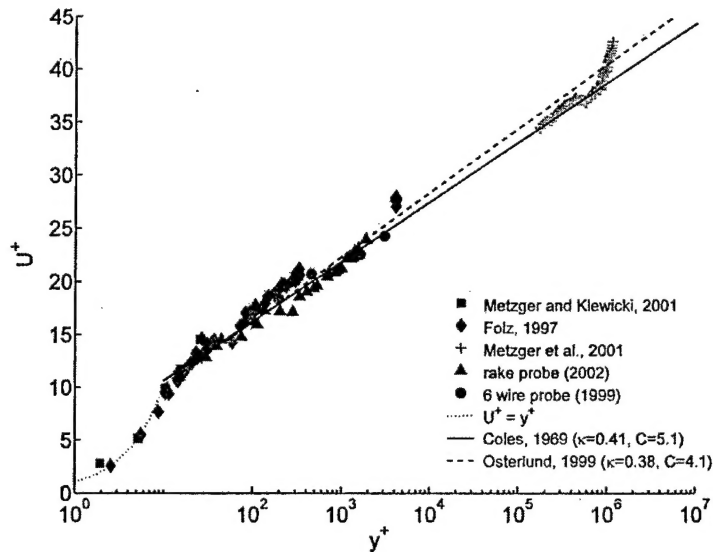


Figure 1. Inner normalized, near smooth-wall, mean velocity data derived from the SLTEST site, from Metzger et al. (2002b).

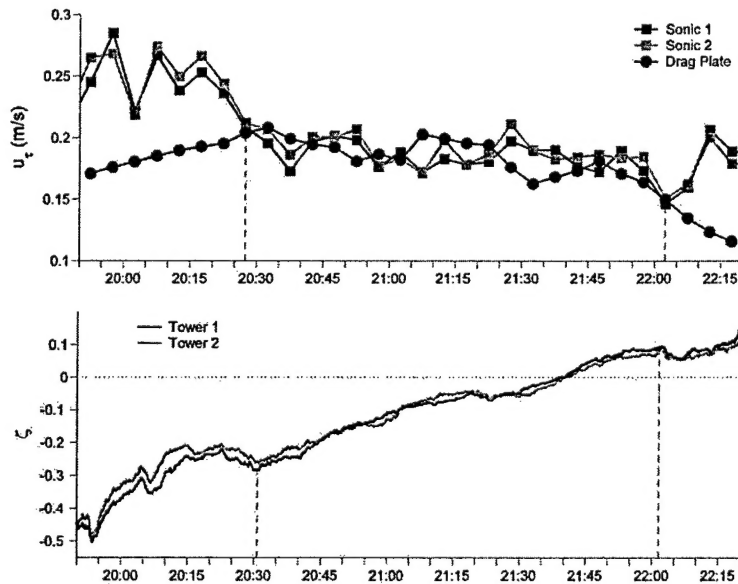


Figure 2. (a) Comparison of friction velocity estimates during near-neutral conditions at the SLTEST site. (b) Linear temporal dependence of $\zeta = z/L$, from Klewicki and Metzger (2002).

Overall, turbulent stress measurements indicate a mixture of roughness and Reynolds number effects. In remarkable agreement with the recent scaling behavior observed by DeGraaff and Eaton (2000), wall layer inner normalized axial intensities at the SLTEST site exhibit a significant and consistent increase with Reynolds number, but only a very mild dependence on surface roughness (for $k^+ < 500$), Metzger and Klewicki (2001), Klewicki et al. (2001). This was exemplified by 2002 measurements using a 15 sensor rake of single wire sensors (see Fig. 3). With regard to the data of Fig. 3, it is also interesting note that both the previous six wire sensor measurements and the 2002 rake data provide some evidence of a slight secondary peak near $y^+ = 2000$. A secondary peak in the axial intensity profile has been observed in other turbulent wall-flow studies (e.g., Morrison et al. 2002), but these studies may have been

influenced by diminished sensor resolution with increasing Reynolds numbers. Confirmation of this observation thus awaits further data and analysis. (The y^+ position of this possible peak at the given Reynolds number is especially intriguing in light of our recent theoretical advancements, see below). In this regard, preliminary indications are that the recently acquired 2003 data (using a 23 sensor rake) are plentiful and of very good quality.

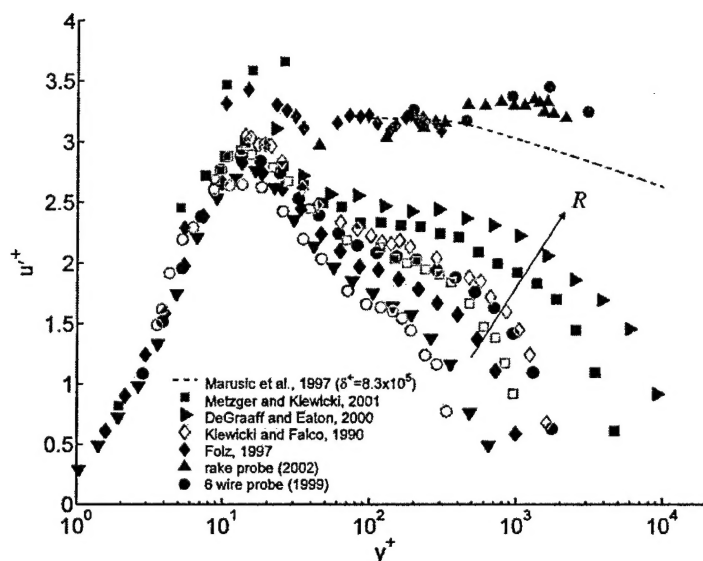


Figure 3. Comparison of SLTEST inner normalized axial intensities (as primarily derived from rake-probe measurements) with lower Reynolds number studies, from Metzger et al. (2002).

As discussed in the 2001/2002 yearly report, in contrast to the axial intensities, the inner normalized wall-normal intensity profile appears to be essentially R_θ independent (for R_θ greater than about 2000). These same data, however, show an apparent sensitivity to increasing roughness, Priyadarshana (2003). The inner normalized spanwise velocity intensities appear to have an R_θ dependence similar to that shown by the axial intensities, but further measurements (and analysis of existing measurements) are required to clarify this observation. Measurements of the Reynolds shear stress correlation coefficient at the SLTEST site consistently indicate smaller values (0.25 - 0.3) than those typically observed for low R_θ boundary layers. (For example, the University of Utah 2001 field measurements yielded a correlation coefficient of about 0.27, while the MSU 2002 data indicate a value of 0.3.) This result is broadly consistent with Townsend's (1961) notion of the inactive component of the turbulence increasing in intensity with increasing R_θ .

Vorticity and Velocity Vorticity Products:

To within the scatter of the data, the measured spanwise vorticity intensities appear to scale reasonably with inner variables regardless of the value of k^+ (for the range of k^+ and y^+ values explored), Priyadarshana (2003). Similar observations have been made with regard to the wall-normal vorticity intensities. Further measurements (replications and y^+ locations) of ω_y are, however, required to solidify this result. More importantly, both spanwise vorticity event durations and wall layer (for y^+ less than about 2000) spectra of the spanwise vorticity exhibit a nearly perfect Reynolds number independence when normalized by the Taylor scale (as opposed to either inner or outer normalization). Evidence of this scaling, from Priyadarshana and Klewicki (2002), is shown in Fig. 4.

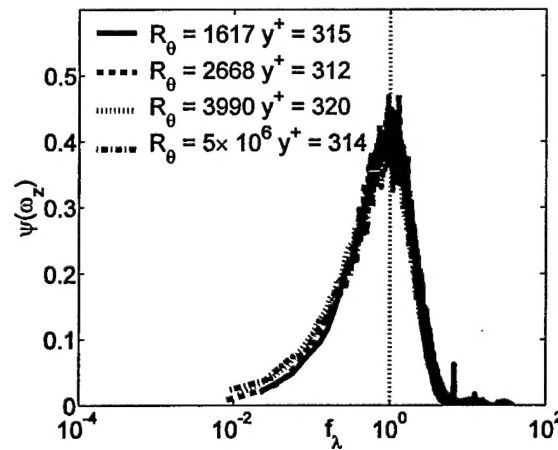


Figure 4. Premultiplied spanwise vorticity frequency spectra normalized by the Taylor microscale, from Priyadarshana and Klewicki (2002).

This observation is given further significance in that the peak in the co-spectra of v and ω_z (and for that matter u and ω_z) at high Reynolds number (and for y^+ less than about 2000) essentially tracks the spectral peak in ω_z , and that this peak occurs at or near the Taylor scale. Examples of these are explicitly shown in Figs. 5 and 6. Thus, given the direct connection between $\langle v\omega_z \rangle$ and the Reynolds stress gradient appearing in the mean momentum equation, these results strongly suggest that the mechanisms underlying momentum transport are of increasingly small scale (relative to the integral scales) with increasing R_θ and that these motions scale with the Taylor scales. (Interestingly, the spectra of the dominant transport terms in the axial stress and scalar variance transport equations also consistently exhibit peak at the Taylor scale, Metzger et al. 2002b) At present, it remains unclear whether the behavior of these spectral peaks is maintained at farther distances from the wall. That is, a more limited set of measurements at larger y^+ provide evidence that the spectral shapes begin to change for y^+ greater than about 3000. These involve the appearance of a second peak, at much lower frequency, in both the $w\omega_y$ and $v\omega_z$ cospectra with increasing distance from the surface, Maher (2002), Priyadarshana (2003). Further observations are, however, needed to clarify these behaviors.

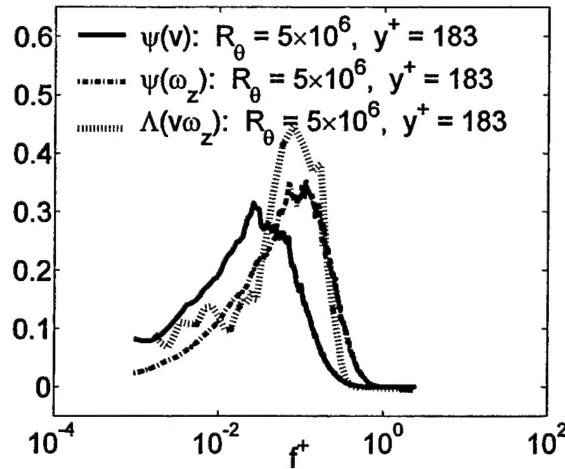


Figure 5. Premultiplied spectra of v and ω_z and the cospectra of v and ω_z .

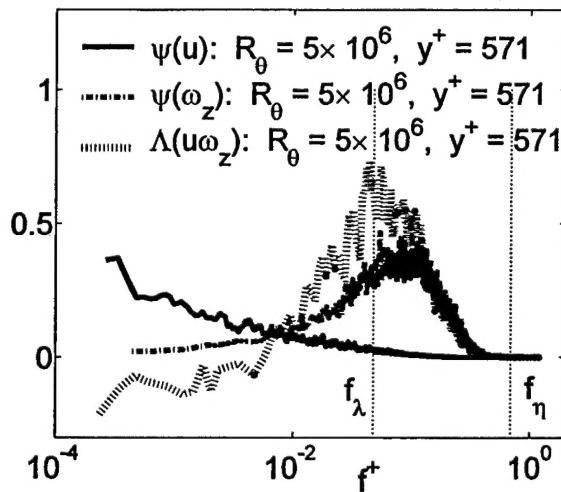


Figure 6. Premultiplied spectra of u and ω_z and the cospectra of u and ω_z .

Surface Pressure:

The surface pressure beneath a turbulent boundary layer has considerable significance to Navy applications. Unfortunately, laboratory-based measurements of surface pressure are plagued with experimental issues relating to, for example, facility noise and vibration. This, among other difficulties such as spatial resolution, has prevented the unambiguous identification of a number of the basic properties of the surface pressure. For example, from dimensional analysis one can show that there should be a k^{-1} region in the wall pressure spectra, and the extent of this layer should roughly scale with the depth of the logarithmic layer in the mean velocity profile, Bradshaw (1967). The aforementioned noise and vibration issues, however, have made it such that there are very few laboratory-based spectra that exhibit this fundamental property. Owing to the fact that the SLTEST flow is completely devoid of fan noise and facility vibration, microphone-based surface pressure fluctuations are exceptionally free of noise. Preliminary measurements at the SLTEST site (Klewicki and Miner 2002) indicate that inner normalized wall pressure intensities exhibit a strong Reynolds number dependence. Furthermore, the pressure spectra indicate virtually noise free signals covering 8 decades in amplitude, and about 2.5 decades of unambiguous k^{-1} behavior. Figure 7 provides an example wall pressure spectrum. The data manipulation involved in computing this spectrum consisted of applying the voltage to pressure

conversion and computing the Fourier transforms. That is, the integrity of the signal is reflected in the lack of need to filter or otherwise remove noise. Regarding these data it is also instructive to note that since k^{-1} behavior is coupled to the existence of a logarithmic layer, this clear feature of the SLTEST wall pressure provides further evidence that the SLTEST boundary layer is largely characteristic of a canonical high Reynolds number boundary layer flow. Such pressure measurements are clearly a unique contribution to the existing boundary layer literature, and thus further measurements are deemed warranted.

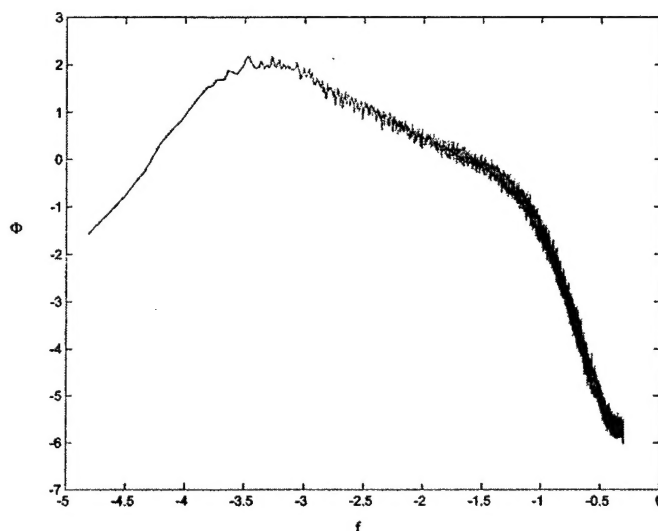


Figure 7. Inner normalized wall pressure spectrum.

New Theoretical Foundations and Their Implications for Rough-Wall High R_0 Flows

Previously unrecognized features relating to the fundamental properties of the boundary layer have been identified and characterized using existing high quality laboratory data sets (largely produced through Navy support). These properties have direct relation to, and strongly promote the validity of, the approach of the present study since they come about through the recognition that momentum transport is related to the stress gradients and not the stresses themselves. In what follows these results will be briefly presented, and their implication regarding rough-wall boundary layers described.

Depending on the ratio of the roughness height to the viscous length, rough wall boundary layers are (independent of Reynolds number) typically classified as hydraulically smooth ($k^+ < 5$), transitionally rough ($5 < k^+ < 70-90$) and fully rough $k^+ > 70-90$), e.g., Schlichting (1979), Ligrani and Moffat (1986). This characterization scheme is based on the observed behavior of the mean velocity profile with increasing normalized roughness height (for a limited range of Reynolds numbers). On the other hand, the effects of roughness on the statistical properties of the turbulent fluctuations are much less clear. For example, some studies indicate that roughness globally effects the turbulent stress field, while others indicate that the effects of roughness are essentially confined to the so-called "roughness sublayer:" the region of flow extending from about 3 to 5 mean roughness heights above the surface. Furthermore, a systematic description of the coupled effects of roughness and Reynolds number remains largely undocumented. (See, for example, the review of data in Piquet (1999).) During 2003, previously unrecognized properties of mean momentum balance were discovered. These have been elucidated in the recently submitted paper by Wei et al. (2003). From this, a new picture of turbulent wall flow structure (and its Reynolds number dependence) is revealed. This picture is derived directly from the mean

statement of Newton's second law. In contrast, the existing and universally held view is based on the structure of the stress field. Of direct significance to the present proposal is that this analysis indicates that previous studies of rough-wall layers have not included an important, Reynolds number dependent, dynamical length scale. This fact, in all likelihood, underlies the rather muddled (i.e., current) understanding of the statistical structure of turbulence in rough-wall layers.

Briefly, consideration of the mean differential momentum balance indicates that it is the stress gradients that are the significant quantities in establishing the net force on a differential fluid element. (In the equation for a channel flow there are three terms: viscous stress gradient, Reynolds stress gradient and a pressure gradient. For the boundary layer the pressure gradient term is replaced by a mean advection term.) It is not the stresses themselves. It is for this reason that the current grant predominantly focuses on the velocity vorticity products related directly to the Reynolds stress gradient. Based on the momentum equation, the *limiting conditions* for the momentum equation are that *i*) the three dynamical effects must all be in balance, or *ii*) have two terms nominally in balance with the third much smaller. Therefore, for the purpose of elucidating the mean momentum transport it is useful to examine the ratio of the gradient of the viscous stress to the gradient of the Reynolds stress. Thus if, for example, this ratio is much less than 1 then the viscous force is small and mean advection and Reynolds stress gradients are essentially in balance. If this ratio is $O(1)$, these effects are nominally in balance and the mean advection term is relatively small. And, if this ratio is greater than 1 the Reynolds stress gradients are small and the mean advection and viscous stress gradient terms approximately balance.

Figures 8 and 9 (from Wei et al. 2003) show the ratio of the gradient of the viscous stress to the gradient of the Reynolds stress for the flat plate boundary layer and channel flow respectively. Figure 8 uses the DNS results of Spalart (1988), and the experimental data of Degraaff and Eaton (2000), while figure 9 uses the DNS results of Moser et al. (1999). These figures show a thin sublayer ($0 < y^+ < 3$) where, in the boundary layer, mean advection and the viscous force dominate the balance equation. (In the channel the balance is between the pressure gradient and viscous stress gradient.) Outside this thin layer is a region clearly defined by a nearly perfect balance between the viscous and Reynolds stress gradients. The thickness of this stress gradient balance layer shows a clear Reynolds number dependence, extending well into the traditionally accepted logarithmic region of the mean velocity profile. Near the location of maximum Reynolds stress, y_p , the viscous force and mean advection (or pressure gradient) are, once again, nearly in balance. Around the peak Reynolds stress location the gradient of the viscous stress is much larger than the gradient of the Reynolds stress, although the Reynolds stress has a much greater magnitude than the viscous stress. For greater distances from the wall, the Reynolds stress gradient changes sign and the viscous stress gradient becomes much smaller than either the Reynolds stress gradient or the mean advection (pressure gradient) terms. In this region the Reynolds stress gradient and mean advection are essentially in balance. As noted in Wei et al. (2003), the primary difference between the boundary layer and channel (or pipe) flow is in the inner viscous advection layer (viscous sublayer) at low Reynolds number.

The behavior of the ratio of the two stress gradient terms, as shown in Figs. 8 and 9, suggests a four-layer description of the turbulent boundary layer. The first region is an inner viscous/advection balance layer where the viscous force becomes smaller while balancing mean advection. (Note that all of the terms in the momentum equation are zero at the wall in the zero pressure gradient boundary layer.) The second region is called the stress gradient balance layer. In this layer the viscous and Reynolds stress gradients are of nearly equal magnitude but opposite sign. The third region is a meso viscous/advection balance layer where the viscous force balances mean advection, while the Reynolds stress gradient is negligible. The fourth region is an inertial/advection balance layer where the Reynolds stress gradient balances mean advection, while the net viscous force is negligible. The sketch in Fig. 10 depicts these four layers at a fixed Reynolds number, while the data of Fig. 11 shows the Reynolds number dependence of the extent

of each layer under outer normalization (note that pipe and channel flow data are included on this plot). In Wei et al. (2003), the borders of the different regions are arbitrarily (but consistently) defined. In a follow-on, asymptotic analysis (Fife et al. 2003), these borders have been given analytical definition that is shown to be very close to those empirically prescribed by Wei et al.

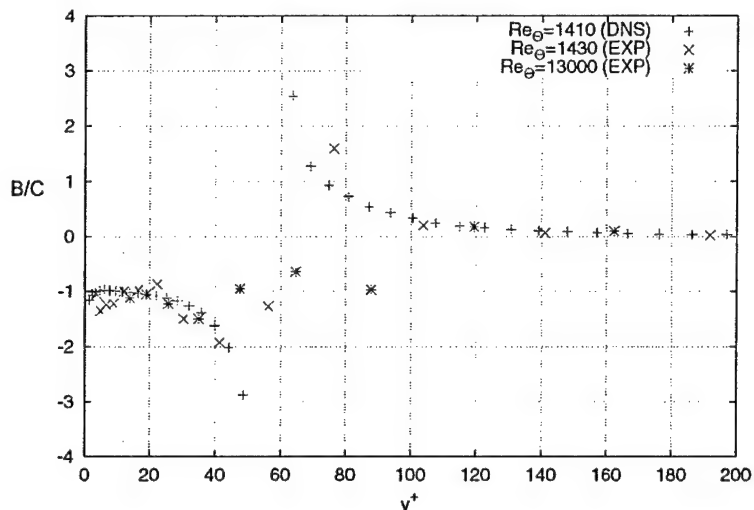


Figure 8. Ratio of the viscous stress gradient to the Reynolds stress gradient in flat plate turbulent boundary layers. Data are from DeGraaff and Eaton (2000) and Spalart (1988).

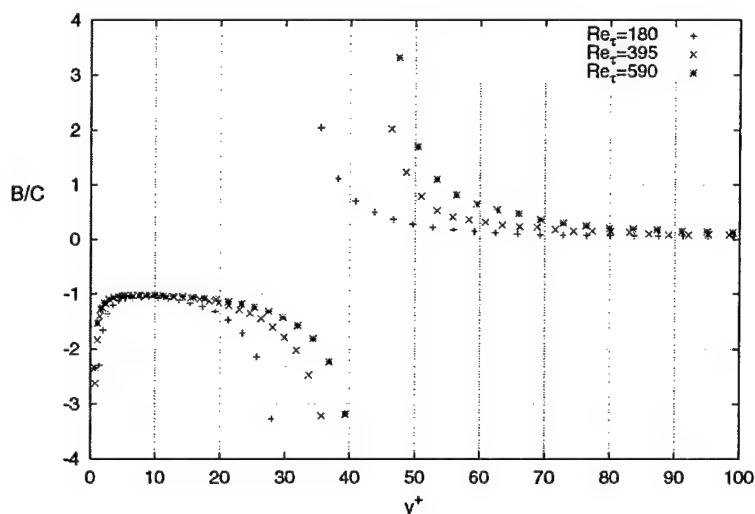


Figure 9. Ratio of the viscous stress gradient to the Reynolds stress gradient in turbulence channel flows. Data are from Moser et al. (1999).

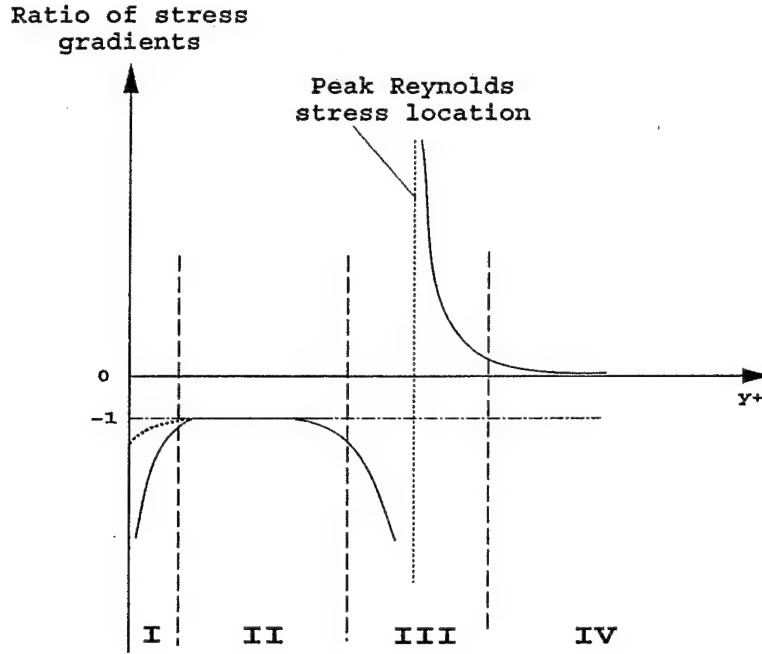


Figure 10. Sketch of the four layers of the turbulent wall-bounded flows for one Reynolds number; Layer I is the inner viscous/advection balance layer, layer II is the stress gradient balance layer, layer III is the viscous/advection balance meso-layer and layer IV is the inertial/advection balance layer. Note layer I in the zero pressure gradient turbulent boundary layer is different from that of channel and pipe flow in that all of the terms in the momentum equation are zero at the wall.

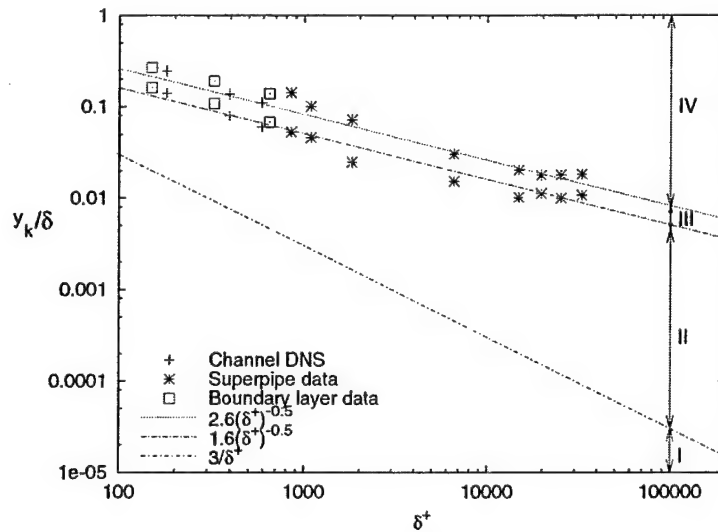


Figure 11. Reynolds number dependence of the outer-normalized physical extent of the four layers in canonical wall flows. The four layers ($k = \text{I, II, III, IV}$) are numbered according to the sketch of Fig. 11. Channel data are from Moser et al. (1999), pipe data are from Zagarola and Smits (1997) and turbulent boundary layer data are from Spalart (1988).

As is evident, all of the Reynolds number dependencies exhibited in Fig. 11 can be tied to the growth rate of the stress gradient balance layer. For this reason, a measure of the thickness of this layer, y_p , is identified as an important intermediate length since, like all similarity variables, it arises solely from the intrinsic dynamics of the problem. Along with the boundary layer thickness and the viscous length y_p is believed to constitute a fundamental length scale of boundary layer turbulence. As shown by Wei et al. (2003), the thickness of the stress gradient balance layer grows like the square root of the boundary layer thickness, which is also the same Reynolds number dependence as the classically defined Taylor microscale. This observation is felt significant, since, as clearly illustrated by the results from our current grant, many of the statistical properties of the variables relevant to momentum transport can be made invariant with Reynolds number when normalized by the Taylor scales.

While the full implications of the above results will probably not be revealed for quite some time, a number of ramifications relevant to rough-wall flows are readily apparent. The first one is that rough-wall boundary layers are clearly Reynolds number dependent in a manner much less trivial than prescribed by the notion that the boundary layer over a "smooth" surface will begin to exhibit roughness effects at sufficiently high flow speeds (i.e., Reynolds number). Thus, the aforementioned notions of hydraulically smooth, transitionally rough and fully rough are, in all likelihood, an incomplete set of characterizations that reflect boundary layer observations over only a moderate range of Reynolds numbers. Specifically, there is now good reason to expect that the ratio k/y_p is a significant parameter specifying roughness effects. (Note that for rough-wall layers, y_p should be measured from the mean (e.g., area averaged) roughness height in order for it to remain a good estimate of the thickness of the stress gradient balance layer.) Given this, the roughness regime $k/y_p = O(1)$ is likely to be associated with the accepted notion of fully rough flow for $k^+ > 70-90$, however, it is now seen that this regime is Reynolds number dependent, and thus the "fully rough" k^+ value will increase with Reynolds number when expressed in inner variables. This notion is given some support by the limited results of Ligrani and Moffat (1986), indicating that an increased roughness height (in viscous units) is required to have the same effect on flow field properties with increasing Reynolds number.

The emerging picture from the current research is that the wall-layer motions responsible for momentum transport scale with y_p with increasing Reynolds number. At its essence (and at a minimum) the roughness problem involves the imposition of an external length scale on wall layer dynamics. Given this, there are at least four broad roughness regimes that should be considered at any fixed high Reynolds number:

1. $k^+ < 3$ (i.e., less than the Layer I thickness in Fig. 10),
2. $k^+ > 3$ and simultaneously $k/y_p \ll 1$,
3. $k/y_p \sim 1$ and simultaneously $k/\delta \ll 1$, and
4. $k/y_p \gg 1$ and simultaneously $k/\delta \ll 1$,

where, as previously explained, under rough-wall conditions y_p is measured from the mean roughness height. At present, these are hypothesized to constitute a more complete set of roughness regimes than the broadly accepted notions of hydraulically smooth, transitionally rough and fully rough respectively. Implicit in these characterizations is the scale separation inherent to high Reynolds numbers. That is, at low Reynolds numbers the criteria of regimes 3 and 4 are impossible to simultaneously satisfy, while at moderate Reynolds number, the criteria of regime 3 cannot be satisfied. Physically, one might expect that at high Reynolds numbers regime 2 roughness would only cause subtle effects; even though k^+ could be quite large. To date, all of the SLTEST site measurements are from within regime 2. Consistent with this notion, observed roughness effects have been relatively small. With increasing roughness, however, there is likely to be a threshold at which the scale of the motions underlying momentum transport is

altered (\sim regime 3), while for even larger roughness, the scales of the vortical motions generating transport may be dominated by the imposed scales (\sim regime 4). Note also that for a relatively large range of k values wall-layer momentum transport will be modified (to varying degrees). Thus, the value of k and the position of the peak Reynolds stress are coupled according to the relevant internal flow dynamics generated; especially those dynamics in the roughness sublayer.

New Spectra-Based Results

Broadly, the above results indicate that the scales motion important to momentum transport undergo important variations with Reynolds number and are significantly altered by the presence of roughness. For this reason, a considerable effort over the past year has been devoted to quantifying the spectral characteristics of high Reynolds number, rough-wall, boundary layer turbulence, and the potential for modeling such flows using classical high R scaling ideas.

Universality/Nonuniversality of the High R_λ Velocity and Vorticity Fields

A prominent idea implicit in the characterization of high Reynolds number turbulence is the notion of local isotropy. In fact, its (approximate) assumption largely underlies the hoped-for success of Large Eddy Simulation techniques at high Reynolds numbers. From classical turbulence theory, it is rational to hypothesize that the small-scale properties of quite large Reynolds number flows exhibit universal behavior. In the study by Foss and Morris (2002), this idea was uniquely tested through the comparison of the spectral behaviors of the velocity and vorticity fluctuations in two high R_λ (~ 850) turbulent flows.

The two flows explored were the SLTEST site boundary layer and a large single stream shear layer. A summary of characteristic scales from the two flows is given in Table 1. A primary purpose of this effort was to explore whether the theoretical predictions of local isotropy satisfactorily described the small-scale properties of these flows, or whether there are significant differences relating to whether the turbulence is being sampled from a single stream shear layer or a boundary layer.

TABLE 1: QUANTITATIVE VALUES FROM THE TWO EXPERIMENTS

| | ABL | SSSL |
|--|-------------|-------------|
| $\lambda_v(\text{mm})$ | 13 | 12.2 |
| $\tilde{u} \text{ (m/sec)}$ | 1.02 | 1.17 |
| $\tilde{\omega}_z \text{ (sec}^{-1}\text{)}$ | 85 | 188 |
| $\eta_k(\text{mm})$ | 0.34 | 0.2 |
| $\delta y/\eta_k$ | ≈ 5 | ≈ 7 |

The spectral plots utilize a reference curve following that described by Pope (2000). Namely, if the x-component velocity power spectral density is fitted with the appropriate low-range, mid-range, high-range coefficients, then the isotropic relationships (as given in Pope 2000) allow all other spectra to be computed. The latter then serve as reference curves for the y-component velocity spectra and the ω_z spectra. The results of this analysis yielded the somewhat surprising outcome that, while the axial velocity spectra could be fit quite satisfactorily (over an extended wave number range) with theoretical spectra (Figure 12), spectral representations of the vertical velocity fluctuations (Figure 13), and especially the spanwise vorticity fluctuations not only showed considerable deviations from the locally isotropic prediction, but large differences (e.g., Figures 14 and 15) between the two high R_λ flows.

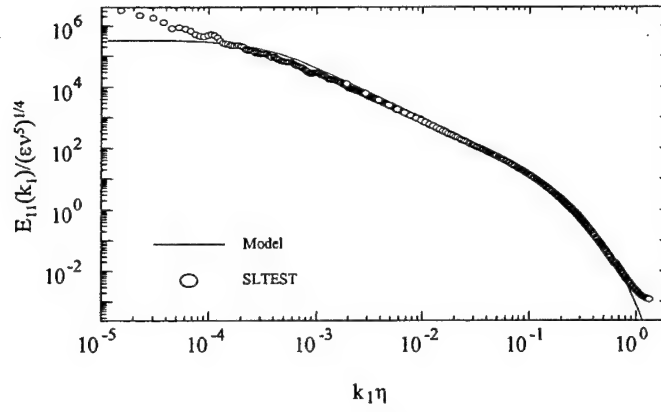


Figure 12. Non-dimensional PSD for u' from the SLTEST flow.

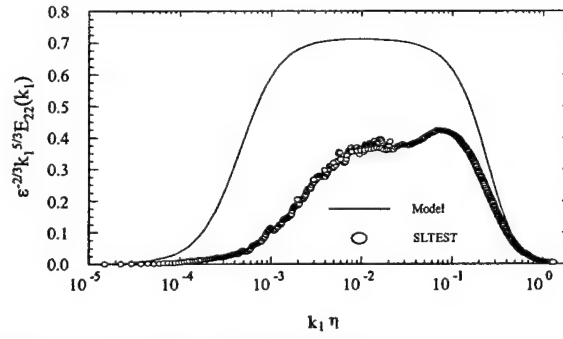


Figure 13. Non-dimensional PSD for v' from the SLTEST flow.

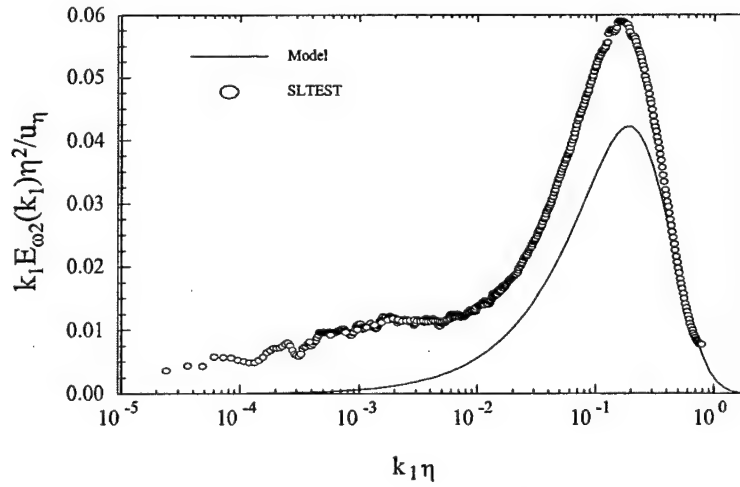


Figure 14. Pre-multiplied, non-dimensional spanwise vorticity PSD, ABL

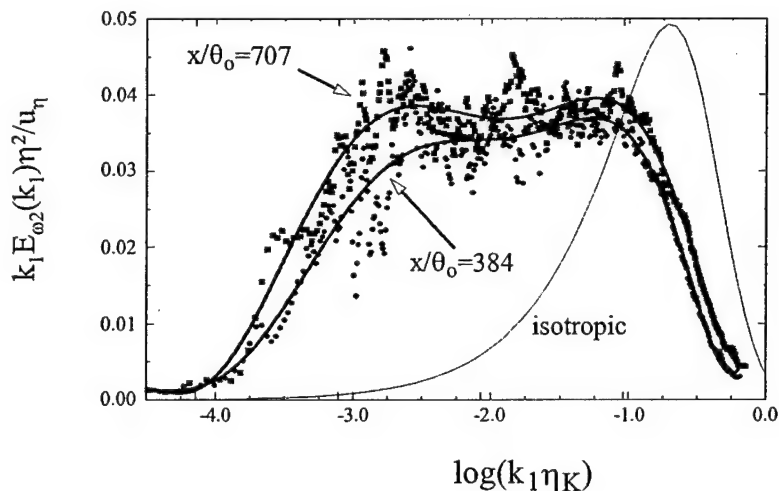


Fig. 15: Pre-multiplied, non-dimensional spanwise vorticity PSD from the single stream shear layer.

The essential message of this contribution is that dramatically different pre-multiplied spectral distributions of vorticity are evidenced for these two flows. It must be inferred that the large scale attributes of the single stream shear layer and the atmospheric surface layer are manifest in the high wave number vorticity field properties in contrast with the understanding that would have been inferred from the similarity in the velocity field spectra in these two high R_λ flows. Given that the stress gradients in these flows are related to the correlation between the velocity and vorticity fields (e.g., Klewicki et al. 1994), this result is likely to have significant bearing on the efficacy of the local isotropy assumption in developing widely applicable models of momentum transport at high Reynolds number. Clearly, further investigation of the rather far-reaching implications of these results is warranted.

Spectral Energy Transfer, u-v Cospectra, and Near-Wall u-spectra

A number of other efforts over the 2002/2003 year focused on understanding the behavior and scaling of wall layer spectra, as well as the nature of spectral energy transfer across wavenumbers. This latter point has connection to the development and understanding of LES methodologies, since the proper representation of the energy transfer between the resolved and subgrid scales is of considerable importance.

In order to better quantify possible Reynolds number dependencies in the scales of motion underlying the Reynolds stress, the u and v spectra and u-v cospectra have been computed and compared. Figures 16 and 17 show these results at high and low Reynolds numbers respectively. A particularly intriguing, and somewhat unexpected result, can be found by comparing the positions of the peaks in the premultiplied u and v spectra with the peak in the u-v cospectra. That is, at low Reynolds number, the position of the cospectral peak occurs nearer the peak in the u spectra, while at high Reynolds number the peak in the cospectra occurs much nearer (orders of magnitude) the peak in the v spectra. (Note that this observation appears to hold independent of distance from the wall.) In either case, the peak in the u spectra occurs near the integral time scale of the flow. Thus, contrary to the notion that the large scale eddies in the flow carry the bulk of the stress, the present results indicate that with increasing Reynolds number the scale of the motions underlying the stress shifts to intermediate scales. These results are currently being prepared for publication.

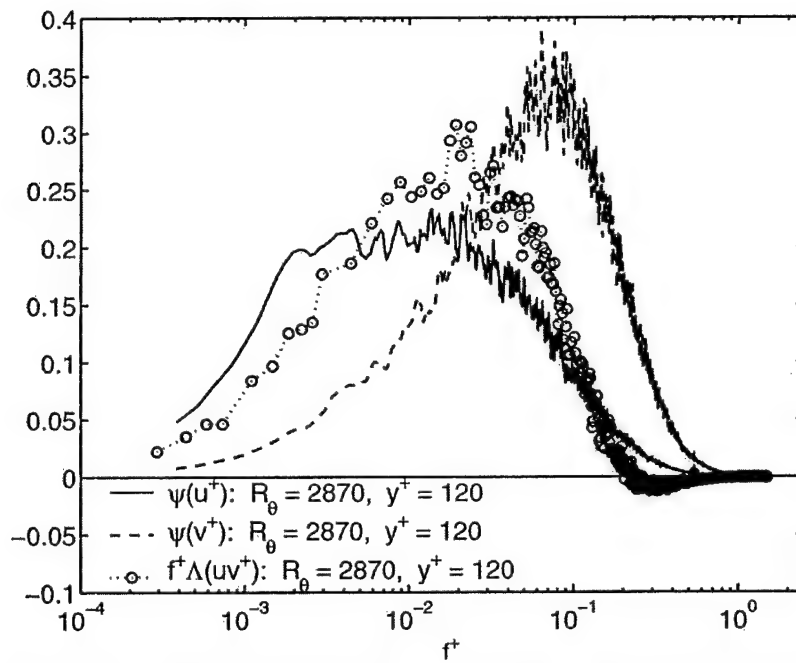


Figure 16. Inner normalized premultiplied spectra of u and v and $u-v$ cospectra at low Reynolds number.

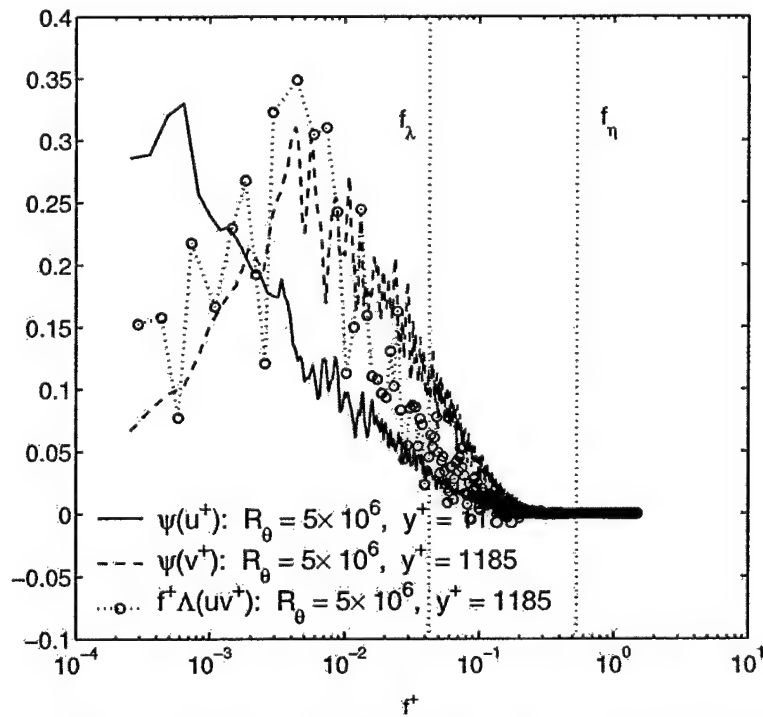


Figure 17. Inner normalized premultiplied spectra of u and v and $u-v$ cospectra at high Reynolds number.

Recent theoretical results by Wyngaard (2002) provide a means of representing the mean spectral energy transfer, Π , across wavenumber, k , using physical space rather than Fourier space variables. This computation requires the simultaneous quantification of velocity and velocity gradients, and thus the measurements in the present project provide the data needed to estimate the dominant contributions to Π . To explore the scales of motion having the greatest involvement in the energy transfer across a given wavenumber (frequency) at high Reynolds number, the mean spectral energy transfer rate was computed as a function of cut-off frequency for a variety of distances from the wall, Priyadarshana and Klewicki (2002b). Results of this procedure are shown in Figure 18. As can be seen, at each distance above the wall, the Π curve exhibits a distinct peak at intermediate frequencies, and this peak moves to lower frequencies with distance from the wall. Similarly, the turbulent transport term (gradient of the triple products) in the kinetic energy equation may be decomposed into contributions arising from resolved motions (below the cut-off frequency), subgrid motions (above the cut-off frequency) and from the cross-correlation between the resolved and subgrid scales, Wyngaard (2002). Representative results of these contributions as a function of cut-off frequency are shown in Figure 19. As expected, the contributions to the total transport from the resolved motions are dominant at high cut-off frequency, and the contributions from the subgrid motions dominate as the cut-off moves to lower frequencies. For all data examined thus far, the cross-term contribution is generally quite small. Another feature of note is that virtually all of the transport may be attributed to the resolved scales at a cut-off corresponding to the Taylor frequency. At any given position away from the wall, the contributions from the resolved and subgrid scales will be equal at a specific "cross-over" cut-off frequency. Generally consistent with the results of Fig. 18, the data of Fig. 20 show that this cross-over frequency moves to considerably lower values with increasing distance from the wall.

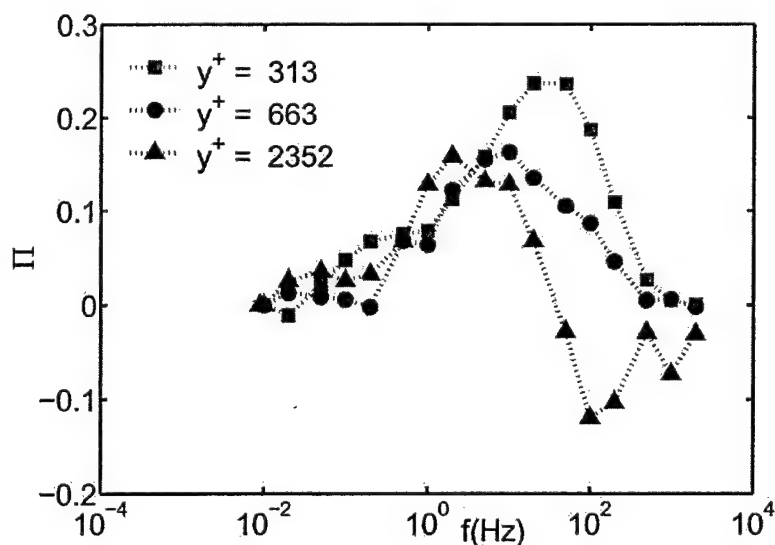


Figure 18. Estimates of the mean rate of spectra energy transfer in the SLTEST site boundary layer as a function of cut-off frequency for increasing distance from the wall.

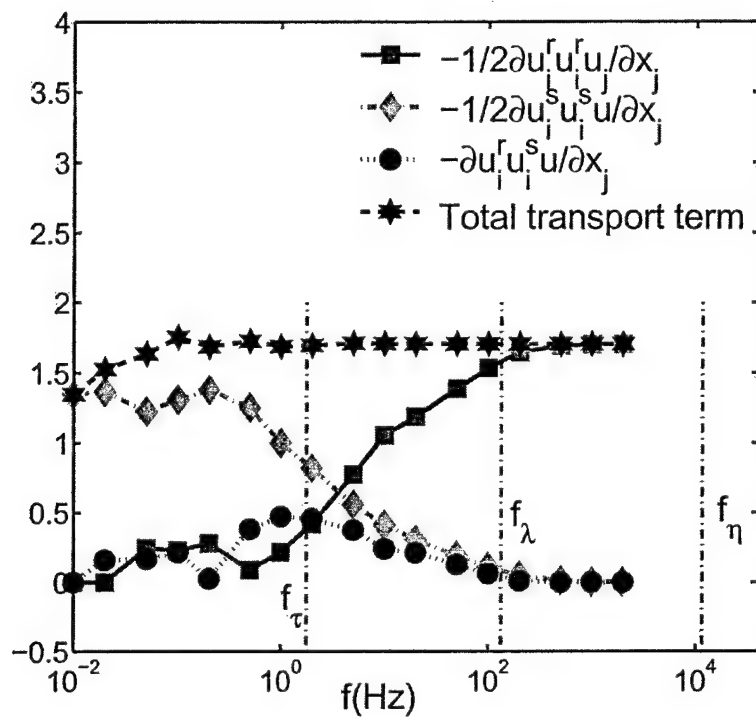


Figure 19. Representative distribution of contributions to turbulent transport as a function of cut-off frequency.

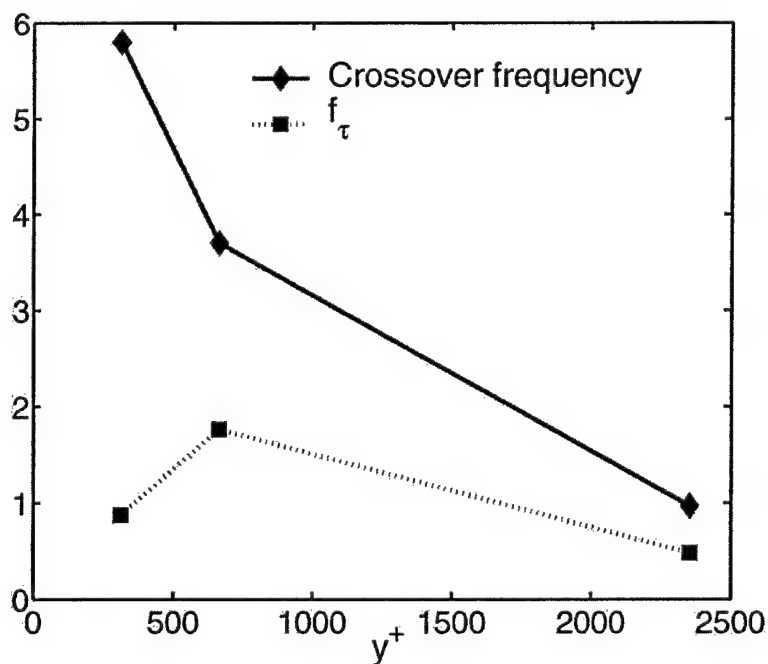


Figure 20. Cross-over frequency (frequency at which the subgrid and resolved scale contributions to turbulent transport are equal) as a function of distance from the wall.

In the 2002 field experiments a 15-wire rake of sensors was used to further explore the nature of the axial velocity fluctuations near the wall. A primary motivation for this experiment was to clarify whether or not a second peak exists in the axial intensity profile. Unfortunately, owing to instrumentation difficulties acquisition of a sufficient number of data sets to confidently address this question was not achieved. (As noted previously, however, the 2003 data sets show significant promise in regard to this issue.) The 2002 data were, however, sufficient to explore the spectral behavior of the u across the buffer layer and lower portions of the logarithmic layer. Of particular interest in this study was the appearance and extent of a k^{-1} region in the axial velocity spectra. This is because the motions supposed to underlie this spectral region are expected to be of very long axial extent (increasing so with increasing Reynolds number), and thus have connection with the observed logarithmic dependence of the magnitude of the axial intensity, Perry et al. (1986). In particular, it is commonly held that the motions corresponding to the k^{-1} region of the spectrum become increasingly dominant in the logarithmic layer. Figure 21, which compares high and low Reynolds number premultiplied spectra at $y^+ = 15$, shows that the high Reynolds number flow develops an extensive k^{-1} region. On the other hand, Figures 22 and 23, which show two different representations of the axial velocity spectra with increasing distance from the wall, indicate the complete disappearance of a k^{-1} region for $y^+ > 100$, and above y^+ values of about 45 the spectra scale with an intermediate range of frequencies. Overall it can be safely surmised that the spectra in these figures indicate a much richer set of results (some unexpected) than can be predicted by existing theory.

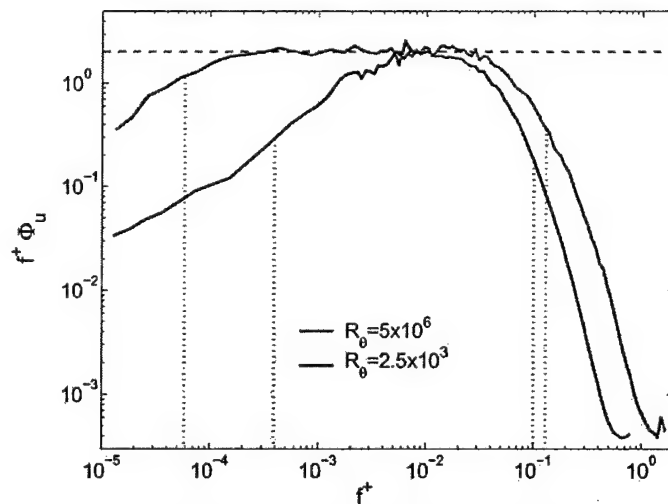


Figure 21. Inner-normalized premultiplied spectra of the axial velocity fluctuations at $y^+ = 15$ at both high and low Reynolds numbers.

Summary

In the third year of the project, on-going quantifications of the turbulent stress field continued to yield results regarding the effects of Reynolds number and roughness consistent with measurements during the first two years. Third year efforts largely focused on the further identification and clarification of the length and time scales of the motions underlying momentum transport in rough-wall, high Reynolds number boundary layers. Spectral analyses indicate that the motions involved in the generation of stress gradients scale with the Taylor scale (or equivalently, the thickness of the newly identified stress gradient balance layer) for distances relatively near the wall. At farther distances from the wall, there is some evidence that larger scale motions may gain importance. Further measurements are needed in this regard. Comparisons of two $R_\lambda = 850$ flows were made relative to the assumptions of local isotropy. These

experiments indicated that the spectral properties of the vorticity field in these flows not only show significant deviations from those predicted via local isotropy, but also that considerable differences existed between small-scale structure of the vorticity field in these two high Reynolds number flows. The implications of these observations are potentially far-reaching. Spectral characteristics of the Reynolds stress indicates that at high Reynolds number the underlying motions shift from close to the integral scale to intermediate scales. Near-wall axial intensity spectra indicate an extended -1 region very near the wall, but its nearly complete disappearance by about 100 viscous units from the wall. In between there exists an intermediate zone in which the spectra appear to scale on the mean velocity and distance from the wall. Important new theoretical foundations for the boundary layer were uncovered through a fundamental examination of the mean momentum balance in turbulent wall-flows. These results provide a redefinition of boundary layer structure, and identify explicit Reynolds number dependencies. Consideration of rough-wall flows in light of these new developments provides a clarification and a basis for the reclassification of roughness effects with increasing Reynolds number.

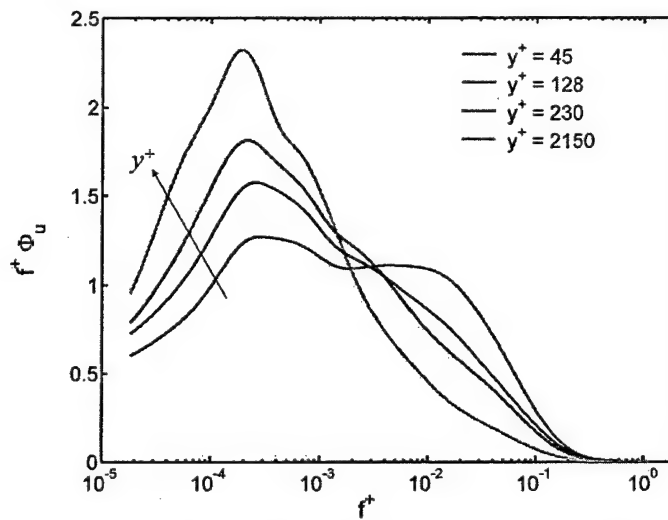


Figure 22. Inner normalized premultiplied axial velocity spectra as a function of distance from the wall at high Reynolds number.

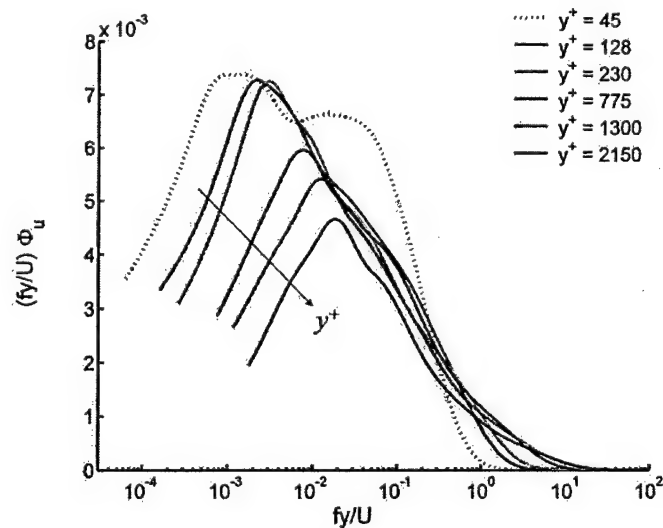


Figure 23. Premultiplied axial velocity spectra normalized by the mean velocity and distance from the wall.

References

- Bradshaw, P. 1967 "Inactive motion and pressure fluctuations in turbulent boundary layers," *J. Fluid Mech.* **30**, 241.
- DeGraaff, D. and Eaton J. 2000 "Reynolds number scaling of the flat plate turbulent boundary layer," *J. Fluid Mech.* **422**, 319.
- Fife, P., Wei, T., Klewicki, J. and McMurtry, P. 2003 "Asymptotic properties of the mean momentum balance in turbulent channel flow," *J. Fluid Mech.*, submitted.
- Foss, J.F. and Morris, S.C. 2002 "The non-universality of the large wave number vorticity field at $R_\lambda = 850$," in the Proceedings of the *IUTAM Symposium of on Reynolds Number Scaling in Turbulent Flow*, to appear, Kluwer, Princeton, N.J.
- Folz, A.B 1997 "An experimental study of the near-surface turbulence in the atmospheric boundary layer", Ph.D. dissertation, University of Maryland, College Park, Maryland.
- Klewicki, J.C. and Falco, R.E. 1990 "On accurately measuring statistics associated with small scale structure in turbulent boundary layer using hot-wire probes," *J. Fluid Mech.* **219**, 119.
- Klewicki, J.C., Murray, J. and Falco, R.E. 1994 "Vortical motion contributions to stress transport in turbulent boundary layers," *Phys. Fluids* **6**, 277.
- Klewicki, J.C. and Falco R.E. 1996 "Spanwise vorticity structure in turbulent boundary layers," *Int. J. Heat and Fluid Flow* **17**, 363.
- Klewicki, J.C. and Metzger, M.M. 2002 "Studies of high Reynolds number turbulence in the atmospheric surface layer over the salt playa of western Utah," in the Proceedings of the *IUTAM Symposium of on Reynolds Number Scaling in Turbulent Flow*, to appear, Kluwer, Princeton, N.J.
- Klewicki, J.C. and Miner, H.E.. 2002 "Wall pressure structure at high Reynolds number," *Bull. Am. Phys. Soc.* **47**.
- Ligrani, P.M. and Moffat, R.J. 1986 "Structure of transitionally rough and fully rough turbulent boundary layers," *J. Fluid Mech.* **162**, 69.
- Maher, M.C. 2002 *Velocity and Vorticity Measurements in the Atmospheric Boundary Layer*, M.S. Thesis, Michigan State University.
- Metzger, M.M. 2002 *Scalar Dispersion in High Reynolds Number Turbulent Boundary Layers*, Ph.D. dissertation, University of Utah.
- Metzger, M.M. and Klewicki, J.C. 2001 "A comparative study of near-wall turbulence in high and low Reynolds number boundary layers," *Phys. Fluids* **13**, 692.
- Metzger, M.M., Klewicki, J.C., Bradshaw, K. and Sadr, R. 2001, "Scaling the near-wall axial stress in the zero pressure gradient boundary layer," *Phys. Fluids* **13**, 1819.

- Metzger, M.M., Klewicki, J.C. and Priyadarshana, P. 2002 "Reynolds number dependencies in the behavior of boundary layer axial stress and scalar variance transport," in the Proceedings of the *IUTAM Symposium of on Reynolds Number Scaling in Turbulent Flow*, to appear, Kluwer, Princeton, N.J.
- Metzger, M.M., Klewicki, J.C. and Atzet, I. 2002 "Log-layer streamwise velocity characteristics at $R_0 = 5 \times 10^6$," *Bull. Am. Phys. Soc.* **47**.
- Morrison, J.F., Jiang, W., McKeon, B.J. and Smits, A.J. 2002 "Reynolds number dependence of streamwise velocity fluctuations in turbulent pipe flow," *AIAA paper no. 2002-0574*.
- Moser, R., Kim, J. and Mansour, N. 1999 "Direct numerical simulation of turbulent channel flow up to $R_\tau = 590$," *Phys. Fluids*. **11**, 943.
- Marusic, I., Uddin, A. and Perry, A. 1997 "Similarity law for the streamwise turbulence intensity in zero pressure gradient boundary layers," *Phys. Fluids* **9**, 3718.
- Perry, A.E., Henbest, S.M. and Chong, M.S. 1986 "A theoretical and experimental study of wall turbulence," *J. Fluid Mech.* **165**, 163.
- Piquet, J. 1999 *Turbulent Flows (Models and Physics)*, Springer, Berlin.
- Pope, S.B. 2000 *Turbulent Flows*, Cambridge Press, Cambridge.
- Priyadarshana, P. and Klewicki, J. 2001 "Effects of surface roughness on high Reynolds number boundary layer cross-stream transport," *Bull. Am. Phys. Soc.* **46**, 105.
- Priyadarshana, P. and Klewicki, J.C. 2002 "Reynolds number scaling of wall layer velocity vorticity products," in the Proceedings of the *IUTAM Symposium of on Reynolds Number Scaling in Turbulent Flow*, to appear, Kluwer, Princeton, N.J.
- Priyadarshana, P. and Klewicki, J. 2002 "Mean rate of energy transfer in a high Reynolds number turbulent boundary layer," *Bull. Am. Phys. Soc.* **47**.
- Priyadarshana, P. 2003 *Reynolds Number Influences on Turbulent Boundary Layer Momentum Transport*, Ph.D. dissertation, University of Utah, to appear.
- Schlichting, H. 1979 *Boundary Layer Theory*, McGraw-Hill, New York.
- Spalart, P. 1988 "Direct simulation of a turbulent boundary layer up to $R_0 = 1410$," *J. Fluid Mech.* **187**, 61.
- Townsend, A.A. 1961 "Equilibrium layers and wall turbulence," *J. Fluid Mech.* **11**, 97.
- Wallace, J.M. and Foss, J.F. 1995 "The measurement of vorticity in turbulent flows," *Ann. Rev. Fluid Mech.* **27**, 469.
- Wei, T., Klewicki, J. and McMurtry, P. 2004 "Scaling properties of the mean momentum balance in turbulent wall flows," *J. Fluid Mech.*, to appear.

Wyngaard, J.C. 1969 "Spatial resolution of the vorticity meter and other hot-wire arrays," *J. Phys. E.* **2**, 983.

Wyngaard, J.C. 2002 "On the mean rate of energy transfer in turbulence," *Phys. Fluids.* **14**, 2426.

Zagorola, M.V. and Smits, A.J. 1997 "Scaling of the mean velocity profile in turbulent pipe flow," *Phys. Rev. Lett.* **78**, 239.

Appendix

This appendix contains four manuscripts that have been derived, either wholly or partially, through the present grant. The titles of papers are:

- 1) "A study of the motions contributing to the Reynolds stress in high and low Reynolds number turbulent boundary layers," under review, *Physics of Fluids*.
- 2) "An experimental study of turbulent boundary layer velocity vorticity products at high and low Reynolds numbers," Chapter 6, Ph.D. Dissertation, P. Priyadarshana (to be amended and submitted to *Journal of Fluid Mechanics*)
- 3) "Properties of the mean momentum balance in turbulent boundary layer, pipe and channel flows," to appear, *Journal of Fluid Mechanics*.
- 4) "Stress gradient balance layers and scale-hierarchies in wall bounded turbulent flows," under review, *Journal of Fluid Mechanics*.

A study of the motions contributing to the Reynolds stress in high and low Reynolds number turbulent boundary layers

P. J. A. Priyadarshana* and J. C. Klewicki†

Physical Fluid Dynamics Laboratory

Department of Mechanical Engineering

University of Utah

Salt Lake City, Utah 84112

(Dated: June 12, 2004)

Abstract

Physical experiments are used to explore the properties of the motions contributing to the Reynolds stresses in high and low Reynolds number turbulent boundary layers. The low Reynolds number smooth wall measurements ($R_\theta = 1010$, $R_\theta = 2870$ and $R_\theta = 4850$) were acquired in a large-scale low speed wind tunnel, while the high Reynolds number measurements ($R_\theta \sim O(10^6)$) were acquired at the SLTEST site, Dugway Utah. These high Reynolds number turbulent boundary layer data were acquired over nearly hydraulically smooth and rough walls. At each Reynolds number and surface roughness, data comparisons are made at approximately $y_p/2$ and $2y_p$, where y_p is the peak position of the Reynolds shear stress. Scale separation effects associated with increasing R_θ are analyzed via spectral measurements (u , v and $u-v$ cospectra), and by segregating the streamwise and wall normal velocities according to their frequency content using simultaneous high and low-pass filtering. A primary observation is that the predominant motions underlying the stress undergo a significant shift from large to intermediate scales as R_θ becomes large, irrespective of surface roughness. Quadrant analysis of the filtered signals is employed to clarify the correlated scales involved in the generation of the stress. Overall, it is apparent that the types of motions contributing to Reynolds stress undergo significant variations at comparable wall normal locations (relative to y_p) over the Reynolds number range explored.

PACS numbers: 47.27.Jv, 47.27.Nz

I. INTRODUCTION

The technological importance of the turbulent boundary layer is immense.¹ Furthermore, many important technological applications operate in high R_θ regimes ($R_\theta = U_\infty \theta / \nu$, where U_∞ is the free stream velocity, θ the momentum deficit thickness and ν the kinematic viscosity). Flow around submarines and aircraft are two characteristic examples. The R_θ values encountered in many such applications, however, are often orders of magnitude higher than those capable of detailed study by computation or even by experimentation.¹ Currently, Direct Numerical Simulations (DNS) are confined to $R_\theta \cong O(10^3)$.^{1,2} Thus, low R_θ experimental and numerical results need to be accurately extrapolated to be useful in predicting high R_θ behavior. This is, however, problematic since the R_θ scaling behaviors of boundary layer turbulence statistics are, at present, unclear.

An important effect of increasing Reynolds number is that the outer length and velocity scales (as characterized by δ and U_∞) become increasingly large relative to the corresponding inner scales (characterized by the friction velocity, $U_\tau (= \sqrt{\tau_w / \rho})$ and ν). Here, τ_w , and ρ are wall shear stress, and density respectively. Currently, the effects of the separation of scales on momentum transport are not well understood. In this regard, it is significant to note that *i*) the gradient of the kinematic Reynolds shear stress, $-\overline{uv}$, appears in the mean momentum balance, shown in (1) for a two dimensional flat plate boundary layer in the (x, y) plane (x is the streamwise direction and y is the wall normal direction), and that *ii*) this gradient may be expressed as the difference of velocity-vorticity correlations (2) for well-developed flow.³⁻⁵

$$U \frac{\partial U}{\partial x} + V \frac{\partial U}{\partial y} = \frac{\partial}{\partial y} \left(\nu \frac{\partial U}{\partial y} - \overline{uv} \right), \quad (1)$$

$$\frac{\partial \overline{uv}}{\partial y} \cong \overline{w\omega_y} - \overline{v\omega_z}. \quad (2)$$

As is customary, the x and y mean velocity components are given by U and V , time averaging is denoted by an overbar and by uppercase letters, instantaneous quantities $(\tilde{\cdot})$ are defined as the sum of a mean and fluctuation (e.g., $\tilde{u} = U + u$) and vorticity components are identified by their subscript. Inner normalization is denoted by a superscript $+$. All rms fluctuations are represented by a superscript $'$. Existing data indicate that for this flow there is a single maximum position for the Reynolds shear stress, $y_p \left(\approx 2 \left(\frac{\delta U_\tau}{\nu} \right)^{1/2} \right)$, and that

its inner-normalized position in the layer is Reynolds number dependent.⁶⁻⁸ By definition, at y_p the Reynolds shear stress gradient is zero. Thus, with regard to affecting a time rate of change of mean momentum, the $-\partial\overline{uv}/\partial y$ term in (1) acts as a source for $y < y_p$ and a sink for $y > y_p$. It is therefore of interest to explore whether characteristics of this behavior are reflected in the Reynolds shear stress itself at representative locations below and above y_p .

Further insight into this momentum source/sink character is provided by (2), showing that $-\partial\overline{uv}/\partial y$ comes about directly through interactions between the velocity and vorticity fields. Regarding scale separation effects, the generally accepted properties of the velocity and vorticity fields in turbulent flows indicate that with increasing Reynolds number the spectral peaks in the fluctuating \vec{v} and $\vec{\omega}$ fields move to increasingly disparate wavenumbers.⁹ Thus the interactions leading to $-\partial\overline{uv}/\partial y$ will likely occur over a decreasingly narrow, intermediate, wavenumber band (relative to the total span of possible wavenumbers) within which the respective spectra overlap. Velocity vorticity cospectra provide direct evidence supporting this notion.³ Thus, another purpose of the present study is to explore whether intermediate scale interactions are prevalent in the motions underlying the Reynolds stress as well. At extremely high R_θ , the inner length scale becomes so small that the wall irregularities become comparatively significant. Thus, wall roughness often becomes significant with an increase in scale separation as well. Data from the present study also provide information regarding wall roughness effects (over a limited roughness range) on the motions contributing to the Reynolds stress at high R_θ .

Of course, modeling the behavior of Reynolds stress has traditionally been one of the primary objectives of various prediction schemes,^{1,10} and is often accomplished by studying and predicting first, second and third order moments of velocity fluctuations.¹⁰ Analysis of the instantaneous signals typically classifies the type of motions contributing to the negative mean of \overline{uv} as sweeps ($u > 0, v < 0$) and ejections¹¹ ($u < 0, v > 0$). There are, of course, positive \overline{uv} producing motions known as outward interactions ($u > 0, v > 0$) and wall-ward interactions ($u < 0, v < 0$). Analyses along these lines are motivated by the fact that, on average, kinetic energy from the free stream is converted into turbulent fluctuations and then dissipated into internal energy by viscous action. A continuous generation of new turbulence must therefore occur if a statistically stationary flow is to be maintained. Given this, a number of previous studies have explored the role of the \overline{uv} generating motions in

the turbulence production process.^{10–14} For brevity, however, only a small number of studies are discussed here.

Corino and Brodkey¹² found that in the near wall region ($0 < y^+ < 50$), ejections produce about 70% of the Reynolds stresses. They studied Lagrangian flow visualization at $R_d \cong 20000$ in a pipe flow. (Here R_d is the Reynolds number based on pipe diameter, and mean velocity). Wallace et al.¹¹ introduced the concept of quadrant splitting. Somewhat in contrast to Corino and Brodkey, they observed that the negative \overline{uv} producing motions are equally distributed between ejections and sweeps at $y^+ = 15$. Wallace et al.¹¹ also found that positive \overline{uv} producing motions occur about 30% of the time. Willmarth and Lu¹³ observed that at $R_\theta = 4230$ and $R_\theta = 38000$, about 60% of the turbulence at $y^+ = 30$ is produced during ejections. Nagano and Tagawa¹⁰ observed at $R_\theta = 1780$, that in the zero pressure gradient logarithmic layer, ejections provide a greater contribution to $-\overline{uv}$ than sweeps. In the near wall region, however, they observed a greater contribution from sweeps.

Currently, little is known regarding the behavior of the motions contributing to Reynolds stress at high Reynolds number. Equally poorly understood are the scaling relations between these motions and those at low R_θ . In this regard, scale separation effects are likely to be significant. For this reason, in the present study particular attention is paid to the relative scales of the motions contributing to the Reynolds stress.

II. EXPERIMENTAL SETUP AND METHODOLOGY

To address the objectives discussed in the Introduction, well-resolved measurements covering the range $O(10^3) \leq R_\theta \leq O(10^6)$ were acquired and compared. The details relating to these experiments configurations are now described and discussed.

The low Reynolds number experiments (at $R_\theta = 1010$, $R_\theta = 2870$ and 4850) come from the data set of Klewicki⁴, and were performed in the open circuit laboratory wind tunnel described in Klewicki et al.^{5,15} The test section of this suction wind tunnel is 17.1m long, 1.21m wide, and has a variable height to provide a zero pressure gradient turbulent boundary layer. Measurements were taken 15m downstream from the inlet. A series of screens and a honeycomb were placed at the inlet of the tunnel. These serve to straighten the flow entering the test section, as well as to isolate the test section flow from the laboratory. The free stream axial turbulence intensity, u'/U_∞ , was less than 0.5%. The long fetch of

the wind tunnel provides an important advantage in that it allows a relatively high R_θ to be achieved at low speeds. This provides very good spatial resolution measurements. For example, a 1mm sensor length has a spatial scale that varies between 2.0 and 7.5 wall units for $1000 < R_\theta < 5000$. In all of the wind tunnel measurements, the Clauser method was used to compute U_τ . Of course, this technique relies on the behavior of the mean velocity profile, and thus is inappropriate to use, for example, in studies exploring possible R_θ dependencies in the mean profile. The present results, however, are considerably less sensitive to such concerns.

The high Reynolds number data were acquired at the Surface Layer Turbulence and Environmental Science Test (SLTEST) facility.^{16,17} This facility is located on the southern end of the Great Salt lake Desert (113°26.5' W, 40°8.1' N). The test site is the bed of ancient Lake Bonneville. It is characterized by an extremely flat playa composed of a mud, clay, and salt mixture. The upstream surface elevation variation is measured at less than 1m over the first 13km north of the site. The upwind fetch remains unobstructed for about 150km.

All the measurements were made around sunset or dawn, under near neutrally stable atmospheric conditions. Thermal stability was computed using the Monin-Obukov stability parameter, ζ ($\zeta = y/l$). Here, y is the wall normal co-ordinate. The Monin-Obukov length, l is defined as

$$l = \frac{\Theta_o U_\tau^3}{\kappa g \theta v}, \quad (3)$$

where, Θ_o is the mean temperature of an adiabatic atmosphere, θ is the fluctuating component of the temperature difference between the actual temperature and Θ_o and κ ($= 0.41$) is the von Karman constant. Sonic anemometer velocity data and associated quartz thermometer temperature data were used to compute ζ . In accordance with the findings of Metzger¹⁸ (see also Klewicki and Metzger,¹⁷) the region of nearly linear temporal variation in this parameter, approximately between $-0.1 < \zeta < 0.1$, was used as the criterion for selecting the near-neutrally stable conditions in the atmospheric surface layer.

The salt playa remains submerged during spring under normal weather conditions and the surface is very smooth during early summer. If there is a dry spring, then the surface will become cracked and rough during July and August. Some of the present high R_θ data were taken under smooth wall conditions and the other data were taken during rough wall conditions. The inner normalized surface roughness, k^+ , values were obtained using the downward shift¹⁹ in the inner normalized mean velocity profile, U^+ vs y^+ , using the

relationship (4) of Krogstad et. al.²⁰

$$\Delta U^+ = \frac{1}{\kappa} \ln k^+ - 3.2 \quad (4)$$

The estimated surface roughness values are given in Table II.

A custom built 2.4m diameter drag balance²¹ was used in the high Reynolds number experiments to measure the wall shear stress directly. In addition, a miniSODAR was used to acquire the mean wind profile data up to between 100m and 200m from the surface. Following the analysis procedures described in Metzger and Klewicki,¹⁶ these profile measurements were also used to estimate boundary layer integral parameters. Experimentally estimated integral parameters for both the wind tunnel and SLTEST facility flows are summarized in Table I.

A. Instrumentation and Data Acquisition

For the high R_θ experiments a custom six wire probe, composed of three X-arrays (Fig. 1), was used to acquire the instantaneous \tilde{u} and \tilde{v} velocities at three closely spaced wall normal locations. Owing to low free stream velocity and large integral length scale, the high R_θ boundary layer data had good spatial resolution with inner normalized spatial scale, l^+ , ranging between 10 – 30 (Table II). Such resolution is extremely difficult to achieve in any high R_θ laboratory facility.

Simultaneous sample and hold analog to digital converters (16 bit) were used to digitize the hot-wire signals. A sampling frequency of 5kHz was used in all the high Reynolds number experiments. Several 3 – 10 minute data files were acquired at each y^+ location. A primary quality measure of the instantaneous signals selected for the analysis was that during acquisition the wind did not exhibit transient (ramp up, ramp down) behavior. Thus, only those series that, when plotted, exhibited a well defined horizontal mean line were selected for analysis. Given this, the fluctuating velocities were computed by simply subtracting the overall mean velocity in each time series.

The Wheatstone bridge circuits in the SLTEST experiments were provided by AA Lab-Systems AN-1003 constant temperature anemometers. A portable facility, as described by Metzger¹⁸ was used to calibrate the six wire probe immediately before and after each experiment. The velocity angle method explained in Bruun²² was used to fit third order bivariate

polynomial surfaces to the voltage velocity pairs of wires in each X-array. Temperature compensation, as explained by Metzger¹⁸ was used as a part of this surface fitting technique. The instantaneous hot-wire velocity components were obtained by solving the coupled non-linear system of equations using a globally convergent Newton method. In both the wind tunnel and the near surface field experiments, the distance of the probe from the wall was measured with a cathetometer having a precision of $\pm 0.0127\text{mm}$.

All the wind tunnel data were acquired using a single X-wire probe¹⁵ with a 1mm sensor length. The probe resolution remained under 8 viscous units for all the low R_θ measurements (Table II). Two DISA 55M01 constant temperature anemometers were used as the Wheatstone bridge circuits. The $R_\theta = 1010, 2870$ and 4850 data were sampled at 500Hz, 1000Hz and 2000Hz respectively. Further details regarding these measurements may be found in Klewicki and Falco¹⁵ and Klewicki et. al.⁵

B. Data Analysis Techniques

The statistical structure of the Reynolds shear stress is explored by computing the u, v cross correlation coefficient, ρ_{uv} , the inner normalized Reynolds shear stress, $-\overline{uv}^+$, and the inner normalized rms of the fluctuating uv product, $(uv)'^+$. Also presented are the skewness and kurtosis of uv , $S(uv)$, and $K(uv)$. In all these statistics, a single high R_θ data point represents a 30 – 40 minute time average. Owing to the care taken to select only the most reliable subset of data acquired, some plots contain measurements spanning several years of field trials.

Apart from quantifying the basic statistical behavior of the Reynolds stresses, the two primary purposes of the data analysis are to: *i*) quantify the scales of motion contributing to $-\overline{uv}$ with increasing R_θ , and *ii*) explore the influence of Reynolds number on the relative contributions to $-\overline{uv}$.

Change of scale effects were identified using two different methods. In the first method, co-spectra between the fluctuating u and v signals were computed and compared with the individual u and v power spectra. These comparisons provide information relating to the influence of the individual u or v components on the scales of motion having the greatest contribution to $-\overline{uv}$. The power spectra were computed using Welch's averaged, modified periodogram method. A Hanning window of the same size as the signal length was used

to minimize spectral leakage. Similar to the method used by Saddoughi and Veeravalli,²³ the low frequency end of the spectrum was obtained by down sampling the signals using an anti-aliasing (low pass) finite-duration impulse response filter. The co-spectra of u and v were obtained using the real part of the cross spectral density.^{24,25}

In the second method, the u and v signals were split into high frequency and low frequency parts according to a cut-off frequency, f_c . In this filtering technique, a square-step Fourier filter was employed such that no correlation remained between the signals above and below f_c . The contributions to $-\overline{uv}$ from the portions of the signals above and below f_c , for a range of f_c , were then computed and examined as a function of Reynolds number. For any given uv signal, there will always be a characteristic cross-over frequency, f_x , at which the contribution to $-\overline{uv}$ below f_c is equal to the contribution above f_c . By definition, f_x is the mean frequency of the motions contributing to $-\overline{uv}$. The behavior of f_x as a function of Reynolds number was explored. On physical grounds, one might expect the cross-over frequency to exhibit a Reynolds number variation similar to the peak in the u - v co-spectra. Owing, however, to the fact that f_x is an integral measure, it can be determined to higher precision than the co-spectral peaks, which tend to be noisy.

As is customary, the underlying composition of $-\overline{uv}$ was explored by separating the contributions in to four quadrants, e.g., Wallace et al.¹¹ The fractional contributions to the Reynolds stress, including the associated joint probability density functions for each quadrant, were then computed and compared for the high and low Reynolds number flows.

III. RESULTS AND DISCUSSION

This section first examines the long-time statistical structure of the uv signals for high and low Reynolds numbers. The influences of scale separation are studied in detail in Section III B. This is done using the u and v co-spectrum, power spectra of individual velocities, as well as through the simultaneous low and high pass filtering technique discussed above. The frequency content of the uv signals, and the dependence of this content on R_θ and possible effects of wall roughness are also analyzed here. Quadrant analyses are performed in section III C.

A. Statistical Structure

In this section, statistics derived from the instantaneous uv product are presented and compared. In making these comparisons it is useful to note that for the high Reynolds number data $\delta^+ = \delta U_\tau / \nu \approx 1 \times 10^6$, and thus all these measurements are derived from deep within the wall layer, say $y^+ < 20000$. In the low R_θ flows examined, however, δ^+ is significantly less than 20000. Thus, for purposes of rational comparison, the outer layer data from the low R_θ statistical profiles have been removed.

Reynolds shear stress correlation coefficients, $\rho_{uv} = \overline{uv} / (u'v')$, at low and high R_θ are shown in Fig. 2. All the low R_θ data are from smooth wall flows. As shown in Table II, some of the high R_θ data were taken over relatively smooth $k^+ \approx 25 \sim 50$ wall conditions while other high R_θ data were taken under fully rough wall conditions with $300 \lesssim k^+ \lesssim 500$. The $R_\theta = 1010$, $R_\theta = 2870$ and $R_\theta = 4850$ results are consistently shown throughout in solid pentagons, solid diamonds and downward pointing solid triangles respectively. The high R_θ relatively smooth, $k^+ \approx 25 \sim 50$ data are shown with solid squares. Solid triangles pointing right represent high R_θ , $k^+ \approx 300$ rough wall data and solid triangles pointing left show high R_θ , $k^+ \approx 500$ rough wall data. As shown, at high R_θ , the effect of surface roughness on ρ_{uv} (for the k^+ values explored) effectively lies within the data scatter. DeGraaff's²⁶ $R_\theta = 13000$ and $R_\theta = 31000$ data are also shown in Fig. 2. For $y^+ < 15$, the current low R_θ ρ_{uv} profiles appear to merge. Farther from the wall, these low R_θ data indicate an apparent R_θ dependence, dramatically so between the $R_\theta = 1010$ and 2870 data. The relatively low R_θ results shown here, and more recently the trends indicated by the data of DeGraaff²⁶ (over a significantly wider R_θ range, $1430 \leq R_\theta \leq 31000$), suggest a decreasing value of the ρ_{uv} with increasing R_θ . Even over the 1 decade variation in R_θ of the DeGraaff and Eaton⁸ study, however, the observed variations are relatively subtle.³⁰ Also, DeGraaff's data show a near wall peak in the ρ_{uv} profile at all Reynolds numbers. This feature is not observed in any of the present low R_θ data. Currently, no high R_θ near wall data are available to further explore this feature.

Of course, an advantage of the SLTEST site measurements is that they are at very high R_θ . Thus, even with their inherently elevated uncertainty, they often allow Reynolds number variations to be discerned. Consistent with a decreasing trend, all the high R_θ data shown in Fig. 2 fall between $0.13 \sim 0.28$. Physically, the behavior of these correlation coefficients

is consistent with the increasing influences of the inactive motion²⁷ with increasing R_θ , as well as the previous high R_θ observations of Metzger and Klewicki.¹⁶ As discussed later in Section III B, the reduction in ρ_{uv} is likely related to a reduction in spectral overlap between u and v signals. A compilation of $\rho_{uv}|_{y=y_p}$ data derived from a number of well resolved measurements²⁸ plotted as a function of R_θ is shown in Fig. 3. The correlation coefficient at the peak Reynolds stress location indicates an approximately logarithmic decrease with increasing R_θ . The curve fit shown was performed for all low R_θ data greater than 2000. As is evident, there is scatter in the low R_θ data, although the decreasing trend is apparent. The low R_θ curve, when extrapolated, slightly underestimates the relatively smooth wall $\rho_{uv}|_{y=y_p}$ at $R_\theta \simeq 2 \times 10^6$ and rough wall ρ_{uv} at $R_\theta \simeq 4 \times 10^6$ with inner normalized surface roughness, $k^+ \approx 300$. The $k^+ \approx 500$ data indicate slightly higher values, although the scatter in the data (as evidenced by the error bars) precludes any definitive conclusions regarding roughness effects.

A comparison of the inner normalized Reynolds stresses for the low and high Reynolds numbers is shown in Fig. 4. As evidenced by the low R_θ data, both the peak value and position of the peak in the Reynolds stress profile, y_p^+ , attain larger values with increasing R_θ . Under the assumption of a single peak in \overline{uv}^+ , it may be shown for channels that the peak value asymptotes to 1.0 as the Reynolds number becomes large. For boundary layers similar behavior is expected on physical grounds, but the mathematical arguments are weaker. Regarding the outer migration of the peak value with increasing R_θ , similar behavior has been observed by a number of studies in both boundary layer, pipe and channel flows (see, for example, Gad el Hak and Bandyopadhyay¹). Unlike ρ_{uv} , the present high R_θ values for this normalized statistic show a degree of scatter that precludes comment on R_θ dependence of the peak value and position. The effects of a reduced ρ_{uv} at high R_θ are not readily apparent in the inner normalized Reynolds stress.

Profiles of the rms of the inner normalized uv product, $(uv)'/U_\tau^2$, are shown in Fig. 5. In addition to the present measurements, the earlier results of Gupta and Kaplan²⁹ at $R_\theta = 6500$ are shown as well. Once again, a rather dramatic difference is seen between the $R_\theta = 1010$ and 2870 data. Even discounting the $R_\theta = 1010$ results, however, the wind tunnel data in this figure provide evidence for an increase in $(uv)'/U_\tau^2$ with increasing R_θ within logarithmic layer portion of the mean profile. The present SLTEST site data lend support to this assertion. (Recall that at $R_\theta \sim (10^6)$, $y^+ = 2 \times 10^4$ is within the inner

region.) An increase in $(uv)'/U_\tau^2$ with increasing R_θ is consistent with the observed decrease in ρ_{uv} , especially if this additional intensity is broadly distributed across all four quadrants of the (u, v) plane. This issue is explored further in section III C below.

Few results regarding the higher order moments of the uv product have been reported. Profiles of the third central moment, $S(uv)$, are shown in Fig. 6. Broadly speaking, the data in this figure indicate that over the interior portion of the layer, $S(uv)$ attains values between -1.5 and -3.5 , with values nearer to zero as the wall is approached. The present data exhibit little discernible variation between $R_\theta = 2870$ and 4850 . In contrast, the $R_\theta = 6500$ profile of Gupta and Kaplan shows an identifiably more negative plateau across the logarithmic layer. The present $R_\theta \cong 10^6$ $S(uv)$ results indicate negative values close to those shown by the Gupta and Kaplan profile. The kurtosis data, $K(uv)$, are shown in Fig. 7. The behavior of $K(uv)$ suggests high intermittency in the uv signals near the wall, and a plateau having values between 10 and 12 across most of the inner layer at low R_θ . These high values (even in the interior of the flow) indicate that, in general and relative to either the u or v signals, the uv signal has a highly intermittent character. Similar to the behavior of $S(uv)$, the $K(uv)$ data suggest a slight increasing magnitude with increasing R_θ , although the scatter in the data is considerable.

B. Spectral Structure

1. The u, v cospectrum

The spectral characteristics of u , v and uv are described in this section. The premultiplied u and v cospectrum together with individual premultiplied power spectra are discussed first, followed by the u and v spectral correlation coefficients.

The premultiplied u, v cospectra, $f^+ \Lambda(uv^+)$, the premultiplied power spectra of u , $\Psi(u^+)$, and v , $\Psi(v^+)$, at $R_\theta = 2870$ are shown in Figs. 8(a) and 8(b) respectively. Fig. 8(a) shows $-f^+ \Lambda(uv^+)$, $\Psi(u^+)$, and $\Psi(v^+)$ at the wall normal location, $y^+ = 30$ and Fig. 8(b) shows the same at $y^+ = 120$. ($y_p/2$ and $2y_p$ respectively). The reasons for examining the data at $y_p/2$ and $2y_p$ were discussed in the Introduction.

Both cospectra show negative correlations at very high frequencies, i.e., in the dissipation range. This is in agreement with the findings of Wallace et al.¹¹ who observed events in the

first and third quadrants tended to be at high frequencies. Another observation is that the u - v cospectrum approximately tracks the general shape of the streamwise velocity power spectrum in the inertial sub-range and within the energy containing scales. The cross over frequency, f_x , as described later in Section IIIB 2 at $y_p/2$ coincides approximately with the peak in the u , v co-spectrum. At $2y_p$, however, the peak in the u , v co-spectrum moves to a slightly higher frequency than f_x . At both wall-normal locations, the two premultiplied power spectra of u and v have peaks that are separated by less than $1/2$ decade in frequency. Thus, at $R_\theta = 2870$, there is considerable spectral overlap between the u and v spectra.

The u - v cospectra at $R_\theta = 4850$ are shown in Figs. 8(c) and 8(d) for the wall normal locations, $y_p/2$ and $2y_p$ respectively. These u - v cospectra as well as the individual power spectra $\Psi(u^+)$, and $\Psi(v^+)$ show behaviors highly similar to those observed at $R_\theta = 2870$. The $-f^+\Lambda(uv^+)$ tracks $\Psi(u^+)$ at both wall normal locations. These results indicate little apparent change in the spectral behaviors underlying the u - v correlations within the range $3000 \lesssim R_\theta \lesssim 5000$.

Behaviors different from the low R_θ data are observed in the premultiplied u v cospectra at $R_\theta \simeq 2 \times 10^6$ shown in Figs. 9(a) and 9(b). As described, the wall is relatively smooth with $k^+ \approx 25 \sim 50$ for these data. In the dissipation range the cospectrum is nearly zero. This is consistent with local isotropy at high Reynolds number. A similar behavior was also observed by Saddoughi and Veeravalli,²³ who did not show data in the dissipation range of the u - v cospectrum, but indicated that at high wave numbers, where local isotropy is approached, the values of the cospectra became very small, and occur with both signs. In contrast to the premultiplied u - v cospectrum at low R_θ , the peak in the high R_θ premultiplied u - v cospectrum moves towards the peak in the premultiplied v power spectrum. From Figs. 8 and 9, it is seen that with increasing R_θ , there is a considerable reduction in the spectral overlap between u and v . Similar to the observation of the cross-over frequency at $R_\theta = 2870$, f_x at $y_p/2$ occurs approximately at the peak of u - v co-spectrum. At $2y_p$, $R_\theta \simeq 2 \times 10^6$, f_x is about an order of magnitude lower than the peak in the u - v co-spectrum.

$R_\theta \simeq 4 \times 10^6$, $k^+ \approx 300$, u and v power spectra and the u - v cospectra at $y_p/2$ are shown in Figs. 9(c) and 9(d). The results shown in these figures are very similar to the relatively smooth wall results of Figs. 9(a) and 9(b). Specifically, these rough wall u - v cospectra show a peak at an intermediate scale at $y_p/2$. The behavior of the u - v cospectrum at $2y_p$ is only subtly different from the relatively smooth high R_θ u - v cospectrum at $2y_p$. There are no

differences in the two power spectra, $\Psi(u^+)$ and $\Psi(v^+)$ at both wall normal locations with increasing wall roughness. Overall, very little effect of wall roughness is apparent in the present $\Psi(u^+)$, $\Psi(v^+)$ and $-f^+\Lambda(uv^+)$ data.

To gain further insight into the apparent reduction of the spectral overlap between $\Psi(u^+)$ and $\Psi(v^+)$ with increasing R_θ , the co-spectra from Figs. 8 and Figs. 9 were normalized by the power spectra of u and v . The premultiplied spectral correlation coefficients, $-f\Lambda/\left(\sqrt{\Psi(u)\Psi(v)}\right)$ at $R_\theta = 2870$ are shown in Fig. 10(a) for $y_p/2$ and $2y_p$. As can be seen, at both locations the maximum spectral correlation is at low frequency, while the correlation is small for large frequency. The spectral correlation coefficients of Fig. 10(a) range between $0.5 \sim 1.0$ at low frequencies, with the correlation at the lowest frequencies being slightly larger at $2y_p$. At high frequencies, the spectral correlation coefficient becomes significantly negative. Fig. 10(b) shows $-f^+\Lambda/\left(\sqrt{\Psi(u^+)\Psi(v^+)}\right)$ at $R_\theta = 4850$. Similar to the $R_\theta = 2870$ results, $\Psi(u^+)$ and $\Psi(v^+)$ are correlated negatively at very high frequency. The low frequency behaviors of $-f^+\Lambda/\left(\sqrt{\Psi(u^+)\Psi(v^+)}\right)$ at $R_\theta = 4850$ are also very similar to those at $R_\theta = 2870$.

Fig. 10(c) shows $-f\Lambda/\left(\sqrt{\Psi(u)\Psi(v)}\right)$ at $R_\theta \simeq 2 \times 10^6$ ($k^+ \simeq 25 \sim 50$). The behavior of this premultiplied spectral ratio at both wall normal locations is significantly different from the low R_θ observations; further reinforcing the emergent notion that the stress producing motions shift from large to intermediate scales with increasing R_θ . The u - v correlation at low frequencies and high R_θ reaches its peak values at frequencies about 2 decades higher than the lowest resolvable frequency. Furthermore, at high frequencies the high R_θ data show little evidence of negative correlation, in contrast to the low R_θ results. There are no apparent differences (within the data scatter) between the high R_θ premultiplied spectral ratios at $y_p/2$ and $2y_p$. The behaviors of the data for $R_\theta \simeq 4 \times 10^6$ ($k^+ \approx 300$) are shown in Fig. 10(d), and are very similar to the relatively smooth wall data shown in Fig. 10(c). The correlation between low frequency u and v motions is small. These results further support the notion that the effect of wall roughness on inner normalized premultiplied spectra, $\Psi(u^+)$ and $\Psi(v^+)$ and inner normalized premultiplied cospectra, $f^+\Lambda(uv^+)$ are small even relatively near the edge of the roughness sublayer.

2. Properties of filtered uv signals

To further study the effects of different scale contributions to the uv product, the individual streamwise and wall normal velocity signals were simultaneously segregated using the low-pass/high-pass filtering technique explained in Section II B. The relative contributions to $-\overline{uv}^+$ and ρ_{uv} were computed from these filtered signals.

The contributions to $-\overline{uv}^+$ from those parts of signal above and below f_c are shown in Fig. 11. As before, the analyses were conducted on signals measured near $y_p/2$ and $2y_p$. As shown in Fig. 11(a), the inner normalized Reynolds stress computed from the high pass filtered signals shows a maximum value at very low cut-off frequency, $f_c^+ \cong 1 \times 10^{-5}$, as essentially the entire signal resides above f_c . Note that at low R_θ , this frequency is also very low compared to the integral frequency, $f_o = U_\infty/\delta$. The value of $-\overline{uv}^+$ as derived from the high pass filtered signals decreases as the low frequencies are removed with increasing f_c^+ . Similarly, the low pass filtered signals (i.e., the large scales) show zero Reynolds shear stress at $f_c^+ = 1 \times 10^{-5}$, and increase with increasing f_c . The two contributions to the total Reynolds stress equal each other at the cross-over frequency, f_x . These f_x values were shown previously in Figs. 8 and 9, and were discussed relative to the peaks in the premultiplied u - v cospectra.

For the $R_\theta = 2870$ data of Fig. 11(a), the cross-over occurs at $f_x^+ \cong 0.0123$ and $f_x^+ \cong 0.0109$ at $y_p/2$ and $2y_p$ respectively. Under outer normalization, these values correspond to $f_x\delta/U_\infty = 0.4750$ and 0.4240 respectively. These results suggest that motions of the order of magnitude of δ have significant contribution to $-\overline{uv}^+$ at $R_\theta = 2870$. Relative to previous observations that v - ω_z cospectral peaks occur near the Taylor frequency,³ f_λ , it is worth noting that f_x is about an order of magnitude larger than f_λ . The value of $-\overline{u_f v_f}^+$ at f_x is very close to $-\overline{uv}^+/2$. At f_λ^+ , the low pass filtered $-\overline{uv}^+$ is nearly equal to the unfiltered Reynolds shear stress. At $R_\theta = 2870$, the behavior of $-\overline{u_f v_f}^+$ is very similar at $y_p/2$ and $2y_p$. This is likely due to the lack of significant scale separation at low R_θ . The inner normalized Taylor frequency essentially remains the same at both wall normal locations as well (not shown). Again, f_x at $2y_p$ is only slightly lower than f_o . The $-\overline{u_f v_f}^+$ derived from low and high pass filtered signals at $R_\theta = 4850$ are shown in Fig. 11(b). These results exhibit very little difference from those at $R_\theta = 2870$. The separation between the f_x values at $2y_p$ and $y_p/2$ increases slightly. This is likely due to the slight increase in scale separation.

The filtered signal contributions to $-\overline{uv}^+$ at $R_\theta \cong 2 \times 10^6$ shown in Fig. 11(c) indicate the existence of considerable R_θ dependence. For reference, the peak Reynolds stress location at this Reynolds number is estimated to be $y_p^+ \cong 2000$ (Table II). The data near $y_p^+/2$ were at $y^+ \cong 600$ and near $2y_p^+$ were at $y^+ \cong 4011$. The cross over frequencies at $R_\theta \cong 2 \times 10^6$ are $f_x^+ = 1.1 \times 10^{-3}$ and 4.5×10^{-4} at $y_p/2$ and $2y_p$ respectively. As anticipated, these normalized cross over frequencies are considerably lower than their $R_\theta = 2870$ and 4850 counterparts. Also, there is a significant increase in presence of low frequencies at $2y_p$, both of which are effects of increasing scale separation. Under outer normalization, the cross-over frequencies, $f_x \delta / U_\infty$, are 39.64 and 15.6 at $y_p/2$ and $2y_p$ respectively. These are nearly two orders of magnitude larger than the $f_x \delta / U_\infty$ values at low R_θ . To exemplify this, the variation of the inner and outer normalized f_x with R_θ is shown in Fig. 12. As indicated, the inner normalized values decrease with R_θ while the outer normalized values increase. Clearly, the scaling required to make these data invariant with R_θ is intermediate to those derived from inner or outer variables.

The analysis of filtered signal contributions to $-\overline{uv}^+$ at $R_\theta \cong 4 \times 10^6$ is shown in Fig. 11(d). The behavior exhibited is very similar to the relatively smooth wall results shown in Fig. 11(c) at the wall normal location $y_p/2$. The behavior at the wall normal location of $2y_p$ is slightly different with presence of (possibly anomalous) negative values at very low frequencies; $f_c^+ \approx 10^{-6} \sim 10^{-5}$. The inner normalized cross over frequencies, f_x^+ , are 6.9×10^{-4} and 1.88×10^{-4} , at $y_p/2$ and $2y_p$ respectively. These values are slightly smaller than the values shown in Fig. 11(c). Thus, there appear to be some slight variations in the filtered product, $-\overline{u_f v_f}^+$. Relative to R_θ dependence, however, the present analysis (for the y^+ values explored) shows little dependence on wall roughness.

To further understand the motions leading to the correlation of u and v at different frequencies, the correlation coefficient, $\rho_{u_f v_f}$, was computed using the simultaneously low-pass and high-pass filtered velocity signals. Relative to interpreting these results, it is useful to note that the high f_c value of $\rho_{u_f v_f}$ under low pass filtering is equal to the low f_c value of $\rho_{u_f v_f}$ under high pass filtering. The results for the $R_\theta = 2870$, $R_\theta = 4850$, $R_\theta \cong 2 \times 10^6$ and $R_\theta \cong 4 \times 10^6$ flows are shown in Figs. 13(a-d) respectively. As shown in Fig. 13(a), for $R_\theta = 2870$ data, the correlation is the highest ($\cong 0.5$ and $\cong 0.6$ at $y_p/2$ and $2y_p$ respectively) for a range of low frequencies. This reinforces the observation that the large scales are well correlated at low R_θ . The $R_\theta = 2870$ correlation remains almost the same until the outer

normalized frequency reaches unity (or equivalently $f^+ \simeq 10^{-2}$) at $y_p/2$. This finding is quite similar to the behavior of the spectral correlation coefficient at $R_\theta = 2870$; further exemplifying the efficacy of the filtering methodology. The low pass filtered $-\rho_{u_f v_f}$ begins to decrease for $f\delta/U_\infty > 1$ at $y_p/2$ and for $f\delta/U_\infty > 0.1$ at $2y_p$. Thus, at $R_\theta = 2870$, the small scales are less correlated. The high pass filtered signals show a constant value of about 0.4 at small f_c^+ at both wall normal locations. The $-\rho_{u_f v_f}$ for these high pass filtered signals begins to decrease at $f\delta/U_\infty \sim 0.1$, and becomes negative around $f^+ \sim 0.1$. Once again, this result agrees with those of Wallace et al.¹¹ and Saddoughi and Veeravalli²³ who observed positive correlations between u and v at high frequencies. As shown in Fig. 13(b), there is a slight change in the filtered correlation coefficient $\rho_{u_f v_f}$ at $R_\theta = 4850$. The correlation remains about 0.4 for the high pass filtered signals, similar to $R_\theta = 2870$. There is, however, a significant reduction in the low pass filtered signal at low frequencies.

The behaviors of $-\rho_{u_f v_f}$ differ significantly for the $R_\theta \cong 2 \times 10^6$ flow. As shown in Fig. 13(c), $-\rho_{u_f v_f}$ computed from low pass filtered signals is very small at low frequencies. This is true at both $y_p/2$ and $2y_p$. Thus, not only is the actual contribution to $-\overline{uv}$ small at low frequencies, (Fig. 11), but the efficiency of these motions to produce $-\overline{uv}$ is low as well. With an increase in f_c ($f_c^+ \approx 10^{-4}$), $-\rho_{u_f v_f}$ exhibits a rapid increase. There is a peak in $-\rho_{u_f v_f}$ between $1 \times 10^{-3} < f_c^+ < 1 \times 10^{-2}$. This peak is essentially midway between the high and low frequency limits of the signals. The $-\rho_{u_f v_f}$ computed using high pass filtered signals show behaviors different from these at low R_θ . As expected, the value at low f_c is essentially the same as ρ_{uv} derived from the unfiltered signal. This value increases slightly with an increase in f_c^+ , and then shows a steady decrease with further increase in f_c^+ ; actually crossing the curves from the low-pass filtered signals. This behavior changes somewhat with high R_θ rough wall data. The main behavior of $-\rho_{u_f v_f}$ does not change significantly with an increase in surface roughness as shown in Fig. 13(d). The peak does, however, drop from 0.4 to about 0.23. Thus, there seem to be some subtle effects of surface roughness on the frequency dependent correlation between u and v . The behavior of all the high R_θ data is in stark contrast to the low R_θ results, and can generally be interpreted as the large scales being less contributive to stress production. In the context of Townsend's notion of active/inactive motions, this result apparently indicates that the active motions are intermediate in scale at high R_θ .

C. Quadrant Analysis

A traditional quadrant analysis^{10,11,14} was conducted. The fractional contributions to the Reynolds shear stress are shown in Figs. 14(a-d) for the present low and high R_θ data. The $R_\theta = 2870$ and $R_\theta = 4850$ data are shown in Figs. 14(a) and 14(b) respectively for $10 < y^+ < 1000$, which includes the traditional buffer layer, logarithmic layer and the wake region. The high R_θ relatively smooth wall data are shown for $200 < y^+ < 4000$ while high R_θ rough wall ($k^+ \approx 300$) data are shown for $1000 < y^+ < 4000$. As mentioned previously, these locations are well within the inner layer at high R_θ .

At $R_\theta = 2870$, two prominent features are observed. The contribution to Reynolds stress during ejections is slightly greater than the contribution during sweeps, except near the wall, and the contribution to positive \overline{uv} during outward interactions is almost the same as during inward interactions. As shown in Fig. 14(b), there are no significant changes between the quadrant contributions at $R_\theta = 4850$ and $R_\theta = 2870$. Furthermore, the contributions from ejections are slightly greater than those from sweeps within the log-law region at $R_\theta = 4850$ and $R_\theta = 2870$. Contributions from the 1st and 3rd quadrants are very similar to those at both low R_θ . Thus, there are no significant changes in the quadrant contributions within the range $3000 \lesssim R_\theta \lesssim 5000$. Regarding this, the present $R_\theta = 2870$ results have also been verified to exhibit quite favorable agreement with the $R_\theta = 1780$ boundary layer results of Nagano and Tagawa.¹⁰

The $R_\theta \approx 2 \times 10^6$ fractional quadrant contributions differ from the low R_θ results in all quadrants. Specifically, there is a greater contribution in each quadrant. In total, these, of course, reflect the features exhibited by \overline{uv}^+ and ρ_{uv} with increasing R_θ . Currently, no reliable Reynolds stress data were available nearer the wall for the high R_θ cases. Within the logarithmic region, however, (and for both the high R_θ flows), the fractional contribution by sweeps is slightly greater than that by ejections. This shift (albeit small) is also likely to be another effect of scale separation. As shown in Fig. 14(c), the quadrant contributions increase significantly in each quadrant with increasing R_θ such that the overall contribution remains essentially the same. It can be seen that there is a small further increase in the quadrant contribution with an increase in wall roughness. The effect of k^+ , however, on \overline{uv}^+ is quite relatively small compared to the effect of R_θ .

The percentages of time the signals spend in each of the quadrants are shown in Figs. 15(a-

d). As indicated, at $R_\theta = 2870$, except for $y^+ \leq 100$, 30%-35% of the total time is associated with ejections. This result remains essentially the same at $R_\theta = 4850$. Comparison indicates that at high R_θ the occurrence of ejection events is slightly lower at 25% – 30% in both the relatively smooth wall and rough wall cases. Sweep event occurrences also decrease slightly, from near 35% at $R_\theta = 2870$ and 4850 to slightly above 25% – 30% at high R_θ . The percentage of time associated with outward interactions increases slightly with increasing Reynolds number. There are no roughness effects observed in these occurrences. There is, however, a significant R_θ dependence regarding the percentage of time associated within inward interactions. These go up from generally less than 15% at $R_\theta = 2870$ to generally greater than 20% at high R_θ . This is possibly related to an increase in intensity of the inactive motions²⁷ at high R_θ . Overall, there are no apparent effects of wall roughness on the percentage of time the signals spend in each of the quadrants.

1. Weighted probability density functions

The weighted probability density function of u and v , $wpdf$, is defined as,

$$wpdf = -uvP(u, v), \quad (5)$$

where, $P(u, v)$ is the joint probability density function of u and v . This function provides a measure of the relative distribution of the contributions to \overline{uv} . The weighted probability density functions at $y_p/2$ are shown for $R_\theta = 2870$, $R_\theta = 4850$, $R_\theta \simeq 2 \times 10^6$ and $R_\theta \simeq 4 \times 10^6$ in Figs. 16(a-d) respectively. As shown in Fig. 16(a), the $wpdf$ distribution at $R_\theta = 2870$ is focused in the 2nd and 4th quadrants with less activity in the 1st and 3rd quadrants. As mentioned previously, at this wall normal location, the contribution to $-\overline{uv}^+$ from ejections is greater than the contribution from sweeps. This behavior does not change significantly at $R_\theta = 4850$ as shown in Fig. 16(b). At low R_θ , contributions from ejections exceed those from sweeps by about 4%. The quadrant contributions, however change slightly from high intensity u^+ motions and not so high intensity v^+ motions at $R_\theta = 2870$ to more equal intensity motions at $R_\theta = 4850$.

The $wpdf$ at $R_\theta \simeq 2 \times 10^6$ exhibits identifiable differences from the low R_θ results. The high R_θ $wpdf$ appears slightly less concentrated in the 2nd and 4th quadrants; instead, is more evenly distributed throughout all four quadrants. This is clearly visible in the high R_θ

rough wall results shown in Fig. 16(d). As indicated previously, contributions from sweeps are slightly greater at both high R_θ at $y_p/2$.

The *wpdfs* at $2y_p$ are shown in Figs. 17(a-d). The quadrant contributions at $2y_p$, $R_\theta = 2870$ and 4850 (Figs. 17(a) and 17(b)) are similar to those at $y_p/2$. They are concentrated in the 2^{nd} and 4^{th} quadrants. The u^+ and v^+ motions are, however, more equally intense at $2y_p$. The *wpdfs* at $2y_p$ shown in Figs. 17(a-d) are very similar to those at $y_p/2$. The distribution in Fig. 17(c), is similar to the distribution in Fig. 16(c) despite noise. Similarly, the more homogeneous distribution in Fig. 17(d) for $R_\theta \simeq 4 \times 10^6$ is similar to the $R_\theta \simeq 4 \times 10^6$, $y_p/2$ distribution in Fig. 16(d).

IV. SUMMARY

This study investigated the R_θ dependence of the motions underlying $-\overline{uv}$ in turbulent boundary layers. In doing so, major emphases were to better understand the scales of motion contributing to $-\overline{uv}$, and the effects of scale separation as R_θ becomes large. Also an effort was made to identify the effects of wall roughness (over a limited k^+ range) on $-\overline{uv}$ at high R_θ .

The major findings of this study are as follows:

1. Relative to the available signal intensity, the correlation between u and v decreases with an increase in R_θ (as reflected in ρ_{uv}). Current results, combined with published results, indicate that this decrease is approximately logarithmic. The peaks in the premultiplied u and v power spectra move apart as R_θ is increased, thereby reducing the spectral overlap. This may underly the reduction in the correlation between the two velocity components. Trends in the reduction in ρ_{uv} attributable to wall roughness (for $k^+ \lesssim 500$) were not apparent.
2. The reduction in the correlation between u and v is not apparent in the inner-normalized $-\overline{uv}$, as the normalizing factor, U_τ^2 , is nearly equal to the peak value of $-\overline{uv}$. All the other uv statistics change with increasing R_θ . The inner-normalized rms, $(uv)'$, and the kurtosis, $K(uv)$, increase and the skewness, $S(uv)$, decreases with increasing R_θ .
3. For the range, $3000 \lesssim R_\theta \lesssim 5000$, the peak of the premultiplied u - v cospectrum

occurs near the peak of the premultiplied u power spectrum. At high R_θ , the peak of the premultiplied u - v cospectrum shifts toward the peak in the premultiplied v power spectrum. At high R_θ , there is very little discernible effect of increasing wall roughness on the u - v cospectrum (for the k^+ and y^+ values explored).

4. The largest contribution to $-\overline{uv}$ comes from low frequencies at $3000 < R_\theta < 5000$. The scales of motion contributing to $-\overline{uv}$ shift from low to intermediate frequencies with increasing R_θ regardless of surface roughness. Furthermore, it was shown that at $R_\theta \sim O(10^6)$, the low frequency u and v motions correlate very little.
5. The mean frequency of the u and v motions, f_x , nominally follows the peak frequency of the u - v cospectrum at low R_θ and even more so at high R_θ . It is shown that neither inner nor outer normalizations effectively scale the R_θ dependence of f_x .
6. The contributions from all (u,v) quadrants increase with increasing R_θ . These contributions increase slightly with increasing wall roughness as well. The *wpdf* is focused in the 2^{nd} and the 4^{th} quadrants for the turbulent boundary layer within the range $3000 \lesssim R_\theta \lesssim 5000$, whereas it is more homogeneously distributed at high R_θ , especially with increasing wall roughness. Except very close to the wall, the contributions to $-\overline{uv}$ are slightly greater from ejections at low R_θ . At high R_θ , the contribution from sweeps remains large up to a greater distance away from the wall. The $R_\theta = 2870$ and 4850 results are highly similar.
7. The effect of R_θ on the u - v correlations is greater than the effects of wall roughness. There is, however, evidence of wall roughness effects on the u - v correlations in individual quadrants. These effects of wall roughness appear to cancel each other in the resultant so that the overall quadrant contribution does not change significantly with increasing wall roughness within the range $0 \lesssim k^+ \lesssim 500$ at $R_\theta \sim O(10^6)$.
8. Overall, for the admittedly limited range of wall roughness ($k^+ \approx 0, 25 \sim 50, 300-500$) and Reynolds numbers explored, the effect of Reynolds number appears to be much greater than the addition of wall roughness (outside the roughness sublayer).

V. ACKNOWLEDGMENTS

This work was supported by the National Science Foundation and Office of Naval Research under grants CTS-0120061 (grant monitor Dr Michael W Plesniak) and N00014-00-1-0753 (grant monitor Dr Ronald D Joslin) respectively.

* Electronic address: priyadar@eng.utah.edu

† Electronic address: klewicki@eng.utah.edu

- ¹ M. Gad el Hak and P. R. Bandyopadhyay, *Reynolds number effects in the wall-bounded turbulent flows*, Appl. Mech. Rev. **47**, 307 (1994).
- ² P. R. Spalart, *Direct simulation of a turbulent boundary layer up to $R_\theta = 1410$* , Journal of Fluid Mechanics **187**, 61 (1988).
- ³ P. Priyadarshana and J. C. Klewicki, *Reynolds number scaling of wall layer velocity-vorticity products*, in *Reynolds Number Scaling in Turbulent Flow*, edited by A. J. Smits (Kluwer, 2003), pp. 117–122.
- ⁴ J. C. Klewicki, *On the interaction between the inner and outer region motions in turbulent boundary layers*, Ph.D. thesis, Michigan State University (1989).
- ⁵ J. C. Klewicki, J. A. Murray, and R. E. Falco, *Vortical motion contributions to stress transport in turbulent boundary layer*, Physics of Fluids **6**, 277 (1994).
- ⁶ K. R. Sreenivasan and A. Sahay, *The persistence of viscous effects in the overlap region, and the mean velocity in turbulent pipe and channel flows*, in *Self sustaining mechanisms of wall turbulence*, edited by R. L. Panton (Computational Mechanics Publications, Billerica, MA, 1997), pp. 153–171.
- ⁷ T. Wei, P. Fife, J. C. Klewicki, and P. A. McMurtry, *Properties of the mean momentum balance in turbulent boundary layer, pipe and channel flows* (2004), to appear in Journal of Fluid Mechanics.
- ⁸ D. B. DeGraaff and J. K. Eaton, *Reynolds-number scaling of flat-plate turbulent boundary layer*, Journal of Fluid Mechanics **422**, 319 (2000).
- ⁹ J. Balint, J. M. Wallace, and P. Vukoslavcevic, *The velocity and vorticity vector fields of a turbulent boundary layer. part 2. Statistical properties*, Journal of Fluid Mechanics **228**, 53

(1994).

- ¹⁰ Y. Nagano and M. Tagawa, *Statistical characteristics of wall turbulence with a passive scalar*, Journal of Fluid Mechanics **196**, 157 (1988).
- ¹¹ J. M. Wallace, H. Eckelmann, and R. S. Brodkey, *The wall region in turbulent shear flow*, Journal of Fluid Mechanics **54**, 39 (1972).
- ¹² E. R. Corino and R. S. Brodkey, *A visual investigation of the wall region in turbulent flow*, Journal of Fluid Mechanics **37**, 1 (1969).
- ¹³ W. W. Willmarth and S. S. Lu, *Structure of the Reynolds stress near the wall*, Journal of Fluid Mechanics **87**, 65 (1972).
- ¹⁴ Y. Nagano, T. Tsuji, and T. Houra, *Structure of turbulent boundary layer subject to adverse pressure gradients*, Internal Journal of Heat and Fluid Flow **19**, 563 (1998).
- ¹⁵ J. C. Klewicki and R. E. Falco, *On accurately measuring statistics associated with small-scale structure in turbulent boundary layers using hot-wire probes*, Journal of Fluid Mechanics **219**, 119 (1990).
- ¹⁶ M. M. Metzger and J. C. Klewicki, *A comparative study of near-wall turbulence in high and low Reynolds number boundary layers*, Physics of Fluids **13**, 692 (2001).
- ¹⁷ J. C. Klewicki and M. M. Metzger, *Studies of high Reynolds number turbulence in the atmospheric surface layer over the salt playa of western Utah*, in *Reynolds Number Scaling in Turbulent Flow*, edited by A. J. Smits (Kluwer, 2002), pp. 45–52.
- ¹⁸ M. M. Metzger, *Scalar dispersion in high Reynolds number boundary layer*, Ph.D. thesis, University of Utah (2002).
- ¹⁹ H. Schlichting and K. Gersten, *Boundary layer theory* (Springer, 2000).
- ²⁰ P. A. Krogstad, R. A. Antonia, and L. W. B. Browne, *Comparison between rough- and smooth-wall turbulent boundary layers*, Journal of Fluid Mechanics **245**, 599 (1992).
- ²¹ R. Sadr and J. C. Klewicki, *Surface shear stress measurement system for boundary layer flow over a salt playa*, Meas. Sci. Technol. **11**, 1403 (2000).
- ²² H. H. Bruun, *Hot-wire anemometry. Principles and signal analysis* (Oxford university press, 1995).
- ²³ S. G. Saddoughi and S. V. Veeravalli, *Local isotropy in turbulent boundary layers at high Reynolds number*, Journal of Fluid Mechanics **268**, 333 (1994).
- ²⁴ J. S. Bendat and A. G. Piersol, *Random data : Analysis and measurement procedures* (New

Yoeck: Wiley, 1986).

- ²⁵ R. Shiavi, *Introduction to applied statistical signal analysis* (San Diego : Academic Press, 1999).
- ²⁶ D. B. DeGraaff, *Reynolds number scaling of the turbulent boundary layer on a flat plate and on swept and unswept bumps*, Ph.D. thesis, Stanford University (1999).
- ²⁷ A. A. Townsend, *Equilibrium layers and wall turbulence*, Journal of Fluid Mechanics **11** (1961).
- ²⁸ H. H. Fernholz and P. J. Finley, *The incompressible zero-pressure-gradient turbulent boundary layer: an assessment of the data*, Prog. Aerospace. Sci. **32**, 245 (1996).
- ²⁹ A. K. Gupta and R. E. Kaplan, *Statistical characteristics of Reynolds stress in a turbulent boundary layer*, Physics of Fluids **15**, 981 (1972).
- ³⁰ In this regard it is worth noting that both the present $R_\theta = 1010$ data and the $R_\theta < 2000$ data of DeGraaff and Eaton often indicate dependencies inconsistent with the Reynolds number trends observed for R_θ greater than about 3000. At present these are believed to constitute effects confined to a low R_θ (post transitional) regime.

| R_θ | U_∞ [m/s] | θ [m] | δ^* [m] | δ [m] | H |
|----------------------|------------------|--------------|----------------|--------------|------|
| $\sim 2 \times 10^6$ | 6.31 | 5.39 | 6.47 | 84 | 1.19 |
| $\sim 4 \times 10^6$ | 17.2 | 4.43 | 5.27 | 69 | 1.24 |
| $\sim 2 \times 10^6$ | 7.35 | 4.57 | 5.58 | 67 | 1.22 |
| 1010 | 0.607 | 0.0248 | 0.0360 | 0.206 | 1.45 |
| 2870 | 1.752 | 0.0245 | 0.0343 | 0.205 | 1.40 |
| 4850 | 2.981 | 0.0243 | 0.0335 | 0.199 | 1.38 |

TABLE I: Estimated integral parameters for the high and low R_θ boundary layers. Note that the values cited for high R_θ experiments are typical, but varied within the ensemble of acquisition runs collected.

| R_θ | U_τ [m/s] | ν [m ² /s] | k^+ | δ^+ | y_p [m] | y_p^+ | y_p/δ | l^+ |
|----------------------|----------------|---------------------------|---------------|--------------------|-----------------------|---------|----------------------|-------|
| $\sim 2 \times 10^6$ | 0.1962 | 1.85×10^{-5} | $25 \sim 50$ | 8.9×10^5 | 0.1783 | 1892 | 2.1×10^{-3} | 11 |
| $\sim 4 \times 10^6$ | 0.5366 | 1.85×10^{-5} | ≈ 300 | 2.0×10^6 | 0.0976 | 2825 | 1.4×10^{-3} | 29 |
| $\sim 2 \times 10^6$ | 0.2803 | 1.87×10^{-5} | ≈ 500 | 1.01×10^6 | 0.1335 | 2010 | 2.0×10^{-3} | 13 |
| 1010 | 0.0282 | 1.5×10^{-5} | smooth | 388 | 2.58×10^{-2} | 39.4 | 0.102 | 2.0 |
| 2870 | 0.0707 | 1.5×10^{-5} | smooth | 966 | 1.63×10^{-2} | 62.2 | 0.064 | 4.3 |
| 4850 | 0.1125 | 1.5×10^{-5} | smooth | 1493 | 1.27×10^{-2} | 77.3 | 0.052 | 7.2 |

TABLE II: Inner normalized wall roughness values, inner parameters and peak locations of $-\overline{uv}^+$ for the high and low R_θ smooth and rough wall turbulent boundary layers.

Fig. 1 The six element hot-wire sensor (6-X) probe.

Fig. 2 The u, v correlation coefficient, ρ_{uv} . \star present $R_\theta = 1010$, \blacklozenge $R_\theta = 2870$, \blacktriangledown $R_\theta = 4850$, \blacksquare $R_\theta \simeq 2 \times 10^6$ $k^+ \simeq 25 \sim 50$, \blacktriangleright $R_\theta \simeq 4 \times 10^6$ $k^+ \simeq 300$, \blacktriangleleft $R_\theta \simeq 2 \times 10^6$ $k^+ \simeq 500$, \diamond DeGraaff's²⁶ $R_\theta = 13000$, \triangle $R_\theta = 31000$.

Fig. 3 Variation of $-\rho_{uv_{yp}}$ vs R_θ . \star present $R_\theta = 1010$, \blacklozenge $R_\theta = 2870$, \blacktriangledown $R_\theta = 4850$, \blacksquare $R_\theta \simeq 2 \times 10^6$ $k^+ \simeq 25 \sim 50$, \blacktriangleright $R_\theta \simeq 4 \times 10^6$ $k^+ \simeq 300$, \blacktriangleleft $R_\theta \simeq 2 \times 10^6$ $k^+ \simeq 500$, \diamond DeGraaff's²⁶ data, \bigcirc Warnack's data²⁸ $l^+ = 15$, ∇ Erm's data²⁸. The error bars at $R_\theta \simeq 5 \times 10^6$, $R_\theta \simeq 3 \times 10^6$ and $R_\theta \simeq 1 \times 10^7$ represent ± 1 standard deviation of scatter in $-\rho_{uv}$ at y_p . The curve fit for low R_θ data is, $\rho_{uv} = -0.0798 \log(R_\theta) + 0.6679$.

Fig. 4 Inner normalized Reynolds stress, $-\overline{uv}/U_\tau^2$. \star Present $R_\theta = 1010$, \blacklozenge $R_\theta = 2870$, \blacktriangledown $R_\theta = 4850$, \blacksquare $R_\theta \simeq 2 \times 10^6$, \blacktriangleright $R_\theta \simeq 4 \times 10^6$ $k^+ \simeq 300$, \blacktriangleleft $R_\theta \simeq 2 \times 10^6$ $k^+ \simeq 500$.

Fig. 5 Inner normalized rms of the uv fluctuation, $(uv)'/U_\tau^2$. \star present $R_\theta = 1010$, \blacklozenge $R_\theta = 2870$, \blacktriangledown $R_\theta = 4850$, \blacksquare $R_\theta \simeq 2 \times 10^6$, \blacktriangleright $R_\theta \simeq 4 \times 10^6$ $k^+ \simeq 300$, \blacktriangleleft $R_\theta \simeq 2 \times 10^6$ $k^+ \simeq 500$, \square Gupta and Kaplan²⁹ $R_\theta = 6500$.

Fig. 6 Skewness of uv fluctuations, $\overline{(uv)^3}/((uv)')^3$. Present \blacklozenge $R_\theta = 2870$, \blacktriangledown $R_\theta = 4850$, \blacksquare $R_\theta \simeq 2 \times 10^6$, \blacktriangleright $R_\theta \simeq 4 \times 10^6$ $k^+ \simeq 300$, \blacktriangleleft $R_\theta \simeq 2 \times 10^6$ $k^+ \simeq 500$, \square Gupta and Kaplan²⁹ $R_\theta = 6500$.

Fig. 7 Kurtosis of uv fluctuations, $\overline{(uv)^4}/((uv)')^4$. Present \blacklozenge $R_\theta = 2870$, \blacktriangledown $R_\theta = 4850$, \blacksquare $R_\theta \simeq 2 \times 10^6$, \blacktriangleright $R_\theta \simeq 4 \times 10^6$ $k^+ \simeq 300$, \blacktriangleleft $R_\theta \simeq 2 \times 10^6$ $k^+ \simeq 500$, \square Gupta and Kaplan²⁹ $R_\theta = 6500$.

Fig. 8 Premultiplied u v cospectrum, $-f^+\Lambda(uv^+)$, with u and v power spectra, $\Psi(u^+)$, $\Psi(v^+)$. — $\Psi(u^+)$, - - - $\Psi(v^+)$, $-f^+\Lambda(uv^+)$ at low R_θ .

Fig. 9 Premultiplied u v cospectrum, $-f^+\Lambda(uv^+)$, with u and v power spectra. — $\Psi(u^+)$, - - - $\Psi(v^+)$, $-f^+\Lambda(uv^+)$ at high R_θ .

Fig. 10 The spectral correlation coefficients, $-f\Lambda/(\sqrt{(\Psi(u)\Psi(v))})$, at — $y_p/2$, and , $2y_p$.

Fig. 11 Contributions of filtered signals, $-\overline{u_f v_f}^+$, to total $-\overline{uv}^+$ as a function of cut-off frequency. \square low pass filtered $-\overline{u_f v_f}^+$, \circ high pass filtered $-\overline{u_f v_f}^+$, at — $y_p/2$, at $2y_p$.

Fig. 12 Behavior of f_x with R_θ under outer normalization ▼ and, inner normalization ■.
The high R_θ data shown are for $R_\theta \simeq 2 \times 10^6$ $k^+ \simeq 25 \sim 50$.

Fig. 13 Filtered signal correlation coefficients, $-\rho_{u_f v_f}$, as a function of cut-off frequency. □
low pass filtered $-\rho_{u_f v_f}$, ○ high pass filtered $-\rho_{u_f v_f}$. ——— $y_p/2$, $2y_p$.

Fig. 14 Fractional contribution to Reynolds shear stress. ○ outward interactions, □ ejections,
★ inward interactions, ◇ sweeps.

Fig. 15 Percentage of time in each quadrant. ○ outward interactions, □ ejections, ★ inward
interactions, ◇ sweeps.

Fig. 16 Weighted probability density functions of u and v at $y_p/2$.

Fig. 17 Weighted probability density functions of u and v at $2y_p$.

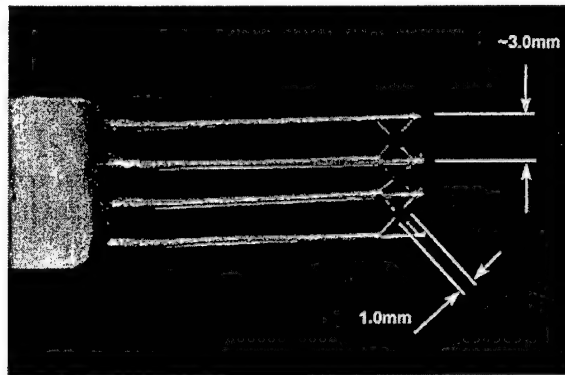


FIG. 1: P. J. A. Priyadarshana, Physics of Fluids

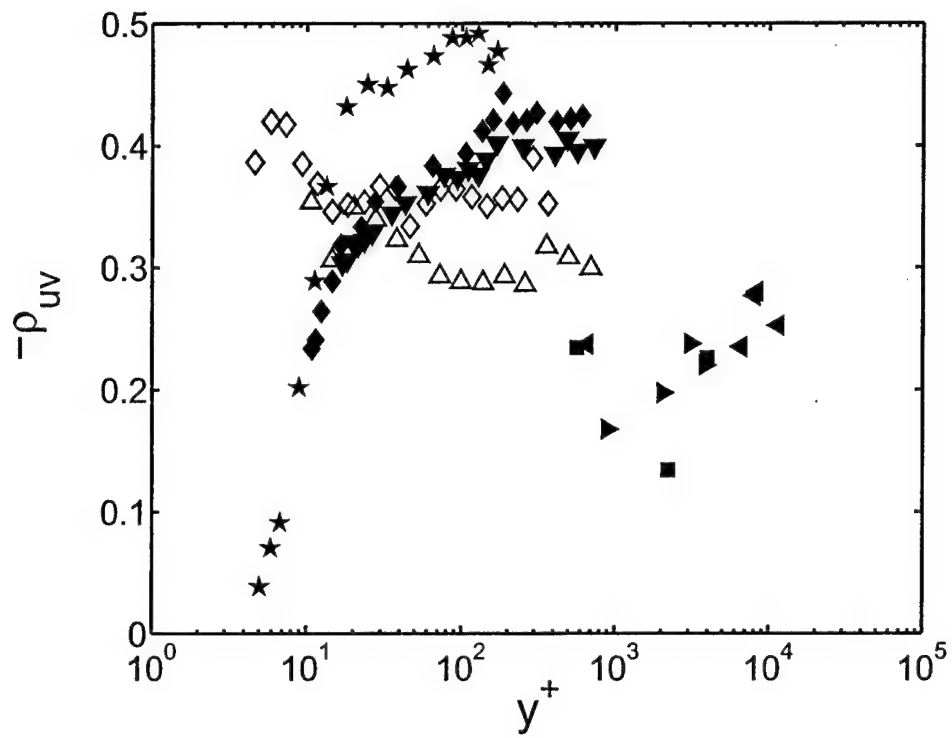


FIG. 2: P. J. A. Priyadarshana, Physics of Fluids

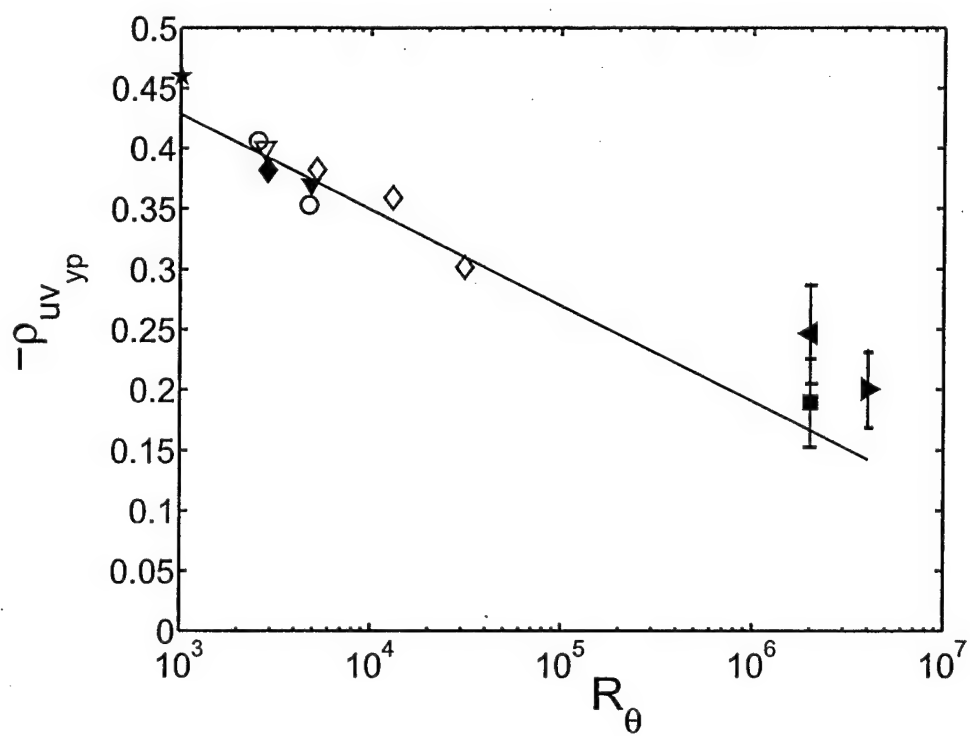


FIG. 3: P. J. A. Priyadarshana, Physics of Fluids

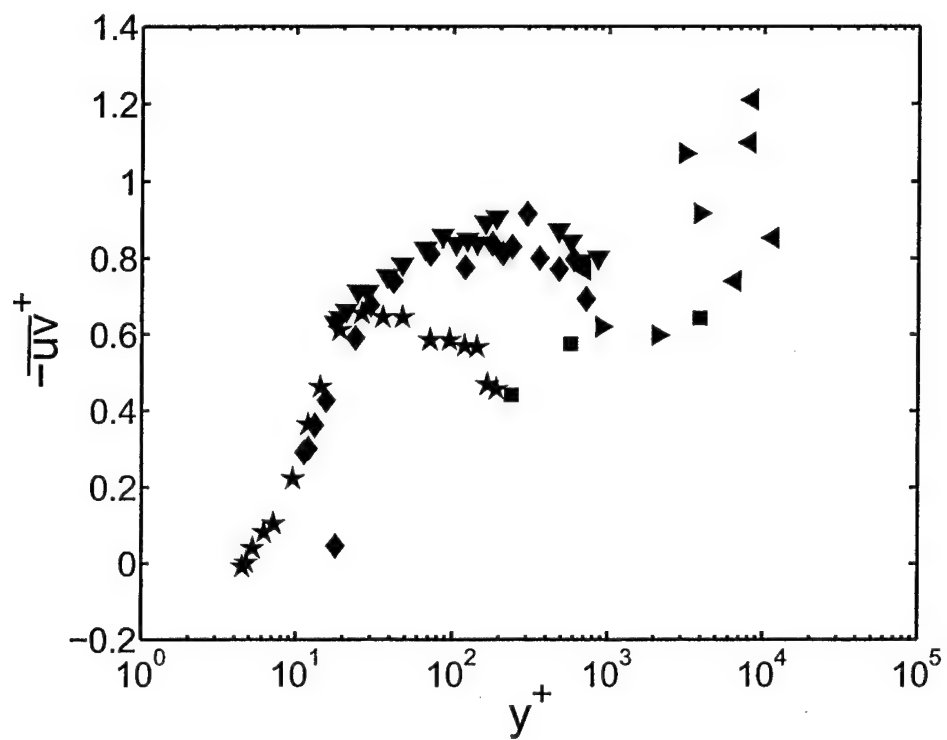


FIG. 4: P. J. A. Priyadarshana, Physics of Fluids

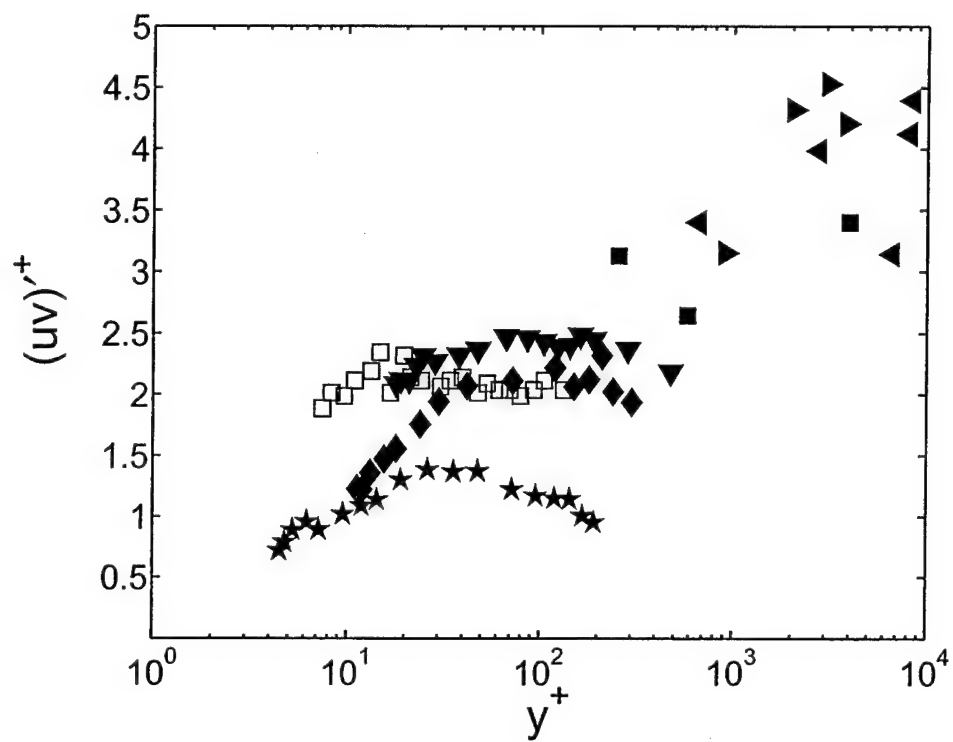


FIG. 5: P. J. A. Priyadarshana, Physics of Fluids

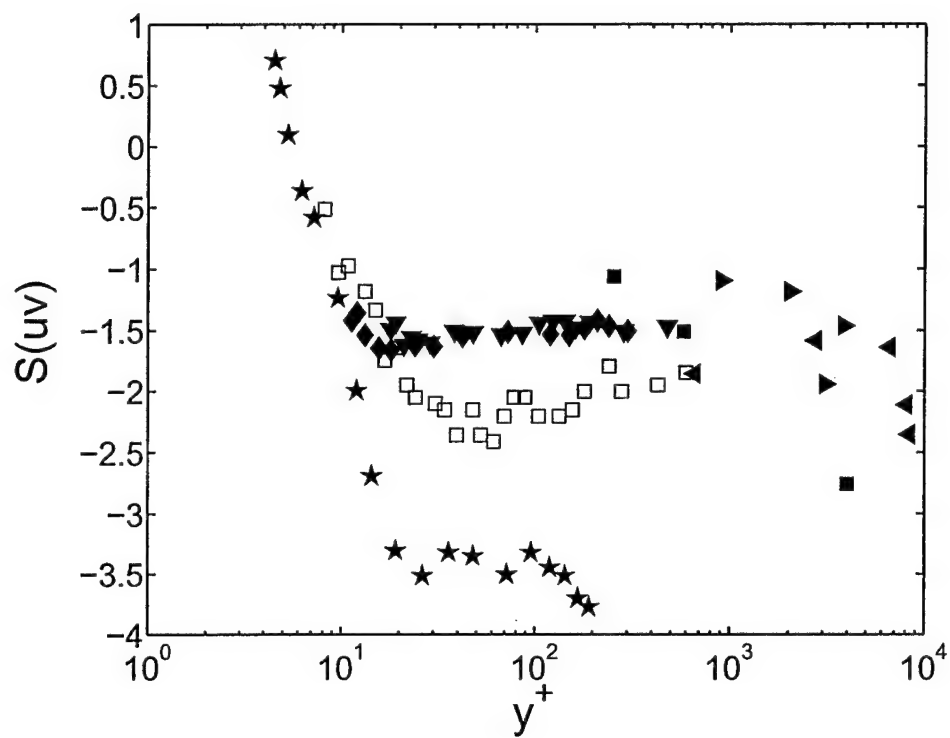


FIG. 6: P. J. A. Priyadarshana, Physics of Fluids

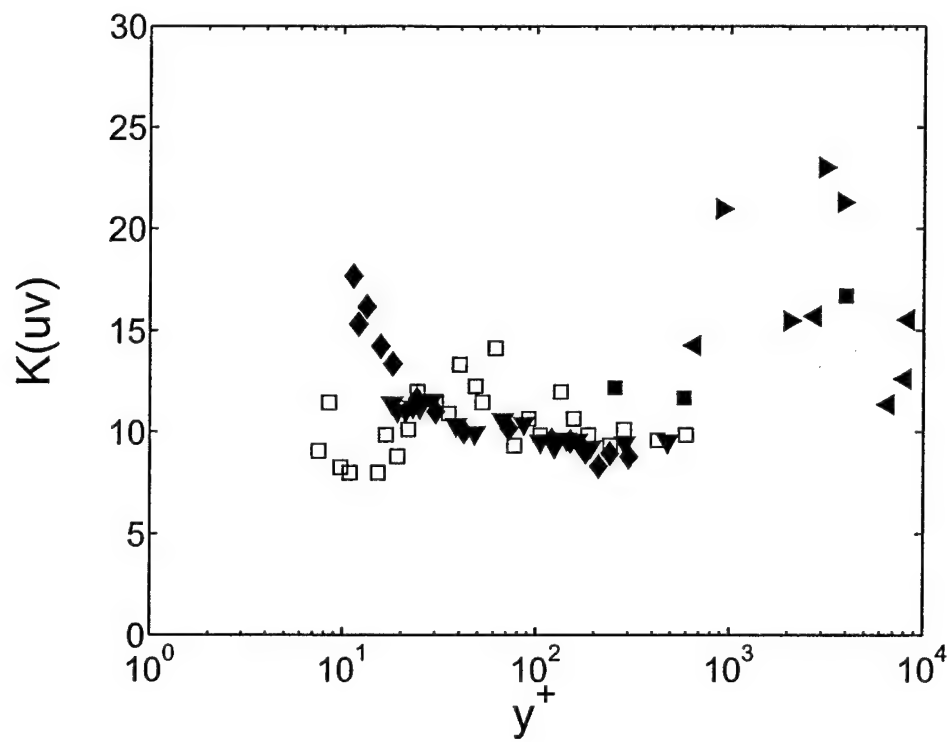
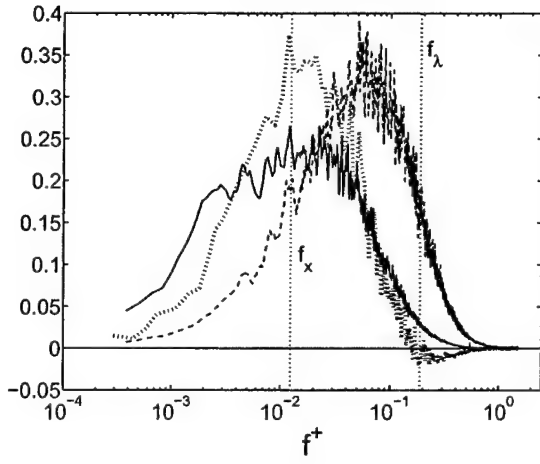
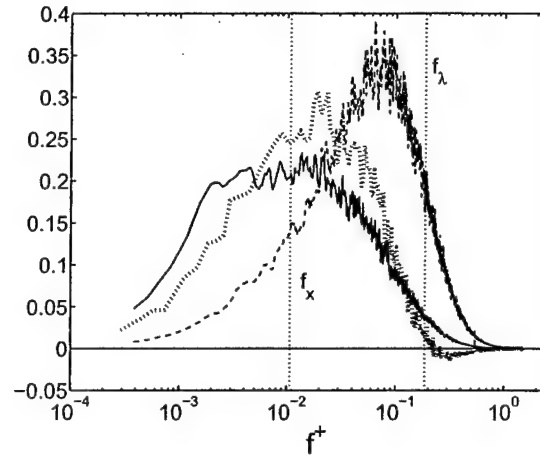


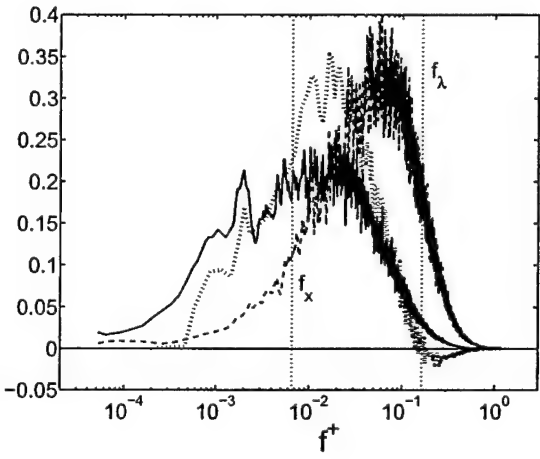
FIG. 7: P. J. A. Priyadarshana, Physics of Fluids



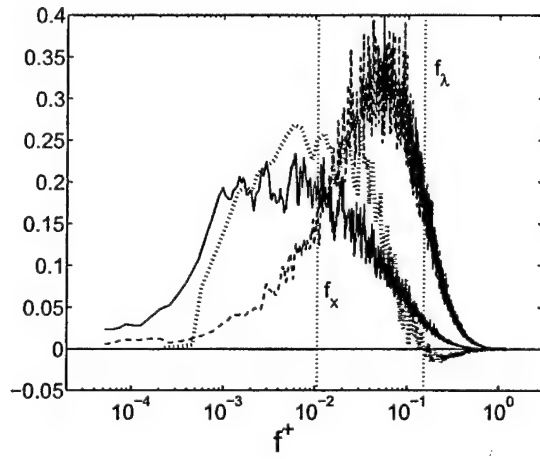
(a) $R_\theta = 2870$ at $y_p/2$



(b) $R_\theta = 2870$ at $2y_p$

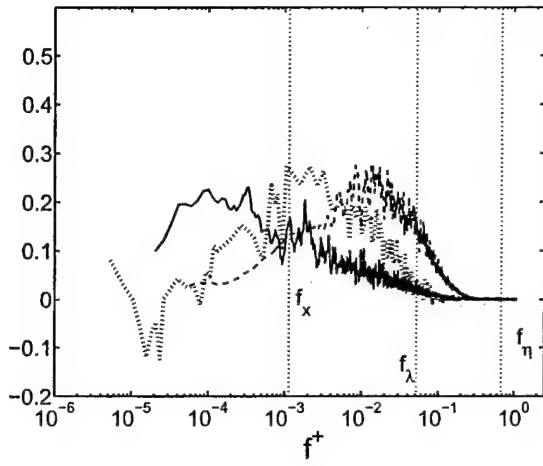


(c) $R_\theta = 4850$ at $y_p/2$

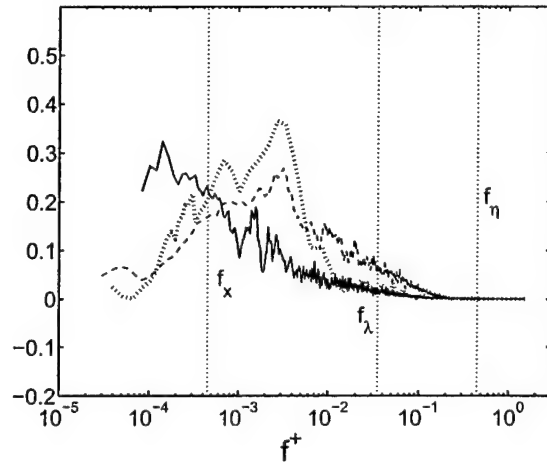


(d) $R_\theta = 4850$ at $2y_p$

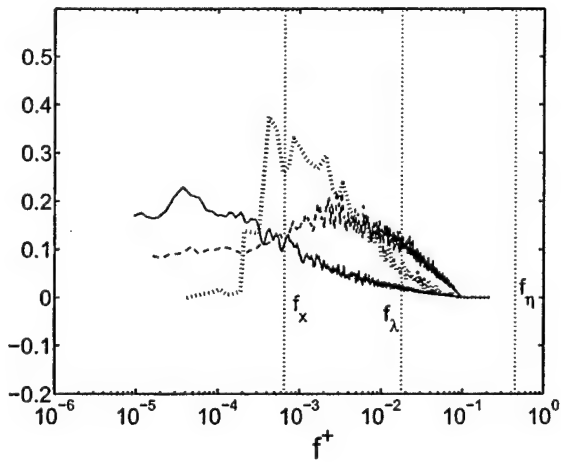
FIG. 8: P. J. A. Priyadarshana, Physics of Fluids



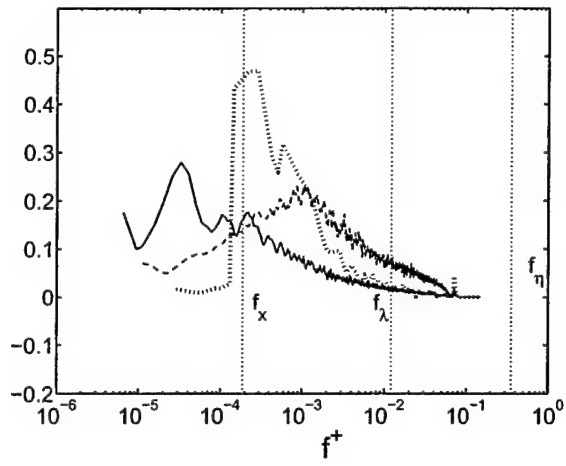
(a) $R_\theta \simeq 2 \times 10^6$ at $y_p/2$



(b) $R_\theta \simeq 2 \times 10^6$ at $2y_p$

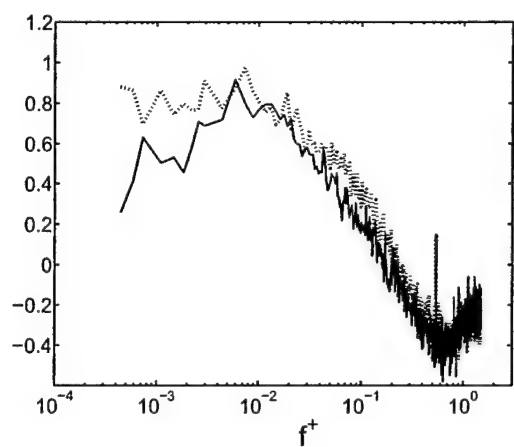


(c) $R_\theta \simeq 4 \times 10^6$ at $y_p/2$

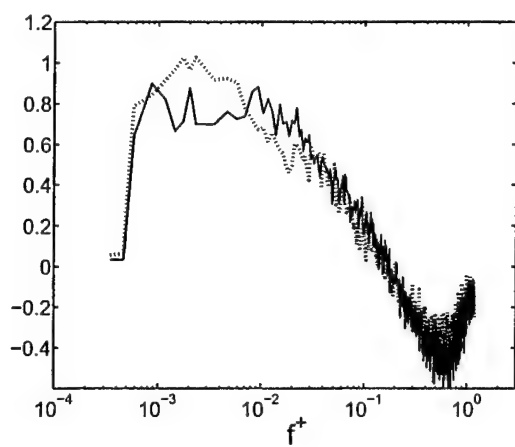


(d) $R_\theta \simeq 4 \times 10^6$ at $2y_p$

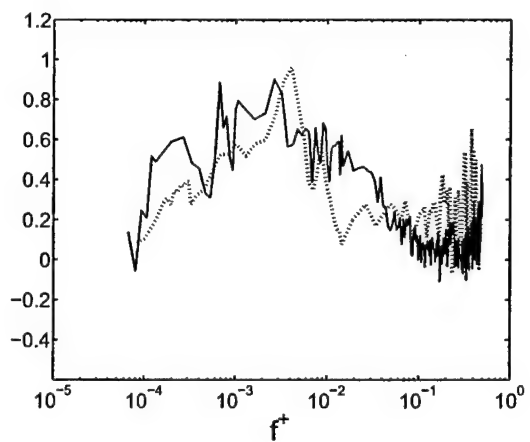
FIG. 9: P. J. A. Priyadarshana, Physics of Fluids.



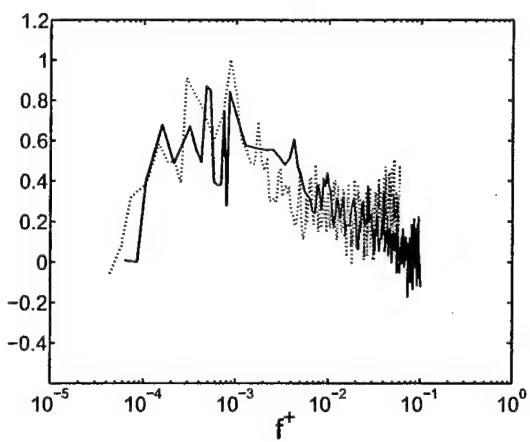
(a) $R_\theta = 2870$



(b) $R_\theta = 4850$

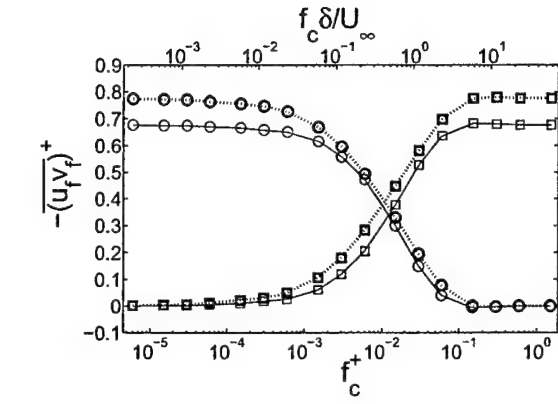


(c) $R_\theta \simeq 2 \times 10^6$, $k^+ \approx 25 \sim 50$

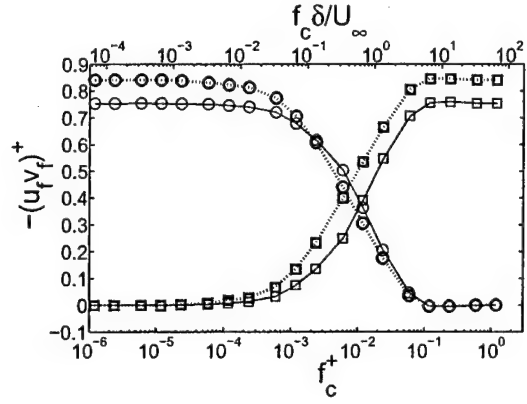


(d) $R_\theta \simeq 4 \times 10^6$, $k^+ \approx 300$

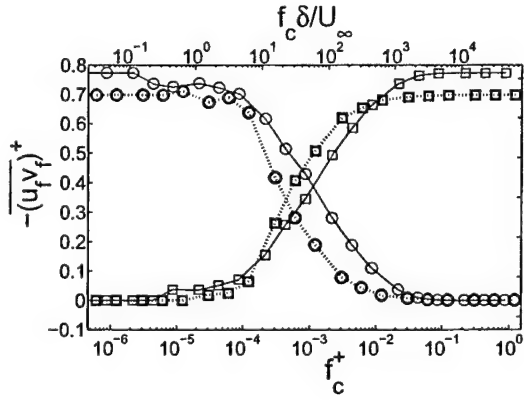
FIG. 10: P. J. A. Priyadarshana, Physics of Fluids



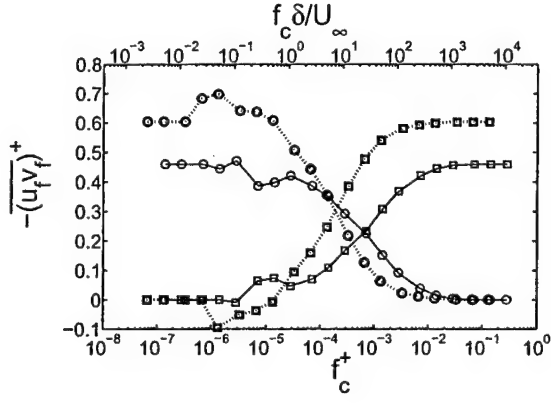
(a) $R_\theta = 2870$



(b) $R_\theta = 4850$



(c) $R_\theta \simeq 2 \times 10^6$, $k^+ \approx 25 \sim 50$



(d) $R_\theta \simeq 4 \times 10^6$, $k^+ \approx 300$

FIG. 11: P. J. A. Priyadarshana, Physics of Fluids

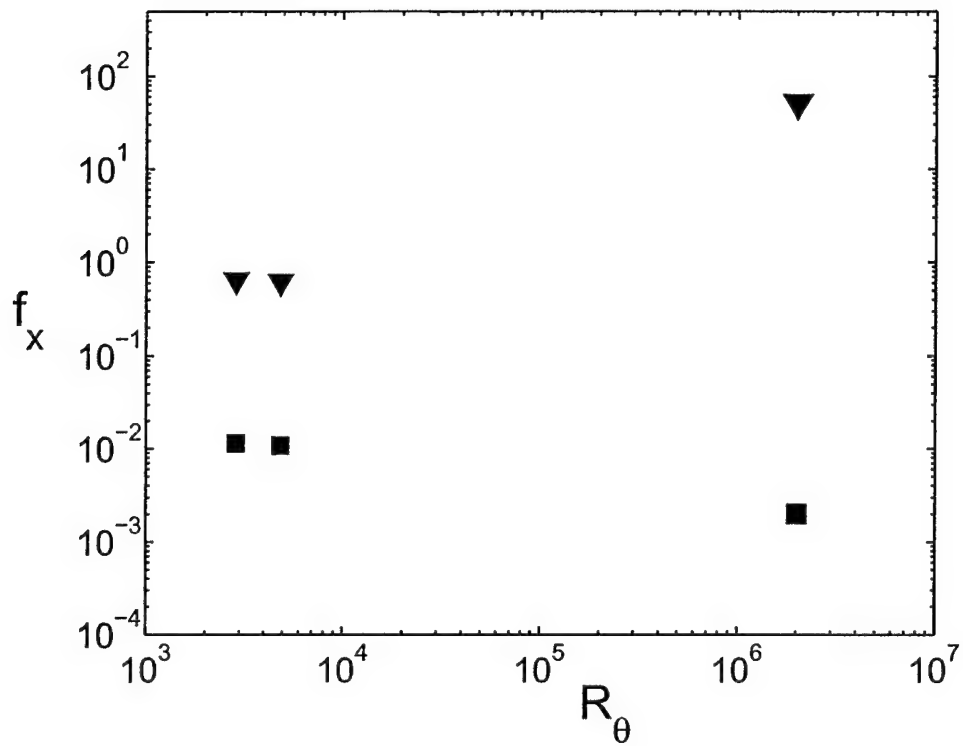
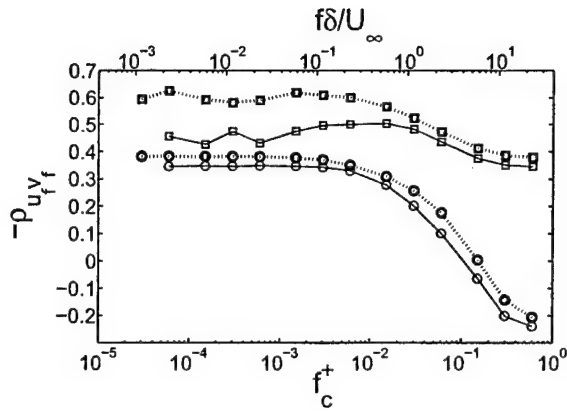
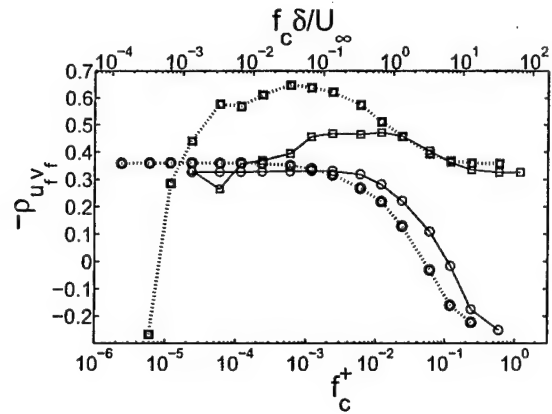


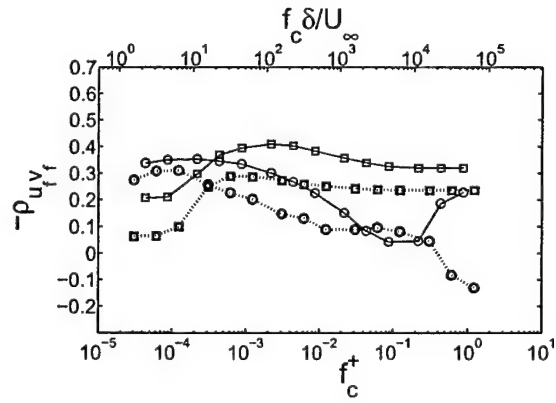
FIG. 12: P. J. A. Priyadarshana, Physics of Fluids



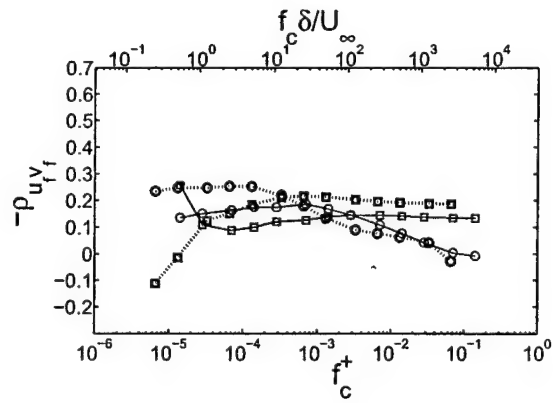
(a) $R_\theta = 2870$



(b) $R_\theta = 4850$

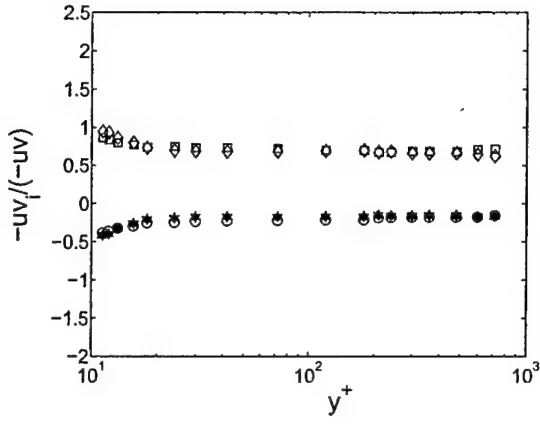


(c) $R_\theta \simeq 2 \times 10^6$, $k^+ \simeq 25 \sim 50$

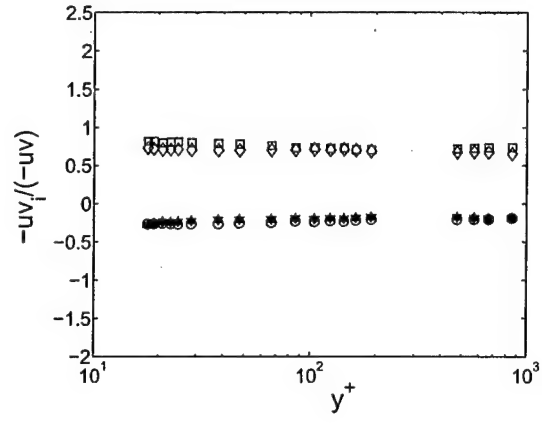


(d) $R_\theta \simeq 2 \times 10^6$, $k^+ \approx 300$

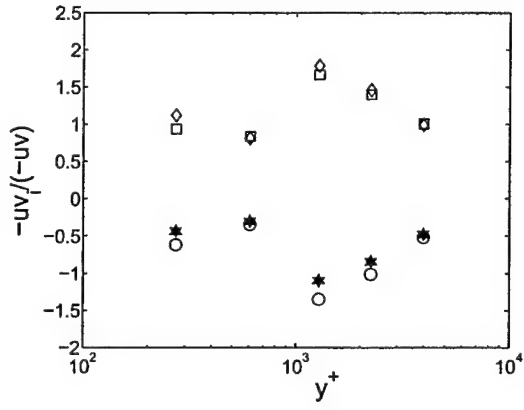
FIG. 13: P. J. A. Priyadarshana, Physics of Fluids



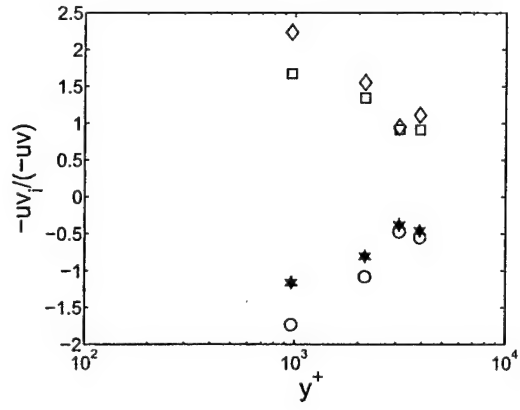
(a) $R_\theta = 2870$



(b) $R_\theta = 4850$

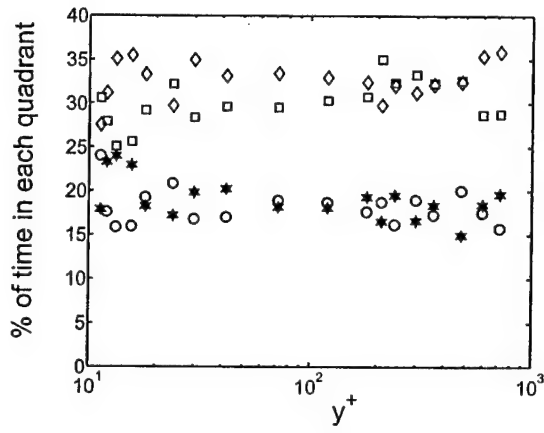


(c) $R_\theta \simeq 2 \times 10^6$, $k^+ \approx 25 \sim 50$

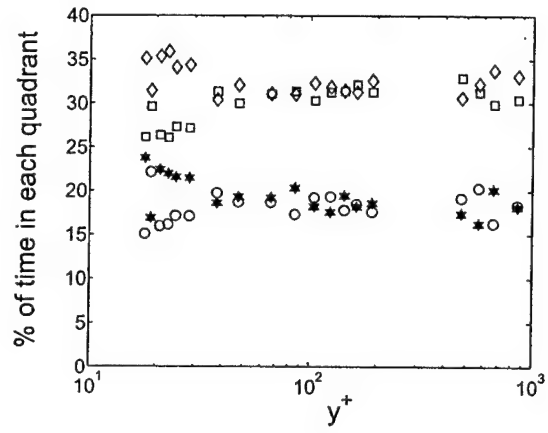


(d) $R_\theta \simeq 4 \times 10^6$, $k^+ \approx 300$

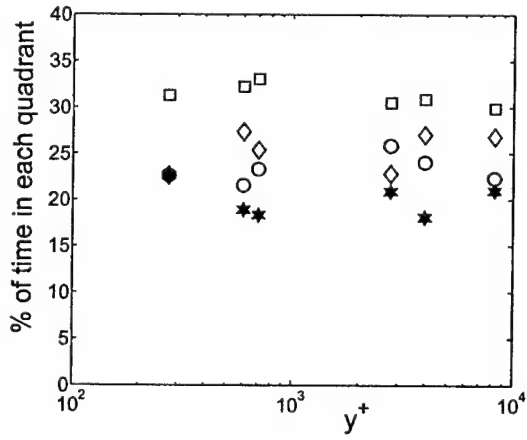
FIG. 14: P. J. A. Priyadarshana, Physics of Fluids



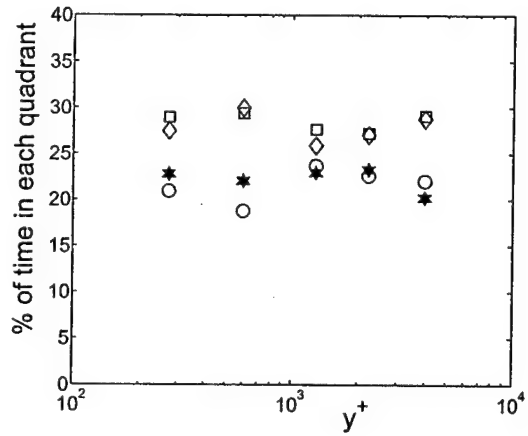
(a) $R_\theta = 2870$



(b) $R_\theta = 4850$

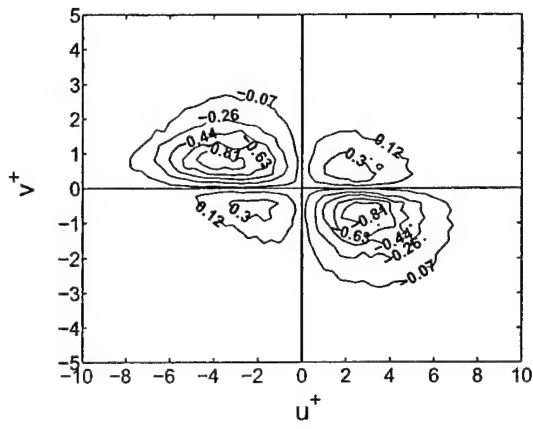


(c) $R_\theta \simeq 2 \times 10^6$, $k^+ \approx 25 \sim 50$

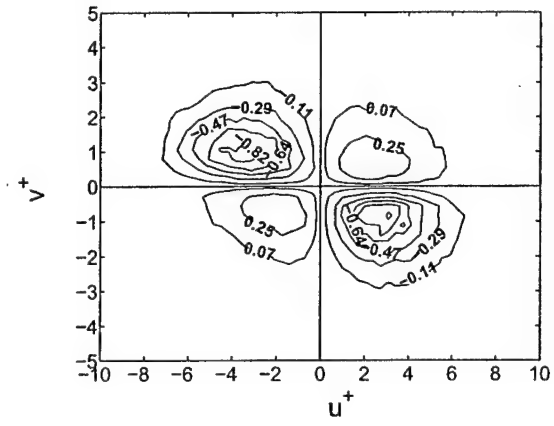


(d) $R_\theta \simeq 4 \times 10^6$, $k^+ \approx 300$

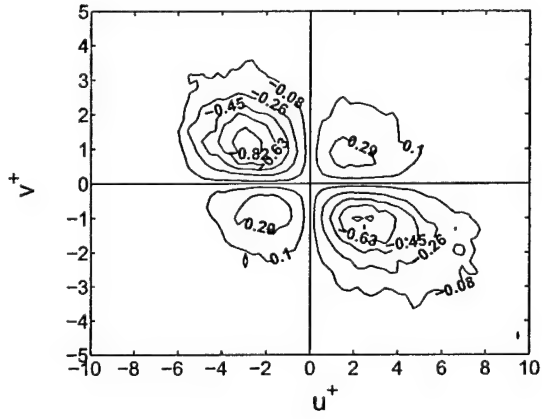
FIG. 15: P. J. A. Priyadarshana, Physics of Fluids



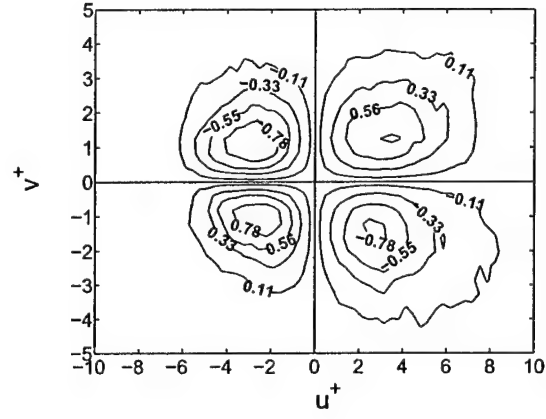
(a) $R_\theta = 2870$



(b) $R_\theta = 4850$



(c) $R_\theta = 2 \times 10^6$, $k^+ \approx 25 \sim 50$



(d) $R_\theta = 4 \times 10^6$, $k^+ \approx 300$

FIG. 16: P. J. A. Priyadarshana, Physics of Fluids

CHAPTER 6

EXPERIMENTAL STUDY OF TURBULENT BOUNDARY LAYER VELOCITY-VORTICITY PRODUCTS AT HIGH AND LOW REYNOLDS NUMBERS

6.1 Abstract

The mean wall normal gradients of the Reynolds shear stress and turbulent kinetic energy have direct connection to the transport mechanisms of the turbulent boundary layer flow. These gradients can be expressed in terms of velocity-vorticity products. Physical experiments were conducted to explore the statistical properties of some of the relevant velocity-vorticity products. The high Reynolds number data ($R_\theta \simeq O(10^6)$) were acquired in the near neutral atmospheric surface layer under both smooth and rough wall conditions. The low R_θ data were from a database acquired in a large scale laboratory facility at $1000 < R_\theta < 5000$. Consistent with a companion study of the Reynolds stresses [98], comparisons of low and high R_θ as well as smooth and rough wall boundary layer results were made at approximate wall normal locations of $y_p/2$ and $2y_p$, where y_p is the peak position of the Reynolds shear stress, at each Reynolds number. In this paper, properties of $v\omega_z$ and $u\omega_z$ products over a three decade variation in Reynolds number are analyzed through their statistics, cospectra, filtered signals and weighted probability density functions. Here, u and v are streamwise and wall normal velocities and ω_z is the spanwise vorticity. It is observed that $v-\omega_z$ correlations exhibit considerable sensi-

tivity to Reynolds number as well as to wall roughness. The low and intermediate frequency motions of $v-\omega_z$ are negatively correlated at low R_θ . The same is observed at high R_θ rough wall flow as well. The low and intermediate motions are positively correlated in the high R_θ , relatively smooth wall flow. The smooth wall low and high R_θ rough wall $v-\omega_z$ quadrant contributions are, however, completely different. Conversely, $u-\omega_z$ correlations are relatively less sensitive to both R_θ and roughness. The dominant scales of $u-\omega_z$ correlations are either of the order of the magnitude of Taylor microscale or intermediate scale. High R_θ $u-\omega_z$ motions show increased contribution in the 4th quadrant.

6.2 Introduction

As discussed in [1, 49], there are numerous important applications involving high R_θ turbulent boundary layer flows. (Here, R_θ is the Reynolds number based on momentum thickness, $R_\theta = U_\infty \theta / \nu$, where U_∞ is the free stream velocity, θ is the momentum deficit thickness and ν is the kinematic viscosity.) The R_θ values encountered in many such applications, however, are often orders of magnitude higher than those capable of detailed study by computation or by laboratory experimentation. An important effect of increasing Reynolds number is that the outer length and velocity scales (as characterized by δ and U_∞) become increasingly large relative to the corresponding inner scales (characterized by the friction velocity, $U_\tau (= \sqrt{\tau_w / \rho})$ and ν). Here, τ_w and ρ are wall shear stress and mass density, respectively. Currently, the effects of the separation of scales on momentum transport are not well understood. Among others, an important objective of this paper is to explore effects of scale separation on the mean turbulent dynamics. In addition, wall roughness can become significant at high R_θ turbulent boundary layers [49, 98]. The present study also provides information regarding the effects of wall roughness (over a limited range) on momentum transport at high R_θ .

There is evidence that the predominant motions participating in stress production and transport have strong vortical signatures [17, 99, 100, 65]. Some of the wall layer features having connections to these vortical motions are low-speed streaks, ejections, sweeps and near-wall internal shear layers. One can also readily show [98, 37] that *i*) the gradient of the kinematic Reynolds shear stress, $-\overline{uv}$, appears in the mean momentum balance, shown in (6.1) for a two dimensional flat plate turbulent boundary layer in the (x, y) plane, and that *ii*) this gradient may be expressed as the difference of velocity-vorticity correlations as shown in (6.4). This relationship is a reduction of the tensor identity shown in (6.2) for well-developed flow [101, 64].

The mean momentum balance for a two-dimensional, incompressible, and statistically stationary flow over a flat plate is given by,

$$U \frac{\partial U}{\partial x} + V \frac{\partial U}{\partial y} = \frac{\partial}{\partial y} \left(\nu \frac{\partial U}{\partial y} - \overline{uv} \right). \quad (6.1)$$

The tensor identity,

$$\frac{\partial \overline{u_j u_i}}{\partial x_j} = -\epsilon_{ijk} \overline{u_j \omega_k} + \frac{1}{2} \frac{\partial \overline{u_j u_j}}{\partial x_i}, \quad (6.2)$$

has relevance to the Reynolds stress gradient term. That is when $i = 1$,

$$\frac{\partial \overline{uv}}{\partial y} = \overline{w \omega_y} - \overline{v \omega_z} + \frac{\partial (\overline{v^2 + w^2 - u^2})}{\partial x}. \quad (6.3)$$

Here, x is in the flow direction and y is the wall normal direction. As is customary, the x and y mean velocity components are given by U and V , time averaging is denoted by an overbar and by uppercase letters, instantaneous quantities $(\tilde{\cdot})$ are defined as the sum of a mean and fluctuation (e.g., $\tilde{u} = U + u$) and vorticity components are identified by their subscript. Inner normalization is denoted by a superscript $+$. All rms fluctuations are represented by a superscript $'$. As originally proposed by Hinze [101], $\overline{w \omega_y} - \overline{v \omega_z}$ may be thought of as Townsend's [96] active or rotational component of motion, and the streamwise gradients, $\frac{\partial}{\partial x} (\overline{v^2 + w^2 - u^2})$

as the inactive or irrotational component of the motion. Klewicki [8, 64] computed these streamwise gradients over the range $1000 \gtrsim R_\theta \gtrsim 5000$ and found that they are generally about three orders of magnitude smaller than $\overline{w\omega_y} - \overline{v\omega_z}$. Thus, for well developed turbulent boundary layer, the wall normal Reynolds stress gradient can be approximated by,

$$-\frac{\partial \overline{uv}}{\partial y} \cong \overline{v\omega_z} - \overline{w\omega_y}. \quad (6.4)$$

As shown by various authors [58, 15], the wall-normal position of the peak Reynolds stress occurs at $y_p \cong 2(\delta^+)^{\frac{1}{2}}$ for the smooth wall turbulent boundary layers. Here, δ^+ is Karman number or the inner normalized boundary layer thickness. Thus, at y_p the wall normal gradient of the Reynolds shear stress is zero. With regard to affecting a time rate of change of mean momentum, the $-\partial \overline{uv}/\partial y$ term in (6.1), therefore, acts as a source for $y < y_p$ and a sink for $y > y_p$. Further insight into this momentum source/sink character is provided by (6.4), showing that $-\partial \overline{uv}/\partial y$ comes about directly through interactions between the velocity and vorticity fields. Regarding scale separation effects, the generally accepted properties of the velocity and vorticity fields in turbulent flows indicate that with increasing Reynolds number the spectral peaks in the fluctuating \vec{v} and $\vec{\omega}$ fields move to increasingly disparate wavenumbers [50]. Thus, the interactions leading to $-\partial \overline{uv}/\partial y$ will likely occur over a decreasingly narrow, intermediate, wavenumber band (relative to the total span of possible wavenumbers) within which the relevant \vec{v} and $\vec{\omega}$ spectral components overlap. Velocity-vorticity cospectra provide direct evidence supporting the notion that this interaction occurs at intermediate scales [87].

Similarly, for $i=2$, the identity (6.2) yields,

$$\frac{\partial q}{\partial y} = 2v \frac{\partial v}{\partial y} - \overline{w\omega_z} + \overline{w\omega_x}. \quad (6.5)$$

Equation 6.5 provides a description of the flow field interactions that establish the wall normal gradient of the turbulent kinetic energy, $q = \frac{1}{2} (\overline{u^2 + v^2 + w^2})$.

A fluctuating vorticity field is one of the important characteristics of turbulent flows. More specifically, vortex stretching has been postulated as the mechanism by which larger eddies transfer angular momentum to smaller eddies, and in doing so sustains the classically defined energy cascade. This reason likely underlies why most turbulent flows are characterized by high levels of high frequency vorticity fluctuations [7, 77]. For the existence of self-sustaining turbulent shear flow, free stream kinetic energy is converted to turbulent kinetic energy and dissipated to internal energy. In addition, (6.4) and (6.5) explicitly indicate how vortical motions via their interaction with the velocity field, participate in generating turbulent stress gradients.

It is well-established that vorticity field information is highly useful in understanding the organized motions in time-dependent viscous flows [77, 63, 85, 50]. Time resolved measurement of vorticity requires a probe with very good spatial and temporal resolution [65, 38, 63, 85, 62, 37, 76, 50]. As shown, velocity-vorticity correlations are important in describing wall-normal stress gradients. Klewicki [64] provides a significant documentation of velocity-vorticity correlations in turbulent boundary layers. Over the range $1000 \lesssim R_\theta \lesssim 5000$, his results indicate considerable R_θ variations in the $\overline{v\omega_z^+}$ profile but much smaller relative variation in $\overline{u\omega_z^+}$. Subsequent studies by Ong [102] and Rovelstad [103] also present velocity-vorticity correlations. Generally, these are in good agreement with Klewicki and Falco [64] as well as Rajagopalan and Antonia [65]. Rajagopalan and Antonia [65] studied the structure of the velocity field associated with spanwise vorticity field in turbulent boundary layer at $R_\theta = 1450$. They present correlation coefficients and cross correlation functions of $v\omega_z$ and $u\omega_z$. Their results are generally found to be in good agreement with those of Klewicki [64]. Similarly, Klewicki et al. [37] reported joint probability density functions of v and ω_z .

As mentioned previously, an issue particularly relevant in understanding the

behavior of the indicated velocity-vorticity products with increasing R_θ is the widening disparity between the scales of motion contributing to the kinetic energy and enstrophy. That is, as $R_\theta \rightarrow \infty$ the spectral intensity of the vorticity concentrates at increasingly higher frequencies while the spectral intensity of the velocity fluctuations moves to lower frequencies. By (6.4), however, the velocity and vorticity must remain correlated for there to be a non-zero contribution to the momentum equation by turbulent inertia. A better understanding of how these two apparent behaviors are accommodated at high R_θ is a major objective of the present effort.

6.3 Experimental Setup and Methodology

6.3.1 Experimental Facility

The high R_θ experimental data used in this study are obtained at the Surface Layer Turbulence and Environmental Science Test (SLTEST) facility [4, 92]. This facility is located on the southern end of the Great Salt lake Desert (113°26.5' W, 40°8.1' N). The test site is characterized by an extremely flat playa composed of a mud, clay, and salt mixture. The upwind fetch remains unobstructed for about 150km. All the measurements were made around sunset or dawn, under near neutrally stable atmospheric conditions. Thermal stability was computed using the Monin-Obukov stability parameter, ζ ($\zeta = y/l$), where, y is the wall normal co-ordinate. The Monin-Obukov length, l is defined as

$$l = \frac{\Theta_o U_\tau^3}{\kappa g \theta v}, \quad (6.6)$$

where, Θ_o is the mean temperature of an adiabatic atmosphere, θ is the fluctuating component of the temperature difference between the actual temperature and Θ_o and κ ($= 0.41$) is the von Karman constant. Sonic anemometer velocity data and associated quartz thermometer temperature data were used to compute ζ . In accordance with the findings of Metzger [39] (see also Klewicki and Metzger [92])

the region of nearly linear temporal variation in this parameter, approximately between $-0.1 < \zeta < 0.1$, was used as the criterion for selecting the near-neutrally stable conditions in the atmospheric surface layer. Further information about this test site may be found in [98, 4, 41, 92].

A custom built 2.4m diameter drag balance [79] was used in the high Reynolds number experiments to measure the wall shear stress directly. A miniSODAR was used to acquire the mean wind profile data up to about 100m from the surface. Following the analysis procedures described in Metzger and Klewicki [4], these profile measurements were used to estimate boundary layer integral parameters. Experimentally estimated integral parameters for different SLTEST facility smooth and rough surface flows are summarized in Table 6.1.

To address scale separation, the above high R_θ data were compared with well-resolved velocity and vorticity measurements of Klewicki and Falco [38, 8, 37, 36]. Some previously unreported results from the data sets of Klewicki [8] relating to the statistics, spectra and joint probability density functions are also shown. All of these data were acquired in the open circuit laboratory wind tunnel described in Klewicki et al. [38, 8, 37]. The estimated integral parameters for all the low and high R_θ data are shown in Table 6.1. The wall roughness, friction velocity, the Karman number and the peak Reynolds stress location at each R_θ are given in

Table 6.1. Estimated integral parameters for the high and low R_θ boundary layers. Note that the values cited for the high R_θ experiments are typical, but varied within the ensemble of acquisition runs collected.

| R_θ | U_∞ [m/s] | θ [m] | δ^* [m] | δ [m] | H |
|----------------------|------------------|--------------|----------------|--------------|------|
| $\sim 2 \times 10^6$ | 6.31 | 5.39 | 6.47 | 84 | 1.19 |
| $\sim 4 \times 10^6$ | 17.2 | 4.43 | 5.27 | 69 | 1.24 |
| $\sim 2 \times 10^6$ | 7.35 | 4.57 | 5.58 | 67 | 1.22 |
| 1010 | 0.607 | 0.0248 | 0.0360 | 0.206 | 1.45 |
| 2870 | 1.752 | 0.0245 | 0.0343 | 0.205 | 1.40 |
| 4850 | 2.981 | 0.0243 | 0.0335 | 0.199 | 1.38 |

the region of nearly linear temporal variation in this parameter, approximately between $-0.1 < \zeta < 0.1$, was used as the criterion for selecting the near-neutrally stable conditions in the atmospheric surface layer. Further information about this test site may be found in [98, 4, 41, 92].

A custom built 2.4m diameter drag balance [79] was used in the high Reynolds number experiments to measure the wall shear stress directly. A miniSODAR was used to acquire the mean wind profile data up to about 100m from the surface. Following the analysis procedures described in Metzger and Klewicki [4], these profile measurements were used to estimate boundary layer integral parameters. Experimentally estimated integral parameters for different SLTEST facility smooth and rough surface flows are summarized in Table 6.1.

To address scale separation, the above high R_θ data were compared with well-resolved velocity and vorticity measurements of Klewicki and Falco [38, 8, 37, 36]. Some previously unreported results from the data sets of Klewicki [8] relating to the statistics, spectra and joint probability density functions are also shown. All of these data were acquired in the open circuit laboratory wind tunnel described in Klewicki et al. [38, 8, 37]. The estimated integral parameters for all the low and high R_θ data are shown in Table 6.1. The wall roughness, friction velocity, the Karman number and the peak Reynolds stress location at each R_θ are given in

Table 6.1. Estimated integral parameters for the high and low R_θ boundary layers. Note that the values cited for the high R_θ experiments are typical, but varied within the ensemble of acquisition runs collected.

| R_θ | U_∞ [m/s] | θ [m] | δ^* [m] | δ [m] | H |
|----------------------|------------------|--------------|----------------|--------------|------|
| $\sim 2 \times 10^6$ | 6.31 | 5.39 | 6.47 | 84 | 1.19 |
| $\sim 4 \times 10^6$ | 17.2 | 4.43 | 5.27 | 69 | 1.24 |
| $\sim 2 \times 10^6$ | 7.35 | 4.57 | 5.58 | 67 | 1.22 |
| 1010 | 0.607 | 0.0248 | 0.0360 | 0.206 | 1.45 |
| 2870 | 1.752 | 0.0245 | 0.0343 | 0.205 | 1.40 |
| 4850 | 2.981 | 0.0243 | 0.0335 | 0.199 | 1.38 |

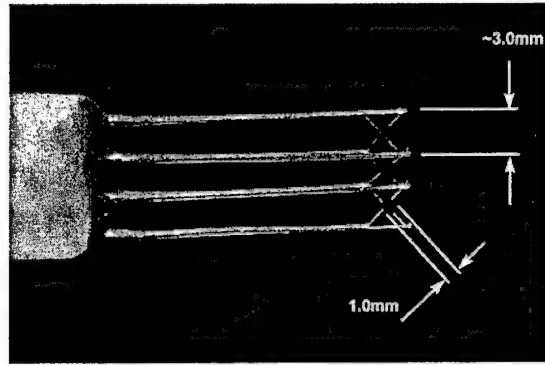


Figure 6.1. The six-wire probe

Table 6.2.

6.3.2 Instrumentation and Data Acquisition

A custom made six wire probe (Figure 6.1) was used in the measurements. This probe, composed of three x-arrays, was used to acquire instantaneous streamwise and wall normal velocities at three closely spaced wall normal positions. The same probe was used in our previous study [98], and was mounted in the orientation shown in Figure 6.1. The distance from the wall to the bottom of the x-array was measured with a cathetometer having a precision of $\pm 0.0127\text{mm}$. Constant temperature hot-wire anemometers (AA Lab-Systems AN-1003) were employed. A 16 bit simultaneous sample and hold analog to digital converter was used to digitize

Table 6.2. Inner normalized wall roughness values, inner parameters and peak locations of $-\overline{uv}^+$ for the high and low R_θ smooth and rough wall turbulent boundary layers.

| R_θ | U_τ [m/s] | ν [m^2/s] | k^+ | δ^+ | y_p [m] | y_p^+ |
|----------------------|----------------|---------------------------------|---------------|--------------------|-----------------------|---------|
| $\sim 2 \times 10^6$ | 0.1962 | 1.85×10^{-5} | $25 \sim 50$ | 8.9×10^5 | 0.1783 | 1892 |
| $\sim 4 \times 10^6$ | 0.5366 | 1.85×10^{-5} | ≈ 300 | 2.0×10^6 | 0.0976 | 2825 |
| $\sim 2 \times 10^6$ | 0.2803 | 1.87×10^{-5} | ≈ 500 | 1.01×10^6 | 0.1335 | 2010 |
| 1010 | 0.0282 | 1.5×10^{-5} | smooth | 388 | 2.58×10^{-2} | 39.4 |
| 2870 | 0.0707 | 1.5×10^{-5} | smooth | 966 | 1.63×10^{-2} | 62.2 |
| 4850 | 0.1125 | 1.5×10^{-5} | smooth | 1493 | 1.27×10^{-2} | 77.3 |

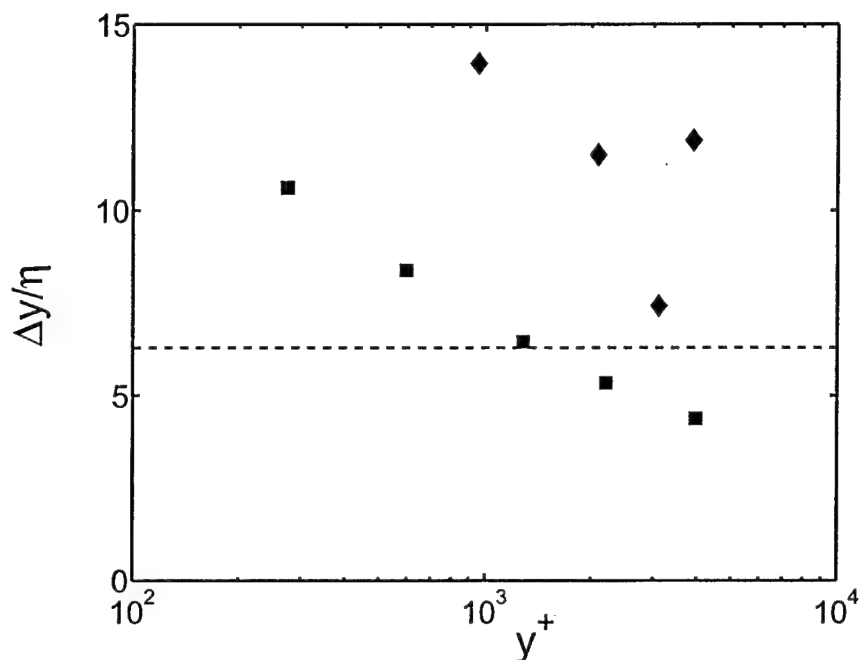


Figure 6.2. Six-element sensor Δy wire separation normalized by the Kolmogorov length, η , as a function of y^+ . ■ $R_\theta = 2 \times 10^6$ smooth wall, ♦ $R_\theta = 4 \times 10^6$ rough wall, — — $\Delta y/\eta = 2\pi$, the optimal probe resolution as suggested by Folz [62]

the hot-wire signals with a sampling frequency of 5kHz. To obtain reasonably well converged statistics, 30 ~ 40 minute time averages were computed for all the high R_θ data.

All of the hot-wires were calibrated immediately before and after each experiment using a portable calibration facility [98]. The velocity angle method explained in Braun [12] was used to fit third order bivariate polynomial surfaces to the voltage-velocity pairs of wires in each X-array. Temperature compensation, as explained by Metzger [39] was used as a part of this surface fitting technique. This is essential as the temperature sometimes dropped more than 5°C during data acquisition. The instantaneous hot-wire velocity components were obtained by solving the coupled nonlinear system of equations using a globally convergent

Newton method [98].

The hot-wire sensors employed $5\mu\text{m}$ diameter tungsten wires. These wires had a sensor length of 1mm, which is 10-15 wall units at $R_\theta \simeq 2 \times 10^6$. This is a very good spatial resolution at high R_θ . However, the wall normal spacing, Δy , between two x-arrays is around 30 wall units. As shown in Figure 6.2, our Δy ranges were between 4η and 15η in the log-law region. Here, η is the Kolmogorov length scale. According to Folz [62], for atmospheric measurements a Δy of about $2\pi\eta$, yields minimal attenuation of the important scales contributing to the vorticity. He also shows that at this Δy , the effect of noise from the instruments is greatly attenuated. This optimal probe resolution is given in Figure 6.2. As indicated, some of the high R_θ data fall above this limit. Thus, some attenuation of the high R_θ ω_z signals is expected.

6.3.3 Data Analysis Techniques

In the present study, 30 – 40min time averages or more were used to compute flow statistics. No specific detrending techniques are used in the data analysis. As described previously, however [98], care was taken to only analyze those signals that did not exhibit a mean trend in the plotted time series (i.e., the mean value was a horizontal line on the plot). All the turbulent quantities were obtained by subtracting the mean of the signals. As mentioned, these high R_θ smooth wall and rough wall statistics were compared with available low R_θ statistics to study the effects of scale separation.

The wall normal velocity gradient, $\partial u / \partial y$, a contribution to $\omega_z = \left(\frac{\partial v}{\partial x} - \frac{\partial u}{\partial y} \right)$ was obtained directly by differencing the u component from the top and the middle x-arrays of the 6 element probe. The streamwise gradient, $\partial v / \partial x$ was computed using Taylor's hypothesis with the v component from the top x-array. A local mean streamwise velocity computed over about 6000 viscous time units was used as the

convection velocity for all high R_θ data. For low R_θ , the local convection velocity was computed over about 50 viscous time scales. According to Kim et al. [104] Taylor's hypothesis is valid in the turbulent boundary layer except very close to the wall ($y^+ \gtrsim 100$). The current high R_θ data were acquired for $y^+ > 200$, well away from the wall.

To obtain the vorticity time scales, event duration analyses were performed. These analyses are very similar to the analyses performed by Klewicki and Falco [76] and Klewicki et al. [105]. The magnitudes of the fluctuating vorticity signals were tracked from the beginning to the end of the signal. When its magnitude increased beyond a particular threshold level, counting of the event duration was started and continued until the magnitude dropped below the threshold. To maintain consistency with the event duration analyses of Klewicki and Falco [76], the present events were sustained for a 20% drop below the peak event value when the signal amplitude dropped below the threshold defining the beginning of the event. Also consistent with these previous studies, the threshold for the present analyses was selected as $1.0\omega'_z$. Here, ω'_z is the rms value of ω_z fluctuations.

Cospectra between fluctuating velocity components and fluctuating vorticity component were computed and compared with the individual velocity and vorticity power spectra. The process used to compute the cospectra and power spectra was the same as the process used in Priyadarshana and Klewicki [98]. The signal was divided into windows of 4096 data points each before taking the fast Fourier transform (FFT). The power spectral density and the cross spectral density were computed using Welch's averaged, modified periodogram method. A Hanning window of the same size as the window size was used to minimize the spectral leakage and the signal was overlapped by 50% to improve averaging. Similar to the method used by Saddoughi and Veeravalli [59], the low frequency end of the spectrum was obtained by down sampling the signals using an anti-aliasing (low

pass) finite-duration impulse response (FIR) filter. The cospectra of velocity and vorticity were obtained using the real part of the cross spectral density [93, 94].

A novel filtering technique [98] was used to analyze the behavior of velocity and vorticity correlations. Under this technique, fluctuating velocity and vorticity signals were split into high frequency and low frequency parts according to a cut-off frequency, f_c . The contributions to velocity-vorticity products from the portions of the signals above and below f_c , for a range of f_c , were then computed and examined as a function of Reynolds number.

The underlying composition of velocity-vorticity correlations was explored by separating the contributions into four quadrants. The joint probability density functions for each quadrant, *jpdfs*, were then computed by sorting velocity and vorticity signals into bins based on amplitudes of fluctuating velocity and vorticity signals and compared for the high and low Reynolds number flows. The fractional contributions to the velocity-vorticity correlations, using the weighted probability density functions, *wpdfs*, between velocity and vorticity were computed after multiplying the *jpdfs* with appropriate velocity and vorticity values.

6.4 Results and Discussion

In this section, results are explained in detail. Section 6.4.1 describes the velocity and vorticity statistics. Statistics of the streamwise velocity, the wall normal velocity and the spanwise vorticity are discussed in this section. The velocity-vorticity correlations, vw_z and uw_z are presented in Sections 6.4.2 and 6.4.3 respectively. These studies include analysis of statistics, spectra, filtered signals and weighted pdfs.

6.4.1 Velocity and Vorticity Statistics

Prior to an analysis of the velocity, vorticity product signals, it is relevant to examine the statistical properties of the individual velocity and vorticity signals.

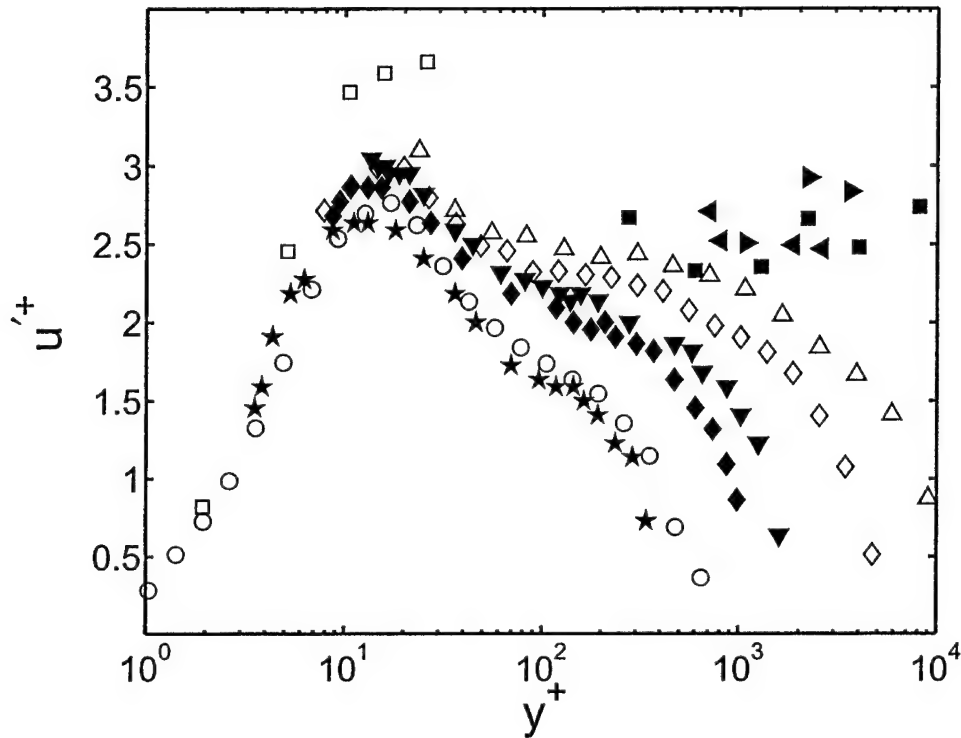


Figure 6.3. Comparison of current high R_θ inner normalized streamwise intensity profiles with available low R_θ data. Current \blacksquare $R_\theta \simeq 2 \times 10^6$ $k^+ \approx 25 \sim 50$, \blacktriangleright $R_\theta \simeq 4 \times 10^6$ $k^+ = 300$, \blacktriangleleft $R_\theta = 2 \times 10^6$ $k^+ = 500$, Klewicki and Falco [76] \star $R_\theta = 1010$, \blacklozenge $R_\theta = 2870$, \blacktriangledown $R_\theta = 4850$, DeGraaff and Eaton [49] \circ $R_\theta = 1430$ smooth wall, \diamond $R_\theta = 13000$ smooth wall, \triangle $R_\theta = 31000$ smooth wall, Metzger and Klewicki \square $R_\theta \simeq 2 \times 10^6$ smooth wall

6.4.1.1 Streamwise Velocity Statistics

Figure 6.3 shows inner normalized streamwise velocity intensities for the current high R_θ relatively smooth wall ($k^+ \approx 25 \sim 50$) and rough wall ($300 \gtrsim k^+ \gtrsim 500$) turbulent boundary layers. The abscissa represents the inner normalized wall normal distance, y^+ , and the ordinate represents the inner normalized streamwise intensity, u'^+ . A key to the symbols is given including R_θ and inner normalized equivalent sand roughness, k^+ . For comparison, smooth wall boundary layer streamwise intensities from Klewicki [8], DeGraaff and Eaton [49] and Metzger

and Klewicki [4] are shown as well. As explained in Section 6.3.3, all the current high R_θ statistics are 30 – 40min time averages and the statistics shown were computed using the data from several year's field trials. For the high R_θ flow, note that the boundary layer thickness is approximately 1×10^6 wall units. Thus, all the current high R_θ data fall well within the classical inner layer. As shown in Figure 6.3, there is a significant dependence of u'^+ on R_θ . At greater y^+ , this expected behavior can clearly be seen from the larger u'^+ values of current high R_θ smooth and/or rough wall data. The current high R_θ u'^+ also provide some evidence of mild surface roughness effects as u'^+ appears to increase slightly with an increase in wall roughness. This is observed well above the roughness sub-layer ($3 \sim 5$ roughness heights). The origin of this result, however requires further investigation. Krogstad et al. [29] observed no significant change in the streamwise intensity outside roughness sub-layer. It is clear, however, that the effects of surface roughness on streamwise intensity are small compared to the effects of Reynolds number.

6.4.1.2 Wall-Normal Velocity Statistics

The inner normalized wall normal velocity intensity, v'^+ , for the current high R_θ , $k^+ \approx 25 \sim 50$ and $300 \gtrsim k^+ \gtrsim 500$, turbulent boundary layer flows are shown in Figure 6.4. According to DeGraaff and Eaton [49], v'^+ measurements in the turbulent boundary layer flows are relatively scarce when compared with u'^+ , measurements. DeGraaff and Eaton [49] present well-resolved LDA measurements of wall-normal stress, $\overline{v'^2}$, for the range $R_\theta = 1430 \sim 31000$. Fernholz and Finley [47] compiled available x-array hot wire measurements of $\overline{v'^2}$. Spatial resolution of these data varies between $7 \sim 70$. Here, the profiles of v'^+ from of Klewicki [8] and DeGraaff and Eaton [49] are presented for comparison. The $R_\theta = 2870$ and 4850 data of Klewicki [8] in Figure 6.4 show very little R_θ dependence. His $R_\theta = 1010$

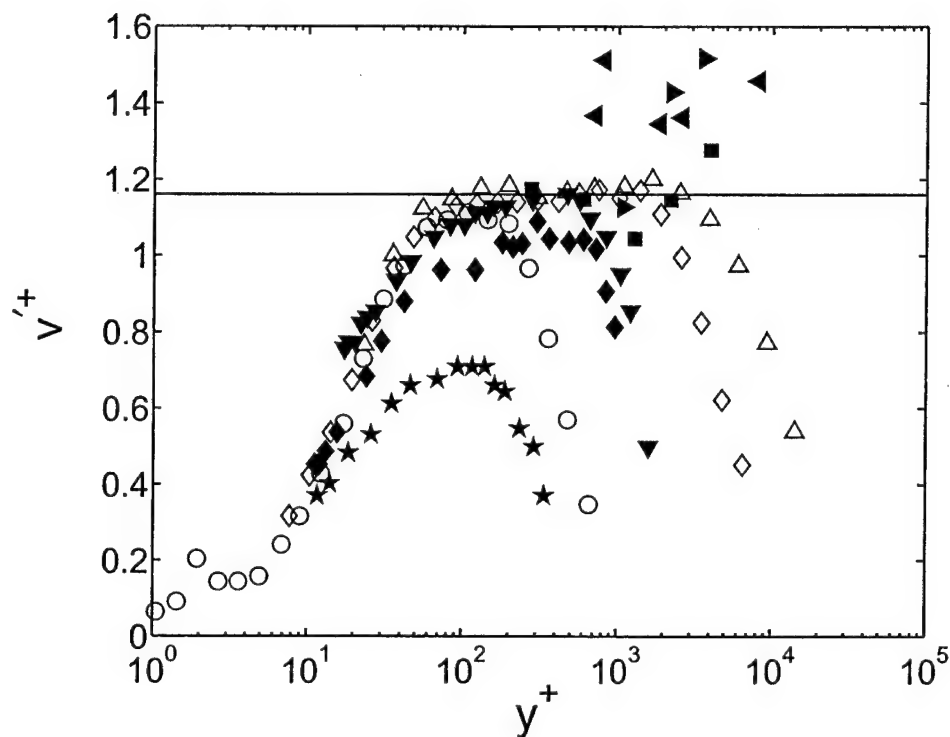


Figure 6.4. Comparison of current high R_θ inner normalized wall normal intensity profiles with available low R_θ data. Current \blacksquare $R_\theta \simeq 2 \times 10^6$ $k^+ \approx 25 \sim 50$, \blacktriangleright $R_\theta \simeq 4 \times 10^6$ $k^+ = 300$, \blacktriangleleft $R_\theta = 2 \times 10^6$ $k^+ = 500$, Klewicki and Falco [76] \star $R_\theta = 1010$, \blacklozenge $R_\theta = 2870$, \blacktriangledown $R_\theta = 4850$, DeGraaff and Eaton [49] \circ $R_\theta = 1430$ smooth wall, \diamond $R_\theta = 13000$ smooth wall, \triangle $R_\theta = 31000$ smooth wall, Metzger and Klewicki \square $R_\theta \simeq 5 \times 10^6$ smooth wall

data, however, show a significant R_θ dependence which could be a low R_θ effect as explained by DeGraaff and Eaton [49]. Above a modest R_θ (say, greater than about 2000), the value of v'^+ exhibits little increase with increasing R_θ . As shown, the low R_θ v'^+ ($\gtrsim 2000$) data have a peak which is in between $1.1 \sim 1.2$. Interestingly, the current relatively smooth $R_\theta \simeq 2 \times 10^6$ data agree well with the peak value of $1.1 \sim 1.2$ and remain nearly constant with increasing y^+ . Therefore, there appear to be very little R_θ dependence in v'^+ . The current high R_θ rough wall v'^+ data, however, exhibit significantly larger magnitudes in comparison with the low R_θ and

high R_θ relatively smooth wall data. The peak magnitude of these data is about 1.4 for the rough wall turbulent boundary layer with $k^+ = 500$ and is about 1.3 with $k^+ = 300$. These measurements are observed well above $3 \sim 5$ roughness heights, and thus is in agreement with Krogstad et al. [29] who observed effects of surface roughness in v'^+ well above the roughness sub layer. Overall, v'^+ appears to depend very little on R_θ (for $R_\theta \gtrsim 2000$), but more significantly on surface roughness.

DeGraaff and Eaton [49] indicate that the wall normal location of peak in v'^+ is R_θ dependent. Similar observations have been made by Sreenivasan [58] and others. According to Sreenivasan [58], R_θ dependence of peak in v'^+ is given by $y_{v'_{max}}^+ \simeq R_\theta^{0.75}$.

6.4.1.3 Spanwise Vorticity Statistics

A comparison of current high R_θ inner normalized spanwise vorticity intensities, $\omega_z'^+$, with available $\omega_z'^+$ is shown in Figure 6.5. The $\omega_z'^+$ shown in Figure 6.5 was computed using the method explained in Section 6.3.3, for the current high R_θ data. Previous comparisons of low R_θ $\omega_z'^+$ are given in Klewicki and Falco [36], Balint et al. [50], Wallace and Foss [85], Honkan and Andreopolous [63], and Metzger and Klewicki [4]. A number of these studies indicate that inner normalization is appropriate while others [86] have suggested outer normalization.

As shown in Figure 6.5, the current high R_θ smooth and rough wall $\omega_z'^+$ data within the log-law region agree quite well with previous high and low R_θ $\omega_z'^+$. In contrast, Metzger and Klewicki's [4] near wall high R_θ $\omega_z'^+$ results show significantly higher $\omega_z'^+$ values. Close examination of the present data in Figure 6.5 indicates some evidence of a small attenuation of $\omega_z'^+$ for $y^+ \lesssim 1000$. As discussed relative to Figure 6.2, this is likely due to the diminished spatial resolution of the sensor. Overall, there is no apparent effect of surface roughness in $\omega_z'^+$ outside the roughness sublayer, or no apparent R_θ effect outside a region near the edge of the viscous sub

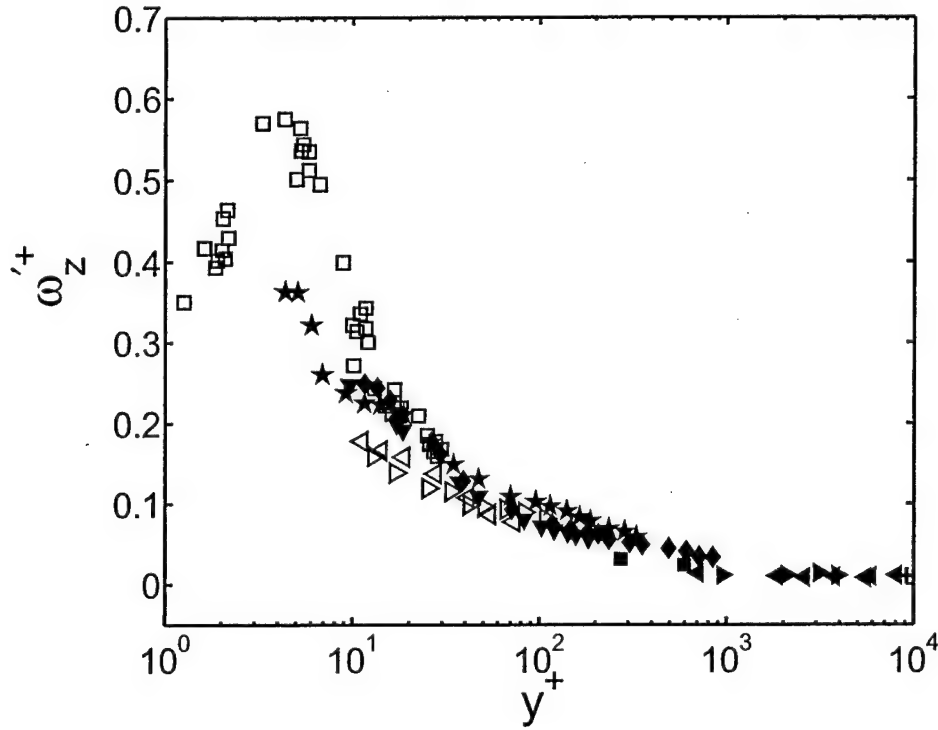


Figure 6.5. Inner normalized spanwise vorticity intensities as a function of y^+ .
 ■ $R_\theta \simeq 2 \times 10^6$ $k^+ \approx 25 \sim 50$, ► $\sim R_\theta = 4 \times 10^6$ $k^+ = 300$, ◄ $R_\theta = 2 \times 10^6$ $k^+ = 500$, Klewicki and Falco [76] ★ $R_\theta = 1010$, ◆ $R_\theta = 2870$, ▼ $R_\theta = 4850$, Metzger and Klewicki [4] □ $R_\theta \simeq 5 \times 10^6$, Metzger [39] + $R_\theta \simeq 5 \times 10^6$, Balint [50] ◁ $R_\theta = 2685$, Honkan and Andreopoulos [63] ▷ $R_\theta = 2790$

layer.

6.4.1.4 Spanwise Vorticity Time Scales

Mixing length arguments often contain the idea that the size of the eddies participating in the generation of the \overline{uv} shear product undergoes a proportional increase with distance from the wall [76]. Previous measurements indicate that the motions contributing to \overline{uv} increase in size with increasing R_θ at a rate intermediate to the rate of increase of δ^+ [98]. As shown in (6.4), however, the wall normal gradient of \overline{uv} can be expressed in terms of velocity-vorticity products. It is therefore of interest to characterize the scales of the ω_z motions with increasing

R_θ and wall normal distance.

The average of the ω_z event durations above a unit rms, $1.0\omega'_z$, were computed for the current high R_θ data using the method explained in Section 6.3.3. Figure 6.6 shows these average event durations as a function of distance from the wall. The $R_\theta = 2870$ and 4850 ω_z event durations of Klewicki and Falco [36] are also shown for comparison. For the current relatively smooth wall data at $R_\theta \simeq 2 \times 10^6$ $T^+(\omega_z)$ remains essentially constant with increasing y^+ . A very similar trend is observed with the current $R_\theta \simeq 2 \times 10^6$, $k^+ \approx 500$ rough wall results despite more scatter. Current $R_\theta \simeq 4 \times 10^6$, $k^+ \approx 300$ data are highly scattered. Nevertheless, they exhibit a significant increase in the event durations compared to the relatively smooth wall high R_θ results. Therefore, both the effects of Reynolds number and surface roughness are clearly visible in these results. Overall, the smooth wall data in this figure show that at any fixed R_θ and outside the near-wall region (say $y^+ > 50$), the event durations exhibit very little variation with y^+ . As is clearly shown, however, this nearly constant value increases with increasing R_θ .

Under outer normalization, however, an R_θ trend opposite to that in Figure 6.6 is observed (not shown). This indicates that the time scale of the event durations is intermediate to inner and outer scaling. Klewicki and Falco [36] observed this behavior for $1000 \gtrsim R_\theta \gtrsim 5000$ and, explored intermediate scaling using the Taylor time scale,

$$\lambda_t = \sqrt{\frac{2u'^2}{(\frac{\partial u}{\partial t})'}}. \quad (6.7)$$

Normalization using λ_t is shown in Figure 6.7. As shown, low R_θ event durations of Klewicki and Falco [36], current $R_\theta \simeq 2 \times 10^6$, $k^+ \approx 25 \sim 50$ event durations and current $R_\theta \simeq 4 \times 10^6$, $k^+ \approx 300$ event durations appear to merge onto a single curve under this normalization. The current $R_\theta \simeq 2 \times 10^6$, $k^+ \approx 500$ rough wall ω_z event durations, however, continue to provide some evidence of slightly higher values.

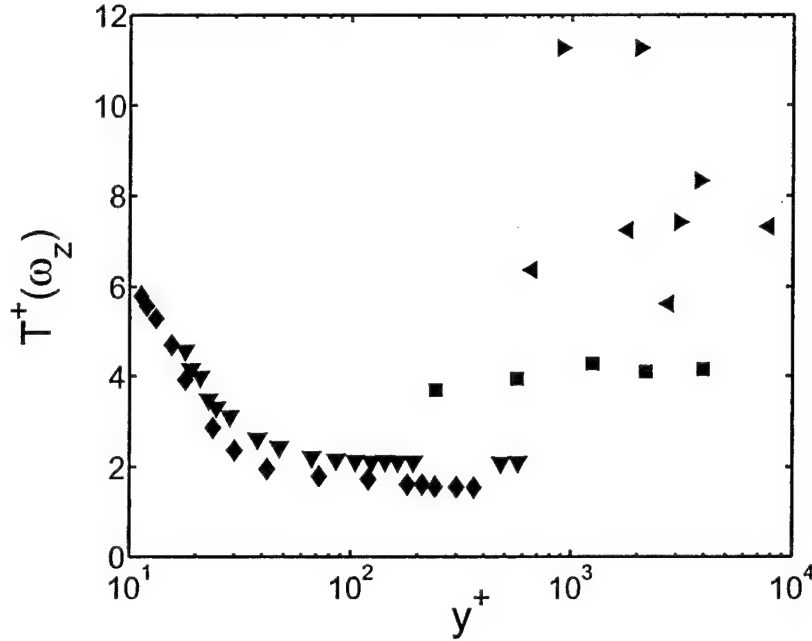


Figure 6.6. Inner normalized spanwise vorticity event durations as a function of y^+ . ■ $R_\theta \simeq 2 \times 10^6$ smooth wall, ► $R_\theta \simeq 4 \times 10^6$ $k^+ \approx 300$, ◄ $R_\theta \simeq 2 \times 10^6$ $k^+ \approx 500$, Klewicki and Falco [36] ♦ $R_\theta = 2870$, ▼ $R_\theta = 4850$

The scatter in the high R_θ rough wall data, which may be introduced due to inner normalization, has been considerably reduced. Overall, these results support the hypothesis the λ_t serves as a characteristic time scale for the ω_z bearing motions. A similar hypothesis was proposed by Falco [21, 106, 107] relative to the Taylor length scale. These were based largely on the scale of motions detected in flow visualizations.

6.4.2 $v\omega_z$ Signals

6.4.2.1 $v\omega_z$ Statistics

As shown in (6.4), $\overline{v\omega_z}$ is one of the two velocity-vorticity correlations contributing to $-\frac{\partial \overline{uv}}{\partial y}$. Figure 6.8 shows inner normalized $\overline{v\omega_z}$ data from the current high R_θ smooth and rough wall experiments. This figure also includes previous low R_θ results of Klewicki [8]. All of the current high R_θ data are acquired within the

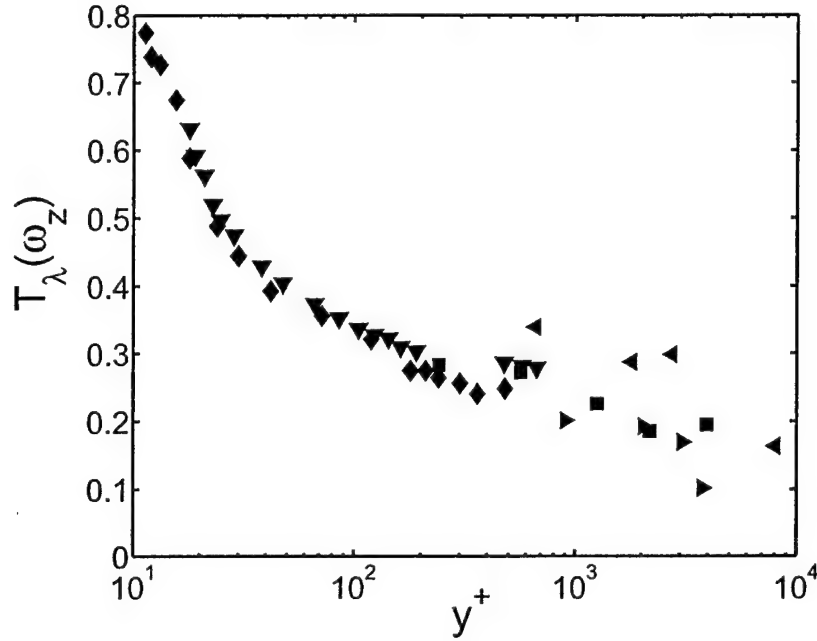


Figure 6.7. Taylor microscale normalized event durations of ω_z as a function of y^+ . ■ $R_\theta \simeq 2 \times 10^6$ $k^+ \approx 25 \sim 50$, ► $R_\theta \simeq 4 \times 10^6$ $k^+ = 300$, ◄ $R_\theta \simeq 2 \times 10^6$ $k^+ = 500$, ◆ Klewicky and Falco [76] $R_\theta = 2870$, ▼ Klewicky and Falco [76] $R_\theta = 4850$

range $200 < y^+ < 10000$. As shown, the $R_\theta \simeq 2 \times 10^6$, $k^+ \approx 25 \sim 50$ results exhibit positive correlations, while the high R_θ rough wall results show slightly negative correlations. Thus, for smooth wall turbulent boundary layers, the trend in Figure 6.8 indicates that in the log layer region of the mean profile, $\overline{v\omega_z}^+$ increases with increasing R_θ (for $10^3 \lesssim R_\theta \lesssim 2 \times 10^6$). Relative to (6.4), the R_θ dependence revealed in Figure 6.8, indicates that as R_θ increases, the contribution from $\overline{v\omega_z}$ to $-\frac{\partial \overline{uv}}{\partial y}$ changes from relatively strong attenuating effect to a relatively weak amplifying effect. Conversely, the addition of increasingly larger roughness appears to suppress this R_θ dependence. This issue is further analyzed through spectra in Section 6.4.2.2.

The inner normalized intensities of $v\omega_z$, $(v\omega_z)^{'+}$, are shown in Figure 6.9. Previously unpublished low R_θ data of Klewicky [8] are also shown for comparison. As

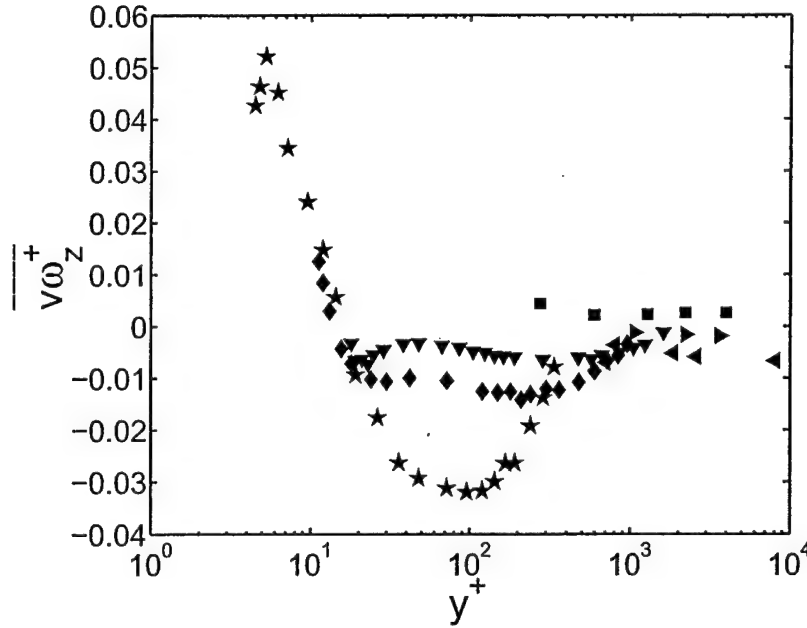


Figure 6.8. Variation $\overline{v\omega_z}^+$ with y^+ . ■ $R_\theta \simeq 5 \times 10^6$ smooth wall, ► $R_\theta \simeq 4 \times 10^6$ $k^+ \approx 300$, ◄ $R_\theta \simeq 2 \times 10^6$ $k^+ \approx 500$, Klewicki and Falco [36] ★ $R_\theta = 1010$, ◆ $R_\theta = 2870$, ▼ $R_\theta = 4850$

evident, there is no discernible difference between high R_θ smooth and rough wall $(v\omega_z)^{+'}$. There is very little R_θ dependence between $R_\theta = 2870$ and 4850 data for $y^+ \gtrsim 30$. However, there are significant differences exhibited by the data at $R_\theta = 1010$. This is likely to have association with other low R_θ effects [49, 8]. The current high R_θ data for $y^+ < 1000$ show good agreement with these low R_θ data. It is uncertain, however, whether $y^+ > 1000$ high R_θ data follow this trend. More near wall high R_θ data and intermediate R_θ data away from the wall are required to verify this.

The v, ω_z correlation coefficient, $\rho_{v\omega_z}$, profiles are shown in Figure 6.10. These results are, once again, compared with the $1000 < R_\theta < 5000$ results of Klewicki [8] (previously unpublished) as well as the $R_\theta = 1450$ results of Rajagopalan and Antonia [65]. The R_θ dependencies exhibited in Figure 6.8 are further exemplified

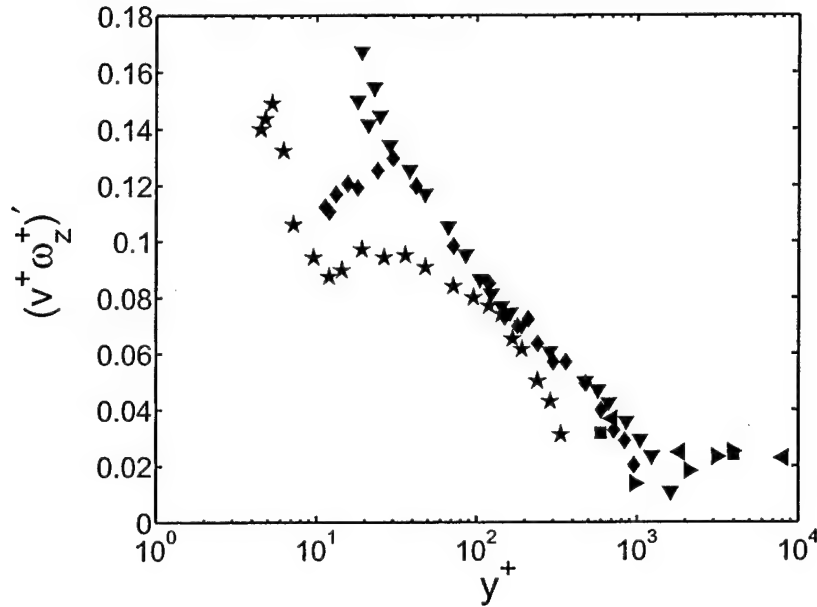


Figure 6.9. Intensity of $v\omega_z$ as a function of y^+ . ■ $R_\theta \simeq 5 \times 10^6$ smooth wall, ► $R_\theta \simeq 4 \times 10^6$ $k^+ \approx 300$, ◄ $R_\theta \simeq 2 \times 10^6$ $k^+ \approx 500$, Klewicki [8] ★ $R_\theta = 1010$, ◆ $R_\theta = 2870$, ▼ $R_\theta = 4850$

and more clearly illustrated here. The current $R_\theta \simeq 2 \times 10^6$ relatively smooth wall $\rho_{v\omega_z}$ results are positive reaching a significant magnitude near 0.2. On the other hand, all the current $R_\theta \simeq 2 \times 10^6$ $k^+ \approx 500$ results are negative with values near 0.2. One point of the $R_\theta \simeq 4 \times 10^6$ $k^+ \approx 300$ indicates a slightly positive value while the other points are generally small and negative. Notable features in Figure 6.10 are, *i*) the apparent R_θ invariance of $\rho_{v\omega_z}$ for $y^+ \lesssim 15$, *ii*) the relatively large values of $|\rho_{v\omega_z}|$ in the log layer (at any R_θ , but especially at low R_θ), and *iii*) the aforementioned change in sign of $\rho_{v\omega_z}$ at high R_θ . Relative to scale separation effects, the second of these is felt particularly significant, since it relates to the degree of interaction between the v and ω_z fluctuations. This issue is further addressed in the spectral analyses below. The high R_θ $k^+ \approx 500$ data show significantly negative $\rho_{v\omega_z}$. At this point, the dependency of $\rho_{v\omega_z}$ on k^+ is uncertain. More high R_θ experiments under different surface roughness are required to more

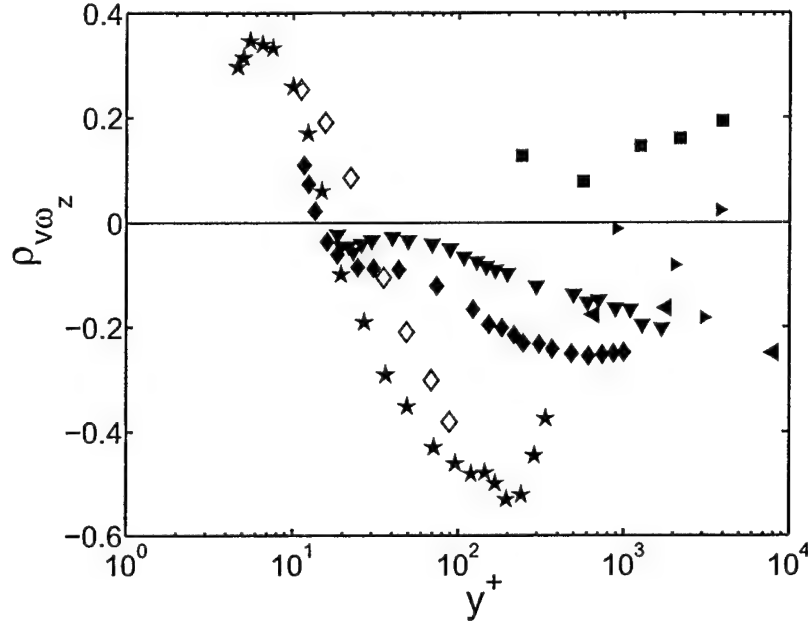


Figure 6.10. Correlation coefficient, $\rho_{v\omega_z}$, as a function of y^+ . ■ $R_\theta \simeq 5 \times 10^6$ smooth wall, ► $R_\theta \simeq 4 \times 10^6$ $k^+ \approx 300$, ◄ $R_\theta \simeq 2 \times 10^6$ $k^+ \approx 500$, ★ Klewicki [8] $R_\theta = 1010$, ◆ Klewicki [8] $R_\theta = 2870$, ▼ Klewicki [8] $R_\theta = 4850$, ◇ Rajagopalan and Antonia [65] $R_\theta = 1450$

fully understand how roughness effects the correlation between v and ω_z .

6.4.2.2 Spectral Structure of $v\omega_z$

In this section, spectral analyses of v and ω_z are presented. In these analyses, both inner and outer normalizations are explored. For reference, the inner and outer length and velocity scales of these data are described in Table 6.1.

The inner-normalized wall normal velocity power spectra, $\Phi(v^+)$, and the inner-normalized spanwise vorticity power spectra, $\Phi(\omega_z^+)$, were computed using the method explained in Section 6.3.3. These power spectra were multiplied with inner normalized frequency, f^+ , to obtain the premultiplied power spectra, $\Psi(v^+)$ and $\Psi(\omega_z^+)$. The same methods were used to compute the cospectrum, $\Lambda(v\omega_z^+)$, and the premultiplied cospectrum, $f^+\Lambda(v^+\omega_z^+)$. Figures 6.11(a-d) show $R_\theta = 2870$,

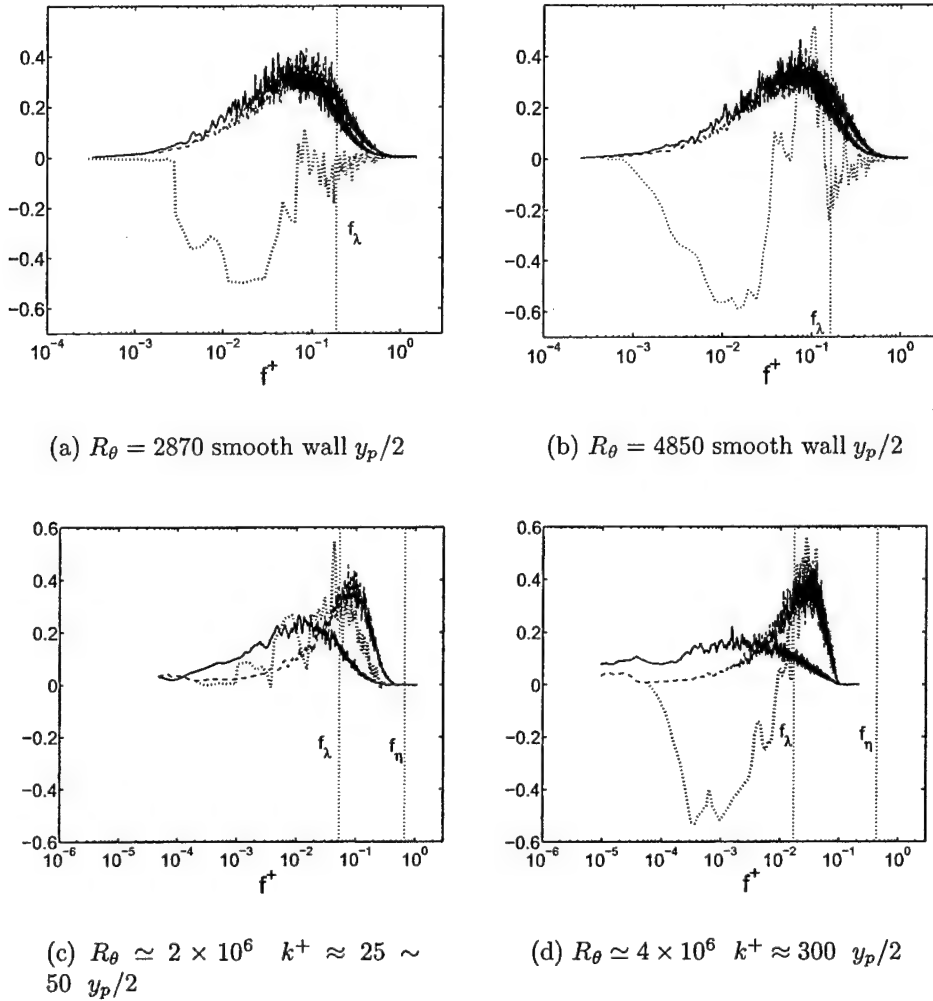


Figure 6.11. Premultiplied power spectra of v and ω_z ($\Psi(v^+)$ and $\Psi(\omega_z^+)$), and premultiplied cospectra of v^+ and ω_z^+ , $f^+ \Lambda(v^+ \omega_z^+)$ at the wall normal location of $y_p/2$. — $\Psi(v^+)$, — — $\Psi(\omega_z^+)$, $f^+ \Lambda(v^+ \omega_z^+)$.

4850, $\sim 2 \times 10^6$ $k^+ \approx 25 \sim 50$, and $\sim 4 \times 10^6$ $k^+ \approx 300$ $\Psi(v^+)$, $\Psi(\omega_z^+)$, and $f^+ \Lambda(v^+ \omega_z^+)$ at the wall normal location of $y_p/2$. As mentioned previously, y_p is the wall normal position of the peak $-\overline{uv}^+$. The abscissa in Figures 6.11(a) - 6.12(b) is the inner normalized frequency, f^+ , and the ordinate is the premultiplied spectral density. As shown in Figure 6.11(a), at $R_\theta = 2870$ and $y_p/2$, the two pre-multiplied power spectra, $\Psi(v^+)$, and $\Psi(\omega_z^+)$ nearly lie on top of each other. The peaks in

these spectra occur at slightly lower frequency than the Taylor frequency, f_λ . As shown, $f^+\Lambda(v^+\omega_z^+)$ inversely tracks $\Psi(\omega_z^+)$ at high frequency (up to about f_λ). At frequencies slightly lower than the $\Psi(\omega_z^+)$ peak, v and ω_z exhibit a strong negative correlation that is large compared with the high frequency positive correlation. The spectra, $\Psi(v^+)$, $\Psi(\omega_z^+)$, and the cospectrum, $f^+\Lambda(v^+\omega_z^+)$, at $R_\theta = 4850$, $y_p/2$ are highly similar to those of $R_\theta = 2870$. As shown in Figure 6.11(b), the $R_\theta = 4850$, $\Psi(v^+)$ and $\Psi(\omega_z^+)$ closely track each other at $y_p/2$. The behavior of $f^+\Lambda(v^+\omega_z^+)$ is also similar, however, the high frequency motions having frequencies near the peak in $\Psi(\omega_z^+)$ exhibit a stronger positive peak than that at $R_\theta = 2870$.

The $y_p/2$ $R_\theta \simeq 2 \times 10^6$, $k^+ \approx 25 \sim 50$ spectra and $R_\theta \simeq 4 \times 10^6$, $k^+ \approx 300$ cospectra of v and ω_z are presented in Figures 6.11(c) and 6.11(d) respectively. When compared to the $R_\theta \simeq 4 \times 10^6$ $k^+ \approx 300$ results, the effects of wall roughness on $R_\theta \simeq 2 \times 10^6$, $k^+ \approx 25 \sim 50$ results are minimal. As seen in Figure 6.11(c), at $y_p/2$ $f^+\Lambda(v^+\omega_z^+)$ closely tracks $\Psi(\omega_z^+)$ at high frequencies. The peak of $f^+\Lambda(v^+\omega_z^+)$ is very close to the peak of $\Psi(\omega_z^+)$, which occurs near f_λ . At relatively low frequencies, $f^+\Lambda(v^+\omega_z^+)$ shows a trend of tracking $\Psi(v^+)$, however, the magnitudes of $f^+\Lambda(v^+\omega_z^+)$ are relatively small at low frequencies. Thus, at $y_p/2$, and high R_θ the relatively smooth wall flow has a peak spectral intensity of $v\omega_z$ product that is dominated by scales of the order of the Taylor microscale. This finding is very similar to previous near wall ($y^+ = 183$) measurements at high R_θ [87]. As shown in Figure 6.11(d), however, the above behavior changes significantly at $y_p/2$ with the introduction of wall roughness of $k^+ \approx 300$. Note that the selected wall normal position is at the edge of the roughness sublayer at $y_p/2$. The viscous time scale, ν/U_τ^2 , in the turbulent boundary layer reduces with increasing wall shear stress due to roughness elements. Thus, the inner normalized frequency axis shifts towards the low frequency end as shown in Figure 6.11(d). The temporal resolution is diminished in these data, however, no apparent effects of aliasing

were observed. Except for the shift in inner normalized frequency, the two inner normalized premultiplied spectra, $\Psi(\omega_z^+)$ and $\Psi(v^+)$ in Figure 6.11(d) are very similar to the relatively smooth high R_θ counterparts shown in Figure 6.11(c). Similarly, the high frequency rough wall $f^+\Lambda(v^+\omega_z^+)$ is similar to the relatively smooth wall $f^+\Lambda(v^+\omega_z^+)$ with its positive peak tracking the peak of $\Psi(\omega_z^+)$. At low frequencies, however, rough wall v and ω_z correlates negatively with a large negative peak in $f^+\Lambda(v^+\omega_z^+)$ very close to the peak of $\Psi(v^+)$. The area under the negative portion of $f^+\Lambda(v^+\omega_z^+)$ is significantly greater than the positive portion of at high frequency, and thus this underlies the negative $\overline{v\omega_z}^+$ values and negative $\rho_{v\omega_z}$ values for the $k^+ \approx 300$ flow. Thus, the low frequency motions of v and ω_z tend to correlate negatively with increasing wall roughness.

The premultiplied spectra, $\Psi(v^+)$, $\Psi(\omega_z^+)$, and the cospectra, $f^+\Lambda(v^+\omega_z^+)$ at $2y_p$ are shown in Figures 6.12(a) and 6.12(b) respectively for $R_\theta = 2870$ and 4850. The premultiplied spectra change considerably at $2y_p$. It should be mentioned that the previous wall normal location, $y_p/2$ is within the classical buffer layer for both $R_\theta = 2870$ and 4850. The current wall normal location, $2y_p$ is within the classical log-law region. At $2y_p$, peaks in $\Psi(v^+)$, $\Psi(\omega_z^+)$ are clearly apart with the peak in $\Psi(\omega_z^+)$ located almost at f_λ , where, f_λ is the Taylor frequency. This separation increases at $R_\theta = 4850$ with increasing R_θ as shown in Figure 6.12(b). At both R_θ , the minimum of $f^+\Lambda(v^+\omega_z^+)$ closely tracks the peak of $\Psi(v^+)$, which peaks at slightly lower frequency than, f_λ .

As shown in Figure 6.12(c) the behavior of relatively smooth wall $f^+\Lambda(v^+\omega_z^+)$ is significantly different on the other side of the peak of $-\overline{uv}^+$ (near $2y_p$) where $-\frac{\partial \overline{uv}}{\partial y}$ is negative. Similar to the $R_\theta = 2870$ and 4850 results, there is a relatively low frequency peak in $f^+\Lambda(v^+\omega_z^+)$ which closely tracks the peak of $\Psi(v^+)$ at $2y_p$, however, this peak is positive. Consistent with the results at $y_p/2$, there is also a small second peak of $f^+\Lambda(v^+\omega_z^+)$ at high frequency that closely tracks the peak

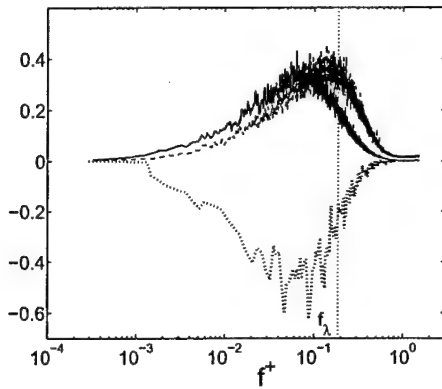
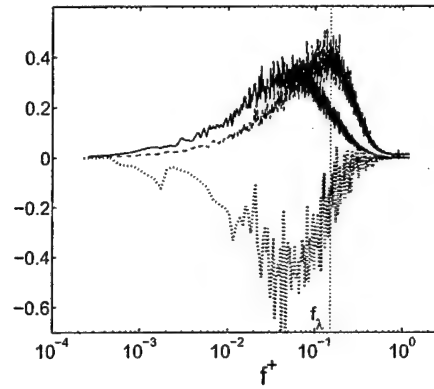
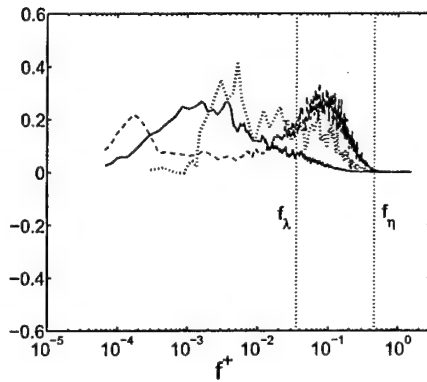
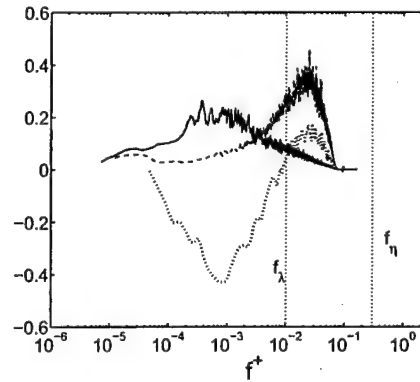
(a) $R_\theta = 2870$ smooth wall $2y_p$ (b) $R_\theta = 4850$ smooth wall $2y_p$ (c) $R_\theta \approx 2 \times 10^6$ $k^+ \approx 25 \sim 50$ $2y_p$ (d) $R_\theta \approx 4 \times 10^6$ $k^+ \approx 300$ $2y_p$

Figure 6.12. Premultiplied power spectra of v and ω_z ($\Psi(v^+)$ and $\Psi(\omega_z^+)$), and premultiplied cospectra of v^+ and ω_z^+ , $f^+ \Lambda(v^+ \omega_z^+)$ at the wall normal location of $2y_p$. — $\Psi(v^+)$, — — $\Psi(\omega_z^+)$, $f^+ \Lambda(v^+ \omega_z^+)$.

of $\Psi(\omega_z^+)$. The amplitude of this second peak is significantly attenuated relative to that at $y_p/2$. Thus, in the high R_θ relatively smooth wall flow, increasing wall normal distance from $y_p/2$ to $2y_p$, the peak in the scales contributing to $\overline{v\omega_z^+}$ shifts to relatively larger scales. It is important to note that, however, the peak in $\Psi(v^+)$ is still in an intermediate range of frequencies that remains at least an order of magnitude less than $\Psi(u^+)$ at $y_p/2$. The rough wall turbulent boundary

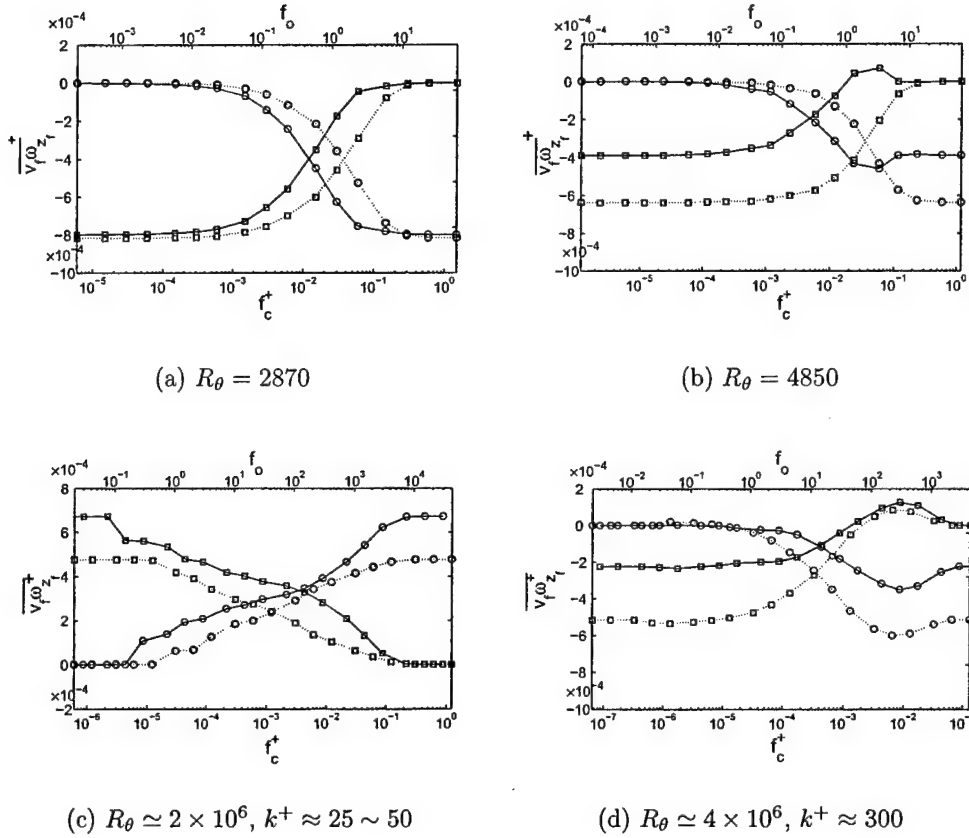


Figure 6.13. Contributions of filtered signals, $\overline{v_f \omega_z f}^+$, as functions of cut-off frequency. \square low pass filtered $\overline{v_f \omega_z f}^+$, \circ high pass filtered $\overline{v_f \omega_z f}^+$, at $-y_p/2$, at $\dots\dots\dots 2y_p$

layer $f^+ \Lambda(v^+ \omega_z^+)$ as shown in Figure 6.12(d) is somewhat similar to the rough wall $f^+ \Lambda(v^+ \omega_z^+)$ at $y_p/2$. As shown in Figure 6.12(d), low frequencies of v and ω_z are negatively correlated giving a negative peak similar to the behavior at $y_p/2$. The amplitude of the high frequency peak is reduced similar to that at relatively smooth wall $f^+ \Lambda(v^+ \omega_z^+)$ and is shown in Figure 6.11(c).

The above v and ω_z signals were further analyzed using the filtering technique explained in Section 6.3.3. Under this technique the v^+ and ω_z^+ signals were simultaneously low pass and high pass filtered using a sharp cut-off Fourier transform based filter. Figures 6.13(a) - 6.13(d) show the $\overline{v_f \omega_z f}^+$ values for a range of inner

normalized cut-off frequencies, f_c^+ , for $R_\theta = 2870 - 4 \times 10^6 k^+ \approx 300$ turbulent boundary layers. Solid curves represent the $\overline{v_f \omega_z f}^+$ at $y_p/2$ and the dotted curves represent $\overline{v_f \omega_z f}^+$ at $2y_p$. The lower abscissa of all figures is the inner normalized cut-off frequency, f_c^+ , and the upper abscissa is the outer normalized cut-off frequency, $f_o (= f_c \delta / U_\infty)$ and the ordinate is $\overline{v_f \omega_z f}^+$. The $\overline{v_f \omega_z f}^+$ computed using the low-pass filtered signals increases with increasing f_c^+ , while those computed using the high-pass filtered signals decreases with increasing f_c^+ . The two curves are equal to each other at the cross over frequency, f_x^+ . As discussed by Priyadarshana and Klewicki [98], f_x represents a convenient measure of the mean frequency of the motions most actively contributing to the correlation between the two signals. As shown in Figure 6.13(a) f_x at $R_\theta = 2870$ $y_p/2$, occurs at a slightly lower frequency than f_x at $2y_p$ indicating that there are contributions from low frequency motions in $\overline{v \omega_z}^+$ at $y_p/2$. Note that at f_x^+ is of the same order of magnitude as U_∞ / δ . This reinforces the spectral analysis in Figure 6.11(a) which shows a peak in $f^+ \Lambda(v^+ \omega_z^+)$ at low frequency. At $2y_p$, however, f_x^+ moves to a significantly higher frequency. This indicates that at $2y_p$, ($R_\theta = 2870$) the $v \omega_z^+$ motions are increasingly dominated by relatively higher frequencies; of the order of f_λ . The behavior of $\overline{v_f \omega_z f}^+$ at $R_\theta = 4850$, as shown in Figure 6.13(b) is very similar. There are however, some positive $v - \omega_z$ correlations at very high frequency, of the order of magnitude of Taylor microscale. This was observed in $f^+ \Lambda(v^+ \omega_z^+)$ as well (Figure 6.11(b)). This behavior is observed only at $R_\theta = 4850$ $y_p/2$ and could be an R_θ effect. This positive correlation between v and ω_z however is not observed at $R_\theta = 4850$ and $2y_p$.

The $R_\theta \simeq 2 \times 10^6$, $k^+ \approx 25 \sim 50$ $\overline{v_f \omega_z f}^+$ results shown in Figure 6.13(c) are positively correlated for all f_c^+ at both wall normal locations, $y_p/2$ and $2y_p$. These results are in agreement with the $f^+ \Lambda(v^+ \omega_z^+)$ results in Figures 6.11(c) and 6.12(c). (Recall that the low frequency peak is smaller than the high frequency peak at $y_p/2$

and is larger than the high frequency peak at $2y_p$.) The f_x^+ value at $y_p/2$ occurs at relatively higher frequency compared to f_x^+ at $2y_p$. This is opposite to the behaviors observed at $R_\theta = 2870$ and 4850 . Note that at $R_\theta \simeq 2 \times 10^6$, $k^+ \approx 25 \sim 50$ $2y_p$, the f_x^+ value is two orders of magnitude larger than U_∞/δ . The $\overline{v_f \omega_z f}^+$ results for $R_\theta \simeq 4 \times 10^6$, $k^+ \approx 300$ shown in Figure 6.13(d), are different from those at $R_\theta \simeq 2 \times 10^6$, $k^+ \approx 25 \sim 50$. As observed in Figures 6.12 and 6.13, introduction of wall roughness induces a negative correlation between v and ω_z at relatively low f . Thus, according to these results and spectral analysis, correlation between v and ω_z motions changes from negative to positive with increasing R_θ . Addition of wall roughness changes this trend completely by changing high R_θ low frequency positive correlations to negative correlations.

6.4.2.3 Weighted Probability Density Functions of $v\omega_z$

The quadrant contribution between v and ω_z was analyzed using the weighted probability density function, $wpdf$, which was computed by multiplying the joint probability density function, $jpdf$, with the relevant v and ω_z values as explained in Section 6.3.3. The $wpdf$ s of v/v' and ω_z/ω'_z at the approximate wall normal position of $y_p/2$ are shown in Figures 6.14(a-d). Here, v' and ω'_z are rms values of wall normal velocity and spanwise vorticity respectively. The abscissa of all the figures is v/v' and the ordinate is ω_z/ω'_z . As shown in Figure 6.14(a), the contributions from quadrants 1, 2 and 4 are nearly equal, the contribution from the quadrant 3 is smaller. Thus, the overall contribution is negative. The quadrant contributions at $R_\theta = 4850$ are very similar with nearly equal contributions from quadrants 1, 2, and 4, as shown in Figure 6.14(b). The contribution from quadrant 3 is relatively low, but is greater than the quadrant 3 contribution at $R_\theta = 2870$. This reflects the R_θ dependence observed in the $\overline{v\omega_z^+}$ data of Figure 6.8. may be an effect of R_θ .

As shown in Figure 6.14(c), the $R_\theta \simeq 2 \times 10^6$, $k^+ \approx 25 \sim 50$ v - ω_z quadrant

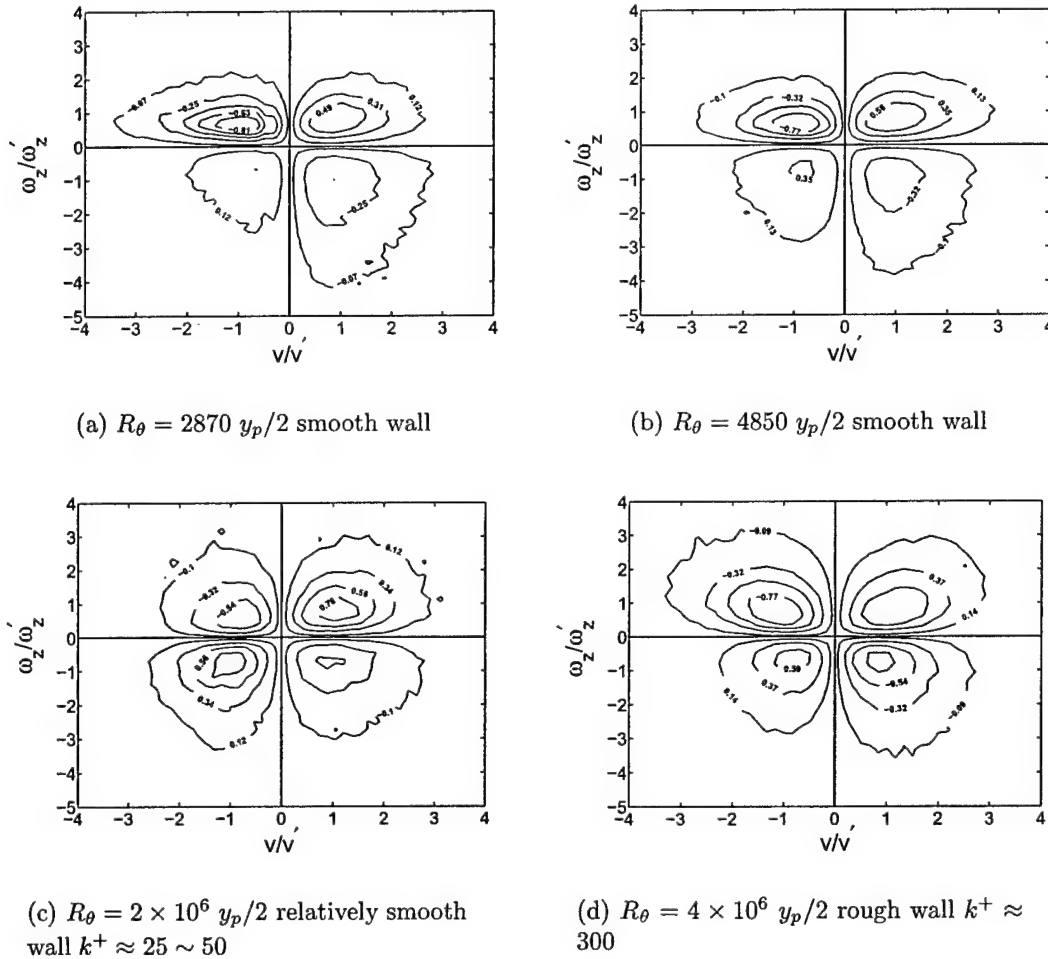


Figure 6.14. Weighted probability density functions of v/v' and ω_z/ω'_z at $y_p/2$.

contributions are considerably different from the low R_θ results. Here, the contributions from quadrants 1 and 3 are nearly equal and outnumber the contributions from quadrants 2 and 4. Thus, the overall contribution to $\overline{v\omega_z}$ from v and ω_z is positive, as observed in spectral analysis. As shown in Figure 6.14(d) the $R_\theta \simeq 2 \times 10^6$ $k^+ \approx 300$ quadrant contributions show a different trend than those in Figure 6.14(c). These data indicate the greatest contribution coming from the 2nd quadrant followed by the 4th quadrant. The 1st quadrant has the highest positive contributions. The negative contributions, however, are larger than the positive contributions, which

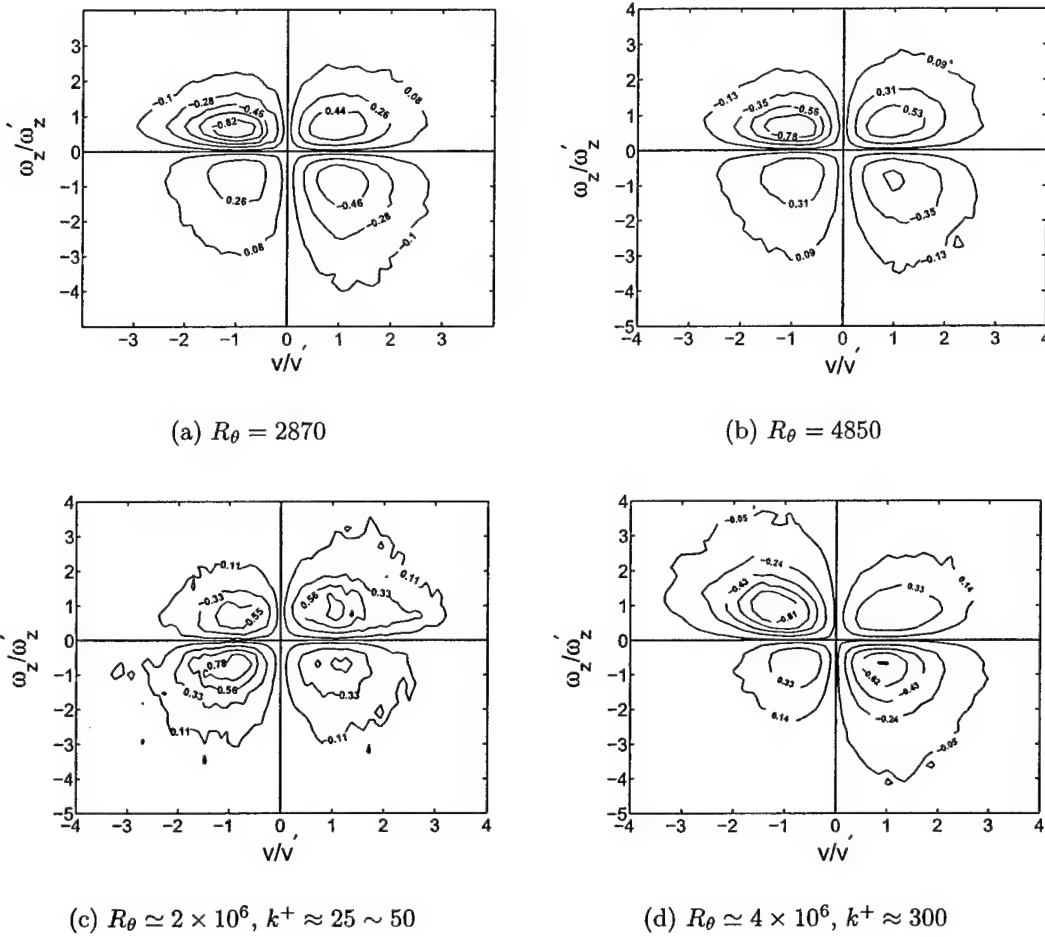


Figure 6.15. Weighted probability density functions of v/v' and ω_z/ω_z' at $2y_p$.

must be the case according to results of Figure 6.8. Overall, the v - ω_z correlations at $y_p/2$ exhibit detectable sensitivity to both R_θ and wall roughness.

The *wpdfs* of v and ω_z computed using the same technique for the above R_θ values at the wall normal location of $2y_p$ are shown in Figures 6.15(a-d). The quadrant contributions at $R_\theta = 2870$ are somewhat similar to the quadrant contributions at $y_p/2$ shown in Figure 6.14(a) with the lowest contribution coming from quadrant 3. Similar to the results at $y_p/2$, the contributions from quadrants 2 and 4 are larger than those from quadrants 1 and 3. The contributions from the quadrant 4 are, however, significantly larger than those from quadrant 2 at $2y_p$.

This increase in quadrant 4 contributions occurs in concert with a reduction in quadrant 1 contributions. At $R_\theta = 4850$ and $2y_p$, the quadrant contributions as depicted in Figure 6.15(b) show a slight increase in quadrant 4 contributions. This increase in quadrant 4 contributions is less than the increase at $R_\theta = 2870$ $2y_p$. Evidently, the $2y_p$ contributions at $R_\theta = 2870$ and 4850 begin to exhibit some small differences.

The *wpdf* quadrant contributions of v and ω_z at $R_\theta \simeq 2 \times 10^6$, $k^+ \approx 25 \sim 50$, are different from those at low R_θ significantly. These contributions are larger in the 1st and the 3rd quadrants and are very similar to those at $y_p/2$. Addition of wall roughness significantly changes these quadrant contributions (Figure 6.15(d)). In this case, contributions from the quadrants 2 and 4 are larger than those from quadrants 1 and 3. Furthermore, the quadrant 2 contributions in Figure 6.15(d) are larger than those from quadrant 4. This is somewhat similar to what was observed at low R_θ . Overall, the rough wall contributions at $2y_p$ remain similar to those at $y_p/2$.

6.4.3 $u\omega_z$ Signals

This section presents, statistics, spectral analysis and *wpdf* studies of u and ω_z for the same R_θ and wall roughness conditions. Section 6.4.3.1 describes inner normalized mean $u\omega_z$, $\overline{u\omega_z}^+$, $u\omega_z$ intensity, $(u\omega_z)'$, and the correlation coefficient between u and ω_z , $\rho_{u\omega_z}$. The spectral analysis of u and ω_z is presented in Section 6.4.3.2 and the *wpdf* studies of u and ω_z are presented in Section 6.4.3.3.

6.4.3.1 Analysis of $u\omega_z$ Statistics

Variation of $\overline{u\omega_z}^+$ with y^+ for the current high R_θ smooth and rough wall data are shown in Figure 6.16. These results are compared with Klewicki et al. [64] low R_θ results. As shown, current high R_θ smooth and rough wall data meld nicely with Klewicki et al. [64] low R_θ results. Thus, there is no apparent effect of surface

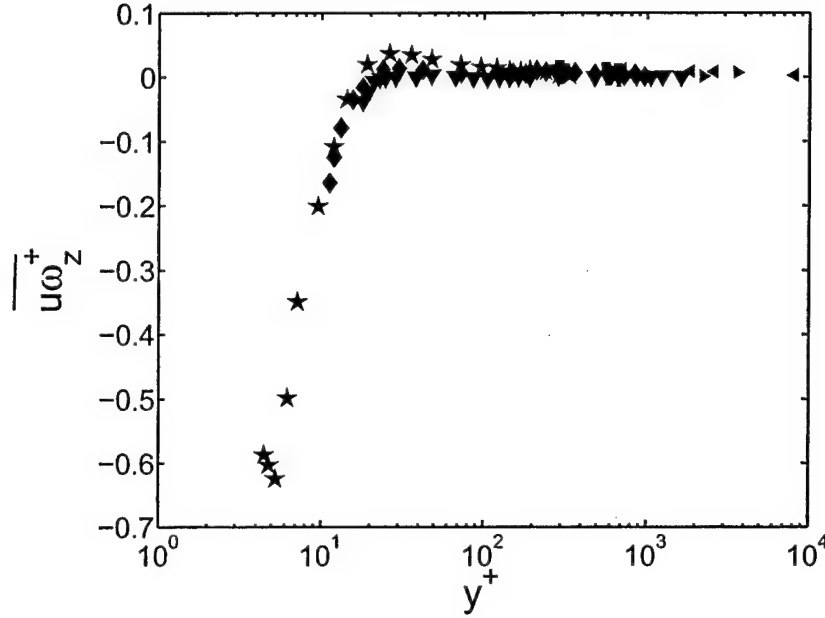


Figure 6.16. Variation of inner normalized $\overline{u\omega_z}$ as a function of y^+ . ■ $R_\theta \simeq 5 \times 10^6$ smooth wall, ► $R_\theta \simeq 4 \times 10^6$ $k^+ \approx 300$, ◄ $R_\theta \simeq 2 \times 10^6$ $k^+ \approx 500$, Klewicki and Falco [76] ★ $R_\theta = 1010$, ◆ $R_\theta = 2870$, ▼ $R_\theta = 4850$

roughness of R_θ in $\overline{u\omega_z}^+$. As mentioned by Klewicki [64], for $R_\theta < 5000$ this statistic shows very little R_θ effect.

Current high R_θ inner normalized intensities of $u\omega_z$, $(u\omega_z)^{'+}$, are shown in Figure 6.17. These data are compared with low R_θ smooth wall $(u\omega_z)^{'+}$ data of Klewicki [8]. As shown, the current high R_θ data in the log-law region tend to meld into $R_\theta = 2870$ and 4850 data of Klewicki [8] around $y^+ \approx 900$. The $R_\theta = 1010$ data, however, show a slight deviation which could again be due to a low R_θ effect. Therefore, it can be concluded that the inner normalized $u\omega_z$ exhibits little R_θ or surface roughness effects for $R_\theta \gtrsim 2000$.

The computed correlation coefficients between u and ω_z , $\rho_{u\omega_z}$, for the same above data are presented in Figure 6.18. The current high R_θ rough wall $\rho_{u\omega_z}$ data are scattered. Despite scatter, most of the current high R_θ $\rho_{u\omega_z}$ data agree well with $R_\theta \simeq 2 \times 10^6$, $k^+ \approx 25 \sim 50$ relatively smooth wall $\rho_{u\omega_z}$ data. Current

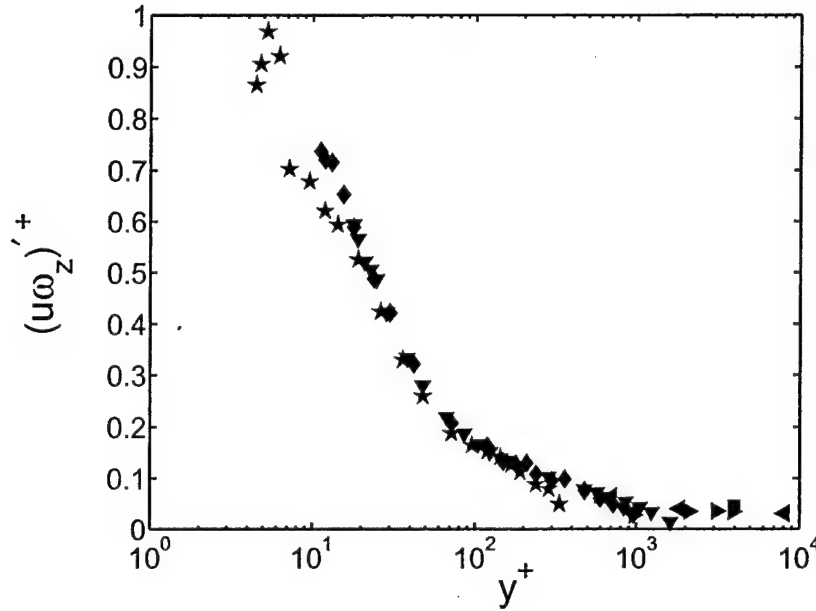


Figure 6.17. Variation of inner normalized $(u\omega_z)^+$ intensity as a function of y^+ . \blacksquare $R_\theta \simeq 5 \times 10^6$ smooth wall, \blacktriangleright $R_\theta \simeq 4 \times 10^6$ $k^+ \approx 300$, \blacktriangleleft $R_\theta \simeq 2 \times 10^6$ $k^+ \approx 500$, Klewicki [8] \star $R_\theta = 1010$, \blacklozenge $R_\theta = 2870$, \blacktriangledown $R_\theta = 4850$

$R_\theta \simeq 2 \times 10^6$, $k^+ \approx 25 \sim 50$ data show good agreement with $R_\theta = 4850$ data of Klewicki [8]. Thus, there is very little effect of R_θ and surface roughness on $\rho_{u\omega_z}$.

6.4.3.2 Spectral Analysis of $u\omega_z$

The spectral analysis of u and ω_z signals is presented in this section. The techniques employed are the same as those used in Section 6.4.2.2.

Figures 6.19(a-d) show the inner normalized premultiplied power spectra of streamwise velocity, $\Psi(u^+)$, spanwise vorticity, $\Psi(\omega_z^+)$, and velocity-vorticity premultiplied cospectra, $f^+ \Lambda(u^+ \omega_z^+)$, near $y_p/2$ for $R_\theta = 2870$, $R_\theta = 4850$, $R_\theta \simeq 2 \times 10^6$, $k^+ \approx 25 \sim 50$ and $R_\theta \simeq 4 \times 10^6$ $k^+ \approx 300$. In all the figures, abscissa is f^+ and the ordinate is the inner normalized power spectral density. As shown in Figure 6.19(a), $\Psi(u^+)$ for $R_\theta = 2870$ and $y_p/2$ peaks at a relatively low frequency, whereas, as shown previously, $\Psi(\omega_z^+)$ peaks at a high frequency close to f_λ . The

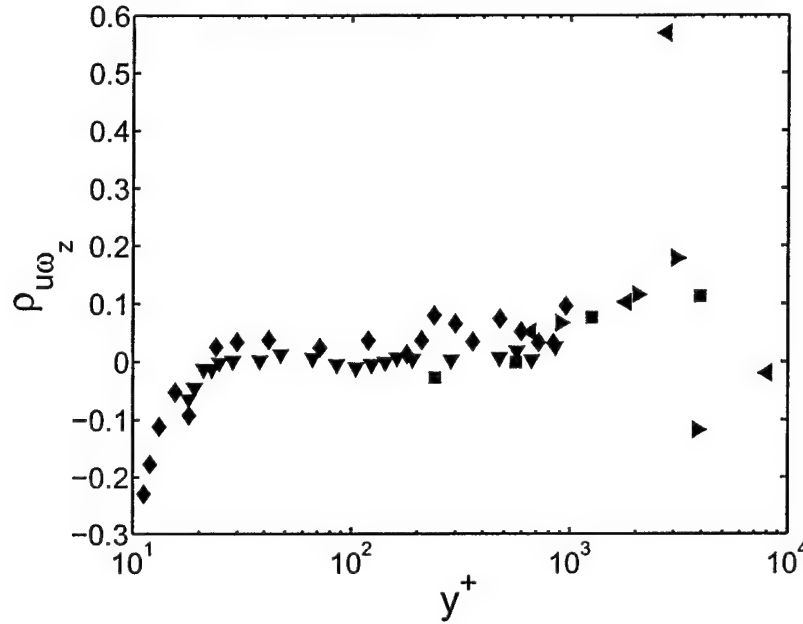


Figure 6.18. Variation of $\rho_{u\omega_z}$ as a function of y^+ . ■ $R_\theta \simeq 5 \times 10^6$ smooth wall, ► $R_\theta \simeq 4 \times 10^6$ $k^+ \approx 300$, ◄ $R_\theta \simeq 2 \times 10^6$ $k^+ \approx 500$, Klewicki [8] ♦ $R_\theta = 2870$, ▼ $R_\theta = 4850$

inner normalized frequencies of these two peaks are separated by about an order of magnitude. The $f^+ \Lambda(u^+ \omega_z^+)$ has two peaks. A positive peak tracks that in $\Psi(u^+)$ and a negative peak tracks that in $\Psi(\omega_z^+)$. This negative peak in $\Psi(\omega_z^+)$ occurs at a frequency slightly larger than f_λ . Also, it should be noted that at $y_p/2$, $\overline{u\omega_z^+}$ is slightly negative. This indicates that at high frequencies, around the peak of $\Psi(\omega_z^+)$, u and ω_z are negatively correlated while at low frequencies, they are positively correlated. As shown in Figure 6.19(b), Somewhat similar behavior is observed at $R_\theta = 4850$. In this case, both the positive and negative peaks in $\Lambda(u^+ \omega_z^+)$ are of greater magnitude. There is positive correlation between u and ω_z at very high frequencies followed by negative correlation at high and intermediate frequencies. Similar to the $f^+ \Lambda(u^+ \omega_z^+)$ at $R_\theta = 2870$, low frequencies are positively correlated.

Figures 6.19(c-d) show $\Psi(u^+)$, $\Psi(\omega_z^+)$ and $f^+ \Lambda(u^+ \omega_z^+)$ at high R_θ . The $\Psi(\omega_z^+)$

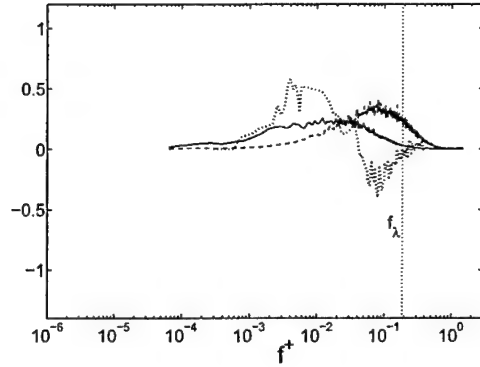
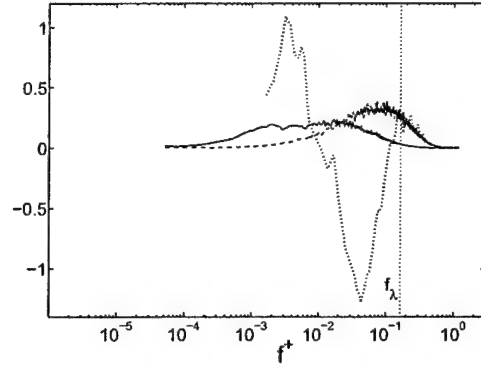
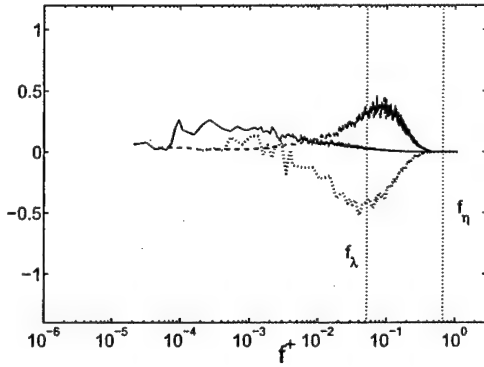
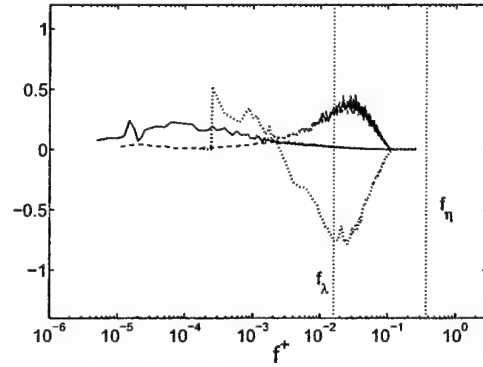
(a) $R_\theta = 2870$ smooth wall $y_p/2$ (b) $R_\theta = 4850$ smooth wall $y_p/2$ (c) $R_\theta \simeq 2 \times 10^6$ $k^+ \approx 25 \sim 50$ $y_p/2$ (d) $R_\theta \simeq 4 \times 10^6$ $k^+ \approx 300$ $y_p/2$

Figure 6.19. Premultiplied power spectra of v and ω_z ($\Psi(v^+)$ and $\Psi(\omega_z^+)$), and premultiplied cospectra of v^+ and ω_z^+ , $f^+ \Lambda(v^+ \omega_z^+)$ at the wall normal location of $y_p/2$. — $\Psi(u^+)$, — — $\Psi(\omega_z^+)$, $f^+ \Lambda(u^+ \omega_z^+)$.

changes somewhat at high R_θ as shown in Figures 6.19(c) and 6.19(d). The peak in $\Psi(\omega_z)$ occurs at a frequency slightly larger than f_λ . The same occurs at a frequency slightly smaller than f_λ low R_θ (Figures 6.19(a) and 6.19(b)). The peak in $\Psi(\omega_z^+)$ is around f_λ . $\Psi(u^+)$ is very much different with its peak shifting to very low frequency due to increasing scale separation at high R_θ . As shown in Figure 6.19(c), all the high frequency motions of u and ω_z are negatively correlated. The range of frequencies with negative correlation has also been increased significantly with

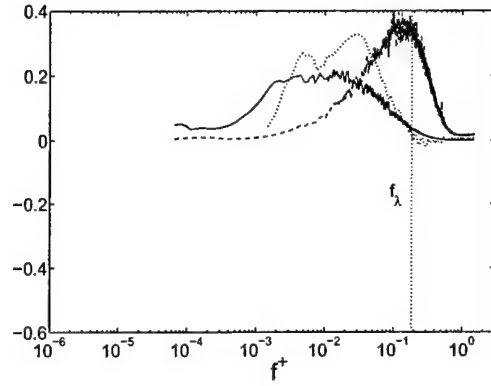
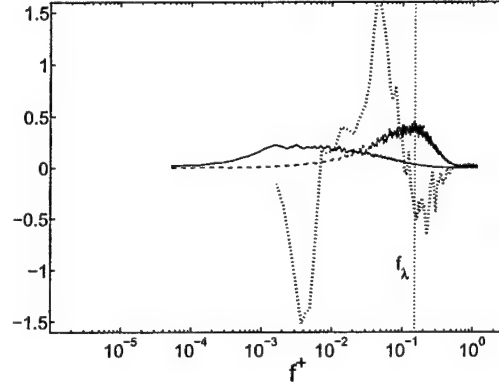
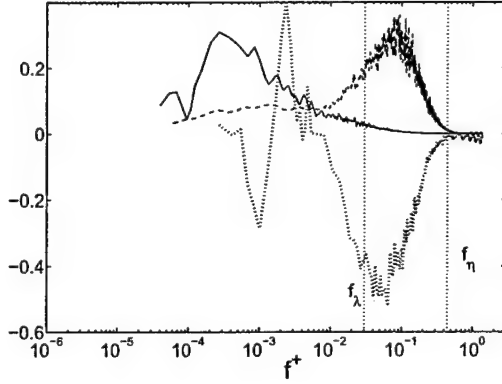
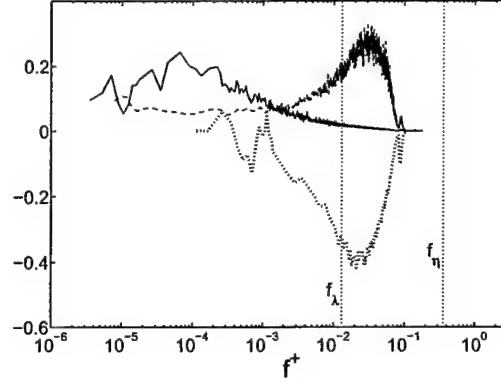
(a) $R_\theta = 2870$ (b) $R_\theta = 4850$ (c) $R_\theta \simeq 2 \times 10^6 \quad k^+ \approx 25 \sim 50$ (d) $R_\theta \simeq 4 \times 10^6 \quad k^+ \approx 300$

Figure 6.20. Premultiplied power spectra of v and ω_z ($\Psi(v^+)$ and $\Psi(\omega_z^+)$), and premultiplied cospectra of v^+ and ω_z^+ , $f^+ \Lambda(v^+ \omega_z^+)$ at the wall normal location of $2y_p$. — $\Psi(u^+)$, — — $\Psi(\omega_z^+)$, $f^+ \Lambda(u^+ \omega_z^+)$.

increasing R_θ . Some low frequency motions of u and ω_z are mildly positively correlated. Recall that $\overline{u\omega_z} \approx 0$ for all R_θ at this wall normal location. As shown in Figure 6.19(d), $\Psi(u^+)$ and $\Psi(\omega_z^+)$ at $R_\theta \simeq 4 \times 10^6$, $k^+ \approx 300$ are very similar to $\Psi(u^+)$ and $\Psi(\omega_z^+)$ in Figure 6.19(c). The $f^+ \Lambda(u^+ \omega_z^+)$ curves show highly similar behavior with negative correlations at high frequency and mildly positive correlations at low frequency.

Figures 6.20(a-d) show $\Psi(u^+)$, $\Psi(\omega_z^+)$ and $f^+ \Lambda(u^+ \omega_z^+)$ near $2y_p$. Figures 6.20(a)

and 6.20(b) indicate that the peaks in $\Psi(\omega_z)$ move to a relatively higher frequency. This is likely $\sim f_\lambda$. In concert with this, the peaks in $\Psi(u^+)$ move to even lower frequencies due to the introduction of relatively large scale motions with increasing y . The $R_\theta = 2870$ result reveal a broad peak in $f^+\Lambda(u^+\omega_z^+)$ positioned between the two peaks of $\Psi(u)$ and $\Psi(\omega_z)$. There are two peaks with different signs in $f^+\Lambda(u^+\omega_z^+)$ at $R_\theta = 4850$ as shown in Figure 6.20(b) which is different from those of $R_\theta = 2870$ and $R_\theta = O(10^6)$.

Figures 6.20(c-d) show $\Psi(u^+)$, $\Psi(\omega_z^+)$ and $f^+\Lambda(u^+\omega_z^+)$ at $2y_p$ for $R_\theta \simeq 2 \times 10^6$, $k^+ \approx 25 \sim 50$ and $R_\theta \simeq 4 \times 10^6$ $k^+ \approx 300$. Here the $f^+\Lambda(u^+\omega_z^+)$ behavior is somewhat similar that at $R_\theta = 4850$. The high frequency $f^+\Lambda(u^+\omega_z^+)$ at high R_θ show negative peaks at frequencies slightly larger than f_λ . The same behavior is observed at $R_\theta = 4850$.

The simultaneous low and high pass filtering technique explained in Section 6.3.3 was employed to analyze u and ω_z correlations. Figures 6.21(a-d) show these $\overline{u_f\omega_zf}^+$ results. As before, the lower abscissa represents the inner normalized cut-off frequency, f_c^+ , and the upper abscissa represents the outer normalized cut-off frequency, f_o ($= f_c\delta/U_\infty$). The ordinate represents the computed $\overline{u_f\omega_zf}^+$ using the low-pass filtered and high pass filtered u and ω_z signals. The $R_\theta = 2870$ result of Figure 6.21(a), $\overline{u_f\omega_zf}^+$ is very similar to the $R_\theta = 2870$ $\overline{v_f\omega_zf}^+$ result of Figure 6.13(a). There is an increasing contribution from relatively low frequency motions in $\overline{u\omega_z}^+$ at $y_p/2$ relative to that at $2y_p$ including a negative contribution from high frequency motions. At $2y_p$ $R_\theta = 2870$, the cross over frequency increases by about a factor of 5 compared to that at $y_p/2$ under inner normalization. Also, f_x is about an order of magnitude larger than the outer scale at $y_p/2$ and is about the order of magnitude of the outer scale at $2y_p$. Thus, at $R_\theta = 2870$, $\overline{u\omega_z}^+$ is dominated by large scales at both wall normal locations. The $\overline{u\omega_z}^+$ at $R_\theta = 2870$ and 4850 is very small at both wall normal locations. The $\overline{u_f\omega_zf}^+$ behavior at

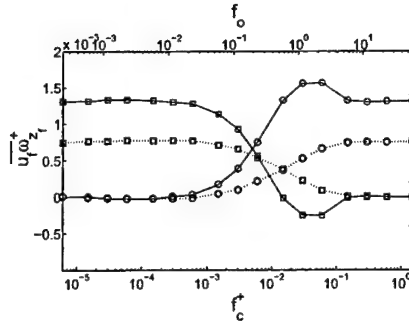
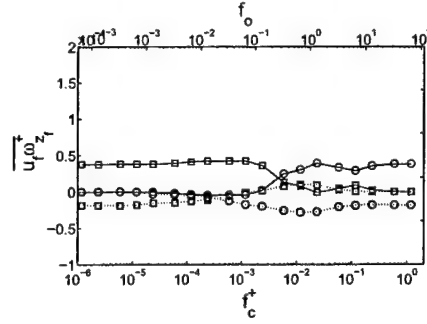
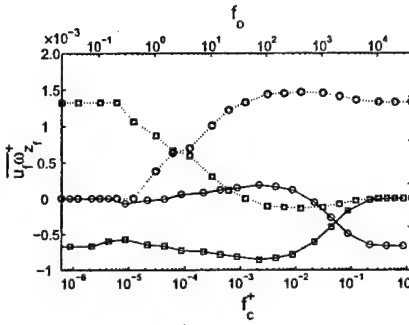
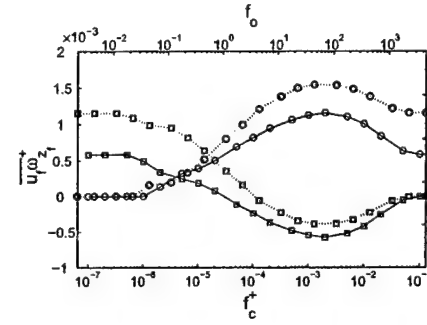
(a) $R_\theta = 2870$ (b) $R_\theta = 4850$ (c) $R_\theta \simeq 2 \times 10^6 \quad k^+ \approx 25 \sim 50$ (d) $R_\theta \simeq 4 \times 10^6 \quad k^+ \approx 300$

Figure 6.21. Contributions of filtered signals, $\overline{u_f \omega_z f^+}$, as functions of cut-off frequency. \square low pass filtered $\overline{u_f \omega_z f^+}$, \circ high pass filtered $\overline{u_f \omega_z f^+}$, at $-y_p/2$, at $\dots\dots\dots 2y_p$.

$R_\theta = 4850$ is slightly different from that at $R_\theta = 2870$. The magnitudes of $\overline{u_f \omega_z f^+}$ are small at $R_\theta = 4850$. The f_x is of the order of outer scales.

Figure 6.21(c) shows $\overline{u_f \omega_z f^+}$ computed at $R_\theta \simeq 2 \times 10^6$, $k^+ \approx 25 \sim 50$. At $y_p/2$, $R_\theta \simeq 2 \times 10^6$, $k^+ \approx 25 \sim 50$ $\overline{u \omega_z^+}$ derives its largest contributions from relatively high frequency motions. This picture, however, changes considerably at $2y_p$ with a significant contribution from low frequency motions. This is shown in Figure 6.21(c), by a decrease in f_x of about 4 orders of magnitude. Thus, f_x at $2y_p$ is almost of the order of outer frequency. This confirms the observation in spectral analysis, that the low frequencies control $\overline{u \omega_z^+}$ at $2y_p$. As shown in Figure 6.21(d),

low frequency motions control $\overline{u\omega_z}^+$ behavior at $R_\theta \simeq 4 \times 10^6$, $k^+ \approx 300$ both wall normal positions. The cross over frequencies are of the order of magnitude of the outer scale. Thus, large scales contribute significantly to $\overline{u\omega_z}^+$.

6.4.3.3 Joint Probability Density Functions of $u\omega_z$

The joint pdf analysis was performed for both u and ω_z at all the above R_θ . The weighted pdf, *wpdf*, between u and ω_z was computed using the technique described in Section 6.3.3. The *wpdf* distributions of u and ω_z at $y_p/2$ are shown in Figures 6.22(a-d). The abscissa in all the figures is the streamwise velocity normalized by its rms value, u' and the ordinate is ω_z normalized by its rms value, ω'_z . As shown in Figures 6.22(a) and 6.22(b), the quadrant 1 contribution is larger than from the other quadrants, at $R_\theta = 2870$ and 4850. The contributions from all the other quadrants are significant and are nearly equal. As shown in Figure 6.22(c), the distribution changes significantly at $R_\theta \simeq 2 \times 10^6$, $k^+ \approx 25 \sim 50$ which could be an R_θ effect. The quadrant contributions are not very uniformly distributed and the contribution from the 4th quadrant is significantly large compared to other quadrants. Distributions in quadrants 1 and 4 are bimodality indicating that there are significant contributions from large amplitude u fluctuations and all ω_z fluctuations. Overall, the $\overline{u\omega_z}^+$ is negative due to large contributions from quadrant 4. As shown in Figure 6.22(d), the high R_θ rough wall distribution is significantly different from relatively smooth wall distribution with the largest contribution coming from quadrant 1. Contribution from quadrant 3 is considerable. Thus, $\overline{u\omega_z}^+$ is positive.

The *wpdf* distributions of u and ω_z at $2y_p$ for the above R_θ values are shown in Figures 6.23(a-d). The abscissa and the ordinate are the same as in Figure 6.22. As shown in Figure 6.23(a), the quadrant contributions of $R_\theta = 2870$ at $2y_p$ are highly similar to those at $y_p/2$ as shown in Figure 6.22(a). This is the same at

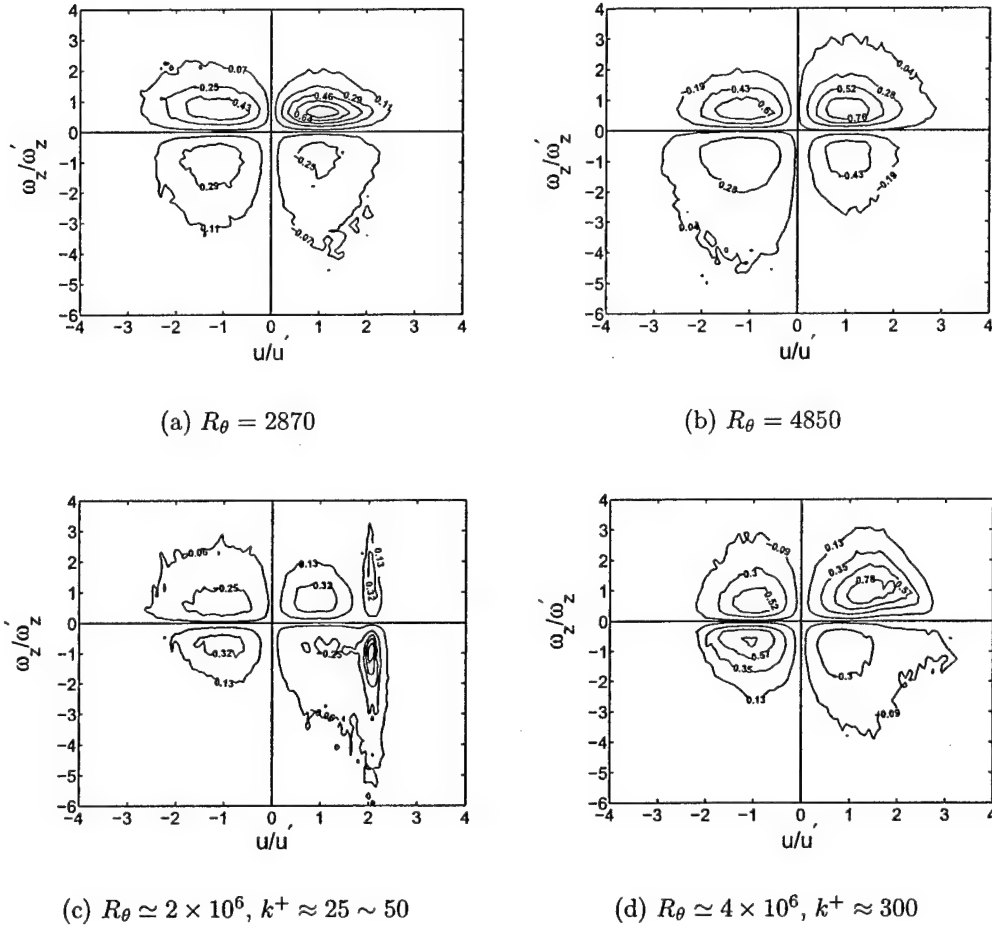


Figure 6.22. Weighted probability density functions of v/v' and ω_z/ω'_z at $y_p/2$.

$R_\theta = 4850$ as shown in Figures 6.23(b) and 6.22(b). Also, there is little apparent R_θ dependence. At $R_\theta \simeq 2 \times 10^6, k^+ \approx 25 \sim 50$ the quadrant contributions at $2y_p$ are slightly different from those at $y_p/2$, which could be an effect of presence of large eddies. The largest contributions come from quadrant 4. These contributions are similar to those at $y_p/2$ coming from large amplitude fluctuations of u and entire range of fluctuations from ω_z . As a result, $\overline{u\omega_z}^+$ is negative. It is worth mentioning again that the contributions from all the quadrants are of the same order of magnitude and $\overline{u\omega_z}$ is very small at these wall normal positions. The high R_θ rough wall turbulent boundary layer quadrant contributions (Figure 6.23(d)) are

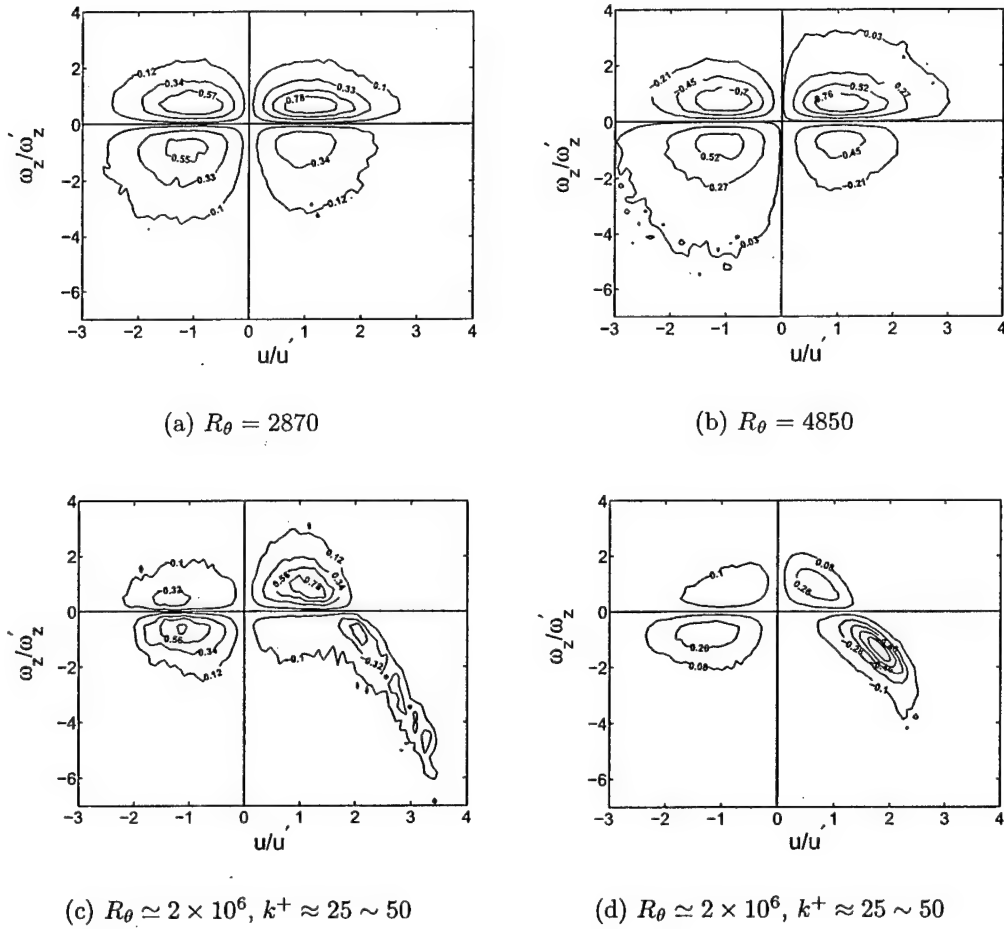


Figure 6.23. Weighted probability density functions of v/v' and ω_z/ω'_z at $2y_p$.

similar to those at relative smooth wall. They are, however, significantly different from those at $y_p/2$. Contributions from quadrant 4 are similar to those of relatively smooth wall. As discussed in Section 6.4.3.1, the inner normalized $\overline{u\omega_z}^+$ does not show any R_θ or wall roughness dependence. The overall distributions of high R_θ smooth wall $jpdf$ (not shown), however, are different from those at low R_θ .

6.5 Conclusions

The velocity-vorticity correlations, $u\omega_z$ and $v\omega_z$ were analyzed. The flow fields considered were smooth wall low R_θ and very high R_θ relatively smooth and rough

wall turbulent boundary layers. The analysis tools used were statistics, spectral analysis, and weighted joint probability density functions. The outcome of this study is as follows:

1. The intensity of streamwise velocity is highly sensitive to large scale fluctuations associated with R_θ . It is less sensitive to wall roughness. Conversely, the intensity of wall normal velocity is less sensitive to R_θ and highly sensitive to wall roughness. Except near the wall, vorticity intensity is less sensitive to R_θ and to wall roughness.
2. The correlation between v and ω_z depends on R_θ and wall roughness. The $\overline{v\omega_z}^+$ and $\rho_{v\omega_z}$ show a clear R_θ and surface roughness dependence while rms fluctuations of $(v\omega_z)^+$ may be insensitive to both R_θ and wall roughness.
3. The inner normalized $v\omega_z$ cospectra and the $wpdf$ of $v\omega_z$ are both R_θ and surface roughness dependent. The dominant scales of $v\omega_z$ cospectrum at smooth wall low R_θ $y_p/2$ and at smooth wall high R_θ $2y_p$ are large scales. Conversely, the dominant scales of $v\omega_z$ cospectrum at smooth wall low R_θ $2y_p$ and at smooth wall high R_θ $y_p/2$ are of the order of Taylor microscale. The dominant scales of the high R_θ rough wall $v\omega_z$ cospectrum are large scales.
4. The velocity vorticity correlation, $u\omega_z$ shows very little R_θ dependence. This correlation is relatively less sensitive to the wall roughness as well. The dominant scales of $u\omega_z$ are different. At low R_θ , near the wall and high R_θ away from the wall, the dominant scales are large. In all other situations, the dominant scales are of the order of Taylor microscale.
5. The $jpdf$ and $wpdf$ distributions of $u\omega_z$ are different at low and high R_θ . These distributions are sensitive to surface roughness as well. There is increase in quadrant 4 contributions at high R_θ .

6.6 Acknowledgments

This work was supported by the National Science Foundation and Office of Naval Research under grants CTS-0120061 (grant monitor Dr Michael W Plesniak) and N00014-00-1-0753 (grant monitor Dr Ronald D Joslin) respectively.

Properties of the Mean Momentum Balance in Turbulent Boundary Layer, Pipe and Channel Flows

By T. WEI¹, P. FIFE², J. KLEWICKI¹ AND P. McMURTRY¹

¹ Department of Mechanical Engineering

² Department of Mathematics

University of Utah

Salt Lake City, UT 84112

(Received 21 June 2004)

The properties of the mean momentum balance in turbulent boundary layer, pipe and channel flows are explored both experimentally and theoretically. Available high quality data reveal a dynamically relevant four-layer description that is a departure from the mean profile four-layer description traditionally and nearly universally ascribed to turbulent wall flows. Each of the four layers is characterized by a predominance of two of the three terms in the governing equations, and thus the mean dynamics of these four layers are unambiguously defined. The inner normalized physical extent of three of the layers exhibit significant Reynolds number dependence. The scaling properties of these layer thicknesses are determined. Particular significance is attached to the viscous/Reynolds stress gradient balance layer since its thickness defines a required length scale. Multiscale analysis (necessarily incomplete) substantiates the four-layer structure in developed turbulent channel flow. In particular, the analysis verifies the existence of at least one intermediate layer, with its own characteristic scaling, between the traditional inner and outer layers. Other information is obtained as well, such as (1) the widths (in order of magnitude) of the four layers, (2) a flattening of the Reynolds stress profile near its maximum, and (3) the asymptotic increase rate of the peak value of the Reynolds stress as the Reynolds number approaches infinity. Finally, on the basis of the experimental observation that the velocity increments over two of the four layers are unbounded with increasing Reynolds number and have the same order of magnitude, there is additional theoretical evidence (outside traditional arguments) for the asymptotically logarithmic character of the mean velocity profile in two of the layers; and (in order of magnitude) the mean velocity increments across each of the four layers are determined. All of these results follow from a systematic train of reasoning, using the averaged momentum balance equation together with other minimal assumptions, such as that the mean velocity increases monotonically from the wall.

1. Introduction

Laminar to turbulent transition in boundary layer, pipe and channel flows is accompanied by dramatic redistributions of the momentum and vorticity fields, e.g., Lighthill (1963), Willmarth (1975). These redistributions, which continue to occur with increasing Reynolds number within the turbulent regime, are reflected in the shape of the mean velocity profile. Over the past decade, research regarding the mean velocity profile in turbulent wall flows has intensified, e.g., Gad-el-Hak & Bandyopadhyay (1994), Barenblatt, Chorin & Prostokishin (1997), George & Castillo (1997), Sahay (1997), Sreenivasan & Sahay (1997), Zagarola & Smits (1998), Wosnik, Castillo & George (2000), Afzal (2001*a,b*), Zanon, Nagib, Durst & Monkewitz (2002), Panton (2002), and Panton (2003). Despite these efforts, fundamental questions concerning the proper analytical forms of the mean velocity profiles in boundary layer, pipe and channel flows remain largely unanswered. At the heart of this matter is the fact that the equations from which the profile is derived (i.e., the time averaged Navier Stokes equations) are unclosed, and thus are resistive to, for example, standard perturbation methods. Apart from this, further progress requires confronting other difficult to resolve issues. These relate to both the quality of the data and the selection of appropriately sensitive, yet measurable, indicator functions employed in distinguishing between the various proposed analytical forms for the velocity profile. For example, considerable discussion has surrounded the potential effects of surface roughness on the Princeton

superpipe data, Perry, Hafez & Chong (2001), while the comparison of the gradient functions, $y^+(dU^+/dy^+)$ and $(y^+/U^+)(dU^+/dy^+)$, for respectively determining logarithmic or power law forms presents stringent demands on the data quality relative to the subtleties of the issues at hand, Wosnik *et al.* (2000).

Given this context, it is useful to remain cognizant of the primary physical/technological motivations underlying the mean profile research efforts. Specifically, a primary (if not the primary) importance associated with determining the velocity profile lies in its inherent description of the momentum/vorticity redistribution processes mentioned at the outset. Specifically, at a practical technical level a knowledge of the mean profile translates to a predictive formula for the skin friction. More generally, turbulent wall-flows are traditionally divided into four layers,

- viscous sublayer: $y^+ < 5$
- buffer layer: $5 < y^+ < 30$
- logarithmic layer: $30 < y^+ < 0.15\delta^+$
- wake layer: $y^+ > 0.15\delta^+$,

where, as is customary, “+” signifies normalization by $u_\tau = \sqrt{\tau_w/\rho}$ and ν , and δ is the boundary layer thickness or half-channel height. As is apparent, these layers are closely tied to the properties of the mean profile, and thus a more subtle influence of mean profile structure relates to the associated physical interpretations of wall-flow physics. In a pipe or channel, the flow dynamics embody the processes by which momentum is extracted from the applied mean pressure force, transported to the wall, and transmitted into a mean surface shear force. In boundary layers the processes are similar, except that the mean pressure force is replaced by mean advection. In either case, a major motivation for correctly determining the mean velocity profile is the property that it inherently, albeit indirectly, reflects these momentum transport dynamics and their scaling with Reynolds number. Since mean dynamics are described by the time-averaged momentum balance, it is rational to expect that explicit study of the mean momentum balance, and its scaling behaviors, will be of considerable utility.

The present study employs existing high quality data sets to reveal the properties of the mean momentum balance in boundary layers, pipe and channel flows. This analysis indicates that these turbulent wall-flows are composed of a basic four-layer structure, with the dynamics in each of these layers predominantly characterized by a balance of two of the three terms in the mean momentum equation. The four layer structure revealed is unambiguous in its connection with the relevant mean dynamics and stands in contrast to the accepted mean profile-based characterization (i.e., the sub-, buffer, logarithmic and wake layer composition mentioned above). The Reynolds number scaling properties of the momentum balance are also revealed. In doing so, clear Reynolds number dependencies in the thicknesses of the four layers, as well as the velocity increments across these layers are identified. Consistent with this, multiscale analyses (under a minimal set of assumptions) are subsequently used to construct a new theoretical framework for turbulent channel flow. These analyses indicate that a length scale intermediate to the traditional inner and outer scales is required to properly describe mean flow structure, and thus embrace the experimental observations made herein.

2. The Mean Momentum Balance

The streamwise mean momentum equation for fully developed channel flow is

$$0 = -\frac{1}{\rho} \frac{dP}{dx} + \nu \frac{d^2 U}{dy^2} - \frac{d\langle uv \rangle}{dy},$$

where the mean pressure gradient is

$$-\frac{dP}{dx} = \frac{\tau_w}{\delta},$$

and δ is the channel half height. Normalizing the mean velocity, U , and Reynolds stress, $-\langle uv \rangle$, by the friction velocity u_τ , and y by the viscous length scale ν/u_τ , gives the normalized streamwise mean momentum equation

$$0 = \frac{1}{\delta^+} + \frac{d^2 U^+}{dy^{+2}} - \frac{d\langle uv \rangle^+}{dy^+}. \quad (2.1)$$

Three physical mechanisms are represented in equation 2.1. The first term, $1/\delta^+$, is the normalized pressure gradient which provides the driving force for the flow, the second term, d^2U^+/dy^{+2} , is the gradient of the viscous stress and the third term, $d(-\langle uv \rangle^+)/dy^+$, is the gradient of the Reynolds stress.

For the zero pressure gradient turbulent boundary layer, the inner normalized mean momentum equation is,

$$U^+ \frac{\partial U^+}{\partial x^+} + V^+ \frac{\partial U^+}{\partial y^+} = \frac{d^2U^+}{dy^{+2}} - \frac{d\langle uv \rangle^+}{dy^+}. \quad (2.2)$$

As in turbulent channel flow, there are three different physical mechanisms represented. Mean advection is represented by the terms on the left hand side of equation 2.2. The other two mechanisms are the same as in channel flow, the gradient of the viscous stress, $\partial^2U^+/\partial y^{+2}$, and the gradient of the Reynolds stress, $\partial(-\langle uv \rangle^+)/\partial y^+$.

2.1. Force balance data

Physically, the above momentum balance equations represent the time-average statement of Newton's second law for a differential fluid element. Examination of the mean momentum equations (equation 2.1 and equation 2.2), indicates that it is the stress gradients (viscous, Reynolds stress, or pressure) that are the significant quantities in the force balance, not the stresses themselves. Based on the momentum equations, the three effects must all be in balance, or have two nominally in balance with the third much smaller. Therefore, for the purpose of elucidating the mean momentum transport it is useful to examine the ratio of the gradient of the viscous stress to the gradient of the Reynolds stress. If, for example, this ratio in a pipe, $|\mu \frac{\partial^2 U}{\partial y^2} / \frac{\partial \rho \langle uv \rangle}{\partial y}|$ is $\ll 1$ then the viscous force is small, and the pressure and Reynolds stress gradients are nominally in balance. If $|\mu \frac{\partial^2 U}{\partial y^2} / \frac{\partial \rho \langle uv \rangle}{\partial y}| \simeq 1$, their effects are in balance and the pressure gradient term is either of the same order or relatively smaller order. And, if $|\mu \frac{\partial^2 U}{\partial y^2} / \frac{\partial \rho \langle uv \rangle}{\partial y}| \gg 1$ the Reynolds stress gradient is small and the pressure and viscous forces approximately balance.

Figure 1 shows the ratio of the gradient of the viscous stress to the gradient of the Reynolds stress for the fully developed channel flow, from the DNS of Moser, Kim & Mansour (1999). This figure shows a thin sublayer ($0 \leq y^+ \leq 3$) where pressure and viscous forces dominate the balance equation. Outside this thin layer is a region defined by a nearly perfect balance between the viscous and Reynolds stress gradients. The thickness of this stress gradient balance layer shows a clear Reynolds number dependence, extending well into the traditionally accepted logarithmic region of the mean velocity profile as Reynolds number increases. Near the location of maximum Reynolds stress, the viscous and pressure force are, once again, nearly in balance. Around the peak Reynolds stress location the gradient of the viscous stress is much larger than the gradient of the Reynolds stress. For greater distances from the wall, the Reynolds stress gradient changes sign and the viscous stress gradient becomes much smaller than either the Reynolds stress gradient or pressure gradient. In this region the Reynolds stress and pressure gradients are essentially in balance.†

The superpipe data of Zagarola & Smits (1997) ‡ and the boundary layer data of Spalart (1988) and DeGraaff & Eaton (2000) exhibit similar behavior. These data are plotted in figures 2 and 3 respectively. Both these sets of data show a Reynolds number dependence consistent with the DNS channel flow data in the inner region. For the superpipe data, the stress gradient balance layer extends out to approximately $y^+ \simeq 300$ at $R^+ \simeq 41,235$. Overall the turbulent boundary layer and superpipe data indicate that the width of stress gradient balance layer is Reynolds number dependent and extends well into the traditionally accepted logarithmic layer. Existing superpipe data at higher Reynolds number cannot be reliably used to explore this issue further as the data point closest to the wall lies beyond the region of interest.

The behavior of the ratio of the two stress gradient terms as shown in figures 1-3, suggests a four-layer structure. The first region is an inner viscous/advection balance layer where the viscous force balances the pressure force (in channel flow), or in the case of the turbulent boundary layer the viscous force becomes smaller while balancing mean advection. (Note that all of the terms in equation 2.2 are zero at the wall in

† A similar presentation of stress gradient ratio data was earlier given by Cenedese, Romano & Antonia (1998), but only explored in the context of viscous sublayer structure.

‡ Note that the corrected superpipe data of McKeon *et al.* (2003) yields nearly identical results as Zagarola & Smits (1997) relevant to the present analyses.

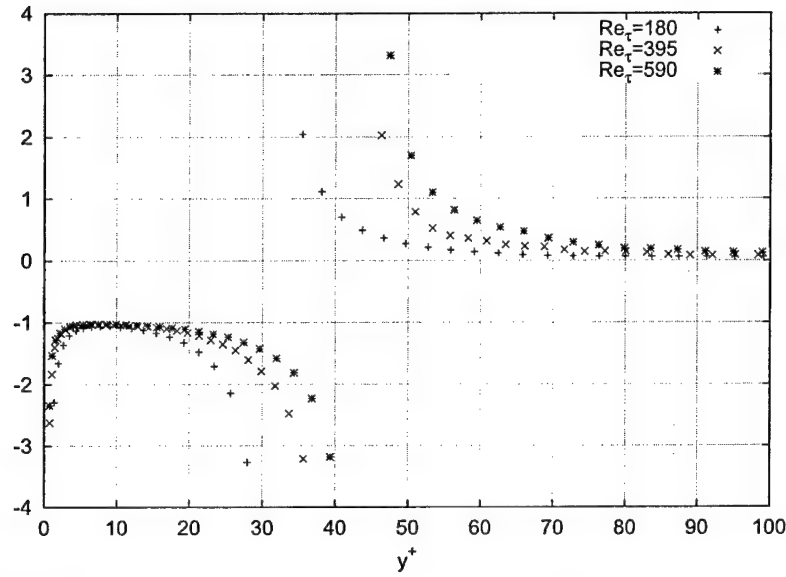


FIGURE 1. The ratio of the gradient of the viscous stress to the gradient of the Reynolds stress in fully developed channel flow, DNS data from Moser *et al.* (1999).

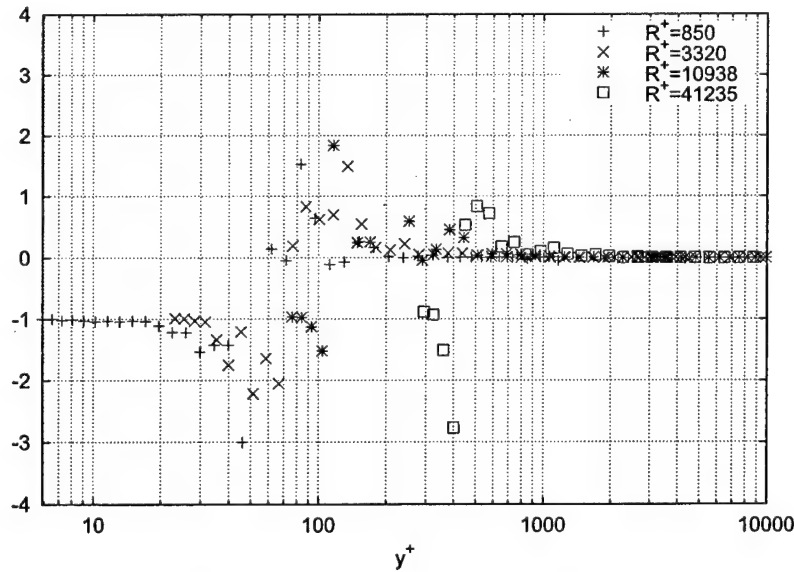


FIGURE 2. The ratio of the gradient of the viscous stress to the gradient of Reynolds stress in a turbulent pipe flow, as derived from the data of Zagarola & Smits (1997).

the zero pressure gradient boundary layer.) The second region is called the stress gradient balance layer. In this layer the viscous and Reynolds stress gradients are of nearly equal magnitude but opposite sign. The third region is a meso viscous/advection balance layer where the viscous force balances the pressure force in channel flow or the mean advection in the turbulent boundary layer, while near the center of this layer the Reynolds stress gradient passes through zero. The fourth region is an inertial/advection balance layer, where the Reynolds stress gradient balances the pressure force in channel flow or the mean advection in the turbulent boundary layer, while the viscous force is negligible. The sketch in figure 4 depicts the four layers as defined by the dynamics of the mean momentum balance at a fixed Reynolds number.

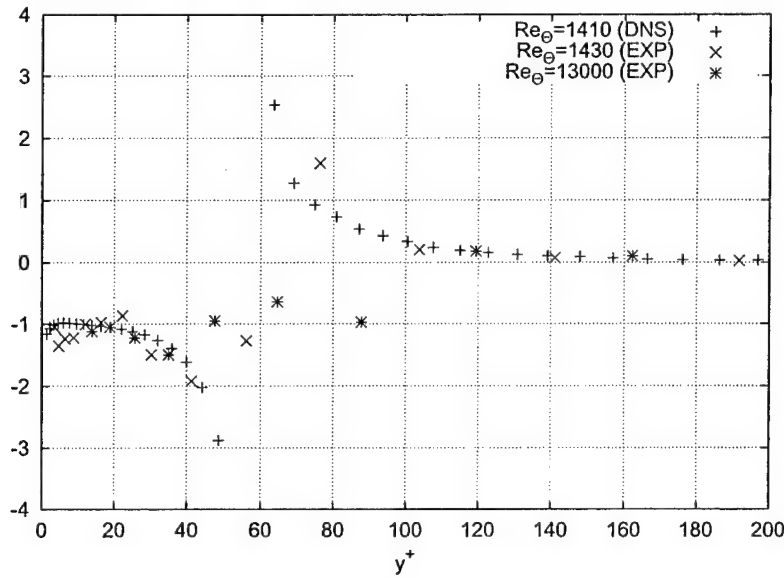


FIGURE 3. The ratio of the gradient of the viscous stress to the gradient of the Reynolds stress in turbulent boundary layers. DNS data are from Spalart (1988) and the experimental data are from DeGraaff & Eaton (2000).

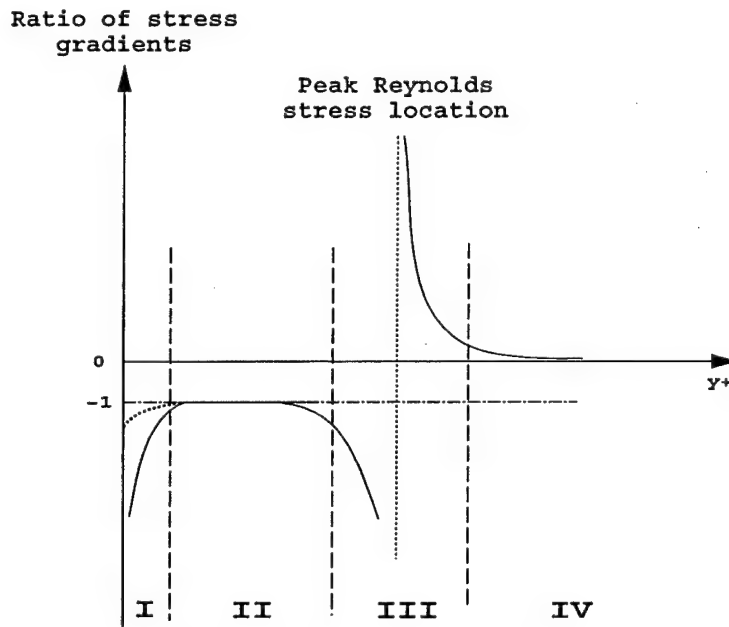


FIGURE 4. Sketch of the four layers of turbulent wall-bounded flows for one Reynolds number; Layer I is the inner viscous/advection balance layer, layer II is the stress gradient balance layer, layer III is the viscous/advection balance meso-layer and layer IV is the inertial/advection balance layer. Note layer I in the zero pressure gradient turbulent boundary layer is different from that of channel & pipe flow in that all of the terms in equation 2.2 are zero at the wall.

2.2. Layer thicknesses

Based on the DNS and laboratory data presented, the physical extent and the Reynolds number dependence of each of the four layers identified above may be characterized. The inner viscous/advection sublayer extends from the wall to $y^+ \cong 3$, and, at most, exhibits only a very weak Reynolds number dependence. The stress-gradient balance layer extends from $y^+ \cong 3$ to $y^+ \cong 1.6 \times (\delta^+)^{1/2}$. For this characterization, the numerical

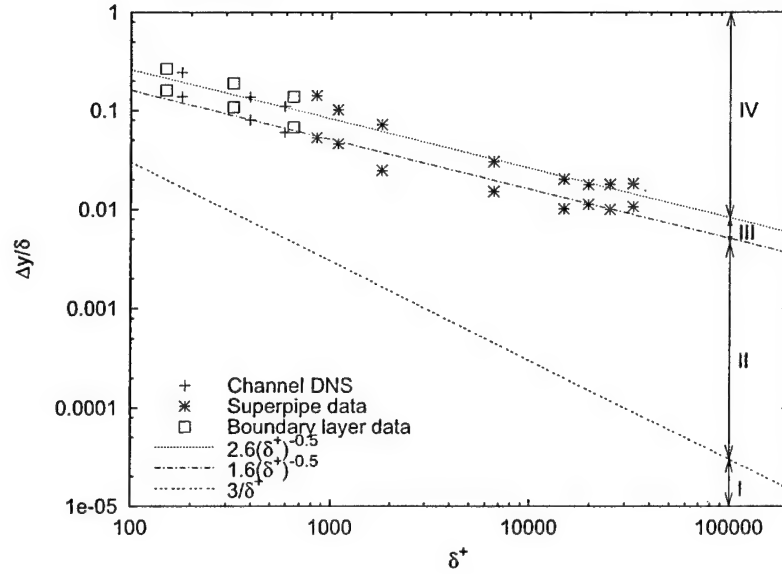


FIGURE 5. Reynolds number dependence of the outer-normalized physical extent of the four layers in canonical wall flows. The four layers are numbered according to the sketch of figure 4. Channel data are from Moser *et al.* (1999), pipe data are from Zagarola & Smits (1997) and turbulent boundary layer data are from Spalart (1988).

constant of 1.6 is based on the criterion that the end of the stress gradient balance layer is located where the ratio of the viscous to Reynolds stress gradients is less than -2 . This definition is somewhat arbitrary in a fashion similar to the definition of δ_{99} . Further discussion regarding the definition of this layer is given in the theoretical considerations below. A meso viscous/advection balance layer extends from $y^+ \cong 1.6 \times (\delta^+)^{1/2}$ to $y^+ \cong 2.6 \times (\delta^+)^{1/2}$. (The numerical constant, 2.6, is determined by the criterion that the stress gradient ratio at the end of this layer decreases below 0.5.) Beyond the end of the meso viscous/advection balance layer, at $y^+ \cong 2.6 \times (\delta^+)^{1/2}$, is the inertial/advection balance layer, whose thickness is about $\delta^+ - 2.6 \times (\delta^+)^{1/2}$.

Except for the inner viscous/advection balance layer, the extent of these layers depends significantly on Reynolds number. The Reynolds number dependence of the physical extent for each layer is shown in figure 5. Channel DNS data of Moser *et al.* (1999) and Superpipe data of Zagarola & Smits (1997) are used for the location of the end of the stress-gradient balance layer and the location of the end of the viscous/advection balance meso-layer. (The turbulent boundary layer data of DeGraaff & Eaton (2000) has been tried, but the second derivative of the mean profile and the derivative of Reynolds stress are noisy.) As is evident, all of the Reynolds number dependencies can be tied to the growth rate of the stress gradient balance layer thickness. For this reason, the thickness of this layer is identified as an important intermediate length since, like all similarity variables, it arises solely from the internal dynamics of the problem. Along with the outer and inner scales, δ and ν/u_τ respectively, the analyses below show that this mesoscale, $\sqrt{\nu\delta}/u_\tau$, is fundamental to the description of the mean flow.

As indicated in figure 5, the thickness of the inertial/advection balance layer is $\delta^+ - 2.6 \times (\delta^+)^{1/2}$, the ratio of this layer thickness to the total layer thickness, δ^+ , is then $1 - 2.6 \times (\delta^+)^{-1/2}$. This is illustrated in figure 6, which shows that the inertial/advection layer is an increasingly larger fraction of the entire boundary layer with increasing Reynolds number. For example, this layer constitutes about 95.2%, 99.1% and 99.7% of the boundary layer thickness at $\delta^+ \cong 3000$, $\delta^+ \cong 10^5$ and $\delta^+ \cong 10^6$ respectively. Figure 6 is a linear-linear plot. These axes were chosen to best illustrate the behavior of the inertial/advection layer at low to moderate Reynolds number. As the Reynolds number decreases, the ratio of the thickness of this layer to δ decreases rapidly. For example, the inertial/advection layer is about 74.0%, 81.6% and 88.3% of δ at $\delta^+ \cong 100$, $\delta^+ \cong 200$, $\delta^+ \cong 500$ respectively). These rapid changes at low Reynolds number are likely to correspond with other significant changes in boundary layer properties. In this regard, there is an increasing body of evidence (e.g., Klewicki (1989), DeGraaff & Eaton (2000)) that the scaling properties of turbulence quantities largely break down at sufficiently low but still fully turbulent Reynolds numbers. The

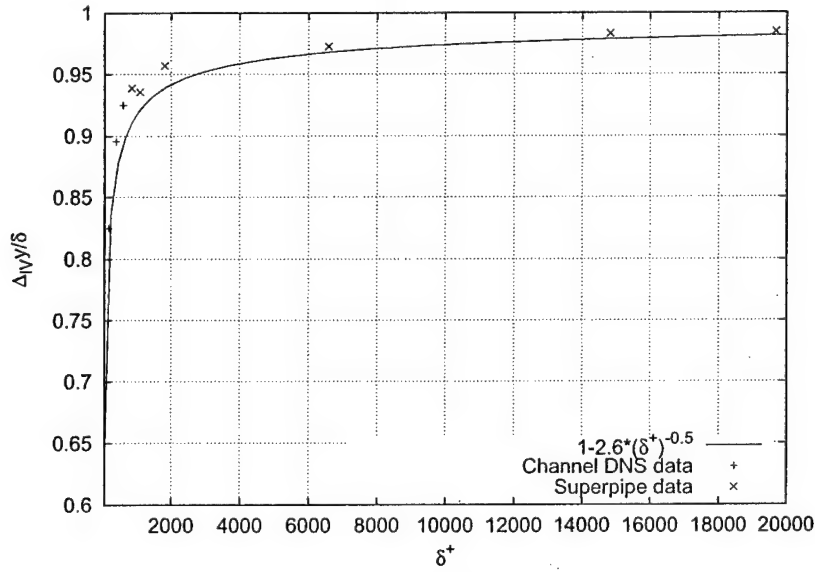


FIGURE 6. Reynolds number dependence of the ratio of the inertial/advection layer thickness to the boundary layer thickness. Note the Reynolds number on the abscissa is δ^+ . For reference, Re_θ for the zero pressure gradient turbulent boundary layer flow is typically about 3 ~ 4 times that of the corresponding δ^+ .

rapid change of scale effects of the inertial/advection balance layer may provide the underlying reason for these observations.

2.3. Velocity Increments

Owing to the fact that it is zero outside the boundary layer and non-zero inside the boundary layer, vorticity, and its wall-normal distribution, are particularly relevant measures of turbulent wall-flow structure. For a two dimensional flow in the (x, y) plane, the circulation, Γ , is a useful integral measure of the total mean z component vorticity present. In the case of the boundary layer (or half channel), it is easy to show that, per unit length, the circulation of the entire layer has a magnitude equaling the total velocity increment across the layer, i.e., $|\Gamma_{total}| = U_\infty$.

Given this, and for the purposes of better understanding the distribution of vorticity across the four balance layers (as well as the Reynolds number dependence of these distributions), the velocity increment across each balance layer was determined as a function of Reynolds number. These results are shown in figure 7. Under outer normalization, the velocity increment across the stress gradient balance layer is essentially constant, equaling about 50% of the total velocity increment. The velocity increment across the inertial/advection balance layer increases rapidly at low Reynolds number and then levels off to a slower rate of increase over the Reynolds number range shown. The initial rapid increase reflects the changes in the mean profile wake structure at low Re_θ . In contrast, the velocity increments across the inner and meso viscous/advection layers become a decreasingly small fraction of U_∞ with increasing Reynolds number. If the scalings discussed here for layers I, II, and III continue to hold for high Reynolds number, the velocity increment across layer IV will asymptotically approach 50% of U_∞ . On the other hand, inner normalization (not shown here) of the velocity increments across the inner and meso viscous/advection layers are essentially invariant with Reynolds number, equal to about $3u_\tau$ and $1u_\tau$ respectively. As expected, the inner normalized velocity increments across the stress gradient balance layer and inertial/advection layer increase like U_∞^+ . It is intriguing to note that while the meso viscous/inertial layer grows like $\sqrt{\delta^+}$ with increasing Reynolds number, its position in the layer is such that the inner normalized velocity increment across it remains essentially constant. Similarly, it is worth noting that the circulation of the stress gradient balance layer is apparently independent of Reynolds number, $0.5|\Gamma_{total}|$.

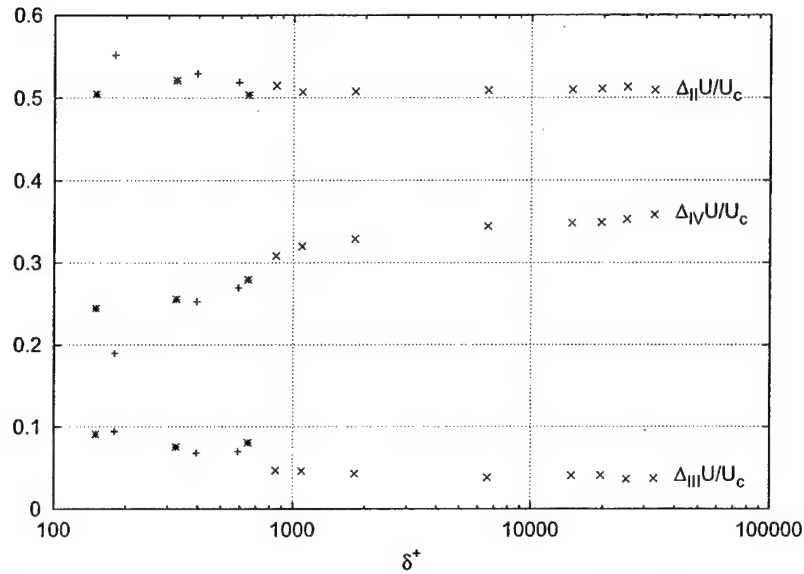


FIGURE 7. Outer normalized velocity increments across the layers as depicted in figure 4. + represents channel data of Moser *et al.* (1999), \times represents superpipe data of Zagarola & Smits (1997) and $*$ represents turbulent boundary layer data of Spalart (1988). $\Delta_{II}U$ is the velocity increment across the stress gradient balance layer, $\Delta_{III}U$ is the velocity increment across the meso viscous/advection balance layer and $\Delta_{IV}U$ is the velocity increment across the inertial/advection balance layer.

2.4. Data Summary

The above experimental results have a number of implications. Perhaps most important is that viscous effects are dynamically significant from the wall out to a (Reynolds number dependent) position beyond the peak in the Reynolds stress. At large but technologically relevant Reynolds numbers this position could be thousands of viscous units from the surface. Thus, the nearly universally held notion, e.g., Tennekes & Lumley (1972); Gad-el-Hak & Bandyopadhyay (1994); George & Castillo (1997); Pope (2000), that viscous effects are, in the mean, dynamically negligible outside the buffer layer ($y^+ \simeq 30$) is not supported by the relevant stress gradient data. The relevance of such viscous effects was an emphasis of the work of Sahay (1997). Coupled to this misconception is the commonly employed approximation that outside the buffer layer equation (2.1) is well represented by a balance between the pressure and Reynolds stress gradients, as is the misconception that the traditionally defined logarithmic layer (say $y^+ \geq 30$ to $y/\delta \leq 0.15$) is a zone of nominally zero Reynolds stress gradient, e.g., Wosnik *et al.* (2000). That is, the traditional logarithmic layer encompasses portions of layers II and IV and all of layer III. This provides a reason to rationally question the efficacy of the representation of the traditional logarithmic layer as the overlap region between an inner and outer layer, Millikan (1939). In fact, the empirical observations suggest the existence of a third, intermediate, dynamical length scale. These and a number of other related observations are given theoretical foundation by the analyses that follow.

3. Scale Analysis of Turbulent Channel Flow

Concepts of multiscale analysis are applied here to the problem of statistically stationary, fully developed turbulent flow in a two-dimensional channel. The reasoning employed corroborates and adds to the understanding of the four-layer structure revealed by the above data presentation. It is shown that the analysis is most properly done using three length scales, each appropriate to its own region.[†] The orders of magnitude of the widths of the scaling regions are given, as well as the governing equations in each of the regions and

[†] Work in progress Fife *et al.* (2004) shows that there is a hierarchy of length scales which serve to smoothly connect the inner, meso and outer scales. These results are forthcoming.

some qualitative features of the flow in each. The question of the merging of adjacent scaling domains is discussed. For completeness, some scaling results that are already well-known are included.

The discussion is systematic, relying only on the averaged momentum equation and as few other assumptions as possible. For example, one important assumption is that U^+ monotonically increases, and its gradient monotonically decreases from the wall to the centerline:

$$\frac{dU^+}{dy^+} > 0, \quad \frac{dU^+}{dy^+} \text{ decreases from 1 (at the wall) to 0 at the centerline and } U_c^+ \rightarrow \infty \text{ as } \delta^+ \rightarrow \infty, \quad (3.1)$$

where U_c^+ is the mean velocity at the centerline.

At this juncture it is worth putting this paper's approach in perspective with what will be called the *classical* approach. The classical approach purports to derive salient properties of the velocity and Reynolds stress profiles by means of the inner and outer scales alone. Based on the suggestion of Izakson (1937) and Millikan (1939) and exemplified by many later writers such as Afzal (1976, 1982, 1984a) and Panton (1990), whose work is possibly most completely expounded in Panton (2003) and Buschmann & Gad-el-Hak (2003), it is assumed, in the classical scenario, that an overlap region of the flow exists, in which the traditional outer and inner forms of the mean velocity profile are simultaneously valid. Incidentally, Gill (1968) rightly showed that at the very least, additional assumptions about the magnitude of the errors in these approximations are needed (such assumptions, as well as assumptions about the location of the overlap zone, would be difficult to validate in an a priori manner). If these estimates are valid, then matching derivatives in the overlap zone produces an equation whose solution for the velocity profile is either (a) $U^+ = \text{constant}$ or (b) U^+ grows logarithmically. Conclusion (a) is unacceptable, since it is known (3.1) that U^+ is a strictly increasing function of distance from the wall.

In the present paper, the mesolayer scaling is shown analytically to have the same legitimacy as the inner and outer scalings, in the sense that the mesolayer is shown theoretically to necessarily exist, by reasoning as valid as any theoretical basis for the traditional scalings. Given this, the classical, two layer, description would appear to constitute an incomplete framework for the problem. In addition, concerns arise about the derivation itself. A derivation, such as the classical one just described, should proceed in a logical manner from assumptions that are both credible and removed from the conclusion that is being derived. In this sense, it seems rational to question whether it is reasonable to assume the existence of an overlap zone in which the profile is not constant.

The motivation for this concern arises from two observations:

- Although the existence of overlap zones associated with two-scale problems in other fields and with mathematical examples is prevalent and well known, the profile is generally constant in the overlap zone.
- There are any number of functions with two scales which reduce to the given outer/inner forms in the outer/inner scaling domains, but do not have overlap zones nor logarithm profiles. In view of this, one must ask whether there is some natural physical reason why one should consider only profiles with overlap zones. This would be an interesting subject of further investigation. .

Therefore, while recognizing that many of the present results could be interpreted or corroborated on the basis of the logarithmic profile emerging from classical Millikan-type arguments, assumed valid in some appropriate region, it is felt that an alternative approach, which would serve as comparison and contrast with the classical one, is highly desirable. Regarding this point, it is also worth noting the lucid arguments of Sahay (1997) that advocate the benefits of a "first principles" approach not reliant on the overlapping layer hypothesis. Consistent with this, the derivations presented in this paper are totally independent of the classical train of thought.

3.1. Momentum Balance Properties in the Four Layers

In terms of the traditional **inner** variables y^+, U^+ , and $T^+ \equiv -\langle uv \rangle^+$, the conservation equation for streamwise momentum is

$$\frac{d^2 U^+}{dy^{+2}} + \frac{dT^+}{dy^+} + \epsilon^2 = 0, \quad (3.2)$$

where the small parameter $\epsilon = \frac{1}{\sqrt{\delta^+}}$, $\delta^+ = \frac{u\tau\delta}{\nu}$ is used so that $\epsilon \rightarrow 0$ as $Re \rightarrow \infty$. Associated with (3.2) are the boundary conditions

$$U^+ = T^+ = 0 \text{ and } \frac{dU^+}{dy^+} = 1 \text{ at } y^+ = 0. \quad (3.3)$$

The traditional **outer** variables are η, U^+, T^+ , where $\eta = \epsilon^2 y^+ = \frac{y}{\delta}$. (The centerline is at $y = \delta$.) Alternatively, the variable U^+ in this list is usually replaced by the defect velocity $U_c^+ - U^+$. Equation (3.2) becomes

$$\frac{dT^+}{d\eta} + 1 + \epsilon^2 \frac{d^2 U^+}{d\eta^2} = 0, \quad (3.4)$$

with boundary conditions

$$T^+ = \frac{dU^+}{d\eta} = 0 \text{ at } \eta = 1. \quad (3.5)$$

It will be shown from scaling arguments alone that an intermediate scaling with its layer (III) exists as well, thus corroborating the empirical finding described in the previous section. All this will result in three different forms for the momentum equation: (3.2), (3.4), and later (3.19).

Equation (3.2), while correct in all cases, is the most appropriate of the three forms of the momentum equation to use in regions where the two derivatives indicated there are $\leq O(1)$, and at least one is not small ($o(1)$). (Here and below, all order of magnitude relations are understood to hold as $\epsilon \rightarrow 0$, and the order symbols, O and o , take their established definitions, e.g., Kevorkian & Cole (1981), with the exception that a relation $a = O(1)$, say, means that both a and $\frac{1}{a}$ are bounded as $\epsilon \rightarrow 0$.) This is the case near the wall in layers I and II. When at least one of the first two terms in (3.2) is not small, i.e., of order $O(\epsilon^2)$, the third term in equation (3.2) may be neglected, leaving

$$\frac{d^2 U^+}{dy^{+2}} + \frac{dT^+}{dy^+} = 0. \quad (3.6)$$

Integrating with use of (3.3) yields

$$\frac{dU^+}{dy^+} + T^+ - 1 = 0. \quad (3.7)$$

Similarly in the region where the derivatives appearing in (3.4) are $\leq O(1)$ and $\frac{dT^+}{d\eta}$ is not small, such as near the midline $\eta = 1$, the $O(\epsilon^2)$ term in (3.4) may be neglected, leaving

$$\frac{dT^+}{d\eta} + 1 = 0, \quad (3.8)$$

and integrated to obtain

$$T^+(\eta) = 1 - \eta. \quad (3.9)$$

The solution $T^+(\eta)$ given by (3.9) approaches the limit 1 as $\eta \rightarrow 0$, instead of 0 as it should do according to (3.3). Thus there is a region near the wall where the stated condition on which the validity of (3.8) depends breaks down. In this wall layer, T^+ drops abruptly to 0 as $\eta \rightarrow 0$; the T^+ derivative in (3.4) then gets very large. From this one can surmise the known fact that T^+ attains a maximal value, say $T_m^+(\epsilon)$, near the wall. (The extra assumption that $\frac{d^2 U^+}{dy^{+2}}$, which is negative, increases towards 0, when applied to (3.2), would entail that T^+ has only a single maximum.) The value of y^+ at which $T^+ = T_m^+$ is designated by $y_m^+(\epsilon)$, and the corresponding value of η by $\eta_m(\epsilon) = \epsilon^2 y_m^+(\epsilon)$.

Although $T_m^+(\epsilon)$ and $y_m^+(\epsilon)$ are unknown at this point, certain general conclusions can be drawn about them. For one thing, $T_m^+ < 1$ since the outer solution (3.9) satisfies that inequality. And since mathematical boundary layers get thinner as the perturbation parameter approaches zero, the position $\eta_m(\epsilon) \rightarrow 0$ as $\epsilon \rightarrow 0$. Finally, another way of saying this is that the domain where the outer solution is valid expands towards the wall as $\epsilon \rightarrow 0$, i.e., (3.9) is valid for values of η in intervals $\eta_0(\epsilon) \leq \eta \leq 1$, where $\lim_{\epsilon \rightarrow 0} \eta_0(\epsilon) = 0$. Thus,

$$\lim_{\epsilon \rightarrow 0} T_m^+(\epsilon) = 1. \quad (3.10)$$

3.1.1. Layers I and II

These are where the inner variables are appropriate. Layer I is the viscous sublayer and layer II is where the viscous and Reynolds stress gradients are balanced. The viscous sublayer is where y^+ is so small (recall $T^+(0) = 0$) that $T^+(y^+) \cong 0$ is negligible. Then from (3.7) and (3.3),

$$U^+ \approx y^+. \quad (3.11)$$

Integrating (3.2) gives

$$\frac{dU^+}{dy^+} = 1 - T^+ - \epsilon^2 y^+. \quad (3.12)$$

The small ϵ^2 term is included here, because this equation will soon be used a little outside the formal range of validity of the approximate version (3.6), namely where layer II merges with layer III. As previously mentioned, when the last term in (3.12) is small (such as when $y^+ = O(1)$), it may be neglected. In any case, (3.12) shows how to find U^+ if the function $T^+(y^+)$ were known. It is, of course, unknown. But it was brought out before that $T^+(0) = 0$ and $T^+(y^+)$ increases to its maximum value $T_m^+(\epsilon)$ at $y^+ = y_m^+(\epsilon)$. By (3.10) the maximum falls just short of 1. It follows then from (3.12) that the gradient $\frac{dU^+}{dy^+}$ starts out being 1 at $y^+ = 0$, and decreases to a small value at $y_m^+(\epsilon)$, provided that $\epsilon^2 y_m^+(\epsilon) \ll 1$. This will be verified later. A function quantifying the deviation of T_m^+ from its upper limit of 1 is

$$\sigma(\epsilon) = 1 - T_m^+(\epsilon). \quad (3.13)$$

Although positive, it approaches 0 with ϵ . Further details regarding the order of magnitude of σ will be given later.

3.1.2. Layer III

This is the meso-layer containing $T_m(\epsilon)$; similar concepts have been described using different tools by others, e.g., Long & Chen (1981); Afzal (1982, 1984a); Sahay (1997); Sreenivasan & Sahay (1997); George & Castillo (1997). For example, Sahay combined empirical data and theoretical reasoning to study the scaling properties of the Reynolds stress profile, and hence velocity profile, near the location of its peak (Sahay (1997)). He presented strong evidence that a mesolayer exists, and noted that data indicate its location and characteristic lengths to be in agreement with what is found by purely theoretical methods in the present paper. For present purposes this layer may roughly be defined as where the approximations made above—replacing (3.2) by (3.6) and dropping the last term in (3.12)—are no longer valid, because the term dropped is no longer smaller (in order of magnitude) than both of the other two individual terms in those equations. The longer smaller of layer II may be described in the following way. For moderate values of y^+ outside layer I, the first two terms in (3.2) are each $O(1)$, and except for an $O(\epsilon^2)$ difference, they cancel each other. As y^+ increases, each of the first two terms decreases in magnitude; the second term does so because T^+ approaches its maximum, and therefore (3.2) itself forces the magnitude of the first term also to decrease. Eventually, $\frac{dT^+}{dy^+} = O(\epsilon^2)$, and by (3.2) $\left| \frac{d^2 U^+}{(dy^+)^2} \right| \leq O(\epsilon^2)$. To be more specific, albeit still arbitrary, let y_1^+ be the value of y^+ at which $\frac{d^2 U^+}{(dy^+)^2} = -2\epsilon^2$. A tentative definition for the transition point between layers II and III is this location $y_1^+(\epsilon)$, although in reality the boundary is not well defined. This choice corresponds to the definition given in section 2.2, i.e., the point where $\frac{d^2 U^+}{(dy^+)^2} / \frac{dT^+}{dy^+} = -2$.

The same may be done with (3.12). Again, for moderate values of y^+ , it represents an approximate balance between the quantities $\frac{dU^+}{dy^+}$ and $1 - T^+$, with error $\epsilon^2 y^+$. As y^+ increases, those two terms decrease and $\epsilon^2 y^+$ increases, until both $\frac{dU^+}{dy^+}$ and $1 - T^+$ are $\leq O(\epsilon^2 y^+)$. Again to be specific, let $y_2^+(\epsilon)$ be the location where $\frac{dU^+}{dy^+}(y_2^+) = 2\epsilon^2 y_2^+$; this is once more an arbitrary criterion. At that point, $1 - T^+ = 4\epsilon^2 y_2^+$ by (3.12).†

Two possible definitions for the transition point between layers II and III, found by similar constructions, are now given by $y_1^+(\epsilon)$ and $y_2^+(\epsilon)$. It is reasonable to expect that at least in order of magnitude, they are the same. This can be verified to be true in the typical case that $\frac{dU^+}{dy^+}$ asymptotically decays for large y^+

† The authors have discovered a more straightforward theoretical method to find the location of this and other layers, using a hierarchy of scales Fife *et al.* (2004).

| Re_τ | y_1^+ | y_2^+ | $y_1^+/\frac{1}{\epsilon}$ | $y_2^+/\frac{1}{\epsilon}$ |
|-----------|---------|---------|----------------------------|----------------------------|
| 180 | 25.1 | 20.2 | 1.88 | 1.51 |
| 395 | 31.7 | 26.2 | 1.60 | 1.32 |
| 590 | 36.7 | 30.5 | 1.51 | 1.26 |
| 850 | 44.3 | 35.8 | 1.52 | 1.23 |
| 2344.7 | 54 | 48.4 | 1.12 | 0.999 |
| 8486.3 | 79.6 | 80.5 | 0.864 | 0.873 |

TABLE 1. Locations of y_1 and y_2 . Data are from Moser *et al.* (1999) and Zagarola & Smits (1998).

according to a power law:

$$\frac{dU^+}{dy^+} \approx C(y^+)^{-m} \quad \text{for some } m > 0, C > 0, \quad (3.14)$$

with the corresponding relation holding after differentiation: $\frac{d^2U^+}{(dy^+)^2} \approx -mC(y^+)^{-m-1}$. For in this case, y_1^+ and y_2^+ are both $O(\epsilon^{-2/(m+1)})$. (Actually, the decay assumption here can be relaxed to hold only up to $y^+ = y_1^+(\epsilon)$, because a different scaling for the function U^+ will be used for greater y^+ .) It is also allowed that C depends on ϵ , as $C = C'\epsilon^\alpha$, where $\alpha < 2$. In addition, the experimentally and computationally determined values of the two numbers shown in table 1 give strong support to the expectation that $y_1^+ \approx y_2^+$ (they both are seen to be $O(1/\epsilon)$). The transition point is therefore specifically defined to be $y_1^+(\epsilon)$.

The location $y^+ = y_1^+$ was designated as the lower edge of layer III, and in an analogous fashion the location $y^+ = y_2^+$ where $\frac{d^2U^+}{(dy^+)^2} = -\frac{1}{3}\epsilon^2$ is defined to be the upper edge, because that corresponds to where $\frac{d^2U^+}{(dy^+)^2} / \frac{dT^+}{dy^+} = \frac{1}{2}$, as was done in the experimental data analysis in section 2.2.

At the transition point $y_1(\epsilon)$, each of the first two terms in (3.2) is $O(\epsilon^2)$, although their formal appearance in that equation does not indicate this fact. This is the beginning of layer III, and a rescaling will now be sought to better reflect the true orders of magnitude of the terms in (3.2). In fact, a scaling is possible that renders all three terms formally the same order of magnitude. In the process, additional information regarding $\sigma(\epsilon)$ and $T_m^+(\epsilon)$ will be revealed. The existence and scaling of a third layer was possibly first found by Afzal (1982, 1984a).

The rescaled y^+ and T^+ variables will be called \hat{y} and \hat{T} . Rescaling is most easily accomplished for the differentials dy^+ and dT^+ ; explicit expressions for the new variables, in terms of the old ones, will be derived later. With factors α and β to be determined (they will depend on ϵ), rescaling begins by setting

$$dy^+ = \alpha d\hat{y}, \quad dT^+ = \beta d\hat{T}. \quad (3.15)$$

This transforms the terms in (3.2) as follows

$$\frac{d^2U^+}{(dy^+)^2} = \frac{1}{\alpha^2} \frac{d^2U^+}{d\hat{y}^2}, \quad \frac{dT^+}{dy^+} = \frac{\beta}{\alpha} \frac{d\hat{T}}{d\hat{y}}. \quad (3.16)$$

The idea now is to assume that the derivatives on the right of (3.16), namely $\frac{d^2U^+}{d\hat{y}^2}$ and $\frac{d\hat{T}}{d\hat{y}}$, are $O(1)$ quantities. By the requirement established above, the orders of magnitude of both terms on the right, namely $\frac{1}{\alpha^2}$ and $\frac{\beta}{\alpha}$, must match (in order of magnitude) the third term in (3.2), namely ϵ^2 : $\alpha^{-2} = \beta/\alpha = \epsilon^2$. This is only possible if $\beta = \epsilon$, $\alpha = \epsilon^{-1}$. Thus from (3.15)

$$d\hat{y} = \epsilon dy^+, \quad d\hat{T} = \epsilon dT^+. \quad (3.17)$$

| Re_τ | $\frac{dU^+}{dy^+} _{y^+=\frac{2}{\epsilon}}$ | $(\frac{dU^+}{dy^+} _{y^+=\frac{2}{\epsilon}})/\epsilon$ |
|-----------|---|--|
| 180 | 0.135 | 1.802 |
| 395 | 0.066 | 1.307 |
| 590 | 0.050 | 1.211 |
| 850 | 0.035 | 1.029 |
| 2344.7 | 0.0191 | 0.927 |
| 8486.3 | 0.0126 | 1.156 |

TABLE 2. Experimentally determined $\frac{dU^+}{dy^+}$ values at $y^+ = \frac{2}{\epsilon}$ (inside the mesolayer, around peak Reynolds stress location). Data are from Moser *et al.* (1999) and Zagarola & Smits (1998).

Integrating (3.17) gives two integration constants, which are chosen to be y_m^+ and T_m^+ ; they will be the values of y^+ and T^+ where $\hat{y} = 0$ and $\hat{T} = 0$. The result is

$$y^+ = y_m^+ + \frac{1}{\epsilon}\hat{y}, \quad T^+ = T_m^+ + \epsilon\hat{T}. \quad (3.18)$$

Thus the scaling to be employed in layer III is now completely defined, along with its lower and upper edges $y_1^+(\epsilon)$ and $y_3^+(\epsilon)$. With the transformation (3.18), (3.2) becomes

$$\frac{d^2U^+}{d\hat{y}^2} + \frac{d\hat{T}}{d\hat{y}} + 1 = 0. \quad (3.19)$$

Now consider the balancing property of (3.12). As in the case of (3.2), it suffices at the transition point, $y^+ = y_2^+(\epsilon)$, to require that the three terms $\frac{dU^+}{dy^+}$, $(1 - T^+)$, $\epsilon^2 y_2^+$ in (3.12) have the same formal order of magnitude. Those orders can be calculated as follows. Since, by definition, \hat{y} and $\frac{dU^+}{d\hat{y}}$ are both $O(1)$ in layer III, it follows that $\left|\frac{dU^+}{dy^+}\right| = \epsilon \left|\frac{dU^+}{d\hat{y}}\right| = O(\epsilon)$. As for the second term in (3.12), write it as $1 - T^+ = (1 - T_m^+) + (T_m^+ - T^+) = \sigma - \epsilon\hat{T}$, so that since $\hat{T} \leq O(1)$, $1 - T^+ = O(\max[\sigma, \epsilon])$. And of course the last term is $\epsilon^2 y_2^+$. Equating the three orders of magnitude yields

$$\max[\sigma, \epsilon] = O(\epsilon), \quad \epsilon^2 y_2^+ = O(\epsilon). \quad (3.20)$$

This implies that

$$\sigma \leq O(\epsilon) \text{ and } y_2^+ = O(\epsilon^{-1}). \quad (3.21)$$

Setting $y^+ = y_m^+$ in (3.12) and using (3.1) gives

$$\sigma = 1 - T_m^+ = \frac{dU^+}{d\hat{y}}(y_m^+) + \epsilon^2 y_m^+(\epsilon) \geq O(\epsilon). \quad (3.22)$$

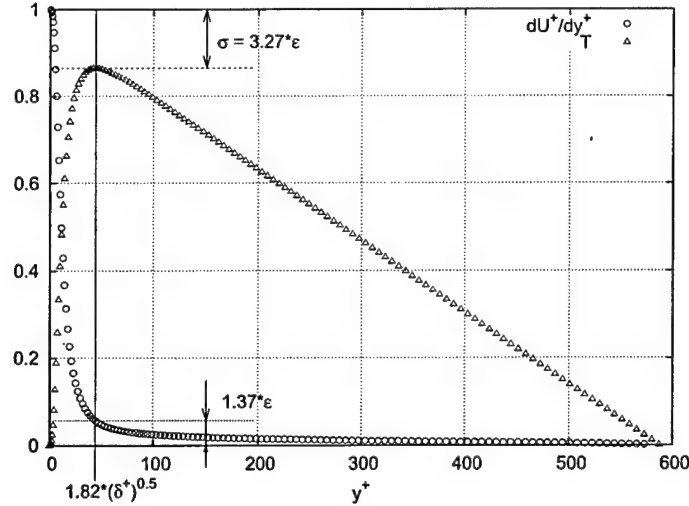
(An argument like this was also supplied in Sreenivasan & Sahay (1997).) Combining (3.22) with (3.21) gives

$$\sigma = O(\epsilon). \quad (3.23)$$

The data of table 3 and figure 8 support these theoretical predictions.

Throughout layer III, U^+ , \hat{T} and their derivatives are, to lowest order in ϵ , regular functions of the rescaled variable \hat{y} . To justify this assertion, consider that the momentum equation written in terms of \hat{y} , (3.19), has no ϵ -dependence, and on each end of layer III, i.e. at $y^+ = y_1^+$ and y_3^+ , each term of that equation is $O(1)$. In

| Re_τ | σ | ϵ | σ/ϵ |
|-----------|----------|------------|-------------------|
| 180 | 0.275 | 0.075 | 3.67 |
| 395 | 0.162 | 0.0505 | 3.21 |
| 590 | 0.135 | 0.0413 | 3.27 |
| 850 | 0.10 | 0.034 | 2.94 |
| 2344.7 | 0.061 | 0.0206 | 2.96 |
| 8486.3 | 0.0328 | 0.0109 | 3.01 |

TABLE 3. Experimentally determined σ values. Data are from Moser *et al.* (1999) and Zagarola & Smits (1998).FIGURE 8. Properties of viscous shear stress and Reynolds shear stress as compared to the present theory. In the mesolayer $\sigma = O(\epsilon)$ and $\frac{dU^+}{dy^+} = O(\epsilon)$. Data are from Moser *et al.* (1999) $Re_\tau = 590$.

fact, $\frac{d^2 U^+}{d\hat{y}^2} = -2$ at the lower end, and $= -\frac{1}{3}$ at the upper end. We take this to be conclusive evidence that those derivatives, and their derivatives in turn, remain $O(1)$ in III. The width of Layer III can now be found. It will be gauged by $\Delta\hat{y} = \hat{y}_3^+ - \hat{y}_1^+$ (corresponding to $y_3^+ - y_1^+$). The corresponding increment in $\frac{d^2 U^+}{d\hat{y}^2}$ is

$$\Delta \frac{d^2 U^+}{d\hat{y}^2} = -\frac{1}{3} - (-2) = \frac{5}{3}.$$

but for some value \hat{y}^* in layer III, the mean value theorem says that the left side $= \frac{d^3 U^+}{d\hat{y}^3}(\hat{y}^*)\Delta\hat{y}$, so that $\Delta\hat{y} = k$ where $k = \frac{5}{3} \left(\frac{d^3 U^+}{d\hat{y}^3} \right)^{-1}$. By differentiating (3.19) and using the data from figure 9, which shows that $\left| \frac{d^2 \hat{\tau}}{d\hat{y}^2} \right| = \left| \frac{d^3 U^+}{d\hat{y}^3} \right|$ is $O(1)$, one finds

$$\Delta\hat{y} = O(1). \quad (3.24)$$

Therefore the width of layer III $= O(1)$ in the variable \hat{y} , i.e. $O(1/\epsilon)$ in y^+ .

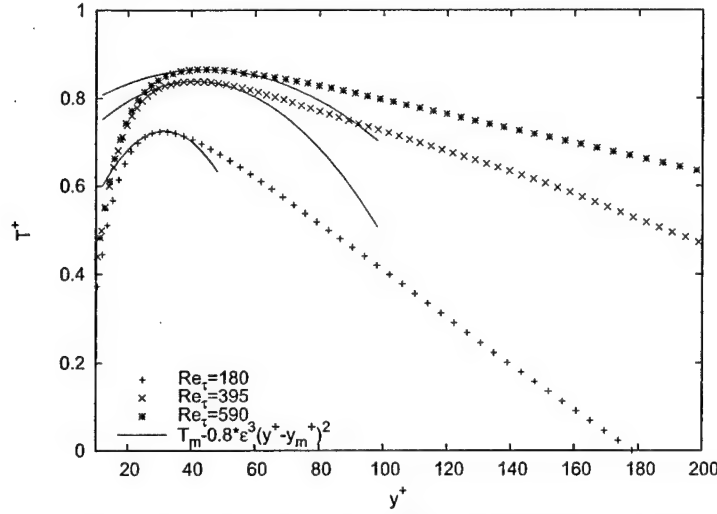


FIGURE 9. Reynolds stress around the peak, showing $\frac{d^2 T^+}{dy^{+2}} = O(\epsilon^3)$. Data are from Moser *et al.* (1999).

In summary, layer III is characterized in part by

$$|\hat{y}| = O(1), \quad y^+ = O(1/\epsilon), \quad \frac{dU^+}{dy^+} = O(\epsilon), \quad \frac{dT^+}{d\hat{y}} = O(1); \quad \text{the higher derivatives of } \frac{dU^+}{d\hat{y}} \text{ and } \hat{T} \text{ are } O(1). \quad (3.25)$$

3.1.3. Qualitative implications of the scaling in layer III

Since by definition $y_1^+(\epsilon)$ is the transition point between layers II and III, and layer I has width (in y^+) $O(1)$, the second part of (3.21) says that the width of layer II is $O(\epsilon^{-1})$. This is the first important consequence of the scaling in layer III. In connection with this it is relevant to note that this result of the analysis is in complete accord with the experimental data. The second important property of layer III comes from the fact (3.25) that $\frac{dU^+}{d\hat{y}} = O(1)$ in layer III, i.e. where $|\hat{y}| \leq O(1)$. Integrating across the layer, it is found that the velocity increment $\Delta_{III}U^+$ across the layer is an $O(1)$ quantity. The significance is that it is (approximately) independent of δ^+ , which is also in explicit agreement with the experimental observations.

A third qualitative effect in layer III concerns the pronounced flattening in the $T(y^+)$ profile near $T^+ = T_m^+$, as seen for example in Sreenivasan & Sahay (1997). This can be explained by measuring the curvature by the second derivative of the function T^+ . With the meso-scaling which has been seen to be appropriate in layer III, it follows that \hat{T} is a regular function of \hat{y} , so that in particular, it is expected that $\frac{d^2 \hat{T}}{(d\hat{y})^2} = O(1)$. In view of (3.17), this means that $\frac{d^2 T^+}{(dy^+)^2} = O(\epsilon^3)$ and $\frac{d^2 T^+}{d\hat{y}^2} = O(\epsilon)$. This is smaller (flatter) than one might anticipate. On the other hand, the second derivative with the respect to the outer variable η at $\eta = \eta_m$ is, as expected, large, so that the profile from the outer perspective is still sharply peaked. The flattening effect of T^+ near T_m^+ is explicitly shown to follow the predicted behavior in figure 9.

It is appropriate to reiterate an assumption which was made here in connection with the characterization of layer III. A scaling was found and an interval $[y_1^+, y_3^+]$ was found for which (1) an ϵ -independent differential equation (3.19) holds, expressing a balance between at least two kinds of scaled forces, and (2) the derivatives in (3.19) are verified to be $O(1)$ on each end of the interval (this latter condition is usually disregarded by other authors). It was then inferred that the physical quantities U^+ and \hat{T} do in fact satisfy (3.19) to lowest order, and that they and their higher derivatives are $O(1)$ within the interval. More generally, it is reasonable to relax condition (2) by requiring only that those derivatives be known to be $O(1)$ at one point; then the interval of validity of (3.19) is not known a priori, except that it is $\geq O(1)$ in the rescaled variable. The reason for the latter is that the higher derivatives are $O(1)$ in the scaling layer, so that it would take an increment in $\hat{y} \geq O(1)$ for the terms in (3.19) to deviate from being $O(1)$. Therefore the width of the layer

must be at least that large. In the present example, $\frac{d^2 \hat{T}}{d\hat{y}^2} = O(1)$, as indicated above. These criteria for establishing a scaling layer constitute an important ingredient of our analysis, and, significantly, are exactly the same criteria used to establish the valid domains for the classical inner/outer scales.

3.1.4. Merging Layers III and IV

There is a transparent matching of T^+ as we proceed into layer IV. In fact in view of (3.10),

$$d\eta = \epsilon^2 dy^+ = \epsilon d\hat{y}, \quad dT^+ = \epsilon d\hat{T},$$

so that

$$\frac{d\hat{T}}{d\hat{y}} = \frac{dT^+}{d\eta}. \quad (3.26)$$

The middle term in (3.19) is therefore the same as the first in (3.4) and (3.8). Thus, under the simple assumption that $\frac{d^2 U^+}{d\hat{y}^2} \rightarrow 0$ as $\hat{y} \rightarrow \infty$, the meso equation (3.19) will approach the outer equation (3.8). This says that the derivatives of T^+ match automatically as one passes from layer III to IV.

The behavior of U^+ is a more complex issue. So far, the only relevant assumption is (3.1). Note that (3.1) was written in terms of the variable y^+ , but it holds also for \hat{y} and η . The simplest way to model the behavior (3.1) (in the variable \hat{y}) is by a power law, say $U^+(\hat{y}) \approx A \hat{y}^\alpha + B$ as $\hat{y} \rightarrow \infty$. The requirements (3.1) compel $0 < \alpha < 1$. Another possibility is a log law: $U^+(\hat{y}) \approx A \ln \hat{y} + B$ as $\hat{y} \rightarrow \infty$. Arguments have been made in the past to support one or the other of these forms; these arguments will not be reviewed here.

The boundary condition (3.5), however, dictates that some modification be made near $\eta = 1$, (i.e., in the wake region). This should be done so that U^+ is smooth and even about the centerline. There are many possibilities. These will not be explored herein.

3.2. Increments in U^+

In layers I and II, $\frac{dU^+}{dy^+}$ starts off with the value 1 at $y^+ = 0$ and, according to (3.25), decreases to $O(\epsilon)$ at $y^+ = O(1/\epsilon)$,

$$\left. \frac{dU^+}{dy^+} \right|_{y^+=\frac{1}{\epsilon}} = O(\epsilon). \quad (3.27)$$

Given this, important questions are, what might be the rate of this decrease, and how does the rate effect the value of U^+ at $y^+ = O(1/\epsilon)$ and the increment $\Delta_{II} U^+$ across layer II? It is natural to propose that $\frac{dU^+}{dy^+}$ decays according to a power law for large y^+ , as in (3.14). The requirement (3.27) says that $C = O(\epsilon^{1-m})$, so set $C = C' \epsilon^{1-m}$. Among these power laws, the simplest is when $m = 1$, so that

$$\frac{dU^+}{dy^+} \approx \frac{C}{y^+}; \quad (3.28)$$

in fact this is the only case in which there is no ϵ -dependence on the right. This case results in a logarithmic law for sufficiently large values of y^+ in layer II

$$U^+(y^+) \approx C \ln y^+ + D. \quad (3.29)$$

The associated velocity increment is given by

$$\Delta_{II} U^+ \approx U^+(1/\epsilon) \approx C |\ln \epsilon| + D, \quad (3.30)$$

which is unbounded as $\epsilon \rightarrow 0$.

Another point is that the choice $m = 1$ coincides with the assumption that the **law of the wall**, i.e. that U^+ depends (to lowest order as $\epsilon \rightarrow 0$) only on y^+ , holds not only for $y^+ = O(1)$, but also for a range of values of y^+ larger than $O(1)$, namely for $y^+ \leq O(1/\epsilon)$. This kind of assumption would be reminiscent of, but not the same as, the classical overlap assumption. More importantly, the possibility of $m \neq 1$ can also be tested, but integration yields the conclusion that if $m \neq 1$, $\Delta_{II} U^+$ is bounded independently of ϵ . This contradicts the velocity increment data which indicates that $\Delta_{II} U/U_c \cong 0.5$, independent of δ^+ . Thus only in the logarithmic case does U^+ grow unboundedly at the end of layer II as $\epsilon \rightarrow 0$. Therefore, several arguments can be given to support the claim that (3.29) is valid for large y^+ . Work in progress Fife, Wei,

Klewicky & McMurtry (2004) points to the existence of a hierarchy of scalings appropriate to the transition zone from II to III; in turn, this hierarchy implies (3.29) and provides still another strong argument in favor of it.

Analogous considerations may apply in part to the transition from III to IV and the increment $\Delta_{IV}U^+$, although that situation is much less clear, as was brought out in section 3.1.4. One replaces y^+ by \hat{y} . In this case, however, one does not set $\frac{dU^+}{d\hat{y}} = O(\epsilon)$ at the end of the zone, and as a result the velocity increment in this transition process always grows as $\epsilon \rightarrow 0$. This, of course, is in accord with the experimental observations. Furthermore, the deviation from a logarithmic-like dependence in the wake region can be excluded from the transition zone; doing so does not effect the unbounded behavior of $\Delta_{IV}U^+$ as $\epsilon \rightarrow 0$. Given that $\frac{dU^+}{d\hat{y}}$ decays asymptotically according to a power law (while not necessarily exactly equal to a power function), the requirement that this latter increment, divided by $\Delta_{II}U^+$, be $O(1)$ (as prescribed by the experimental data), demands a logarithmic dependence in the mean profile both in the upper part of layer II (transition zone to layer III) and in the lower part of layer IV (transition from layer III).

4. Discussion

The results presented herein have a number of physical and theoretical implications, some of which are now discussed.

4.1. Physical Implications

A picture of boundary layer structure is revealed that provides a different perspective to the predominant view held in the literature, e.g., Townsend (1976), Monin & Yaglom (1971), Hinze (1975), Tennekes & Lumley (1972), Panton (1990, 1997, 2003), Pope (2000). That is, the traditional thought on turbulent wall layer structure is that viscous forces are significant only in the near-wall region (i.e., buffer layer and below) Gad-el-Hak & Bandyopadhyay (1994). Outside of this near-wall region it is assumed that viscous forces play a negligible role. This is believed to underlie the Reynolds number similarity for the law of the wall, as well as the characterization of the logarithmic layer as an inertial sublayer in physical space (e.g., Tennekes & Lumley (1972)). From this, turbulent wall layers are usually divided into the four regions of the mean velocity profile, i.e., the viscous sublayer, buffer layer, log-layer and wake layer mentioned in the Introduction.

The traditional picture is primarily supported by the properties of the stress field and the mean velocity profile. As is widely known, the viscous stress is high very near the wall. At $y^+ \cong 10$, however, the viscous and Reynolds stress are approximately equal, and by $y^+ \cong 30$ the viscous stress is only about 10% of the Reynolds stress. Farther from the wall the viscous stress becomes an even smaller fraction. However, it is the gradients of these stresses that are the relevant dynamical quantities. Considering this, the traditional interpretation of turbulent wall-flows is deemed inappropriate for educing the correct time averaged dynamics.

The present results indicate that the inner viscous/pressure gradient layer structure in channels is different from the inner viscous/advection layer in boundary layers. That is, at the channel wall the viscous stress gradient balances the pressure gradient (so it is not the only significant term in the momentum balance equation), and there is an associated flux of vorticity from the surface. In the zero pressure gradient boundary layer, however, all of the terms in the mean momentum equation are zero at the wall, and there is no net flux of vorticity. The influence of these differences can be seen by expanding the near-wall region of the stress gradient ratio profiles in figures 1 and 3. When this is done, it becomes apparent that in the channel the viscous/advection layer is thicker at low Reynolds number, and that the ratio of -1 in the stress gradient balance layer is approached asymptotically, likely owing to the net diminishing effect of the diffusive surface flux of vorticity. In the boundary layer, however, the value of this ratio is apparently -1 even at very low Reynolds number.

Also significant are modifications to the interpretation of logarithmic layer structure. As mentioned previously, the commonly held interpretation of the logarithmic layer as constituting an inertial subrange in physical space requires revision. That is, since viscous effects are significant in both the stress gradient balance layer and the meso viscous/advection layer, only the outer portion of the logarithmic layer (i.e., the portion that adjoins with the inertial/advection layer) might rationally be considered an inertial sublayer. Given this, characteristics of logarithmic layer turbulence are also likely to change depending on the force balance layer from which it is sampled. The present results also provide evidence that characterization of the logarithmic

layer as a simple overlap layer is inappropriate. In connection with this it is instructive to note the recent observations of Osterlund *et al.* (1999). Specifically, while they assert that there is no significant Reynolds number dependence for the classical logarithmic relation, they do point out that a viscous influence exists in an extended “buffer region” to $y^+ \cong 200$, instead of the more traditionally held value of $y^+ \cong 50$. Their experiments, however, ranged from $Re_\theta = 2500$ to 27000 . Given this, the present results indicate that the stress gradient balance layer extends to about $y^+ \cong 40$ followed by a meso viscous/advection layer extending to about $y^+ \cong 66$ for their lowest Reynolds number. For their highest Reynolds number, $Re_\theta \cong 27000$, the stress gradient balance layer extends to about $y^+ \cong 120$ followed by the meso viscous/advection layer out to about $y^+ \cong 203$. Similar empirically-based conjectures have been made regarding the existence of two distinct logarithmic/power law-like scaling regions in pipe and channel flow, Zagarola & Smits (1998), Wosnik *et al.* (2000) and Afzal (2001*a,b*). The present results provide a physical explanation for these observations.

Across the meso viscous/advection layer the Reynolds stress gradient changes sign. This indicates that turbulent inertia shifts from a net momentum source for $y < y_m$ to a net momentum sink for $y > y_m$. For this reason, it is likely that the significant inner/outer interactions occur across the meso viscous/advection layer. Similarly, the re-emergence of mean advection effects in the inner viscous/advection layer are likely associated with the recent observations of Metzger & Klewicki (2001) indicating that low frequency motions are prevalent at high Reynolds number even very near the wall, as well as the successful scaling of the near-wall axial stress using the mixed velocity scale, $\sqrt{U_\infty u_\tau}$, as found by DeGraaff & Eaton (2000).

Regarding flow physics, it is also worth noting that the present findings hold considerable promise in classifying and/or characterizing non-canonical boundary layer flows. That is, non-equilibrium effects (associated with, for example, pressure gradients and/or added strain rates) are likely to be clearly reflected in deviations from the force balance layer structure depicted herein. Similarly, since surface roughness imposes external length scales within the flow, the relation between these imposed scales and the thickness of the stress gradient balance layer thickness is likely to be a significant measure of roughness influences, as well as the Reynolds number dependence of roughness effects.

4.2. Theoretical Implications

Unlike more familiar multiscale analyses, the present one is not amenable to a full-blown matched asymptotics, such as where matching conditions lead to boundary conditions at ∞ or at 0 , and are used to determine inner and outer solutions uniquely. The differential equations in this case are underdetermined, and thus cannot be used to obtain a unique solution for the mean velocity. Nevertheless, considerable qualitative information about these unknown solutions was extracted. Since this information directly reflects the behaviors of the mean momentum balance, it is felt to be particularly useful in assessing the viability of proposed analytical/approximate formulas for the mean velocity profile. That is, the mathematical properties derived herein comprise a set of criteria that any candidate mean velocity profile equation (e.g., once inserted in the mean momentum balance) must satisfy. In connection with this, it is important to note that at least some of these criteria are rather robust relative to the inherent capabilities of experimental data. For example, the analysis in section (3.2) indicated that effectively distinguishing between a power or logarithmic form for the mean profile required determining whether $\Delta_{II}U^+$ remained $O(1)$ or undergoes an unbounded increase with increasing Reynolds number. Such a distinction is considerably more attainable with experimental measurements than via use of the $y^+(dU^+/dy^+)$ and $(y^+/U^+)(dU^+/dy^+)$ indicator functions mentioned in the Introduction.

The present analysis provides a theoretical justification for the intermediate boundary layer length scale empirically identified via examination of the stress gradient ratios. This intermediate meso-scale, $l_m = \sqrt{\nu\delta/u_\tau}$, follows directly from the layer III rescaling given in section (3.1.2). Note that this rescaling was formally derived and is required to render all the terms in the mean momentum balance formally of the same magnitude in layer III. Simply stated, l_m has the same theoretical relevance as either the inner scale, $l_i = \nu/u_\tau$, or the outer scale, $l_o = \delta$. Note further that normalization of wall normal distance by l_m yields $\sqrt{y^2}/\sqrt{\nu\delta/u_\tau} = \sqrt{\eta y^+}$. This is both \hat{y} (as measured relative to y_m) and the geometric mean of the inner and outer normalized distance from the wall. Regarding the former, it is apparent that given any two of the three length scales, the third may be determined. Regarding the latter, it would seem that geometric mean (intermediate or mixed) scalings, often empirically identified as being superior to either inner or outer scalings, Alfredsson & Johansson (1984); Afzal (1984*b*); Klewicki & Falco (1996); DeGraaff & Eaton (2000);

Priyadarshana & Klewicki (2003); Metzger *et al.* (2003), but just as often discounted owing to their purported lack of physical significance or theoretical justification, e.g., Gad-el-Hak & Bandyopadhyay (1994), are worthy of continuing investigation.

Lastly, the current work provides a unifying context for several previous boundary layer observations and analyses that have identified 'intermediate' (Afzal (1982), Sahay (1997)), 'critical' (Sreenivasan & Sahay (1997)), and 'meso'-layers (Long & Chen (1981)). Each of these identify an important region around the peak in the Reynolds stress that scales with mixed variables. The analysis and empirical observations of Sahay (1997); Sreenivasan & Sahay (1997) focused on the viscous stress gradient-Reynolds stress gradient ratio in the vicinity of the peak in the Reynolds stress, with an emphasis of the importance of viscous effects in this region. Afzal (1982) developed a scaling for an intermediate layer around the peak in the Reynolds stress (which he subsequently used to match with both the inner and outer layer using classical overlap ideas) by assuming all terms in the 'once-integrated' momentum equation are of the same order in this region. This resulted in the intermediate scalings developed here in section 3.1.2. In each of these works, the intermediate layer identified is essentially the mesolayer (layer III) discussed in this work with its dynamical relevance revealed by the examination of the stress gradient data in figures. 1-3 herein. The present work expands upon these earlier works by revealing (1) the existence of the stress gradient balance region (layer II), in which viscous effects are important at all y^+ up to a point beyond the peak in the Reynolds stress (and not simply in the vicinity of this peak), and (2) by revealing the mathematical requirement for the intermediate length to adequately describe the scaling behavior of the mean momentum balance.

5. Conclusions

The time-mean differential momentum equation for canonical turbulent wall flows indicates that stress gradients are the appropriate quantities to examine for educing dynamics. Given this, available premier quality experimental data and DNS simulations were used to reveal the properties and Reynolds number dependence of the mean structure of boundary layer, pipe and channel flows. A four layer structure of these canonical wall flows was revealed. The dynamical structure of each layer was described and the Reynolds number dependent properties of the thickness and circulation of each layer quantified. From this analysis, a Reynolds number dependent, intermediate length scale for turbulent wall flows was identified. This length scale arises directly from the internal dynamics and characterizes the thickness of the viscous-inertial stress gradient balance layer. The present view of wall flow structure is in contrast to the established and pervasive view. The present picture of mean dynamics is directly founded in the mean statement of Newton's second law for turbulent wall layers.

To complement these empirical observations, a multiscale analysis of the properties of the mean momentum balance in statistically stationary, fully developed, turbulent channel flow has been developed. The analysis employed minimal assumptions beyond the averaged momentum equation itself, an example being that the mean velocity monotonically increases from the wall to the channel centerline. With this, all properties and Reynolds number scalings shown empirically were derived in a systematic manner. Three different scalings (inner, outer and meso) were shown to be relevant, each in their own region, with the regions characterized by Reynolds number dependent intervals of distance from the wall. Specific mathematical properties and scaling behaviors of the mean streamwise velocity, Reynolds stress and their wall-normal gradients were derived for each of the domains, and, in each case, were shown to be in full agreement with channel flow DNS and Princeton Superpipe data. These properties include the physical extent and Reynolds number dependent scaling of the layer thicknesses, a flattening of the Reynolds stress profile near its maximum, the mean velocity increment across each layer, the rate of decay of the mean velocity gradient (especially in the stress gradient balance layer), the asymptotic rate of increase of the peak value of the Reynolds stress, as well as compelling evidence for the logarithmic character of the mean profile in two distinct regions of the flow.

This work was supported by the U. S. Department of Energy through the *Center for the Simulation of Accidental Fires and Explosions* under grant W-7405-ENG-48, the National Science Foundation under grant CTS-0120061 (grant monitor, M. Plesniak), and the Office of Naval Research under grant N00014-00-1-0753 (grant monitor, R. Joslin). Thanks are extended to Drs. Moser, Kim and Mansour, Zagarola and Smits,

Spalart, DeGraaff and Eaton for putting their data on the web for public use. We would also like to thank Dr. McKeon for providing her superpipe data.

REFERENCES

- AFZAL, N. 1976 Millikan's argument at moderately large Reynolds number. *Physics of Fluids* **19**, 600–602.
- AFZAL, N. 1982 Fully developed turbulent flow in a pipe: an intermediate layer. *Ingenieur-Archiv* **52**, 355–377.
- AFZAL, N. 1984a Mesolayer theory for turbulent flows. *AIAA J.* **22**, 437–439.
- AFZAL, N. 1984b Periods between bursting in turbulent shear flow: Intermediate layer. *CURRENT SCIENCE* **53**, 640–642.
- AFZAL, N. 2001a Power law and log law velocity profiles in fully developed turbulent boundary layer flow: equivalent relations at large Reynolds number. *ACTA Mechanica* **151**, 195–216.
- AFZAL, N. 2001b Power law and log law velocity profiles in fully developed turbulent pipe flow: equivalent relations at large Reynolds number. *ACTA Mechanica* **151**, 171–183.
- ALFREDSSON, P. H. & JOHANSSON, A. V. 1984 Time scales in turbulent channel flow. *Phys. Fluids* **27** (8), 1974–1981.
- BARENBLATT, G. I., CHORIN, A. & PROSTOKISHIN, V. M. 1997 Scaling laws for fully developed flow in pipes. *Appl. Mech. Rev.* **50**, 413–429.
- BUSCHMANN, M. H. & GAD-EL-HAK, M. 2003 Debate concerning the mean-velocity profile of a turbulent boundary layer. *AIAA J.* **41**, 565–572.
- CENEDESE, A., ROMANO, G. P. & ANTONIA, R. A. 1998 A comment on the “linear” law of the wall for fully developed turbulent channel flow. *Experiments in Fluids* **25**, 165–170.
- DEGRAAFF, D. B. & EATON, J. K. 2000 Reynolds-number scaling of the flat-plate turbulent boundary layer. *J. Fluid Mech.* **422**, 319–346.
- FIFE, P., WEI, T., KLEWICKI, J. & MCMURTRY, P. 2004 Stress gradient balance layers and scale hierarchies in wall-bounded turbulent flows. *J. Fluid Mech.* Under review.
- GAD-EL-HAK, M. & BANDYOPADHYAY, P. R. 1994 Reynolds number effects in wall-bounded turbulent flows. *Appl. Mech. Rev.* **47** (8), 307–365.
- GEORGE, W. K. & CASTILLO, L. 1997 Zero-pressure-gradient turbulent boundary layer. *Appl. Mech. Rev.* **50** (12), 689–729.
- GILL, A. E. 1968 The Reynolds number similarity argument. *Journal of mathematics and physics* **47**, 437–441.
- HINZE, J. O. 1975 *Turbulence*, 2nd edn. McGraw-Hill, New York.
- IZAKSON, A. 1937 On the formula for the velocity distribution near walls. *Technical Physics of the U. S. S. R.* **IV**, 2, 155–162.
- KEVORKIAN, J. & COLE, J. D. 1981 *Perturbation Methods in Applied Mathematics*. Springer Verlag.
- KLEWICKI, J. C. 1989 On the interactions between the inner and outer region motions in turbulent boundary layers. PhD thesis, Michigan State University.
- KLEWICKI, J. C. & FALCO, R. E. 1996 Spanwise vorticity structure in turbulent boundary layer. *International Journal of Heat and Fluid Flow* **17**, 363–376.
- LIGHTHILL, M. J. 1963 *Laminar boundary layers* (ed. L. Rosenhead), chap. ii. Clarendon Press, Oxford.
- LONG, R. R. & CHEN, T.-C. 1981 Experimental evidence for the existence of the mesolayer in turbulent systems. *J. Fluid Mech.* **105**, 19–59.
- MCKEON, B. J., LI, J., JIANG, W., MORRISON, J. F. & SMITS, A. J. 2003 Pitot probe corrections in fully developed turbulent pipe flow. *Measurement Science and Technology* **14**, 1449–1458.
- METZGER, M. M. & KLEWICKI, J. C. 2001 A comparative study of near-wall turbulence in high and low Reynolds number boundary layers. *Physics of Fluids* **13**, 692–701.
- METZGER, M. M., KLEWICKI, J. C. & PRIYADARSHANA, P. A. 2003 Reynolds number dependence in the behavior of boundary layer axial stress and scalar variance transport. In *Reynolds Number Scaling in Turbulent Flow* (ed. A. J. Smits), pp. 83–88. Kluwer Academic Publishers.
- MILLIKAN, C. B. 1939 A critical discussion of turbulent flows in channel and circular tubes. In *Proceedings of the Fifth International Congress of applied Mechanics* (ed. J. P. D. Hartog & H. Peters), pp. 386–392. Wiley, New York.
- MONIN, A. S. & YAGLOM, A. M. 1971 *Statistical Fluid Mechanics*, 1st edn. MIT Press.
- MOSER, R. D., KIM, J. & MANSOUR, N. N. 1999 Direct numerical simulation of turbulent channel flow up to $Re_\tau = 590$. *Physics of Fluids* **11** (4), 943–945.
- OSTERLUND, J. M., JOHANSSON, A. V., NAGIB, H. M. & HITES, M. H. 1999 Wall shear stress measurements in high Reynolds number boundary layers from two facilities. In *30th AIAA Fluid Dynamics Conference*. Norfolk, VA.
- PANTON, R. L. 1990 Scaling turbulent wall layers. *Journal of Fluids Engineering* **112**, 425–432.
- PANTON, R. L. 1997 A Reynolds stress function for wall layers. *Journal of Fluids Engineering* **119**, 325–330.

- PANTON, R. L. 2002 Evaluation of the Barenblatt-Chorin-Prostokishin power law for turbulent boundary layers. *Physics of Fluids* **14**, 1806–1808.
- PANTON, R. L. 2003 Wall turbulence described by composite expansions. Preprint.
- PERRY, A. E., HAFEZ, S. & CHONG, M. S. 2001 A possible reinterpretation of the Princeton superpipe data. *J. Fluid Mech.* **439**, 395–401.
- POPE, S. B. 2000 *Turbulent Flow*, 1st edn. Cambridge University Press.
- PRIYADARSHANA, P. A. & KLEWICKI, J. C. 2003 Reynolds number scaling of wall layer velocity-vorticity products. In *Reynolds Number Scaling in Turbulent Flow* (ed. A. J. Smits), pp. 117–122. Kluwer Academic Publishers.
- SAHAY, A. 1997 The Mean Velocity And The Reynolds Shear Stress In Turbulent Channel And Pipe Flow. PhD thesis, Yale University, <http://wwwlib.umi.com/dissertations>.
- SPALART, P. R. 1988 Direct simulation of a turbulent boundary layer up to $Re_\theta = 1410$. *J. Fluid Mech.* **187**, 61–98.
- SREENIVASAN, K. R. & SAHAY, A. 1997 The persistence of viscous effects in the overlap region, and the mean velocity in turbulent pipe and channel flows. In *Self-Sustaining Mechanisms of Wall Turbulence* (ed. R. Panton), pp. 253–272. Computational Mechanics Publications, Southampton, U.K.
- TENNEKES, H. & LUMLEY, J. L. 1972 *First Course in Turbulence*, 1st edn. MIT Press.
- TOWNSEND, A. A. 1976 *The Structure of Turbulent Shear Flow*, 2nd edn. Cambridge University Press, Cambridge, Great Britain.
- WILLMARTH, W. W. 1975 Structure of turbulence in boundary layers. *Adv. Appl. Mech.* **15**, 159–254.
- WOSNIK, M., CASTILLO, L. & GEORGE, W. K. 2000 A theory for turbulent pipe and channel flow. *J. Fluid Mech.* **421**, 115–145.
- ZAGAROLA, M. V. & SMITS, A. J. 1997 Scaling of the mean velocity profile for turbulent pipe flow. *Physical Review Letters* **78** (1), 239–242.
- ZAGAROLA, M. V. & SMITS, A. J. 1998 Mean-flow scaling of turbulent pipe flow. *J. Fluid Mech.* **373**, 33–79.
- ZANOUN, E., NAGIB, H., DURST, F. & MONKEWITZ, P. 2002 Higher Reynolds number channel data and their comparison to recent asymptotic theory (Invited). *AIAA paper* 2002–1102.

Stress gradient balance layers and scale hierarchies in wall-bounded turbulent flows

By P. FIFE¹, T. WEI², J. KLEWICKI² AND P. McMURTRY²

¹ Department of Mathematics

² Department of Mechanical Engineering

University of Utah, Salt Lake City, UT 84112

(Received 23 March 2004)

Steady Couette and pressure driven turbulent channel flows have large regions in which the gradients of the viscous and Reynolds stresses are approximately in balance (stress gradient balance regions) Wei *et al.* (2004). In the case of Couette flow, this region occupies the entire channel. Moreover, the relevant features of pressure driven channel flow throughout the channel can be obtained from those of Couette flow by a simple transformation. It is shown that stress gradient balance regions are characterized by an intrinsic hierarchy of “scaling layers” (analogous to the inner and outer domains), filling out the stress gradient balance region except for locations near the wall. The spatial extent of each scaling layer is found asymptotically to be proportional to its distance from the wall.

There is a rigorous connection between the scaling hierarchy and the mean velocity profile. This connection is through a certain function $A(y^+)$ defined in terms of the hierarchy, which remains $O(1)$ for all y^+ . The mean velocity satisfies an exact logarithmic growth law in an interval of the hierarchy if and only if A is constant. Although A is generally not constant in any such interval, it is arguably almost constant under certain circumstances in some regions. These results are obtained completely independently of classical inner/outer/overlap scaling arguments, which require more restrictive assumptions.

A discussion is given concerning possible physical implications of these theoretical results.

1. Introduction

Boundary layer and pressure driven or shear driven channel flows transition to turbulence at sufficiently high Reynolds numbers.† Within the turbulent regime, numerous empirical observations, e.g., Gad-el-Hak & Bandyopadhyay (1994), indicate that many of the statistical properties of these flows are similar, even though they possess different driving mechanisms. This apparent statistical similarity supports claims for an underlying similarity in the dynamical structure of the turbulence as well. In the case of pressure and shear driven turbulent flows, structural similarity will be one of the themes in this paper.

Theoretical approaches to the description of the mean velocity profile in both shear and pressure driven flows often start by assuming the physical properties of the flow are captured by a mathematical structure composed of functions formally describing behavior in two separate scaling regions—the inner, where the law of the wall holds, and the outer, where the defect law governs the flow. Subsequent analyses (classical and modern) employing this mathematical framework then typically propose the existence of a region of *overlap* between these inner and outer functions. Such methodologies have their origin in the work of Izakson (1937) and Millikan (1939). (Gill (1968) rightly showed that in addition to assuming the existence of an overlap region, one must assume appropriate maximal rates of growth, as the outer variable approaches 0, of the discrepancy between the outer approximation and the true solution, and similarly with the inner approximation as that variable approaches ∞ .)

For the mean velocity profile, the so-called overlap layer is traditionally handled by matching the velocity gradient, as simultaneously represented by the inner and outer functions, e.g. Tennekes & Lumley (1972). In this way a logarithmic velocity profile is obtained. The logic of this procedure is hampered, firstly, by the fact that while generic prototypical two-scale problems with an overlap region arising in other contexts lead to the solution being constant in the overlap domain, such constancy in the present case is not acceptable. It is indispensable that the mean velocity profile be a strictly increasing function of distance from the wall. Secondly, it is straightforward to construct quite arbitrary mathematical functions with inner and outer

† This paper will primarily employ the so-called Karman number, $\delta^+ = \delta u_\tau / \nu$, where δ is the boundary layer thickness or channel half-height, ν is the kinematic viscosity, u_τ is the friction velocity ($\equiv \sqrt{\tau_{wall}/\rho_m}$), τ_{wall} is the surface shear stress, and ρ_m mass density.

scaling regions in which the traditional forms for the corresponding approximations are satisfied, but which have no overlap zone of joint validity, and no logarithmic profile. (Apparently the issue of whether an assumption of overlap has a physical basis has not been explored.)

Therefore it is not at all obvious from the start that the pair of hypotheses (i) an overlap zone exists, plus (ii) the profile is strictly increasing, can form a reasonable basis for a derivation (see the further discussion in Wei *et al.* (2004)). To serve as a rational explanation for a phenomenon, a train of reasoning must begin with very credible hypotheses disconnected from the phenomenon to be explained.

These considerations point to the desirability of an approach to the derivation of features of the mean velocity and Reynolds stress profiles which is distinct from the classical one. That is one of the aims of this paper.

The implications of the traditional framework are pervasive in that they constitute the basis for a number of the theoretical approaches attempting to describe the physical behaviors of wall turbulence. For example, this inner/outer overlap structure promotes the notion that the logarithmic region of the mean profile is an inertial sublayer in physical space, e.g., Tennekes & Lumley (1972), and has been employed in constructing descriptions of the Reynolds normal and shear stresses, Monin & Yaglom (1971); Panton (1997, 2003). More generally, the classical train of thought has been at the foundation of a great many theoretical treatments of wall-bounded turbulence in the last decade or so Afzal (1993), Afzal (2001*a,b*); Panton (1997, 2003); Buschmann & Gad-el-Hak (2003*a,b*); George & Castillo (1997).

The results just mentioned, as well as those presented in Wei *et al.* (2004), provide fundamentally sound reasons to believe that the classical, overlap-based, approaches are inadequate. The present paper greatly expands on those analyses. Specifically, the arguments in the cited paper reveal that while Reynolds number dependencies in the mean velocity profile (using inner scaling) appear only very subtly, the Reynolds number dependent behavior of the terms in the mean momentum balance are both clearly evident in existing data, and derivable from the equations of motion. From these new results one is also led to conclusions regarding flow structure that are contrary to a number of well-established notions within the turbulent wall-flow literature. Notable among the latter are *i*) that viscous forces are only comparable to turbulent inertia in the buffer layer and below (say $y^+ = yu_\tau/\nu$ less than about 30), *ii*) the aforementioned correspondence between

a logarithmic mean profile and an inertial sublayer-like structure in physical space, and *iii*) the exclusivity of the inner and outer scales with regard to describing the behavior of mean momentum transport and its Reynolds number dependence. The new assertions contrary to those just listed are unambiguously supported by the highest quality data available, Zagarola & Smits (1997), Moser, Kim & Mansour (1999), DeGraaff & Eaton (2000), McKeon *et al.* (2004), as well as via multiscale analyses under a minimal set of well-founded assumptions. At the heart of this theory is the actual balance of terms in the mean momentum equation (as opposed to the mean profile and stress-based interpretations, Tennekes & Lumley (1972); Townsend (1976); Hinze (1975); Panton (1990); Pope (2000)). Resulting from this effort is the identification of a layer structure for boundary layer, pipe and channel flows that is well-founded in the mathematical representation of mean flow dynamics. A primary element of this layer structure is the so-called stress gradient balance layer.

As the name implies, a stress gradient balance layer exists when there is a balance between the viscous and Reynolds stress gradient terms in the mean momentum equation (see Eq. 2.1 below). In boundary layers, pipes and channels, the stress gradient balance layers extend from the edge of the viscous sublayer ($y^+ \approx 3$) to an inner normalized wall-normal position that is proportional to the square root of the global Reynolds number, $\sqrt{\delta^+}$. As is readily apparent, at high Reynolds numbers, the position $y^+ \sim \sqrt{\delta^+}$ extends well into the traditional logarithmic layer of the mean profile. In terms of non-normalized physical dimension, this layer thickness is given by the intermediate length, $\sqrt{\delta\nu/u_\tau}$ (Long & Chen (1981); Afzal (1984); Sreenivasan & Sahay (1997)). These scaling behaviors find resounding support from existing empirical data, and have been theoretically derived through the aforementioned multiscale analyses of the equations of motion. In addition to showing the need for this intermediate length to describe the mean momentum field in boundary layer, pipe and channel flows, there is evidence that a mean profile having features of a logarithmic profile can occur entirely owing to the flow physics intrinsic to the stress gradient balance layer, i.e., independent of any flow structure requiring description via inner/outer overlap ideas (Wei *et al.* (2004), together with the much stronger argument and more exact definition of these features given in the present paper).

Herein these basic results are extended to show that stress gradient balance layers have a mathematical structure composed of a hierarchy of length scales. The picture of only two scaling regions—inner and outer—with their attendant analysis, is thus shown unequivocally to be inadequate for a full understanding. It is

shown here through rescaling arguments that the mathematical structure of the flow involves a continuum of length scales, in a sense to be explained below. Each has its own “scaling layer”, with characteristic length asymptotically proportional to distance from the wall as that distance, in wall coordinates, increases. In all, this continuum of layers serves to connect the traditional “outer” region with a region close to the “inner” one. Although the analysis here is sound, the relationship between this mathematical structure and the instantaneous motions in the flow is speculative. Possible physical implications of this hierarchy are briefly discussed in Section 5.

The scale hierarchy, however, has another remarkable consequence: a rigorous connection is established between a certain precisely defined characteristic function $A(y^+)$ associated with the hierarchy, and the mean velocity profile. The function A is guaranteed to take on $O(1)$ values for all y^+ in the hierarchy, and to be constant in any interval if and only if the profile is logarithmic in that same interval. If A is almost constant (and there are indications when this may be the case), then the profile is close to being logarithmic. Although it is generally not constant, an argument pointing to its constancy in certain regions in the limit as $Re \rightarrow \infty$ is given in Sec. 3.5.2. For finite Re other functions such as certain power laws could be accommodated, and certainly Re -dependence as well. But nevertheless it is the firmest theoretical basis yet found for a generalized logarithm-type growth, and is totally independent of the classical arguments for logarithmic growth based on two scaling domains with an overlapping region of validity.

Finally, the general location where the hierarchy begins can be predicted, and coincides roughly with the empirical onset of the traditional logarithmic part of the velocity profile. Specifically, this location is theoretically shown to be identified with where the derivative of the Reynolds stress, namely $\frac{d}{dy^+} \langle uv \rangle^+$, is in a range near -0.1 , with its second derivative positive. This implies that the start of the log profile is near $y^+ = 30$.

The theoretical and empirical evidence to date provide compelling reasons to explore further the physical and mathematical properties of stress gradient balance layers. In this regard, consideration of purely shear driven flow (turbulent Couette flow) is especially relevant. As will be shown, the properties of turbulent Couette flow are exclusively derived via stress gradient balance layer dynamics. Moreover, the scaling properties of turbulent channel flow can be derived from those of Couette flow by a simple transformation. The latter

therefore provides a particularly useful and general context for educing the essential characteristics of stress gradient balance layer dynamics, which is a primary objective of this paper. The analysis of Couette and turbulent channel flow will be preceded by a review of existing results relating to the structure of pressure driven turbulent flow in a channel, and followed by a discussion of the implications of the major results.

2. Momentum Balance Layer Structure of Turbulent Channel Flow

This section gives a brief recapitulation of known results about the structure of the mean momentum balance in turbulent channel flow. Its intent, in part, is to provide a context for comparisons with turbulent Couette flow. The most important difference is that in the pressure-driven channel case, the flow is partitioned into zones according to the dominant terms comprising the force balance. Couette flow, on the other hand, has no such partitioning; the only kind of force balance present is between viscous and Reynolds stress gradients. Nevertheless, the problem of determining the channel flow profile can, surprisingly, be reduced to that of Couette flow through a simple transformation.

In this and subsequent sections, the time averaged form of the axial momentum balance will be considered for statistically stationary, fully developed flow in a channel of height 2δ . As is customary, the mean velocity, $U(y)$, is in the x direction with the transverse coordinate, y , extending from its origin at the lower wall to the channel centerline at $y = \delta$. In the case of pressure driven flow in the channel, the inner normalized mean momentum equation is

$$0 = \frac{1}{\delta^+} + \frac{d^2 U^+}{dy^{+2}} - \frac{d\langle uv \rangle^+}{dy^+}. \quad (2.1)$$

In this equation, the terms on the right represent three different physical mechanisms: the net pressure force driving the flow, and transverse gradients of the viscous and Reynolds stresses respectively. (Note that in a boundary layer mean advection has an effect similar to that of mean pressure gradient.)

Physically, the above momentum balance represents the time-average statement of Newton's second law for a differential fluid element. This equation also unambiguously indicates that it is the stress gradients that are the significant quantities in establishing the net force on a differential fluid element. (It is not the

stresses themselves.) Based on the momentum equation, the *limiting conditions* for (2.1) are that *i*) the three dynamical effects must, in order of magnitude, all be in balance, or *ii*) two terms are in balance with the third much smaller. Therefore, for the purpose of elucidating mean momentum transport it is useful to examine the ratio of two of the three terms in (2.1): the gradient of the viscous stress and the gradient of the Reynolds stress. Thus if, for example, this ratio, $|\frac{d^2 U^+}{dy^{+2}} / \frac{d\langle uv \rangle^+}{dy^+}| \ll 1$ then the viscous force is small and the pressure and Reynolds stress gradients are essentially in balance. If $|\frac{d^2 U^+}{dy^{+2}} / \frac{d\langle uv \rangle^+}{dy^+}| \sim 1$, these effects are in balance and the pressure gradient term is relatively small, or comparable to the other two terms. And, if $|\frac{d^2 U^+}{dy^{+2}} / \frac{d\langle uv \rangle^+}{dy^+}| \gg 1$ the Reynolds stress gradients are small and the pressure and viscous stress gradient terms approximately balance.

Consideration of the balance of terms in (2.1) reveals the layer structure shown schematically in Figure 1 (from Wei *et al.* (2004)). This figure depicts a thin sublayer ($0 \leq y^+ \leq 3$) where the mean pressure gradient and the viscous stress gradient dominate the balance equation. Outside this thin layer is a region defined by a nearly perfect balance between the viscous and Reynolds stress gradients. The thickness of this stress gradient balance layer exhibits a clear Reynolds number dependence, extending well into the traditionally accepted logarithmic region of the mean velocity profile at sufficiently large Reynolds number. Near the location, y_m^+ , of maximum Reynolds stress the viscous force and pressure gradient are, once again, nearly in balance. Around y_m^+ the gradient of the viscous stress is much larger than the gradient of the Reynolds stress, although $|\langle uv \rangle^+| \gg dU^+/dy^+$. For greater distances from the wall, the Reynolds stress gradient has changed sign and the viscous stress gradient becomes much smaller than either the Reynolds stress gradient or the mean pressure gradient terms. In this region the Reynolds stress and pressure gradients are essentially in balance. As noted in Wei *et al.* (2004), a primary difference between the boundary layer and channel flow is in the inner viscous/pressure gradient layer at low Reynolds numbers. The four layers depicted in Fig. 1 are respectively labeled according to the predominant dynamical mechanisms. Thus, layer I is termed the inner viscous/pressure gradient layer, layer II the Reynolds stress/viscous stress gradient balance layer, layer III the viscous/pressure gradient mesolayer, and layer IV the Reynolds stress/pressure gradient balance layer. As is readily apparent, the layer structure depicted in Fig. 1 constitutes a considerable departure from the sub-, buffer, logarithmic, wake layer structure typically ascribed to turbulent wall-flows.

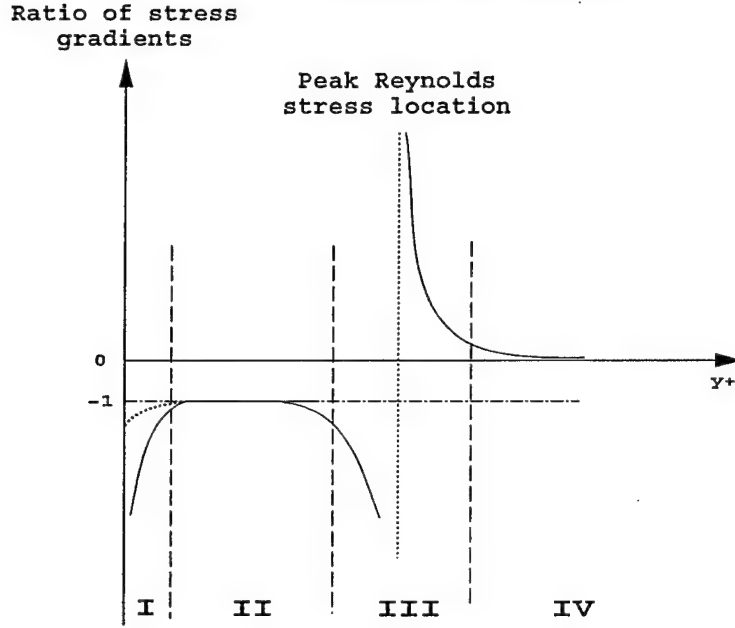


FIGURE 1. Sketch of the four layers of turbulent channel flow at a fixed Reynolds number; layer I is the inner viscous/pressure gradient balance layer, layer II is the stress gradient balance layer, layer III is the viscous/pressure gradient balance mesolayer and layer IV is the Reynolds stress/pressure gradient balance layer. Note layer I in the zero pressure gradient turbulent boundary layer is different from that of channel & pipe flow in that all of the terms in the boundary layer equation are zero at the wall.

The Reynolds number dependent behaviors of the thicknesses of the four layers and the velocity increments across each layer have been determined empirically and through multiscale analyses, Wei *et al.* (2004). Specifically, layer I remains a constant inner normalized thickness ($\Delta_I y^+ \simeq 3$) with increasing Reynolds number. Of course, under outer normalization the thickness of this layer becomes a diminishingly small fraction of the channel half-height as $\delta^+ \rightarrow \infty$. The inner normalized thicknesses of both layers II and III increase like $\Delta y^+ \sim \sqrt{\delta^+}$ with increasing Reynolds number, and thus correspondingly decrease under outer normalization like $\Delta \eta \sim 1/\sqrt{\delta^+}$, $\eta = y/\delta$. Layer IV becomes an increasingly larger fraction of the overall channel half height with increasing Reynolds number. This relative fractional increase is more pronounced at low Reynolds number. Both layers I and III have inner normalized velocity increments that remain essentially fixed independent of Reynolds number. For layer I $\Delta U^+ \simeq 3$, while for layer III the increment is $\Delta U^+ \simeq 1$. An intriguing observation is that, apparently independent of Reynolds number, the velocity increment across layer II equals one half of U_c (or $U_\infty/2$ in a boundary layer). Like its thickness, the velocity increment across

layer IV increases slowly with increasing Reynolds number, and extrapolation suggests that with increasing Reynolds number this velocity increment approaches $U_c/2$. (Recall that both $\Delta_I U^+$ and $\Delta_{III} U^+$ remain constant as $\delta^+ \rightarrow \infty$.)

The layer structure revealed via analysis of the mean momentum balance has a number of significant implications. Some of these implications, relative to long-held views regarding turbulent wall-flow structure, were discussed at the outset. Central to the analytical developments discussed below is the now apparent reality that in pressure driven channel flow viscous effects are dynamically significant from the wall out to a Reynolds number dependent position beyond the peak in the Reynolds stress. Intimately related to this physical reality is that all of the Reynolds number dependencies exhibited in the layer structure can be tied to the growth rate of the stress gradient balance layer. For this reason, a measure of the thickness of this layer, $\Delta_{II} y \sim \sqrt{\nu \delta / u_\tau}$, is identified as an important intermediate length since, like all similarity variables, it arises solely from the intrinsic dynamics of the problem. Along with the outer and inner scales, δ and ν / u_τ , this length is viewed as fundamental to the description of boundary layer, pipe and channel flows. In what follows, the structure of a turbulent flow that is entirely characterized by stress gradient balance layer dynamics (i.e., Couette flow) is contrasted with, yet found to be intimately connected to, the pressure driven channel flow.

3. Scaling Analysis of Turbulent Couette Flow

This section is devoted to an investigation of steady turbulent Couette flow, via the averaged equation of (streamwise) momentum balance and concepts from multiscale analysis. Specifically, implications relating to the scaling layer structure of the flow and the behavior of the mean velocity $U^+ = \frac{U}{u_\tau}$ and Reynolds stress $T^+ = -\frac{\langle uv \rangle}{u_\tau^2}$ profiles across the channel will be explored.

The two channel walls are situated at positions $y = 0$ and $y = 2\delta$. The lower one is stationary and the upper one is in steady motion. The dimensionless inner scaled half-width of the channel is denoted by $\delta^+ = \frac{u_\tau \delta}{\nu}$. The parameter $\epsilon = \frac{1}{\delta^+}$, which is assumed to be small, will figure prominently in the various scalings. The traditional inner and outer scaled distances from the lower wall are y^+ and $\eta = \epsilon^2 y^+$, respectively. The latter is simply the physical distance from the lower wall, normalized by δ . The centerline is at $\eta = 1$, i.e.

$y^+ = \epsilon^{-2} = \delta^+$. A major conclusion will be that the designation of coordinates as being either “inner” or “outer” may be misleading, because they represent only the extreme ends of a spectrum of scaled distances. In fact, the theoretical basis for judging the relevance of using y^+ near the wall and η near the centerline is extended here to derive the existence of the intermediate scaling regions. The new intermediate scalings therefore enjoy a theoretical foundation as firm as that of the traditional inner and outer regions.

3.1. *The averaged momentum balance equations*

The averaged equation of streamwise momentum balance for steady turbulent Couette flow expresses an exact balance between the transverse gradients of the viscous and Reynolds stresses:

$$\frac{d^2 U^+}{dy^{+2}} + \frac{dT^+}{dy^+} = 0. \quad (3.1)$$

The variables U^+ and T^+ satisfy the following boundary conditions at $y^+ = 0$:

$$T^+(0) = \frac{dT^+}{dy^+}(0) = U^+(0) = 0; \quad \frac{dU^+}{dy^+}(0) = 1. \quad (3.2)$$

In terms of η , (3.1) becomes

$$\epsilon^2 \frac{d^2 U^+}{d\eta^2} + \frac{dT^+}{d\eta} = 0. \quad (3.3)$$

At the centerline, there are boundary conditions

$$\frac{dT^+}{d\eta} = \frac{d^2 U^+}{d\eta^2} = 0 \quad \text{at } \eta = 1. \quad (3.4)$$

Beyond $\eta = 1$, U^+ and T^+ can be continued by symmetry considerations: U^+ is odd and T^+ is even with respect to their values at the centerline (see the details following (3.11)). This means, for example, that the centerline velocity U_c^+ is equal to $V^+/2$, where V^+ is the inner normalized velocity of the upper wall.

Equation (3.1) can be integrated with use of (3.2) to obtain

$$\frac{dU^+}{dy^+} - 1 + T^+ = 0; \quad (3.5)$$

or in terms of variable η ,

$$\epsilon^2 \frac{dU^+}{d\eta} - 1 + T^+ = 0. \quad (3.6)$$

The “outer approximation” is found by setting $\epsilon = 0$ in (3.6), which yields

$$T^+(\eta) = 1. \quad (3.7)$$

Alternatively, one can define a scaled Reynolds stress $\hat{T}(\eta)$ by

$$T^+ = T_m^+ + \epsilon^2 \hat{T}, \quad (3.8)$$

where $T_m^+ = T_{\eta=1}^+$, and thereby rewrite (3.3) as

$$\frac{d^2 U^+}{d\eta^2} + \frac{d\hat{T}}{d\eta} = 0. \quad (3.9)$$

This, together with the observation from (3.4) that both terms in (3.9) vanish at $\eta = 1$, expresses a balance between rescaled forces and therefore suggests that the rescaling in question (U^+ and \hat{T} as functions of η) is the correct one in the outer regime. Later in Sec. 3.4.6 a stronger corroboration of this conclusion will be presented.

To reiterate, scaling arguments imply that near the centerline, (3.7) holds to lowest order as $\epsilon \rightarrow 0$, $\hat{T}(\eta)$ is a regular function (i.e. its derivatives with respect to η up to some finite order are bounded dependently of ϵ), and (3.9) holds to next order, again as $\epsilon \rightarrow 0$. Some of these conclusions are well known (e.g., Panton (2003)); they are given here as an illustrative example of the methodology used in this paper to reveal a hierarchy of layers (Sec. 3.4.3).

Since the outer solution (3.7) does not satisfy the boundary condition (3.2) at the lower wall, it cannot be uniformly valid; there is a thin layer near that wall where the outer scaling gives way to the inner scaling. More precisely, it will be shown, in fact, that a whole hierarchy of scalings are appropriate, forming a transition between the outer and the inner regions. First, however, a more detailed comparison with channel flow will be provided, as well as some features of the flow near the centerline.

3.2. Comparative formulation of turbulent channel flow

In this section a digression is made in order (a) to make pertinent comparisons between Couette and channel flow, and (b) to introduce a transformation (3.12) whose generalizations will lead to far-reaching implications for the profiles of both Couette and channel flows.

Physically, pressure driven turbulent channel flow differs from Couette flow in the nature of the force driving the flow. A pressure gradient, present throughout the flow, provides that forcing in place of the differential motion of the upper and lower walls characteristic of Couette flow.

The mean momentum balance for channel flow is

$$\frac{d^2 U^+}{dy^{+2}} + \frac{dT^+}{dy^+} + \epsilon^2 = 0 \quad (3.10)$$

The extra term $\epsilon^2 \equiv 1/\delta^+$ represents the dimensionless pressure gradient. And (3.4) is replaced by

$$T^+ = \frac{dU^+}{dy^+} = 0 \quad \text{at } \eta = 1. \quad (3.11)$$

In Couette flow, U^+ is odd about the point $\{\eta = 1, U^+ = U_c^+\}$ where U_c^+ is the centerline velocity (at $\eta = 1$). This means that $U^+(2 - \eta) = 2U_c^+ - U^+(\eta)$, which results in a positive velocity $V^+ = 2U_c^+$ at the upper wall, $\eta = 2$. Also T^+ is even in the sense that $T^+(2 - \eta) = T^+(\eta)$. In contrast, channel flow has $U^+(2 - \eta) = U^+(\eta)$ and $T^+(2 - \eta) = -T^+(\eta)$, which imply (3.11). Thus the two kinds of flow differ with respect to simple symmetry considerations.

There is, however, a deeper mathematical relation between them. In the Couette flow case, one can define an adjusted Reynolds stress

$$\tilde{T} \equiv T^+ - \epsilon^2 y^+. \quad (3.12)$$

Then (3.1) becomes

$$\frac{d^2 U^+}{dy^{+2}} + \frac{d\tilde{T}}{dy^+} + \epsilon^2 = 0, \quad (3.13)$$

which in form coincides with (3.10). Thus, this simple transformation from T^+ to \tilde{T} converts the differential equation for Couette flow to that for channel flow. Moreover, the boundary conditions satisfied by the variables in (3.13) turn out to be approximately the same as those satisfied by the corresponding variables in pressure driven channel flow.

Qualitatively, the portion $\{0 < \eta < 1\}$ for Couette is analogous to a region close to the wall, $\{0 < \eta < \eta_m = O(\epsilon)\}$, for channel flow, Wei *et al.* (2004), since T^+ rises in both cases to a maximum and U^+ rises to a point where $\frac{dU^+}{d\eta}$ has a smaller order of magnitude than it does at $\eta = 0$. That is, in both cases the flow domain interior to the peak in T^+ constitutes a stress gradient balance layer. It will be shown that this observation leads to methodological similarities in describing other aspects of the two flows.

3.3. Properties of T^+ and U^+ at the centerline

Based on all empirical evidence, it may be assumed that for $0 < \eta < 1$

$$\begin{aligned} \frac{dU^+}{dy^+} &> 0, \quad \frac{d^2U^+}{dy^{+2}} < 0, \quad (\text{Couette and channel}), \\ \frac{dT^+}{dy^+} &> 0, \quad \frac{d^2T^+}{dy^{+2}} < 0, \quad (\text{Couette}), \text{ the latter for } y^+ > \text{a certain value.} \end{aligned} \quad (3.14)$$

From this and (3.5), one sees that for Couette flow, $T^+ < 1$ and that T^+ increases monotonically as one proceeds from the lower wall to the centerline. Let $T_m^+ \equiv T_{\eta=1}^+$ be the maximal value of T^+ . Recall the definition of \hat{T} in (3.8) and Eqn. (3.9). As mentioned, they suggest that near the centerline, both \hat{T} and U^+ scale with η , in the sense that all their derivatives with respect to η are $\leq O(1)$ quantities. Further justification of this assertion will be provided in Sec. 3.4.6. In particular, $\frac{d^2\hat{T}}{d\eta^2} \leq O(1)$, so that $\frac{d^2T^+}{d\eta^2} \leq O(\epsilon^2)$. Therefore in that neighborhood

$$T^+ \approx T_m^+ - K\epsilon^2(\eta - 1)^2$$

for some K independent of ϵ , or

$$T^+ \approx T_m^+ - K\epsilon^6(y^+ - \delta^+)^2. \quad (3.15)$$

This provides the order of magnitude of the curvature of the T^+ profile at the centerline. Very good experimental support for this analytical prediction is given in Figure 2, albeit only over a small range of Reynolds numbers.

In this paper, the order symbol $O(\cdot)$ will be used with respect to $\epsilon \rightarrow 0$ or $\rho \rightarrow 0$ (ρ is a small parameter introduced in Sec. 3.4.1). For example in the former context, $a = O(b)$ for positive $a(\epsilon)$ and $b(\epsilon)$ will be taken to mean that a/b and b/a are both bounded for small ϵ .

Use of (3.6) at the centerline also provides the order of the deviation of T_m^+ from the value 1. Since it was noted above that η is the correct scaled variable for U^+ at the centerline, it is now seen that

$$T_m^+ = 1 - O(\epsilon^2). \quad (3.16)$$

Again, Table 1 provides remarkable corroboration of (3.16).

In contrast, in pressure driven turbulent channel flow the proximity of T_m^+ to 1 is given by $T_m^+ = 1 - O(\epsilon)$, and the curvature of the graph of $T^+(y^+)$ is $O(\epsilon^3)$ near the peak, Wei *et al.* (2004). Table 2 provides a

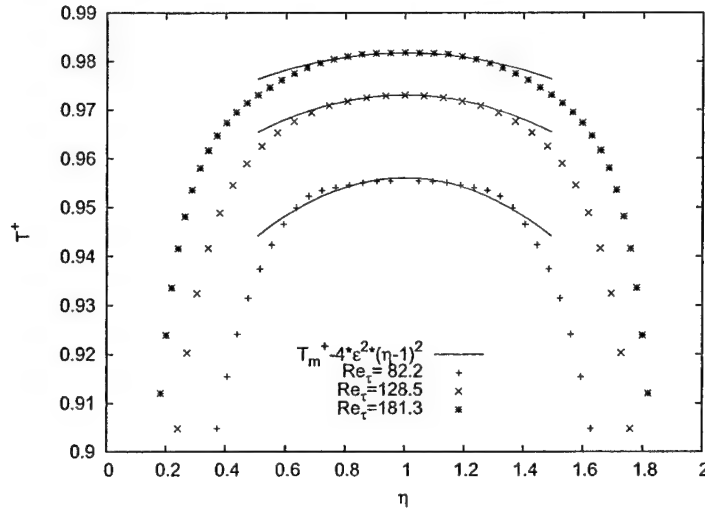


FIGURE 2. Reynolds stress around the peak, showing $\frac{d^2 T}{d\eta^2} = O(\epsilon^2)$ and $1 - T_m = O(\epsilon^2)$. Although these order of magnitude relations are clear, it is difficult to read off even the approximate value of $\frac{d^2 T}{d\eta^2}$. The case $Re_\tau = 82$ is from DNS of Bech *et al.* (1995), and the other two cases are from DNS of Kawamura, Abe & Shingai (2000)

| Investigators | Re_τ | T_m^+ | $\frac{1-T_m^+}{\epsilon}$ | $\frac{1-T_m^+}{\epsilon^2}$ |
|-----------------|-----------|---------|----------------------------|------------------------------|
| Bech et al. | 82.2 | 0.955 | 0.4080 | 3.699 |
| Kawamura et al. | 128.5 | 0.9729 | 0.3066 | 3.476 |
| Kawamura et al. | 181.3 | 0.9817 | 0.2459 | 3.311 |

TABLE 1. Properties of T_m^+ for turbulent Couette flow. DNS data from Bech *et al.* (1995) and Kawamura *et al.* (2000)

review of data corroborating the relation for channel flow. The contrast between the data of Tables 1 and 2 is strong evidence of (3.16), despite the small range of Re_τ .

Finally since $\frac{dU^+}{d\eta} \leq O(1)$ at $\eta = 1$,

$$\frac{dU^+}{dy^+} \leq O(\epsilon^2) \quad (3.17)$$

at $y^+ = \epsilon^{-2}$. Note that $\frac{d^2 U^+}{d\eta^2} = 0$ at $\eta = 1$, which illustrates that the actual order of derivatives of scaled quantities may be $\leq O(1)$ rather than $= O(1)$.

| <i>Investigators</i> | Re_τ | T_m^+ | $\frac{1-T_m^+}{\epsilon}$ | $\frac{1-T_m^+}{\epsilon^2}$ |
|----------------------|-----------|---------|----------------------------|------------------------------|
| Moser et al. | 180 | 0.7321 | 3.696 | 49.321 |
| Moser et al. | 395 | 0.8370 | 3.228 | 69.935 |
| Moser et al. | 590 | 0.8647 | 3.278 | 79.447 |
| Iwamoto et al. | 109.4 | 0.6071 | 4.110 | 42.995 |
| Iwamoto et al. | 150.4 | 0.689 | 3.815 | 46.799 |
| Iwamoto et al. | 297.9 | 0.8006 | 3.442 | 59.401 |
| Iwamoto et al. | 395.7 | 0.8321 | 3.340 | 66.448 |
| Iwamoto et al. | 642.5 | 0.8746 | 3.179 | 80.574 |

TABLE 2. Properties of T_m^+ for turbulent channel flow. DNS data from Moser *et al.* (1999) and Iwamoto *et al.* (2002)

3.4. The scale hierarchy

The transformation (3.12), when generalized, leads to remarkable consequences regarding the structure of stress gradient balance layers.

3.4.1. Adjusted Reynolds stresses

Let ρ be a small positive number. Restrictions on it will be given later. Let

$$T^\rho(y^+) = T^+(y^+) - \rho y^+. \quad (3.18)$$

(Note that ρ is a superscript not an exponent.) These are simply mathematical constructs that define the adjusted Reynolds stresses T^ρ . They satisfy

$$\frac{dT^\rho}{dy^+} = \frac{dT^+}{dy^+} - \rho, \quad (3.19)$$

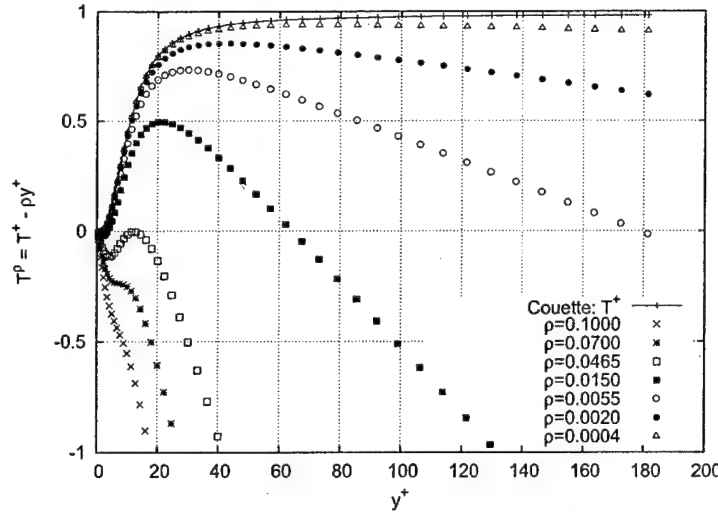


FIGURE 3. Adjusted Reynolds stress profile for various values of ρ . The case $\rho = \epsilon^4$ corresponds to within $O(\epsilon^2)$ to the genuine Reynolds stress for Couette flow (see Section 3.4.6), and $\rho = \epsilon^2$ is an approximation to that for pressure driven channel flow. The DNS data is from Kawamura, Abe & Shingai (2000), $\delta^+ = Re_\tau = 181.3$ and $\epsilon = .074$.

and from (3.1) (as always, for Couette flow),

$$\frac{d^2 U^+}{dy^{+2}} + \frac{dT^\rho}{dy^+} + \rho = 0. \quad (3.20)$$

From DNS data of Kawamura *et al.* (2000), the adjusted Reynolds stresses for different ρ are shown in Figure 3.

The main interest is in those adjusted stress functions that exhibit local maxima. This happens when ρ is sufficiently small. The reasoning below (Sec. 3.5) uses these functions to educe the existence of a special scaling region (layer) L_ρ for each ρ in a certain range. Part of the argument involves obtaining an exact differential equation (3.29) for rescaled variables having no explicit dependence on ϵ or ρ . Another part entails the recognition that (3.20) expresses an approximate balance between its first two terms, and (since ρ is small) that this balance must be broken and changed to another kind of balance when y^+ attains a value such that the three terms in (3.20) have the same order of magnitude.

Balance-exchange occurs when ρ is such that there are locations for which the middle term in (3.20) is positive and significantly greater than the last term. Calling such a location $y^+ = y_0^+$, one requires

$\frac{dT^\rho}{dy^+}(y_0^+) \gg \rho$. From (3.19), this will be the case when

$$\frac{dT^+}{dy^+}(y_0^+) \gg \rho. \quad (3.21)$$

Temporarily, (3.21) will be replaced by

$$\frac{dT^+}{dy^+}(y_0^+) \geq 10\rho. \quad (3.22)$$

Since this may be too restrictive, however, it will be relaxed at a later point by allowing the coefficient 10 to be changed to some number in the interval 5 to 20. Moreover, only points where $\frac{d^2 T^\rho}{dy^{+2}}, \frac{d^2 T^+}{dy^{+2}} < 0$ will be relevant, i.e. only points on the decreasing part of Fig. 4.

From Figure 4, one sees that $\max \left[\frac{dT^+}{dy^+} \right] \sim .07$, attained at $y^+ \sim 7$, so that (3.22) will be true for some y_0^+ if

$$0 < \rho \leq .007. \quad (3.23)$$

3.4.2. Peaks of T^ρ

Let ρ satisfy (3.23). There is a point on the right (descending) branch of Figure 4 at which $\frac{dT^+}{dy^+}(y^+) = \rho$, hence from (3.19) the function T^ρ has a maximum there (since its slope is 0 and its second derivative negative). Call the position of that maximum $y_m^+(\rho)$. As ρ decreases, y_m^+ increases toward its maximal allowed value, which is $1/\epsilon^2$ since that is the centerline. It will be shown later (Section 3.4.6) that $\rho = O(\epsilon^4)$ at the centerline.

A balance-exchange argument will be used to show that for each ρ satisfying (3.23) and $\rho \geq O(\epsilon^4)$, there exists a “scaling layer” L_ρ with characteristic width $O(\rho^{-1/2})$ in the inner variable y^+ containing $y_m^+(\rho)$, such that in this layer, the functions U^+ and T^+ vary with characteristic length $\rho^{-1/2}$. It will also be shown that the characteristic width $\rho^{-1/2}$ is of the order of the actual layer position $y_m^+(\rho)$ as y_m^+ increases.

To reiterate, at the point $y_m^+(\rho)$ (where T^ρ is maximal), it follows from (3.19) that

$$\frac{dT^+}{dy^+}(y_m^+(\rho)) = \rho. \quad (3.24)$$

Hence since $\frac{dT^+}{dy^+}$ is a decreasing function of y^+ , $y_m^+(\rho)$ increases as ρ decreases, with (as was mentioned) $y_m^+ \rightarrow 1/\epsilon^2$ as $\rho \rightarrow O(\epsilon^4)$. On the other hand, the range of ρ is limited (3.23) from above by .007, and hence by Fig. 4, the lower bound on y_m^+ is about 30.

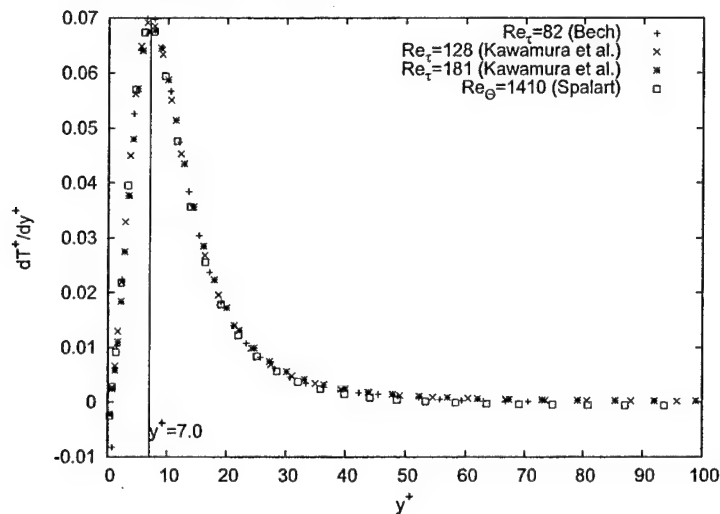


FIGURE 4. Inner normalized Reynolds stress gradient for a variety of flows. The turbulent Couette flow data are from Bech *et al.* (1995) and Kawamura *et al.* (2000). Also included are the turbulent channel DNS data from Moser *et al.* (1999) and turbulent boundary layer DNS from Spalart (1988).

This provides a lower bound on the allowable values of y_m^+ which will be considered here as peaks in the graphs of T^ρ , with ρ subject to (3.22). Since the coefficient 10 in that inequality was quite arbitrary, it is worthwhile exploring the consequences of replacing it by some number between 5 and 20. If that is done, it is found that the lower bound on y_m^+ is between 20 and 36.

In summary,

$$(20 \text{ to } 36) < y_m^+(\rho) < 1/\epsilon^2 \text{ when } (.0035 \text{ to } .014) > \rho > O(\epsilon^4). \quad (3.25)$$

This range in y^+ will be the predicted range of the hierarchy, constructed below.

3.4.3. A continuum of scalings

It will be shown that within each layer L_ρ (to be defined below), the variables y^+ and T^ρ may be rescaled in such a way that the basic differential equation (3.20) is transformed into an exact equation having no explicit dependence on ϵ or ρ . This continuum of scales can be parameterized by either ρ or y_m^+ , since $y_m^+(\rho)$ is a monotone function. It will be called a scale hierarchy. As will be shown and discussed further, there are compelling reasons to believe that scale hierarchies constitute a fundamental structural feature of the wall-turbulence equations; underlying, for example, the possible logarithmic behavior of the mean profile,

and replacing the traditional overlap ideas as the theoretical paradigm for that behavior. The prediction that the beginning of the layered domain lies between $y^+ = 20$ and $y^+ = 36$ is interesting, in that it roughly coincides with the traditional empirical onset of the logarithmic-like profile. More generally, the striking connection between the hierarchy and the profiles of U^+ and T^+ is explored in Sec. 3.5.

The details of the origin and properties of the layer L_ρ are now explained. Take ρ in the interval (3.23). Then (3.22) holds for some $y_0^+ < y_m^+(\rho)$. Therefore for $y^+ = y_0^+$, it follows from (3.22) that the first two terms in (3.20) are each much larger than the last term and balance, except for an error term ρ . This, in fact, continues to be true as y^+ increases to larger values, except that as y^+ approaches the location $y_m^+(\rho)$ where T^ρ achieves its maximum (denoted by $T_m^\rho(\rho)$) the middle term in (3.20) gets smaller than $O(1)$, and therefore the first term does as well. The middle term eventually attains the value ρ (say) at some point, which will be called $y^+ = y_1^+(\rho)$. By (3.20), the first term $\frac{d^2 U^+}{dy^{+2}} = -2\rho$ there. Therefore at $y^+ = y_1^+(\rho)$, all three terms in (3.20) have the same order of magnitude, and it is natural to seek a rescaling which reflects this equality. The new variables will be called \hat{y} (which also depends on ρ) and \hat{T}^ρ . As exemplified in Wei *et al.* (2004), rescaling is best done using the differentials, dy^+ and dT^ρ . For coefficients α and β , to be determined depending on ρ , one sets

$$dy^+ = \alpha d\hat{y} \quad \text{and} \quad dT^\rho = \beta d\hat{T}^\rho. \quad (3.26)$$

Under this transformation, the first two terms in (3.20) become $\alpha^{-2} \frac{d^2 U^+}{d(\hat{y})^2}$ and $\frac{\beta}{\alpha} \frac{d\hat{T}^\rho}{d\hat{y}}$ respectively. They must match, in formal order of magnitude, the third term, ρ . This requires $\alpha = \rho^{-1/2}$ and $\beta = \rho^{1/2}$. Therefore

$$dy^+ = \rho^{-1/2} d\hat{y}, \quad dT^\rho = \rho^{1/2} d\hat{T}^\rho. \quad (3.27)$$

The equations (3.27) can be integrated with integration constants chosen such that $\hat{y} = 0$ when $y^+ = y_m^+(\rho)$ and $\hat{T}^\rho = 0$ when $T^\rho = T_m^\rho(\rho)$:

$$y^+ = y_m^+(\rho) + \rho^{-1/2} \hat{y}, \quad T^\rho = T_m^\rho + \rho^{1/2} \hat{T}^\rho. \quad (3.28)$$

The basic equation (3.20) then becomes

$$\frac{d^2 U^+}{d\hat{y}^2} + \frac{d\hat{T}^\rho}{d\hat{y}} + 1 = 0. \quad (3.29)$$

This is an exact equation with no explicit dependence on any parameters, and it suggests that the ρ -

dependent rescaling just described (3.28) accurately depicts the behavior of U^+ and \hat{T}^ρ (hence T^+) in some “scaling patch”. But that evidence is not quite sufficient. It should also be independently demonstrated that at some location in the channel, the individual derivatives appearing in (3.29) are actually $\leq O(1)$ quantities. Then the existence of a scaling patch containing that location can be surmised. In the patch, U^+ and \hat{T}^ρ will be regular functions of \hat{y} , which means in particular that the derivatives of those functions (to orders 1, 2 and 3, say) with respect to \hat{y} will also be $O(1)$ quantities. There are, in fact, two candidates for such a location: $y_1^+(\rho)$ and $y_m^+(\rho)$. For example by construction, at $y_1^+(\rho)$ the terms of (3.29) are $-2, 1, 1$ respectively. This, together with the fact that y_1^+ is not at a boundary, where external influences could occur, is evidence of the presence of a local “scaling layer” L_ρ containing that point. In other words, the characteristic length scale in this interval, referred to the variable \hat{y} , has the order unity, and thus by (3.28) in wall units is $O(\rho^{-1/2})$.

The other candidate is the point $y_m^+(\rho)$ where the three terms in (3.29) are $-1, 0$, and 1 , respectively. The layer L_ρ will contain both points, but the latter, $y_m^+(\rho)$, will be chosen in this paper to pinpoint the layer. In view of the left part of (3.28), the characteristic length ℓ^+ in the layer can be taken as $\ell^+ = \rho^{-1/2}$.

At this point, it has been shown that for each value of ρ in the range (3.25), there exists an interval L_ρ containing $y_m^+(\rho)$ and $y_1^+(\rho)$ within which U^+ and \hat{T}^ρ are regular functions of \hat{y} , so that with reference to the inner variable y^+ , these functions vary with characteristic length $\rho^{-1/2}$.

The “width” of L_ρ in the inner variable y^+ can then be surmised as being $O(\rho^{-1/2})$, although its width is not a well defined concept, since L_ρ overlaps with nearby layers ($L_{\rho'}$, for ρ' near ρ .) Since $y_1^+(\rho)$ and $y_m^+(\rho)$ are in L_ρ , some corroboration of its magnitude being $O(\rho^{-1/2})$ may be obtained by estimating $y_m^+(\rho) - y_1^+(\rho)$, which by (3.28) is $\Delta y^+ = \rho^{-1/2} \Delta \hat{y}$, $\Delta \hat{y} = 0 - \hat{y}_1$.

The corresponding increment in $\frac{d^2 U^+}{d\hat{y}^2}$ is

$$\Delta \frac{d^2 U^+}{d\hat{y}^2} = -1 - (-2) = 1.$$

But for some value \hat{y}^* in layer L_ρ , the mean value theorem says that the left side $= \frac{d^3 U^+}{d\hat{y}^3}(\hat{y}^*) \Delta \hat{y}$, so that $\Delta \hat{y} = \left(\frac{d^3 U^+}{d\hat{y}^3} \right)^{-1}$. By differentiating (3.29), it is seen that $\frac{d^3 U^+}{d\hat{y}^3} = -\frac{d^2 \hat{T}^\rho}{d\hat{y}^2}$. This derivative, evaluated at $\hat{y} = 0$ ($y^+ = y_m^+(\rho)$) will be called

$$A(\rho) = -\frac{d^2 \hat{T}^\rho}{d\hat{y}^2}(0), \quad (3.30)$$

although it depends also (probably weakly except for ρ values corresponding to maxima near the centerline) on ϵ . It is the curvature of the peak in T^ρ , in locally scaled coordinates, so that $A(\rho) > 0$. It will be shown below in Sec. 3.4.4 that $A(\rho) = O(1)$ for all ρ . Therefore $\Delta\hat{y} = \frac{1}{A} = O(1)$ as well. This corroborates the characteristic width $\Delta y^+ = O(\rho^{-1/2})$ found before.

If ρ_1 and ρ_2 are close to each other, L_{ρ_1} and L_{ρ_2} overlap. However, a discrete set of values of ρ may be chosen so that the associated layers do not overlap but nevertheless fill out the entire domain of the hierarchy (3.25). If this is done, the number of members in the ensemble increases indefinitely as $\epsilon \rightarrow 0$.

In summary, layer L_ρ is characterized in part by the characteristic length (in inner units) of variation of U^+ and T^+ being $O(\rho^{-1/2})$ and

$$\begin{aligned} \frac{dU^+}{d\hat{y}} &= O(1); \quad \frac{dU^+}{dy^+} = O(\rho^{1/2}); \\ \text{the higher derivatives of } \frac{dU^+}{d\hat{y}} \text{ and } \hat{T} &\leq O(1). \end{aligned} \quad (3.31)$$

Its location will be considered below in Sec. 3.4.4.

This process, by which the layer L_ρ appears, involves a breaking of the approximate balance of the first two terms in (3.20) as y^+ increases past a critical value, and its replacement by a balance among all three terms in (3.20), as indicated formally by (3.29). However, the middle term of (3.29) soon vanishes (at $y^+ = y_m^+(\rho)$), resulting in a balance between the first and third terms alone. This breaking and reestablishing of a balance can be called a “balance exchange”. It plays a very prominent role in the scaling analysis of turbulent channel flow, Wei *et al.* (2004), and as shown here is an embedded property of stress gradient balance layers.

The above constitutes the theoretical foundation for the scale hierarchy. Namely, it provides the existence of a layer L_ρ , for each value of ρ in the interval $O(\epsilon^4) < \rho < (\text{a value between } .035 \text{ and } .014)$, located at $y_m^+(\rho)$. There will be considerable overlapping of layers. This translates into the range of y_m^+ given by (3.25).

An important question remains as to how the unadjusted Reynolds stress T^+ scales in L_ρ . The answer comes from (3.18): $T^+ = T^\rho + \rho y^+ = T_m^\rho + \rho y_m^+ + \rho^{1/2}(\hat{T}^\rho + \hat{y}) = T_m^\rho + \rho y_m^+ + \rho^{1/2}\hat{T}_*(\hat{y})$, where this expression defines $\hat{T}_*(\hat{y}) = \hat{T}^\rho(\hat{y}) + \hat{y}$. It is a regular function of \hat{y} . Therefore the conclusion is that in L_ρ , T^+ also scales with \hat{y} . In fact

$$T^+ = T_m^\rho + \rho y_m^+ + \rho^{1/2}\hat{T}_*, \quad (3.32)$$

where \hat{T}_* is a regular function of \hat{y} (i.e. its derivatives are bounded independently of ϵ or ρ). Of course, U^+ is also a regular function of \hat{y} in L_ρ . This result is self-consistently reinforced by the fact that (3.32) is analogous to the rescaling derived in (3.28).

3.4.4. Locations of the layers

An important piece of information is still lacking. This relates to how the location $y_m^+(\rho)$ (which serves to pinpoint L_ρ) of the maximum of T^ρ depends on ρ . Once this is found, the behavior of the velocity $U^+(y^+)$ and the Reynolds stress $T^+(y^+)$ can in principle be obtained. It is shown, in fact, that for large $y_m^+(\rho)$, the characteristic extent of the layer has the order of magnitude of its distance $y_m^+(\rho)$ from the wall. This means that the layer occupies a fraction of the distance y^+ from the wall to the center of the layer itself.

By differentiating (3.24) with respect to ρ , one obtains

$$\frac{d^2 T^+}{dy^{+2}}(y_m^+(\rho)) \frac{dy_m^+}{d\rho} = 1. \quad (3.33)$$

This equation holds for all y_m^+ for which $y_m^+(\rho)$ is defined, and in particular for all y_m^+ of interest, given by (3.25). Also by (3.27)

$$\frac{d^2 T^+}{dy^{+2}} = \rho^{1/2} \frac{d^2 T^+}{dy^+ d\hat{y}} = \rho \frac{d^2 T^+}{d\hat{y}^2} = \rho^{3/2} \frac{d^2 \hat{T}^\rho}{d\hat{y}^2}. \quad (3.34)$$

In L_ρ , derivatives such as $\frac{d^2 \hat{T}^\rho}{d\hat{y}^2}$ are $O(1)$ quantities (independent of ϵ to dominant order). Recall (3.30) $A = -\left(\frac{d^2 \hat{T}^\rho}{d\hat{y}^2}\right)_{\hat{y}=0}$. Then $A = O(1)$ (see below). Although it will generally depend on ρ , i.e. on y_m^+ , its order of magnitude will not change. From (3.34),

$$\frac{d^2 T^+}{dy^{+2}} = -A(y_m^+) \rho^{3/2}. \quad (3.35)$$

Putting this into (3.33) gives

$$\frac{dy_m^+}{d\rho} = -\frac{1}{A} \rho^{-3/2}. \quad (3.36)$$

Since $A(\rho) = O(1)$, it satisfies bounds of the form $0 < \alpha_1 < \frac{1}{A} < \alpha_2$, and from (3.36), there is a C independent of ρ with $y_m^+(\rho) = C - \int \frac{1}{A} \rho^{-3/2} d\rho$, so that

$$2\alpha_1 \rho^{-1/2} + C < y_m^+(\rho) < 2\alpha_2 \rho^{-1/2} + C. \quad (3.37)$$

In short, $y_m^+(\rho) = O(\rho^{-1/2})$ ($\rho \rightarrow 0$). And since $\rho^{-1/2}$ is the characteristic length in L_ρ , this establishes the claim that the characteristic length of L_ρ is asymptotically proportional to its distance $y_m^+(\rho)$ from the wall.

It is appropriate here to discuss further the issue of the constancy of the order of magnitude of $A(\rho)$. It was shown that the rescaled variables belonging to each member of the scaling hierarchy satisfy (3.29) exactly (no approximation). The parameters ρ and ϵ do not appear in that equation (except implicitly in the definitions of the rescaled variables). Therefore although the definitions (3.28) of the rescaled variables \hat{y} and \hat{T}^ρ depend on ρ (3.28), the equation they satisfy does not. This suggests that in each scaling patch the functions $U^+(\hat{y})$ and $\hat{T}^\rho(\hat{y})$, of the ρ -dependent variable \hat{y} would be invariant (approximately) when ρ changes, i.e. would enjoy some ρ -independence when evaluated at the same value of \hat{y} within the various different scaling patches. This would hold as well for their derivatives. This conclusion is given more credence, in fact, by the observation that at the point $y^+ = y_m^+(\rho)$, i.e. at $\hat{y} = 0$, each term appearing in (3.29) has a value $(-1, 0, 1)$, respectively, independent of ρ , and the undifferentiated quantity $\hat{T}^\rho = 0$ does as well. It is to be concluded that $A(\rho) = O(1)$ for all ρ , and that there may be circumstances when the function A itself is almost constant.

3.4.5. Determination of $U^+(y^+)$ from A .

Knowledge of the characteristic function $A(\rho)$ of the hierarchy leads rigorously and uniquely, up to integration constants, to the profiles of U^+ and T^+ . This is done by integrating (3.36), (3.24) and (3.47), which are written here in terms of the general coordinate $y^+ = y_m^+$ in the hierarchy, representing the location of the maximal point of T^ρ :

$$\frac{dy^+}{d\rho} = -\frac{1}{A(\rho)}\rho^{-3/2}, \quad (3.38)$$

$$\frac{dT^+}{dy^+} = \rho, \quad (3.39)$$

$$\frac{dU^+}{dy^+} = 1 - T^+. \quad (3.40)$$

Integration of (3.38) yields $y^+ - C$ as a function of ρ , where C is an integration constant which can be determined by fitting a known value of y^+ with its known value of ρ . Inverting that function gives ρ as a function of $y^+ - C$. Integrating (3.39) and then (3.40) finally provides T^+ and U^+ . As mentioned, the resulting function U^+ is logarithmic if and only if $A = \text{constant}$.

3.4.6. *The case $\rho = \epsilon^4$*

It is seen from (3.27) that in the case $\rho = \epsilon^4$

$$d\hat{y} = \epsilon^2 dy^+ = d\eta, \quad (3.41)$$

so that \hat{y} and η differ only in their origins:

$$\hat{y} = \eta - \eta_m, \quad (3.42)$$

where η_m is defined as the value of η where $T^{(\rho=\epsilon^4)}$ has its maximum. Therefore it is to be expected that $\eta = 1$ is in the layer $L_{\rho=\epsilon^2}$. In fact, the order of magnitude of $1 - \eta_m$ can be found. At that point, the left side of (3.19) = 0, and the right side, by differentiating (3.15), is $O(2C\epsilon^6(1/\epsilon^2 - y_m^+)) - \epsilon^4$. The graphs in Fig. 2 suggest that $C \sim 4$. Therefore $1/\epsilon^2 - y_m^+ \sim (1/8)\epsilon^{-2}$, i.e.

$$1 - \eta_m \sim 1/8. \quad (3.43)$$

Empirical data show, in fact, that $1 - \eta_m \sim .1$.

In summary, when $\rho = \epsilon^4$, the location of the maximum adjusted Reynolds stress $T^{(\rho=\epsilon^4)}$ lies within a distance of about .1 (in η , i.e. in \hat{y} for this value of ρ) of the maximum of T^+ itself, which is at $\eta = 1$. Thus for $\rho = \epsilon^4$, except for a small shift of the order $\sim .1$, \hat{y} and η are identical scaled distances. Thus the centerline $\eta = 1$ lies in the layer $L_{\rho=\epsilon^2}$, where U^+ and $\hat{T}^\rho = \frac{T^\rho - T_m^\rho}{\epsilon^2}$ (3.28) are regular functions of η . This corroborates the assertion to that effect following (3.9).

3.5. *The question of logarithmic-type growth*

A central issue in the history of turbulent channel flow investigations is whether and where the mean velocity profile exhibits a logarithmic growth. The approach adopted in this paper provides new insight into this issue. The first conclusion to be reached is that logarithmic profiles of U^+ depend crucially on $A(\rho)$ (Section 3.4.4) being constant. If it is constant, then exact logarithmic growth follows easily from the calculations below. If it is not constant, then the growth is not logarithmic. Finally if A is almost constant (and reasons for supposing that it is so under certain circumstances are given), then the profile of U^+ is bounded between two nearby logarithmic functions. Finally in Sec. 3.5.2, a nonrigorous argument is presented leading to the

conclusion that as $Re \rightarrow \infty$, A approaches a constant in certain moving ranges (characterized explicitly) of y^+ values.

3.5.1. The issue of the constancy of $A(\rho)$

The reasoning following (3.37) and below in Sec. 3.5.2 indicates that A may be approximately constant for values of y_m^+ far from the limits of its allowed range (3.25). For now, suppose that $A = \text{constant}$ in some interval. From (3.38), one finds

$$y_m^+ = C + \frac{2}{A} \rho^{-1/2}, \quad \rho = \frac{4}{A^2} (y^+ - C)^{-2}, \quad (3.44)$$

and hence from (3.39),

$$\frac{dT^+}{dy^+} (y_m^+) = (2/A)^2 (y_m^+ - C)^{-2}, \quad (3.45)$$

Replacing y_m^+ by the general variable y^+ and integrating,

$$T^+(y^+) = C' - (2/A)^2 (y^+ - C)^{-1}. \quad (3.46)$$

Since $T^+ \rightarrow 1$ as $y^+ \rightarrow \infty$, the constant $C' = 1$.

Putting this into (3.5) yields

$$\frac{dU^+}{dy^+} = 1 - T^+ = (2/A)^2 (y^+ - C)^{-1}. \quad (3.47)$$

Integrating again,

$$U^+(y^+) = (2/A)^2 \ln(y^+ - C) + C'', \quad (3.48)$$

providing logarithmic growth with a "von Karman constant" $\kappa = \frac{1}{4} A^2$, although the usual empirical law lacks the constant C . An estimate for C could be found from (3.45) by matching the coordinates of some point on the right hand branch of Figure 4.

The conclusions (3.48) and (3.46) were under the assumption that $A = \text{constant}$, and under that very restrictive assumption are valid in the region (given explicitly) where the hierarchy was constructed. That assumption of constancy is unlikely ever to be exactly true. However the trend shown in the computed values of A in Fig. 5 (unknown accuracy) suggests that for large Re $A(\rho)$ may be "relatively" constant in interior regions of its range. An extreme case is discussed below in Sec. 3.5.2.

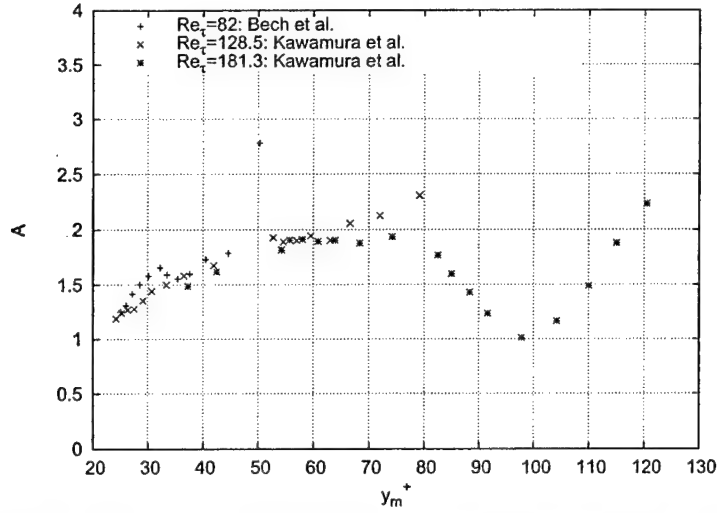


FIGURE 5. $A(y^+)$ for different Reynolds numbers as estimated by finite difference of $T^+(y^+)$. These estimates indicate a trend to larger internal intervals of relatively constant A for larger Re , thus agreeing with the present theory. The total range of the function A also increases with Re . The values of A were calculated from finite differencing DNS data of Bech *et al.* (1995) and Kawamura *et al.* (2000), (3.35), with locations y_m^+ determined from Fig. 3.

The effect of an approximate constancy of A on the validity of (3.46) and (3.48) can be easily seen. Write the dependence of A on ρ as dependence on $y_m^+ = y_m^+(\rho)$, i.e. $A = A(y_m^+(\rho))$. Suppose that the function $A(y_m^+)$ has range lying in the interval $A_0 - \sigma \leq A(y_m^+) \leq A_0 + \sigma$ for some constant A_0 and some small positive number σ . Then (3.36) becomes a pair of inequalities which bound the left side inside an interval depending on σ . The integration steps (3.45)–(3.48) then result in inequalities of the form

$$1 - (c_0 + \sigma c_1)(y^+ - C)^{-1} \leq T^+ \leq 1 - (c_0 - \sigma c_1)(y^+ - C)^{-1}, \quad (3.49)$$

$$(c_2 - \sigma c_3) \ln(y^+ - C) \leq U^+ - C'' \leq (c_2 + \sigma c_3) \ln(y^+ - C). \quad (3.50)$$

3.5.2. A limiting situation

In the hierarchy, each y^+ can be identified as being a point $y_m^+(\rho)$ for some ρ . The corresponding ρ will be called $\rho(y^+)$. In this way, each y^+ has a layer $L_{\rho(y^+)}$ containing y^+ , such that $-A(\rho)$ is the scaled second derivative of T^ρ at its peak. What mechanism will cause $A(\rho)$ to vary? Certainly not the mean momentum balance partial differential equation (3.29) in that vicinity, nor the values of the scaled derivatives $\frac{dT^\rho}{dy} = 0$ or $\frac{d^2U^+}{dy^2} = -1$ (from (3.29)) at that peak location, because these things do not change with ρ . The only

source for such a variation would be influence from neighboring layers. Extending that chain of influence, one could speak, on the one hand, of the influence due to layers $L_{\rho'}$ lower in the hierarchy with $\rho' > \rho$, stretching down to those values of y^+ at or near the lower limit of the hierarchy, i.e. the smallest values of y^+ which accommodate a layer, $y^+ \sim 20$ to 36 (3.25). It stands to reason that this influence of the lower part of the hierarchy will diminish as it becomes more remote, i.e. as the original y^+ becomes large.

The similar chain of influence extends toward higher values of y^+ , i.e. $\rho' < \rho$, capped only by the upper bound $y^+ = \epsilon^{-2}$, at or near the centerline. The centerline, however, becomes further, as $\epsilon \rightarrow 0$, from the original point y^+ if the latter is fixed or moves outward as $\epsilon \rightarrow 0$ more slowly than ϵ^{-2} .

Consider, then, a band of values of y^+ , depending on ϵ , which migrate away from the wall (measured in the wall coordinate y^+) as $\epsilon \rightarrow 0$, but more slowly than ϵ^{-2} . An example would be the intermediate band $\{\epsilon^{-1/2} < y^+ < \epsilon^{-3/2}\}$. In that interior band, the above argument suggests that the values of A will become more and more independent of any influence from the upper and lower limits of the hierarchy, and therefore would tend to become constant. In the limit as $\epsilon \rightarrow 0$, therefore, the analysis relating to the case $A = \text{constant}$ would apply so that (3.46) and (3.48) would be approached in that band.

3.6. Summary

These arguments verify that for

$$(\text{a value between } 20 \text{ and } 36) < y^+ \leq 1/\epsilon^2, \quad (3.51)$$

there is a layer L_ρ with $y^+ = y_m^+(\rho)$, where \hat{y} and \hat{T}^ρ are the proper scaled variables for distance and adjusted Reynolds stress \hat{T}^ρ (3.18). The characteristic length in this layer is $O(1)$ in the scaled variable \hat{y} , and $O(\rho^{-1/2})$ in y^+ . Thus for small enough ρ , the characteristic length coincides in order of magnitude with its position y^+ . In regions where A is approximately constant, logarithmic-type growth (3.49), (3.50) holds.

4. Turbulent channel flow induced by a pressure gradient

The purpose of this section is to illustrate that scale hierarchies exist in pressure driven flow. In fact, the evidence below indicates why these hierarchies not only comprise the stress gradient balance layer, but the entire flow domain of the traditionally defined logarithmic layer.

4.1. Previous analytical results

The following is a summary of the main findings contained in Wei *et al.* (2004). Each of these results is in accord with the scaling analysis in that paper and the data compiled there from past experimental and DNS sources. The same notation, such as y^+ , η , U^+ , T^+ , δ^+ , ϵ , is used in both that previous paper and the present one. The averaged mean momentum equation is (3.10), with boundary conditions (3.2) and (3.11).

- The channel is divided into four principal layers with the properties described previously in section 2.
- The Reynolds stress profile has the following features. The function T^+ vanishes with its derivative at $y^+ = 0$, increases monotonically with y^+ to a maximum value $T_m^+ = 1 - O(\epsilon)$ at a point $y_m^+ = O(1/\epsilon)$, and then slowly decreases, approaching the value 0 in a linear fashion as $\eta \rightarrow 1$. The expression for T^+ in this latter region is

$$T^+(\eta) = 1 - \eta + O(\epsilon^2). \quad (4.1)$$

- In a vicinity of the maximum, the function $T^+(y^+)$ has the behavior

$$T^+(y^+) \sim T_m^+ - C\epsilon^3(y^+ - y_m^+)^2. \quad (4.2)$$

- The mesolayer constitutes a region in which $|y^+ - y_m^+| \leq O(1/\epsilon)$. In it, the profiles are properly described in terms of \hat{T} and U^+ as functions of \hat{y} , where $T^+ = T_m^+ + \epsilon\hat{T}(\hat{y})$ and $y^+ = y_m^+ + \epsilon^{-1}\hat{y}$.

4.2. Hierarchy

To exhibit a hierarchy of layers in the channel flow profile, all that is needed is to revise slightly the definition of the adjusted Reynolds stresses (3.18). The new one is defined by

$$T^\rho(y^+) = T^+(y^+) + \epsilon^2 y^+ - \rho y^+. \quad (4.3)$$

This transforms the basic momentum balance equation (3.10) into

$$\frac{d^2 U^+}{dy^{+2}} + \frac{dT^\rho}{dy^+} + \rho = 0, \quad (4.4)$$

which is of the same form as (3.20).

Therefore, with the newly adjusted Reynolds stresses, the channel flow context is amenable to the balance exchange processes described in Section 3.4.1, the construction of a continuum of scalings with associated layers L_ρ in Section 3.4.3, and (under some assumptions) the derivation of logarithmic-like profiles in Section

3.5. The mean profile calculations are given here only for the simplest case $A = \text{constant}$, although analogs of (3.38)–(3.40) can be derived. As before, the expressions (3.36) and (3.35) are obtained in the present setting as well. But the integration of (3.35) yields a different integration constant. It is required that $\frac{dT^+}{dy^+} = 0$ at $y^+ = y_m^+$, the location of the maximum of the original unadjusted T^+ . Therefore (3.45) is replaced, under the same supposition that $A = \text{constant}$, by

$$\frac{dT^+}{dy^+}(y^+) = (2/A)^2 [(y^+ - C)^{-2} - (y_m^+ - C)^{-2}], \quad (4.5)$$

where now the variable y^+ is the same variable as in (3.46) and y_m^+ was just defined. Note that this derivative changes sign as y^+ passes through y_m^+ , as it should. Integrating once again, one obtains

$$T^+(y^+) = C' - (2/A)^2 (y^+ - C)^{-1} - (2/A)^2 (y_m^+ - C)^{-2} y^+. \quad (4.6)$$

But there is now a known boundary condition, $T^+ = 0$ at $y^+ = 1/\epsilon^2$; this serves to determine the constant C' .

Similar to the previous procedure, one may now use the integrated form of (3.10) to determine $\frac{dU^+}{dy^+}$ and integrate it with the boundary conditions that the derivatives of U^+ vanish as $y^+ \rightarrow \infty$ to obtain the same log dependence as in (3.48):

$$U^+(y^+) = (2/A)^2 \ln(y^+ - C) + C'', \quad (4.7)$$

Again, this is all under the (doubtful) assumption that A is constant. In the case that it is almost constant, one gets a pair of bounds like (3.50), valid now for the mean velocity in channel flow for the range of y^+ constructed as before. Note that in the case $\rho = \epsilon^2$, by (4.3) $T^\rho = T^+$.

4.3. The mesolayer

When $\rho = \epsilon^2$, the adjusted Reynolds stress T^ρ (4.3) coincides with the actual Reynolds stress T^+ , so that the corresponding layer $L_{\rho=\epsilon^2}$ will be located near the location of the maximum of T^+ . As mentioned in Section 4.1, this is how the mesolayer III was identified in Wei *et al.* (2004).

Each of the layers L_ρ can be thought of as an adjusted mesolayer, constructed by replacing the actual T^+ by T^ρ . In this sense, the actual mesolayer $L_{\rho=\epsilon^2} = \text{III}$ is just one among many. It is distinguished, however,

on the one hand as the location where the actual Reynolds stress reaches its maximum and its gradient changes sign, and on the other hand as the location where an important force balance exchange takes place.

5. Summary and Discussion

Theoretical tools of multiscale analysis were shown in Wei *et al.* (2004) to be useful in elucidating the structure of fully developed pressure driven turbulent channel flow found, in the same paper, by an examination of empirical data. That structure consists of four primary layers, one of them being a stress gradient balance layer, wherein the gradients of the viscous and Reynolds stresses balance, to within a very good approximation.

The analogous fully developed turbulent Couette flow consists of only the stress gradient balance layer, since those two gradients provide the only forces internal to the flow. In the present paper the range of applicability of the same multiscale techniques was shown to be much greater than shown in Wei *et al.* (2004). Applied to Couette flow, they reveal a mathematical structure in which the mean axial velocity and Reynolds stress exhibit a hierarchy of characteristic lengths and corresponding layers (in a sense secondary to the primary stress gradient balance layer) covering the major part of the flow domain. Other important information is also found, such as

(a) the characteristic lengths are asymptotically proportional to distance between the wall and the layer (they are reminiscent of, but different from, the mixing lengths of Prandtl (Prandtl (1925); Karman (1930));

(b) there is a rigorous connection between the $O(1)$ function $A(\rho)$, defined explicitly in terms of the layer hierarchy, and the mean velocity and Reynolds stress profiles;

(c) the U^+ profile is logarithmic in an interval only if $A = \text{constant}$ in that same interval; there is evidence, theoretical and computational, that it is relatively constant in some intervals in some cases. However, the focus of the paper has been more on offering explanations and reasons for important phenomena than on obtaining numerical information.

(d) The range of values of y^+ at which the layered region begins is predicted, and matches the empirical location of the onset of the traditional logarithmic profile; and

(e) order of magnitude properties of the Reynolds stress profile near the centerline (its curvature and the deviation of its maximum from 1) are found.

Another important finding is that a simple transformation, applied to the Reynolds stress, provides the way to transfer almost all of this information to the analogous pressure driven turbulent flow. Namely, in the latter setting there is also a hierarchy of scales and layers with properties (a)–(d) (properties (e) were already obtained in Wei *et al.* (2004)).

The hierarchical layer structure is associated with *exchange of balance* phenomena very similar to that used to reveal the properties of the mesolayer in Wei *et al.* (2004). The generalization in this paper used “adjusted Reynolds stresses”.

The success of theoretical tools applied only to the Reynolds averaged momentum balance equation may be surprising, since the equation is not closed, underdetermined, and therefore not capable of supplying an exact solution. Along with the analysis, some crucial, but minimal, assumptions of essentially physical nature were needed. The existence of a correct scaling of the variables with its concomitant scaling layer was in each case surmised by showing (i) that it leads to a differential equation which, to leading order, expresses a force balance between at least two of the three terms in an adjusted conservation of momentum equation, and (ii) that at some location, the terms in that differential equation are, when properly scaled, each $O(1)$ in magnitude. These criteria for the existence of a layer, in fact, also form the theoretical basis for the traditional inner and outer scalings. Other useful information, gleaned from empirical data, are that the mean velocity and Reynolds stress profiles are monotone increasing in distance from the lower wall, with their slopes decreasing beyond a certain point.

Overall, the formulations herein provide considerable information relative to the mathematical structure of the equations governing wall-turbulence. An overarching element of this analysis is the manner by which the terms in the momentum equation undergo the exchange of balance just mentioned. As shown regarding the fundamental layer structure of pressure driven channel flow by Wei *et al.* (2004) and herein with regard to the continuum of layers constituting the scale hierarchy, the particular exchange of balance phenomenon under consideration (others may occur under different flow configurations) takes place across a Reynolds number dependent layer and is characterized by specific scaling behaviors derivable from the properties of

the momentum equation within this layer. For the pressure driven flow equation employing the unadjusted Reynolds stress, this physically represents a transition from mean flow dynamics characterized by a balance between the viscous and Reynolds stress gradient to dynamics described by a balance involving all three forces, and on to a balance between the Reynolds stress gradients and the mean axial pressure gradient. For the members of the scale hierarchy (described by equations containing the adjusted Reynolds stresses), the physical interpretation is less clear cut. In either case, however, the flow field decomposition resulting from exchange of balance mathematics is retained as a property intrinsic to the structure of the mean flow equations. The implications of these conclusions are significant with regard to both modeling and theoretical considerations.

For example, since the mean flow equations have been shown inherently to contain a hierarchical layer structure, hierarchy-based models, e.g., Townsend (1976); Perry & Chong (1982); Perry & Marusic (1995); Kerstein (1999) would seem to have natural advantages. That is, irrespective of the details of any given model, the hierarchical property alone would likely yield a relatively high degree of efficacy. It is relevant to note that the results of section 3.4.3 revealed that for large (inner) distance, the distance from the wall is a length scale embodied in the composition of the scale hierarchy. While the distance from the wall is often invoked as a characteristic length in turbulent wall layers, e.g., Schlichting & Gersten (2000); Townsend (1976), its use relies on physical arguments that are not necessarily supported by observations. Perhaps the most common assertion in this regard is that the scale of the largest eddy near the wall is well represented by the distance from the wall. Measures of the scale of the vorticity bearing motions, however, do not lend direct support for such an assertion, Klewicki & Falco (1996). Indeed, the series of recent results from the University of Illinois and elsewhere (see below) indicate a significantly more complex situation in which instantaneous agglomeration of eddies (i.e., packets) collectively exhibit a distance from the wall scaling. Independent of empirical evidence, the present results provide theoretical justification for the distance from the wall as a characteristic length that is founded in the mathematical structure of the mean momentum balance. As revealed herein, this property comes about nontrivially through the structure of the scale hierarchy.

The mathematics underlying the mean momentum balance layer structure and the embedded scale hierarchy argue quite strongly against the appropriateness of the classical overlap ideas (as outlined in the

Introduction) for describing the mean velocity profile. That is, while consequences of overlap ideas have obviously been empirically verified to provide a useful framework for curve-fitting the data, the present analyses indicate that a conceptual framework in the form of outer and inner domains, plus something else in between, is contrary to the actual structure, in which the inner and outer scales are simply two extremes in a spectrum of scaling domains. The discussion is first clarified by noting that the inner/outer matching procedure described by Izakson (1937) and Millikan (1938) must be supplemented by the extremely limiting additional physical assumption that the mean velocity profile is strictly increasing with distance from the wall. Generic examples (Wei *et al.* (2004)), however, show that this is an unusual occurrence among two-scale problems. Another generic class of examples (discussed in the cited paper) questions the hypothesis that there even exists a domain of overlap. Moreover, in the case of Couette flow, simultaneously satisfying an outer (inertial) functional form and an inner (viscous) one is not conceptually consistent with the fact that the entire flow constitutes a stress gradient balance layer. Similarly, in boundary layer and pressure driven channel flow the empirical and theoretical evidence given herein and in Wei *et al.* (2004) show that, according to the mean momentum balance, the traditionally defined overlap layer actually contains all or part of three (principal) layers described by distinctly different dynamics. On the other hand, the exchange of balance property elucidated herein not only describes the layer-to-layer transitions and the internal structure of stress gradient balance layers, but also analytically predicts the existence of a generalized logarithmic-like variation in the mean profile. Specifically, in section 3.5 it was shown that under some circumstances the scale hierarchy naturally leads to mean profile variations close to logarithmic functions. These inequalities are, to date, believed to constitute the most theoretically well-founded bounds for the shape of the mean profile.

Given the loss of information associated with time averaging, these may in fact be the most that can be said with much theoretical rigor. It is important to note that the inexactness expressed by these bounds no doubt allows Reynolds number dependence, and both “logarithmic” and some limited power law forms to be fit between the bounds. Thus, even though the ideas of Izakson and Millikan yield conclusions which are generally consistent with those obtained here, overlapping function mathematics have little connection to either mean flow dynamics or to the origin of the logarithmic-like behavior of the mean profile.

Lastly, while the scale hierarchy is born from the mathematics associated with the structure of the time averaged equations of motion, speculative connections to the instantaneous motions in turbulent wall flows are worthy of brief mention. In particular, recent detailed PIV measurements provide mounting evidence that organized packets of hairpin-like vortices are an important (arguably irreducible) element of the instantaneous structure of boundary layers Meinhart & Adrian (1994); Adrian *et al.* (2000); Christensen & Adrian (2001); Ganapathisubramani *et al.* (2003); Tomkins & Adrian (2003). Key attributes of these vortex packets have intriguing similarities to the scale hierarchy, including: *i*) an embedded hierarchical structure, *ii*) linear scale growth with distance from the wall, and *iii*) a distinct velocity increment embedded within each level of the vortex packet structure. While these similarities may simply be coincidence, the identification of an instantaneous connection to the time averaged structure of the governing equations would constitute an enormous advance. For this reason, further investigation and experiments (especially at higher Reynolds numbers) are felt to be warranted.

Acknowledgments

This work was supported by the U. S. Department of Energy through the *Center for the Simulation of Accidental Fires and Explosions* under grant W-7405-ENG-48, the National Science Foundation under grant CTS-0120061 (grant monitor, M. Plesniak), and the Office of Naval Research under grant N00014-00-1-0753 (grant monitor, R. Joslin). The authors thank K. H. Bech, N. Tillmark, P. H. Alfredsson and H. Andersson; R. D. Moser, J. Kim and N. N. Mansour; K. Iwamoto, Y. Suzuki and N. Kasagi†; and H. Kawamura, H. Abe and K. Shingai‡ for supplying their DNS data; and M. Buschmann, M. Gad-el-Hak, and R. L. Panton for discussions relating to some of these issues.

REFERENCES

- ADRIAN, R. J., MEINHART, C. D. & TOMKINS, C. D. 2000 Vortex organization in the outer region of the turbulent boundary layer. *J. Fluid Mech.* **422**, 1–54.
- AFZAL, N. 1984 Mesolayer theory for turbulent flows. *AIAA J.* **22**, 437–439.

† <http://www.thtlab.t.u-tokyo.ac.jp/DNS/>

‡ <http://murasun.me.noda.tus.ac.jp/db/DNS.html>

- AFZAL, N. 1993 Asymptotic analysis of turbulent couette flow. *Fluid Dynamics Research* **12**, 163–171.
- AFZAL, N. 2001a Power law and log law velocity profiles in fully developed turbulent boundary layer flow: equivalent relations at large reynolds number. *ACTA Mechanica* **151**, 195–216.
- AFZAL, N. 2001b Power law and log law velocity profiles in fully developed turbulent pipe flow: equivalent relations at large reynolds number. *ACTA Mechanica* **151**, 171–183.
- BECH, K. H., TILLMARK, N., ALFREDSSON, P. H. & ANDERSSON, H. I. 1995 An investigation of turbulent plane couette flow at low reynolds numbers. *J. Fluid Mech.* **304**, 285–319.
- BUSCHMANN, M. H. & GAD-EL-HAK, M. 2003a Debate concerning the mean-velocity profile of a turbulent boundary layer. *AIAA J.* **41**, 565–572.
- BUSCHMANN, M. H. & GAD-EL-HAK, M. 2003b Generalized logarithmic law and its consequences. *AIAA J.* **41**, 40–48.
- CHRISTENSEN, K. T. & ADRIAN, R. J. 2001 Statistical evidence of hairpin vortex packets in wall turbulence. *J. Fluid Mech.* **431**, 433–443.
- DEGRAAFF, D. B. & EATON, J. K. 2000 Reynolds-number scaling of the flat-plate turbulent boundary layer. *J. Fluid Mech.* **422**, 319–346.
- GAD-EL-HAK, M. & BANDYOPADHYAY, P. R. 1994 Reynolds number effects in wall-bounded turbulent flows. *Appl. Mech. Rev.* **47** (8), 307–365.
- GANAPATHISUBRAMANI, B., LONGMIRE, E. K. & MARUSIC, I. 2003 Characteristics of vortex packets in turbulent boundary layers. *J. Fluid Mech.* **478**, 35–46.
- GEORGE, W. K. & CASTILLO, L. 1997 Zero-pressure-gradient turbulent boundary layer. *Appl. Mech. Rev.* **50** (12), 689–729.
- GILL, A. E. 1968 The reynolds number similarity argument. *Journal of mathematics and physics* **47**, 437–441.
- HINZE, J. O. 1975 *Turbulence*, 2nd edn. McGraw-Hill, New York.
- IWAMOTO, K., SUZUKI, Y. & KASAGI, N. 2002 Reynolds number effect on wall turbulence: Toward effective feedback control. *Int. J. Heat and Fluid Flow* **23**, 678–689.
- IZAKSON, A. 1937 On the formula for the velocity distribution near walls. *Tech. Phys. U. S. S. R.* **IV**, 2, 155.
- KARMAN, V. 1930 Mechanische Ähnlichkeit und turbulenz. *Nachr. Ges. Wiss. Göttingen, Math-Phys. Klasse* pp. 58–76.
- KAWAMURA, H., ABE, H. & SHINGAI, K. 2000 DNS of turbulence and heat transport in a channel flow with different reynolds and prandtl numbers and boundary conditions. In *Turbulence, Heat and Mass Transfer 3 (Proc. of the 3rd International Symposium on Turbulence, Heat and Mass Transfer)*, pp. 15–32. Aichi Shuppan.

- KERSTEIN, A. R. 1999 One-dimensional turbulence: model formulation and application to homogeneous turbulence, shear flows and buoyant stratified flows. *J. Fluid Mech.* **392**, 277–334.
- KLEWICKI, J. C. & FALCO, R. E. 1996 Spanwise vorticity structure in turbulent boundary layer. *International Journal of Heat and Fluid Flow* **17**, 363–376.
- LONG, R. R. & CHEN, T.-C. 1981 Experimental evidence for the existence of the mesolayer in turbulent systems. *J. Fluid Mech.* **105**, 19–59.
- MCKEON, B. J., MORRISON, J. F., LI, J., JIANG, W. & SMITS, A. J. 2004 Further observations on the mean velocity in fully-developed pipe flow. *J. Fluid Mech.* **501**, 135–147.
- MEINHART, C. D. & ADRIAN, R. J. 1994 On the existence of uniform momentum zone in a turbulent boundary layer. *Phys. Fluids* **7** (4), 694–696.
- MILLIKAN, C. B. 1939 A critical discussion of turbulent flows in channel and circular tubes. In *Proceedings of the Fifth International Congress of applied Mechanics* (ed. J. P. D. Hartog & H. Peters), pp. 386–392. Wiley, New York.
- MONIN, A. S. & YAGLOM, A. M. 1971 *Statistical Fluid Mechanics*, 1st edn. MIT Press.
- MOSER, R. D., KIM, J. & MANSOUR, N. N. 1999 Direct numerical simulation of turbulent channel flow up to $Re_\tau = 590$. *Physics of Fluids* **11** (4), 943–945.
- PANTON, R. L. 1990 Scaling turbulent wall layers. *Journal of Fluids Engineering* **112**, 425–432.
- PANTON, R. L. 1997 A Reynolds stress function for wall layers. *Journal of Fluids Engineering* **119**, 325–330.
- PANTON, R. L. 2003 Wall turbulence described by composite expansions. Preprint.
- PERRY, A. E. & CHONG, M. S. 1982 On the mechanism of wall turbulence. *J. Fluid Mech.* **119**, 173–217.
- PERRY, A. E. & MARUSIC, I. 1995 A wall-wake model for the turbulence structure of boundary layers. Part 1. Extensions of the attached eddy hypothesis. *J. Fluid Mech.* **298**, 361–388.
- POPE, S. B. 2000 *Turbulent Flow*, 1st edn. Cambridge University Press.
- PRANDTL, L. 1925 Bericht uber die entstehung der turbulenz. *Z. Angew. Math. Mech.* **5**, 136–139.
- SCHLICHTING, H. & GERSTEN, K. 2000 *Boundary Layer Theory*, eighth edn. Berlin: Springer-Verlag.
- SPALART, P. R. 1988 Direct simulation of a turbulent boundary layer up to $Re_\theta = 1410$. *J. Fluid Mech.* **187**, 61–98.
- SREENIVASAN, K. R. & SAHAY, A. 1997 The persistence of viscous effects in the overlap region, and the mean velocity in turbulent pipe and channel flows. In *Self-Sustaining Mechanisms of Wall Turbulence* (ed. R. Panton), pp. 253–272. Computational Mechanics Publications, Southampton, U.K.
- TENNEKES, H. & LUMLEY, J. L. 1972 *First Course in Turbulence*, 1st edn. MIT Press.

- TOMKINS, C. D. & ADRIAN, R. J. 2003 Spanwise structure and scale growth in turbulent boundary layers. *J. Fluid Mech.* **490**, 37–74.
- TOWNSEND, A. A. 1976 *The Structure of Turbulent Shear Flow*, 2nd edn. Cambridge University Press, Cambridge, Great Britain.
- WEI, T., FIFE, P., KLEWICKI, J. & MCMURTRY, P. 2004 Properties of the mean momentum balance in turbulent boundary layer, pipe and channel flows. *J. Fluid Mech.* Under review.
- ZAGAROLA, M. V. & SMITS, A. J. 1997 Scaling of the mean velocity profile for turbulent pipe flow. *Physical Review Letters* **78** (1), 239–242.